Master's thesis

NTNU
Norwegian University of Science and Technology
Faculty of Natural Sciences
Department of Physics

Hursanay Turgun

Electron Microscopy Characterization of Aluminium-Copper-Titanium-Steel Joint made using the Hybrid Metal Extrusion & Bonding Method

Master's thesis in Applied Physics and Mathematics
Supervisor: Per Erik Vullum, Tina Bergh, Randi Holmestad
June 2020

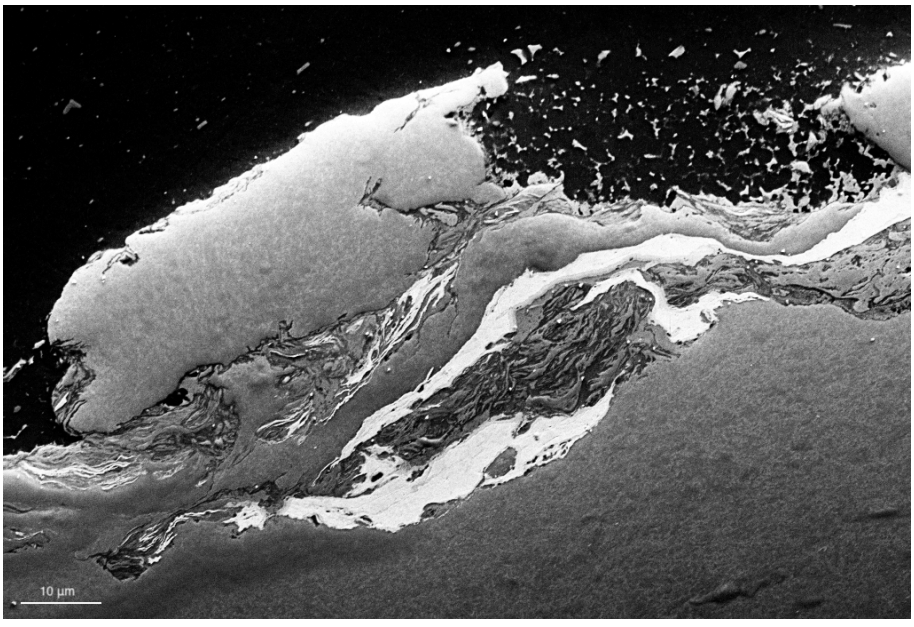

NTNU
Norwegian University of
Science and Technology

Hursanay Turgun

Electron Microscopy Characterization of Aluminium-Copper-Titanium-Steel Joint made using the Hybrid Metal Extrusion & Bonding Method

Master's thesis in Applied Physics and Mathematics
Supervisor: Per Erik Vullum, Tina Bergh, Randi Holmestad
June 2020

Norwegian University of Science and Technology
Faculty of Natural Sciences
Department of Physics

NTNU

Kunnskap for en bedre verden

This master's thesis has been completed as a conclusion of my studies in the 10 semester integrated master's degree in Applied Physics and Mathematics at the Norwegian University of Science and Technology (NTNU). The work started in January 2020 and the thesis was submitted in June 2020. This thesis is my independent work undertaken with supervision from Per Erik Vullum, Tina Bergh and Randi Holmstad.

This thesis is continuation of my project work titled "Electron Microscopy Characterization of Hybrid Metal Extrusion and Bonding Joint" (December 2019). Some of the content from this project work have been re-given here. This was done to be able to better present the scope of the scientific work that has been done during the final year of my master's degree in its entirety.

I thank my supervisors for their valuable guidance. I thank Filippo Berto and Øystein Grong for fruitful discussions. I thank Per Erik Vullum and Tina Bergh for making the FIB specimens. I thank Tina Bergh for providing me with the code that was used as a basis for the data analysis in HyperSpy. I thank Lise Sandnes and Jørgen Blindheim for doing the mechanical tests in this thesis.

Abstract

Multi-material joints are useful in production of lightweight structures with high performance and functionality. This thesis examines a joint welded together using the innovative Hybrid Metal Extrusion & Bonding (HYB) method. The joint has three base metals, copper Cu-H02, titanium (Ti) grade 2 and steel HTC590, joined together by an aluminium (Al) alloy filler metal, AA6082-T4, in one pass. The main objective in this thesis is to investigate the bonding mechanisms and bond strength of the joint in three steps. That is, the joint is investigated on the microscale by use of scanning electron microscopy (SEM), on the nanoscale by use of transmission electron microscopy (TEM), and mechanical properties are investigated by use of Vickers hardness test and tensile test.

The SEM studies of the joint, done through SE-imaging, focused on gaps and deformations, differences in grain structure between the bulk and the part close to the interface and to what extent there are regions of mixing between the metals along the interface. Results show that the Al-Cu interface is the only one that exhibits large pores and deformations, while the Al-Ti and Al-steel interfaces are tightly bonded. In addition, there are several fragments in the Al filler metal that originate from the Ti interface despite being close to the more deformed Cu interface. SE images show that grain refinement is only visible at the Al-steel interface. Intermixed swirl-like regions, indicating possible intermetallic compound (IMC) formation, seem to be present at all three interfaces.

The TEM studies were done through high-angle annular dark field scanning-TEM (HAADF-STEM) imaging, bright field (BF) TEM imaging, selected-area diffraction (SAD) and energy-dispersive spectroscopy (EDS) mapping. Four specimens were examined in TEM with focus on IMC formation, two from each of the Al-Cu and Al-Ti interfaces. In the Al-Cu specimens, the BF-TEM and HAADF-STEM images show that the IMCs grew uniformly and continuously along the interface, while the SAD and EDS results show that there are three types of IMCs present. The discovered Al-Cu IMCs are Al_2Cu, Al_4Cu_9 and AlCu, and their average thicknesses, as seen in the HAADF-STEM images, are 260 ± 43 nm, 217 ± 51 nm and 200 ± 44 nm, respectively. In the Al-Ti specimens, BF-TEM and HAADF-STEM images show presence of large regions of mixing at the interface, with significant concentration of Al, Si and Ti at these regions. Such regions resemble a combination of mechanical interlocking and IMC formation. At the rest of the Al-Ti interface without these large mixing regions, images and EDS maps reveal presence of a thin layer containing significant concentration of Al, Si and Ti, with an average thickness of 51 ± 4 nm. Regions with significant concentration of both Al, Si and Ti are possibly Al-Si-Ti IMCs. SAD or layerwise EDS analysis to determine exact IMC composition could not be performed on the Al-Ti specimens due to the regions with possible IMCs being too thin. In both the Al-Cu and Al-Ti specimens, the IMCs are thinner than what is typically obtained by other joining methods.

The results from the Vickers hardness tests show that all three base metals have been affected by the pressure during the welding process and got harder close to the interfaces. This means that both Cu, Ti and steel have work hardened closer to the interfaces and have higher resistance to deformation. Al does not display a significant difference in hardness closer to the interfaces and further away, since all of the Al experienced similar conditions when getting pressed through

the extrusion pin during welding.

The tensile tests were performed on four specimens from each of the Al-Ti and Al-steel interfaces. All the Al-Cu specimens broke during machining and could not be tensile tested. The fracture surfaces of the tensile tested specimens were subsequently examined in SEM. The results show the ductile nature of the Al-Ti specimens as they undergo elastic deformation and subsequent plastic deformation, including necking, before fracturing. The Al-Ti specimens fractured well within Al, indicating a strong bonding mechanism at the interface most likely due to IMCs and mechanical interlocking. The Al-steel specimens were more brittle as they fractured sharply at the interface between Al and steel without plastic deformation. There were remnants of both Al, steel and possibly IMCs on the fracture surfaces, indicating significant bonding between the metals at the interface. The mean ultimate tensile strength of the Al-Ti and Al-steel specimens were 305 ± 1 MPa and 266 ± 21 MPa, respectively. These large numbers indicate that both of the interfaces, Al-Ti and Al-steel, have high strength.

Finally, several suggestions are given to guide further work for better understanding of HYB. SAD and EDS mapping of the Al-steel interface with focus on the IMC formation is advised as it is the only interface of the joint that has not been studied in TEM in this thesis. Scanning precession electron diffraction (SPED) should be used to investigating the composition of the IMCs formed in thin layers, such as at the Al-Ti interface. To measure the hardness of the IMCs, a hardness test with smaller indentation diameter than that of the Vickers test used in this thesis should be used. A suggestion is nanohardness testing. To better understand the impacts HYB has had on the metals, electron backscatter diffraction (EBSD) in SEM, imaging in TEM or SPED in TEM could be used to examine difference in the grain structure of the metals' bulk region and parts close to the interface. If new joints could be made using HYB method to be studied as in this thesis, the initial conditions should be monitored in order to facilitate a better comparison. This includes the properties such as the surface roughness of the metals, which can be measured prior to welding. The macroscopic pores at the Al-Cu interface in the joint, which are disadvantageous for the weld quality, could be a result of the placement of Cu during welding. It would be of interest to have new joints made with different placements of the metals to test whether placement is significant for the formation of gaps, pores or deformations.

All in all, the results in this thesis are promising for HYB as a viable and robust welding technique. The small thickness of the intermetallic compunds gives it a competitive advantage compared to other welding techniques. As such, HYB should be pursued further as a way to create the high-performance and lightweight multi-material structures that could bring us one step closer to a more energy efficient future.

Sammendrag

Multimaterielle skjøter er nyttige i produksjon av lette strukturer med høy ytelse og funksjonalitet. Denne avhandlingen undersøker en skjøt sammensveiset ved bruk av den innovative Hybrid Metal Extrusion & Bonding (HYB) metoden. Skjøten har tre basismetaller, kobber Cu-H02, titan (Ti) klasse 2 og stål HTC590, som er sammenføyd ved hjelp av et aluminium (Al) legeringsfyllmetall, AA6082-T4. Hovedmålet i denne oppgaven er å undersøke bindingsmekanismene og bindingsstyrken til skjøten i tre trinn. Skjøten blir undersøkt på mikroskalaen ved bruk av skanningselektronmikroskopi (SEM), på nanoskalaen ved bruk av transmisjonselektronmikroskopi (TEM), og mekaniske egenskaper blir undersøkt ved bruk av Vickers hardhetstest og strekkprøve.

SEM-studiene, gjort gjennom SE-avbildning, fokuserte på gap og deformasjoner, forskjeller i kornstruktur mellom bulk og delen nær grensesnittet og i hvilken grad det er områder av blanding mellom metallene langs grensesnittet. Resultatene viser at Al-Cu-grensesnittet er det eneste som viser store porer og deformasjoner, mens Al-Ti og Al-stål-grensesnittene er tett bundet. I tillegg er det flere fragmenter i Al-fyllstoffmetallet som stammer fra Ti-grensesnittet til tross for at de er nær det mer deformerte Cu-grensesnittet. SE-bilder viser at kornforfining bare er synlig på Al-stål grensesnittet. Steder med blanding, som indikerer mulig dannelse av intermetallisk forbindelse (IMC), ser ut til å være til stede ved alle de tre grensesnittene.

TEM-studiene ble gjort gjennom high-angle annular dark field scanning TEM (HAADF-STEM) avbildning, bright field (BF) TEM avbildning, selected-area diffraction (SAD) og energy-dispersive spectroscopy (EDS). Fire prøver ble undersøkt i TEM med fokus på IMC-dannelse, to fra Al-Cu-grensesnittet og to fra Al-Ti-grensesnittet. I Al-Cu-prøvene viser SAD og EDS resultatene at det er tre typer IMC-er til stede, mens BF-TEM og HAADF-STEM bildene viser tykkelsene på IMC-ene og også at IMC-ene vokser jevnt og kontinuerlig langs grensesnittet. De oppdagede Al-Cu IMC-ene er Al_2Cu, Al_4Cu_9 og AlCu, og deres gjennomsnittlige tykkelse er henholdsvis 260 ± 43 nm, 217 ± 51 nm og 200 ± 44 nm. I Al-Ti-prøvene viser bilder av BF-TEM og HAADF-STEM tilstedeværelse av store områder med blanding ved grensesnittet, med betydelig konsentrasjon av Al, Ti og Si i disse områdene. På resten av Al-Ti-grensesnittene, uten disse blandingsområdene, avslører EDS-kart tilstedeværelsen av et tynt lag som inneholder betydelig konsentrasjon av Al, Si og Ti, med en gjennomsnittlig tykkelse på 51 ± 4 nm. Steder med betydelig konsentrasjon av Al, Ti og Si er muligens Al-Si-Ti-IMCer. SAD eller lagvis EDS-analyse for å bestemme nøyaktig IMC-sammensetning kunne ikke utføres på Al-Ti-prøvene på grunn av at områdene med mulige IMC-er er for tynne. I både Al-Cu-prøvene og Al-Ti-prøvene dannes IMC-ene i mye tynnere lag enn hva som dannes når det benyttes andre sveisemetoder enn HYB.

Resultatene fra Vickers hardhetstester viser at alle tre basismetallene har blitt påvirket av trykket under sveiseprosessen og har blitt arbeidsherdet nær grensesnittene. Dette betyr at både Cu, Ti og stål er sterkere nærmere grensesnittene og har høyere motstand mot deformasjon. Al viser ikke en vesentlig forskjell i hardhet nærmere grensesnittene og lenger bort, siden hele Al opplevevde lignende tilstander når den blir presset gjennom ekstruderingsstiften under sveising.

Strekkprøvene ble utført på fire prøver fra Al-Ti-grensesnittet og fire prøver fra Al-stål-grensesnittet. Alle Al-Cu-prøvene ble ødelagt under maskinering og kunne ikke testes. Bruddflatene i strekkprøvede prøver ble deretter undersøkt i SEM. Resultatene viser at Al-Ti-prøvene

er duktile, siden de gjennomgår elastisk deformasjon og påfølgende plastisk deformasjon, inkludert necking, før brudd. Al-Ti-prøvene sprekker godt innenfor Al, noe som indikerer en sterk bindemekanisme ved grensesnittet muligens på grunn av IMC-er og mekanisk sammenlåsning. Prøvene fra Al-stål er sprøere ettersom de brytes ved grensesnittet mellom Al og stål uten plastisk deformasjon. Det var rester av både Al, stål og muligens IMC på bruddflatene, noe som indikerte betydelig binding mellom metallene ved grensesnittet. Den gjennomsnittlige ultimate strekkfastheten for Al-Ti-prøvene er 305 ± 1 MPa, og for Al-stål-prøvene er den 266 ± 21 MPa. Disse tallene indikerer at begge grensesnittene, Al-Ti og Al-stål, har høy styrke.

Til slutt gis det flere forslag til hva som kan gjøres i forbindelse med videre arbeid for bedre forståelse av HYB. SAD og EDS-kartlegging av Al-stål-grensesnittet med fokus på IMC-formasjonen anbefales, da det er det eneste grensesnittet til leddet som ikke er studert i TEM i denne oppgaven. Skanningspresesjonselektrondiffraksjon (SPED) bør brukes til å undersøke sammensetningen av IMC-ene som er dannet i tynne lag, for eksempel ved Al-Ti-grensesnittet. For å måle IMCs hardhet bør det brukes en hardhetstest med mindre innrykkdiameter enn Vickers-testen som brukes i denne oppgaven. Et forslag er nanohardhetstesting. For bedre å forstå hvilken innvirkning HYB har hatt på metallene, kunne elektron-tilbakespredningsdiffraksjon (EBSD) i SEM, avbildning i TEM eller SPED i TEM brukes til å undersøke forskjell i kornstrukturen i metallenes bulkregion og områder nært grensesnittet. Hvis nye skjøter lagd ved bruk av HYB-metoden skal studeres, bør de opprinnelige forholdene bli observert for å legge til rette for en bedre forståelse av resultatene. Dette inkluderer egenskaper slik som overflatenes ruhet, som kan måles før sveising. De makroskopiske porene ved Al-Cu-grensesnittet, som er ugunstige for sveisekvaliteten, kan være komme av plasseringen av Cu under sveising. Det ville vært av interesse å få nye skjøter laget med forskjellige plasseringer metallene for å teste om plassering er viktig for dannelse av gap, porer eller deformasjoner.

Alt i alt er resultatene i denne oppgaven lovende for HYB som en levedyktig og robust sveiseteknikk. Den smale tykkelsen til de intermetalliske komponentene gir HYB et konkurransefortrinn sammenlignet med andre sveiseteknikker. Derfor bør HYB forfølges videre som en måte å skape de lette multimateriale strukrurene med høy ytelse som trengs for å bringe oss ett skritt nærmere en mer energieffektiv fremtid.

List of Abbreviations

ADF	Annular Dark Field
at%	Atomic Percentage
bcc	Body Centered Cubic
BF	Bright Field
BFP	Back Focal Plane
BM	Base Metal
BSE	Backscattered Electrons
CDF	Centered Dark Field
CP	Commercially Pure
DF	Dark Field
DP	Diffraction Pattern
EDS	Energy-Dispersive Spectroscopy
EZ	Extrusion Zone
fcc	Face Centered Cubic
FEG	Field Emission Gun
FET	Field-Effect Transistor
FFP	Front Focal Plane
FIB	Focused Ion Beam
FM	Filler Metal
HAADF	High-Angle Annular Dark Field
HAZ	Heat-Affected Zone
hcp	Hexagonal Close Packed
HRTEM	High Resolution TEM
HT	High Tension
HV	Vickers Hardness Number
HYB	Hybrid Metal Extrusion & Bonding
IMC	Intermetallic Compound
OM	Optical Microscope
SAD	Selected-Area Diffraction
SADP	Selected-Area Diffraction Pattern

sc	Simple Cubic
SDD	Si-Drift Detectors
SE	Secondary Electrons
SEM	Scanning Electron Microscope
STEM	Scanning Transmission Electron Microscope
SVD	Singular Value Decomposition
TEM	Transmission Electron Microscope
UTS	Ultimate Tensile Strength
WD	Working Distance
wt%	Weight Percentage

Contents

Chapter

1 Introduction

> *Take a magnifying glass to any part of your house and you will find a whole new world to explore. Use a powerful microscope and you will find another, complete with a zoo of living organisms of the most fantastic nature.*
>
> Mark Miodownik, Stuff Matters (2013)

1.1 Motivation and Context

Cost effective and energy efficient structures that also satisfy the goal of reducing environmental emissions are desired by industries worldwide, including transportation and infrastructure. Lightweight and durable structures with high performance and functionality are important in achieving this goal. By combining various materials together, their different properties can be utilised to improve the product performance, including the quality, weight and mechanical properties. This insight has created the emerging trend of using of multi-material and hybrid structures and thus the need for joining dissimilar materials [1]. Industries where multi-materials are becoming important include automotive industry, aerospace, clothing, implants, power generation and marine applications [1].

An example illustrating the usefulness of multi-material joining is to combine lightweight and corrosion resistant aluminium with strong and stiff steel in the products in the automotive and aerospace industries [2]. Combining strong and lightweight materials means that the fuel consumption and thus the CO_2 emission can be reduced, which significantly decreases the environmental impacts [2, 3]. There is also another benefit to introduce aluminium into parts previously made solely from steel. If the entire steel component is replaced with Al, for instance to reduce weight, the production process must be adjusted for Al. This might be costly and not always easily manageable. However, if the component can be produced with Al at the most parts except the ends which are steel, the ends can be processes in the same way as before.

When it comes to joining metals together there are several alternatives. Many joining techniques, such as soldering, brazing and fusion welding, involve melting of metals which can deteriorate the properties of the metals and cause uncontrolled solidification. Solid-state welding processes do not melt the metals and can thus produce welds without degrading the metals in the same way [4]. Solid-state welding is additionally suitable for joining both similar and dissimilar metals, which is not the case for many other methods, such as fusion welding [4]. Another common joining technique is use of rivets which mechanically fasten metals together. An example can be found in aircrafts, where rivets are used to join stringers to airframe skins [4]. Rivets have the disadvantage of adding weight to the structure and causing stress concentration at the rivet holes thus tripling the local stress [4]. Due to this disadvantage, high quality welds can have superiority over rivets. Despite this, rivets are often used rather than welding, for instance in aircraft construction, due them being more consistent. This adds to the motivation of developing

and investigating solid-state welding processes that can produce excellent welds without degrading the metals.

In this thesis, a joint welded together using the newly developed solid-state welding method called Hybrid Metal Extrusion & Bonding (HYB) is examined. HYB has many superior characteristics over other common solid-state welding techniques, including performing welding at lower temperatures (approximately 400 °C) with shorter welding time (around few seconds) [5]. This preserves the properties of the metals better, including reducing the extent of the HAZ/soft zone, especially in Al, and avoiding dissolution of strengthening precipitates and dispersoids in Al. HYB offers great flexibility and possibility to join a broad range of metals. As an example, the joint examined in this thesis has four dissimilar metals welded together in one passing. To be able to join four metals simultaneously both decreases the cost and increases the efficiency.

The joints produced by HYB can be used in the industries by themselves or can act as intermediaries. Many easily available traditional methods exist to join similar metals together, but these can be inadequate when it comes to joining dissimilar metals. To solve this, HYB-joints of dissimilar metals at smaller scale can be supplied to the industries. Industries can than use the common traditional methods available for them to join the base metals of the joint to similar metals easily. This way, industries will be able to create large scale dissimilar metal joints with the methods they already possess by using HYB-joints as intermediaries.

Since the HYB process is relatively new, not much previous research exist on HYB-joints. Therefore, the work done in this thesis is important as it produces improved understanding of HYB's benefits and disadvantages. A multi-material joint made using the HYB process is examined in this thesis primarily through means of electron microscopy, but also with the help of mechanical tests. The electron microscopy used in this thesis are scanning electron microscopy (SEM), transmission electron microscopy (TEM) and scanning transmission electron microscopy (STEM) performed in TEM, and they are all powerful tools for the purpose of this thesis. Electron microscopes can resolve structures of smaller objects than what can be done using optical microscopes. Ernst Ruska developed the first prototype for electron microscopy in 1931 and contributed hugely to the research in electron optics, for which he won the Nobel Prize in Physics in 1986 [6]. Ever since then, the electron microscopes have become invaluable tools in many different kinds of research, including research about biological and inorganic specimen, crystals and metals. In this work, electron microscopy is used to determine effects of HYB on the morphology of the weld-interfaces and the crystal structure of the interfacial IMCs.

1.2 Objectives and Scope

The aim in this thesis is to examine nano- and microscale properties and mechanical properties of a joint made using the HYB method. This leads to inceased understanding of HYB such that contributions can be made to future use and improvements of the method. The investigation is carried out in three parts. Firstly, SEM is used to examine whether a tight bonding has been formed. This is done by looking for gaps, deformations and potential changes to the grain structure by the use of SEM. Secondly, TEM is used to establish whether and which intermetallic compounds (IMCs) are formed on the interface of the different metals. In joints, IMCs sometimes occur at the interface between two metals, and they play critical role in how well the metals are joined together. The morphologies, chemical composition and crystal structure of possible IMCs are studied in TEM through high-angle annular dark field scanning-TEM imaging, bright field imaging, selected area diffraction (SAD) and energy-dispersive spectroscopy (EDS). Finally, the third step is to determine mechanical properties through Vickers hardness tests and tensile tests.

Three interfaces, Al-Cu, Al-Ti and Al-steel, were investigated in SEM, and two interfaces, Al-Cu and Al-Ti, were investigated in TEM. The reason for doing only the SEM characterization

of the Al-steel interface and omitting the subsequent TEM characterization is as the following. The HYB method was originally invented for Al-Al and thereafter Al-steel joining. At the Norwegian University of Science and Technology, the university at which HYB was invented, there are already other research units that are examining the Al-steel welding using HYB. However, no such work has been done or is being done on Al-Cu and Al-Ti joints made using HYB. Therefore, it is reasonable to focus on the Al-Cu and Al-Ti interfaces. In addition, it was necessary to limit the scope of this thesis, both due to the fact that the work done in this thesis is already a tremendous amount, and also because the thesis was written during a global pandemic, which limited the access to the experimental equipment.

The thesis starts with providing the necessary background theory needed to perform examinations of the joint and further assessments and interpretations of the results, in chapter 2. In the beginning, section 2.1 starts with introducing general concept of joining of metals, and explains some of the most common solid-state welding techniques as well as presenting the workings of HYB itself. The same section also introduces methods to tests these techniques through mechanical tests. Section 2.2 goes through theory of crystallography, which is essential in understanding the arrangement of atoms in crystalline solids, which gives important information about the materials being studied in this thesis. Combining this knowledge with the theory of diffraction in section 2.3, a successful investigation of the IMCs formed on the interfaces of the joint can be performed with the results from TEM.

The joint being examined in this thesis has three base metals (BM), copper (Cu) in half hard condition Cu-H02, titanium (Ti) in grade 2 and dual phase steel HTC590. These three base metals are joined together by the filler metal (FM) AA6082-T4, which is an aluminium (Al) alloy with magnesium and silicon as the principal alloying elements and is wrought and heat-treatable with good machinability and weldability. The general properties of Al, Cu, Ti and steel are presented in section 2.4. The same section also introduces general concept of IMCs as well as the IMCs that can be formed between the FM, Al, and the three BMs, Cu, Ti and steel. Understanding the properties of these metals and the interplay between them makes it possible to interpret the observations made in electron microscopes and evaluate the quality of the joint. Thereafter, one can better understand the effect HYB has on the metals themselves, and also the properties of the interfaces between the different metals in the joint. The theory of TEM, including the STEM mode, is given in section 2.5, and the theory of SEM is given in section 2.6.

In chapter 3, a report of the experimental methods and the materials used is given. The chapter starts with presenting the exact composition of the metals constituting the joint being studied as well as the HYB process parameters used during welding of that joint, in section 3.1. Thereafter, SEM and TEM specimen preparation procedures are explained in section 3.2. The SEM and TEM characterization methods are described in section 3.3. The mechanical test procedures, i.e. Vickers hardness test and tensile test procedures, are explained in section 3.4. The method for data analysis of the results from SEM, TEM and mechanical tests are all described in section 3.5.

The results gathered by employing the experimental methods explained in chapter 3 are presented in chapter 4. The results are then discussed in chapter 5 in relation to the theory, and concluding remarks highlighting the main findings are given in chapter 6. Suggestions for further work is given in chapter 7. Additional information is provided in appendices A–H.

Chapter

2 Theory

2.1 Joining

This section aims to provide an overview over existing welding techniques before moving on to introduce the Hybrid Metal Extrusion & Bonding (HYB) method that was used to make the multi-material metallurgical joint examined in this thesis. A description of two different mechanical tests commonly used on joints has also been provided.

For metallurgical joints, there exist several different joining techniques, such as soldering, brazing, mechanical fastening, adhesive bonding and welding [7]. Welding is the technique that is most commonly used for the case of metals. Welding processes can be divided into two main categories, fusion welding and solid-state welding.

Fusion welding works by localized melting of the metals, followed by fusing the metals together while they cool and solidify [7]. Fusion welding is mainly used when joining similar metals, which are metals with similar chemical composition and mechanical properties. This technique is insufficient for dissimilar metals with large differences in properties. In regular fusion welding, external heat is applied and only a small fraction contributes to the melting of the materials and thus to coalesence. The rest of that energy leads to local heating of the metals and the formation of a wide *heat-affected zone (HAZ)* around the weld region [8]. This excess energy also contributes to global deformations and distortions [9]. HAZ represents a major problem as it causes permanent mechanical degradation of the base materials as a result of the microstructural changes that occur [10, 11]. The degradation then becomes the limiting factor in the resulting joint, restricting for example the load bearing capacity [12]. In addition to this melting heat-degradation of regions near the weld, the relatively uncontrolled solidification in the melt pool are the key problems in fusion welding.

Solid-state welding is a common term for welding processes that happen below the melting temperature of the materials thus involving neither melting nor solidification [7]. Contrary to fusion welding, solid-state welding processes are suitable for joining both similar and dissimilar materials, and can easily be automated without applying external heat thus without affecting the properties of parent materials through heat. Note that small amount of heat generation due to friction is unavoidable. Solid-state welding provides a more optimal structural performance as strength is not compromised by large amounts of HAZ or solidification, also, it achieves much higher joint efficiencies than that which can be attained by fasteners and adhesives [4].

Several commonly used solid-state welding techniques will be introduced in section 2.1.1 together with their advantages and limitations and properties of the joint interface post welding. Thereafter, HYB which is used to make the joint examined in this thesis will be introduced in section 2.1.2. Lastly, two different mechanical tests that are commonly used to assess the quality of joints are explained in section 2.1.3.

2.1.1 Selected solid-state welding techniques

This section will introduce some of the most common solid-state welding techniques. They are friction welding, friction stir welding, impact welding and diffusion bonding. For an even more detailed review, the reader is referred to the paper by Cai et al. [4].

Friction welding, including linear and rotary friction welding, is the oldest solid-state joining process that produces coalescence of materials under compressive force contact of workpieces rotating or moving relative to one another to produce heat and plastically displace material from the faying surfaces [13]. The general advantages and limitations of friction welding are as the following [4]. The advantages include that dissimilar materials can be joined together better than with fusion welding, the cycle time is relatively short. The limitations include that equipment can be costly. When joining dissimilar metals, the high temperature at the joint interface together with the severe deformation can result in intermetallic compound formation [14]. The maximum welding temperature during friction welding can be around 1000 °C [15] and the welding time lies on the scale of few seconds depending on the specimen.

Friction stir welding is another friction based welding process where a probe of material harder than the base material plunges into the abutting faces of the base-material plates and traverses with cyclic movement along the joint line to form the weld [16]. Here again, frictional heat gets generated to plasticize the interface materials and weld them together upon solidifying. The advantages and limitations of this process include the following [4]. The advantages include good mechanical properties in the weld region, absence of excessive intermetallics. The limitations, on the other hand, include high cost, and high temperatures that can cause undesirable thick intermetallic compounds. The maximum welding temperature during friction stir welding can be around 450 °C [17] and the process could take only few seconds of welding time depending on the specimen.

Impact welding is the process of welding together two or more pieces of metals by colliding them together with high speed. This action works by scouring off the oxides and other contaminants on the surfaces and achieving metallic bonding due to high pressure contact between these clean surfaces. The high speed characteristic for impact welding can be produced in different ways, including by using explosives in larger scale [18] or by using vaporizing foils [19], electromagnetic forces and laser-induced shock [20] in smaller scales. In the case of this thesis, the first mentioned explosive welding is the most relevant method with respect to the thickness of the metals that can be joined. *Explosive welding* has different advantages and limitations including the following [4]. Explosive welding can weld over extremely large areas (> 25 m^2), but can require high costs and secluded facilities. This method can result in sound welds that are stronger than the base metals since the interface zone is strong and does not have traditional heat damage (heat-affected zone) [21]. However, voids, cracks and melt zones can still occur in some cases [22] . The maximum temperature at the welding interface during explosive welding can be above 2000 °C [23], depending on the specimen. Since explosions happen fast, very short time is needed to perform explosive welding.

Diffusion bonding is, as defined by the International Welding Institute, a process for making a monolithic joint through the formation of bonds at atomic level, as a result of closure of the mating surfaces due to local plastic deformation at elevated temperature which aids interdiffusion at the surface layers of the materials being joined [24]. The advantages and limitations of diffusion bonding include the following [4]. The advantages include that high quality joints can be produce with no metallurgical discontinuities or porosity across the interface, and dissimilar metals can be joined. The disadvantages include that surface preparation beforehand is required, the primary bonding interface produced is weak thus require post bonding heat treatment, and high bonding pressure with long bonding time are required also. The maximum temperature at the welding

interface during diffusion bonding can be around 1000 °C [25, 26], depending on the specimen.

2.1.2 Hybrid Metal Extrusion & Bonding

Hybrid Metal Extrusion & Bonding (HYB) is a solid-state welding method invented by professor Øystein Grong [8] at NTNU for the purpose of aluminium welding. HYB process can produce sound joints at relatively low operating temperatures, with maximum temperature at around 400 °C over the span of only few seconds [5]. The patented HYB method utilises continuous extrusion as a technique to squeeze the aluminium *filler metal (FM)* into the groove between the two *base metal (BM)* plates to achieve joining between the metals under high pressure [27]. A third BM plate can be placed at the bottom also, to be joined at the same time.

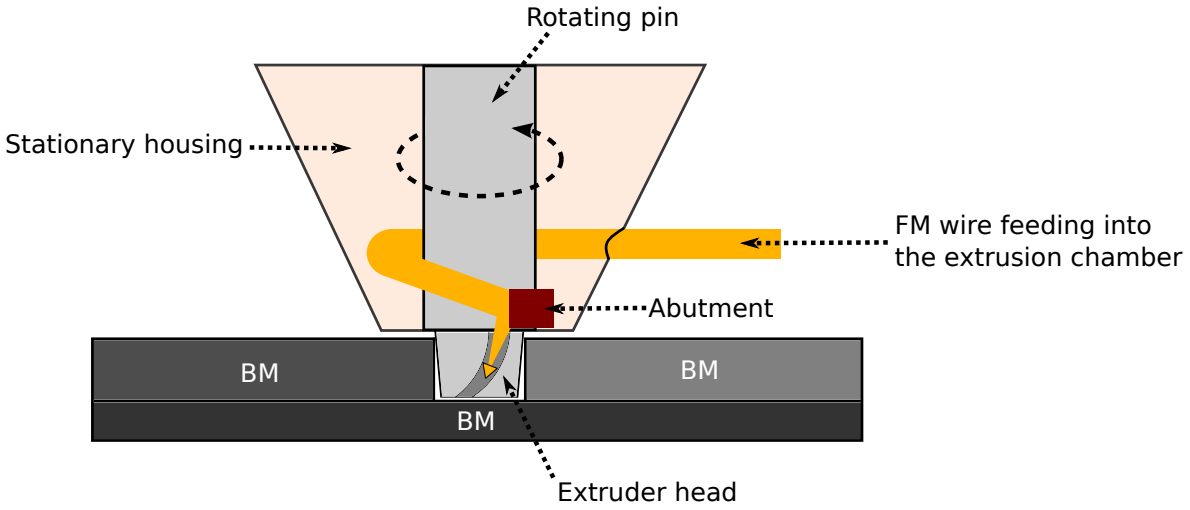

Figure 2.1: *Simplified illustration of a HYB process where three base metals (BM) are being joined together. The extruder head built around a rotating pin slides along the groove between the BMs. The filler metal (FM) wire gets fed into the extrusion chamber and flows against the abutment, which results in extrusion of the plasticized FM into the groove.*

A simplified illustration is shown in figure 2.1. During welding, firstly, the BMs are mounted in a fixture with a groove in between. Then, the FM extruder head which is built around a rotating cylindrical pin slides at a constant speed along the groove. The Al filler wire gets continuously dragged by friction into the extrusion chamber. The Al is then forced to flow against the abutment blocking the extrusion chamber. Finally, due to compression and pressure build-up, the process leads to extrusion of the plasticized aluminium in the axial direction through the rotating pin and downwards into the groove [28]. The rotation of the pin during the joining process will cause some of the BM along with the oxide layer on the groove sidewalls to be dragged around and get mixed into the FM, creating the *extrusion zone (EZ)*. With this, the HYB process can manage to joint the metals together. Other factors that contribute to the joining during HYB is shear deformation, surface expansion and pressure [5]. Due to the highly improved energy efficiency and low temperature of HYB compared to fusion welding, HAZ gets considerably reduced together with residual stresses and contaminants in the weld zone [29].

At present, up to four different metals can be joined together in one pass [30]. This thesis aims to undertake further identification of the process' advantages and weaknesses by examining a four metal joint made using HYB.

2.1.3 Mechanical tests

It is common to perform various mechanical tests to measure quantitatively the strength of a joint. This is done in the industry to evaluate if the joint is strong enough to be employed to different usages. There are many factors that can affect the strength of a joint. Metals in joint can, at some places, have macro and micro locks, called mechanical locks, where the metals are held together due to their surface deformations and without any metallic bonding at the atomic level. Metals that are welded together can also have formed intermetallic compounds which are desired in thin layers but can be damaging in thick layers due to their often brittle nature. Other factors than thick IMCs layers that are damaging for the efficiency of the joint include voids, tunnels, cracks [4] and HAZ. Although, mechanical tests on joints cannot always differentiate the individual contribution of these factors, they can provide knowledge about the general quality of the joint. Two mechanical tests that are relevant for this thesis are Vickers hardness test and tensile test.

2.1.3.1 Vickers hardness test

Vickers hardness test is a test in which a diamond pyramid indenter is pressed onto the surface of a test specimen with a certain force, and the surface area of the resulting indentation is measured [31]. The results reflect the hardness of the material under the assumption that hardness is proportional to the load necessary to produce a constant sized impression. The hardness of a material is widely used as an important property for estimating the wear resistance and strength of the metal [32]. The results from the test is given in terms of Vickers hardness number HV which is the pressure calculated from the average projected diagonal length d (mm) of the resultant indentation by the following equation [32]

$$HV = \frac{F}{A}, \tag{2.1}$$

where F is the force exerted and $A = \frac{d^2}{2\sin\theta}$ is the sloping area of the indentation with θ being the face angles of the pyramidal diamond. The unit of F here is kgf where 1 kgf = 9.8 N is the unit called kilogram-force. The unit of A here is mm^2.

If many measurements are carried out along a straight line crossing the interface between two metals in a metallic joint, it will be possible to investigate how the hardness of the metals have changed after the joining process. By comparing the measurement results from the bulk region (far away from the joint-interface) and the results from the region closer to the joint-interface, the effects of e.g. HAZ and intermetallic compounds can be investigated.

2.1.3.2 Tensile test

Tensile test is a destructive test process that provides information about the tensile strength, yield strength and ductility of materials [33]. Tensile test measures the force, often referred to as the load, required to break a material and the extent to which the specimen stretches or elongates to that breaking point. The results produce stress-strain diagrams. An example of such is shown in figure 2.2.

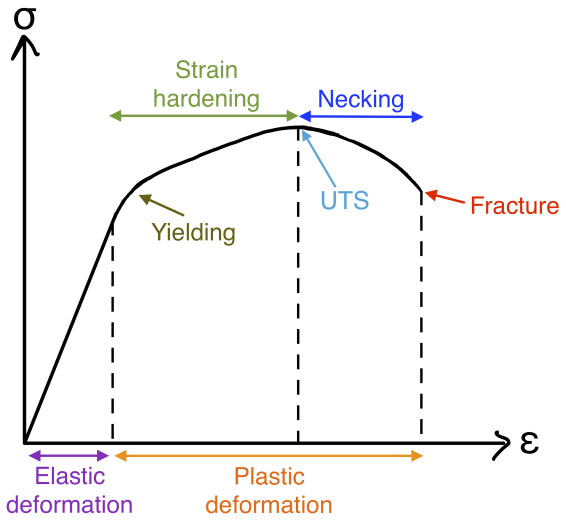

Figure 2.2: *An typical stress (σ) versus strain (ε) curve which can result from a tensile test. During tensile testing, the material firstly undergoes elastic deformation. After yielding, the material then undergoes plastic deformation, during which the material experiences strain hardening and necking before it fractures. The ultimate tensile strength (UTS) is the value of the maximum stress in the curve.*

Here, *stress* (σ) is experienced force F per unit area A and *strain* (ε) is relative change in length L of the specimen, i.e.

$$\sigma = \frac{F}{A} \tag{2.2}$$

and

$$\varepsilon = \frac{\Delta L}{L}. \tag{2.3}$$

Depending on where in the testing process these quantities are measured, various useful information about the material can be extracted from them. As can be seen in figure 2.2, in the beginning when strain is relatively small, an elastic deformation will occur to the material being tensile tested resulting in a linear relationship between stress and strain [34]. *Elastic deformation* is a reversible deformation process after which the material will be returned to its original shape. During this process, the cross sectional area and the length of the specimen material do not deviate much from the original value. Therefore it is common to use the so-called *engineering stress and strain* during this process. They are stress and strain values calculated from equations (2.2) and (2.3) by setting A and L equal to their constant original values before the testing begun [34]. During elastic deformation process, the limits of the Hooke's law apply and Young's modulus E can be measured. *Young's modulus*, also called elastic or tensile modulus, is a constant measuring the stiffness of a solid material given by the gradient of the stress-strain diagram, i.e. [35]

$$E = \frac{\sigma}{\varepsilon}. \tag{2.4}$$

Materials with low Young's modulus tend to be ductile and materials with high Young's modulus tend to be brittle [36].

Figure 2.2 shows that after the point of *yielding*, an increase in stress will cause permanent irreversible deformation called *plastic deformation* [34]. During this process, the material will undergo strain hardening and necking. *Strain hardening* denotes the effective strengthening of the material when many dislocations are created during plastic deformation [37]. *Necking* is a process during which the material is stretched while they get steadily thinner until fracture [38]. *Ultimate*

tensile strength (UTS) is the value of the maximum stress in the engineering stress-strain curve. During the process of plastic deformation, the area and length of the specimen material change significantly, which means that the engineering stress and strain defined earlier give considerably inaccurate measures. This raises the need to use the *true stress and strain* which are calculated form equations (2.2) and (2.3) by using the instantaneous values of A and L [34].

2.2 Crystallography

Crystallography is the study of the arrangement of atoms in crystalline solids which gives important information about the materials being studied. Compared to gases and liquids, the atoms in solids have more stable links with each other and are more likely to attain a crystalline state. This section will introduce the basic concepts of crystallography, which for the most part is based on the book, **Introduction to solid state physics, by Kittel (2005)** [39]. Other sources will be cited along the way.

Crystals are built by periodic repetition of identical groups of atoms. These groups are called *basis* and can contain either one or several atoms. The periodic repetition of the basis can be associated with mathematical set of points called a *lattice*. A lattice can be defined through three *translation vectors* $\boldsymbol{a}_1$, $\boldsymbol{a}_2$ and $\boldsymbol{a}_3$. These are defined such that a translation along an integer multiple of each translation vector takes one lattice point to another. Together the translation vectors constitute a *unit cell* [40], as shown in figure 2.3.

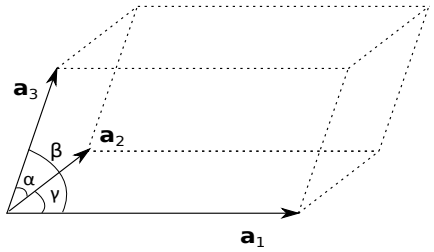

Figure 2.3: *Notation for a unit cell and its translation vectors $\boldsymbol{a}_1$, $\boldsymbol{a}_2$ and $\boldsymbol{a}_3$. [40]*

The angles

$$\alpha = \arccos\left(\frac{\boldsymbol{a}_2 \cdot \boldsymbol{a}_3}{|\boldsymbol{a}_2||\boldsymbol{a}_3|}\right), \tag{2.5a}$$

$$\beta = \arccos\left(\frac{\boldsymbol{a}_1 \cdot \boldsymbol{a}_3}{|\boldsymbol{a}_1||\boldsymbol{a}_3|}\right), \tag{2.5b}$$

$$\gamma = \arccos\left(\frac{\boldsymbol{a}_1 \cdot \boldsymbol{a}_2}{|\boldsymbol{a}_1||\boldsymbol{a}_2|}\right), \tag{2.5c}$$

are also shown in the same figure. A crystal lattice is built from repetition of a unit cell using the associated translation vectors. The smallest unit cell is called a *primitive unit cell* which contains only one lattice point in total. From figure 2.3 one can see that the volume of the unit cell is

$$V_c = |\boldsymbol{a}_1 \cdot \boldsymbol{a}_2 \times \boldsymbol{a}_3|\,. \tag{2.6}$$

Due to the periodic properties of the crystals, their lattices exhibit *translational symmetry*, meaning that the view of the atomic arrangements seen from every lattice point is the same. An operation applied on a crystal is a *symmetry operation* if all the properties of the crystal remain unchanged after the application [40]. It is important to note that this perfect symmetry only

holds under the assumption of *ideal crystals*. In reality, *real crystals* can deviate from this and have defects.

Defining a origin at one lattice point, every other lattice point can be reached with the vector

$$\boldsymbol{R}_{hkl} = h\boldsymbol{a}_1 + k\boldsymbol{a}_2 + l\boldsymbol{a}_3, \tag{2.7}$$

where h, k and l are integers called *Miller indices* and $\boldsymbol{a}_1$, $\boldsymbol{a}_2$ and $\boldsymbol{a}_3$ defines a primitive unit cell. If the crystal has a basis with N atoms, then the relative position from each lattice point to the center of atom $j \in 1, \cdots, N$ can be written

$$\boldsymbol{r}_j = x_j\boldsymbol{a}_1 + y_j\boldsymbol{a}_2 + z_j\boldsymbol{a}_3, \tag{2.8}$$

with $0 \leq x_i \leq 1$, $0 \leq y_j \leq 1$ and $0 \leq z_j \leq 1$.

Directions in a lattice parallel to $\boldsymbol{R}_{hkl}$ is denoted as $[hkl]$. All directions that are equivalent to $[hkl]$ by symmetry are denoted by $\langle hkl \rangle$. Additionally, (hkl) denotes a set of parallel planes where the Milled indices h, k and l is found in the following way [41]: Determine the points of intersection of the plane closest to the origin along the crystallographic axes represented by the three unit cell translation vectors. Then take the reciprocal of these numbers and reduce them to the lowest integers. All planes equivalent to (hkl) by symmetry are denoted by $\{hkl\}$. Note that a bar is typically used instead of a minus sign. That is $[\bar{h}kl] \equiv [-hkl]$.

In three dimensions, there are 14 different lattice types, together termed as *Bravais lattices*. They include *simple cubic (sc)*, *face centered cubic (fcc)*, *body centered cubic (bcc)* and *hexagonal*. Lattices are categorized into seven systems, which are triclinic, monoclinic, orthorhombic, tetragonal, cubic, trigonal and hexagonal. In addition to Bravais lattices there are other crystal types which will be of interest. One example is the *hexagonal close packed (hcp)* structure, which is a hexagonal Bravais lattice with two atoms in its basis.

When indexing hcp structures, it is common to use a four-axis hexagonal system called *Miller-Bravais indices*, unlike the three-axis system of Miller indices. This method gives rise to similar indices for crystallographically equivalent directions and planes, thus permits an easier crystallographic analysis. The four axes in the Miller-Bravais indexing system follows three translation vectors, $\boldsymbol{a}_1$, $\boldsymbol{a}_2$ and $\boldsymbol{a}_3$, 120° to each other at the basal plane of the hexagonal crystal and the last vector, c, perpendicular to all three previous axes [42]. With this, the indices of a plane will be of the type $(hkil)$ with the restriction that

$$h + k + i = 0. \tag{2.9}$$

Furthermore, an arbitrary crystal vector $\boldsymbol{R}_{uvtw}$ can be written in the form

$$\boldsymbol{R}_{uvtw} = u\boldsymbol{a}_1 + v\boldsymbol{a}_2 + t\boldsymbol{a}_3 + w\boldsymbol{c}, \tag{2.10}$$

where

$$u + v + t = 0. \tag{2.11}$$

In addition to the translational symmetry discussed above, crystals also exhibit other symmetry operations. The combined set of all symmetries of the crystal forms a group since successive applications of different symmetry operations must itself be a symmetry operation. This group of all possible symmetry operations which leaves the crystal unchanged is known as its *space group* [40]. The translational symmetries defined by the Bravais lattice is always a subgroup of the space group, since consecutive translations is just another translation. Since the translational subgroup is also normal [43], the quotient group of the space group and translational group is well-defined. These quotient groups describes all symmetries of crystal when leaving out

translations and are known as *point groups* [40]. There is a total of 230 space groups and 32 point groups.

The symmetry operations of a crystal is determined in reference to the *symmetry elements* which are points, axes, or planes with respect to which symmetry operations are performed. Possible symmetry operations are translation, rotation around an axis, rototranslation (also called screw; combination of rotation and translation), inversion with respect to a point, reflection with respect to a plane, rotoinversion (combination of rotation around an axis and an inversion with respect to a point on the axis and inversion), glide plane (combination of reflection and translation), rotoreflection (combination of rotation and reflection) [40]. A symmetry axis will be identified as being of order $n \in \{1, 2, 3, 4, 6\}$ if properties of the crystal remain unchanged after a rotation of $2\pi/n$ around that axis. Similarly, a symmetry axis will be identified as being of order $\bar{n} \in \{\bar{1}, \bar{2}, \bar{3}, \bar{4}, \bar{6}\}$ if properties of the crystal remain unchanged after a rotation of $2\pi/n$ around that axis and an inversion with respect to a point located on the same axis.

2.3 Diffraction

When sending a plane wave of electrons, with wavevector $\boldsymbol{k}_i$, towards a crystal, each position in the crystal will give rise to a spherical wave with amplitude proportional to the scattering probability [44]. Far away from the crystal, the scattered spherical waves are well approximated by plane waves with wavevector $\boldsymbol{k}_f$. In the first Born approximation, valid when the scattering is weak, the scattering amplitude is proportional to the potential energy multiplied with the incident wave [44]. Hence, the sum of the scattered electron waves with wavevector $\boldsymbol{k}_f$ is proportional to

$$A = \int_{\text{crystal}} \phi(\boldsymbol{r}) \mathrm{e}^{-i\boldsymbol{q}\cdot\boldsymbol{r}} \mathrm{d}V, \tag{2.12}$$

where $\boldsymbol{q} = \boldsymbol{k}_f - \boldsymbol{k}_i$ and ϕ is the electric potential. Using that ϕ satisfies Poisson's equation,

$$\nabla^2 \phi = -\frac{\rho}{\varepsilon} \tag{2.13}$$

where ρ is the charge density and ε is the permittivity, equation (2.12) can be rewritten

$$A = -\frac{1}{q^2} \int_{\text{crystal}} \phi(\boldsymbol{r}) \nabla^2 \mathrm{e}^{-i\boldsymbol{q}\cdot\boldsymbol{r}} \mathrm{d}V = \frac{1}{q^2 \varepsilon} \int_{\text{crystal}} \rho(\boldsymbol{r}) \mathrm{e}^{-i\boldsymbol{q}\cdot\boldsymbol{r}} \mathrm{d}V, \tag{2.14}$$

where it has been assumed that $\phi = 0$ outside of the crystal. Hence, the sum of scattered waves with wavevector $\boldsymbol{k}_f = \boldsymbol{q} + \boldsymbol{k}_i$ is related to the charge density of the crystal through the Fourier transform,

$$\mathcal{F}\{\rho(\boldsymbol{r})\} = \int_{\text{crystal}} \rho(\boldsymbol{r}) \mathrm{e}^{-i\boldsymbol{q}\cdot\boldsymbol{r}} \mathrm{d}V. \tag{2.15}$$

It can be useful to divide the whole crystal into unit cells. With n^{th} unit cell located at the lattice vector $\boldsymbol{r}_n$, the charge density can be written as

$$\rho(\boldsymbol{r}) = \rho_{\text{cell}}(\boldsymbol{r}) * \sum_{n=1}^{N} \delta\left(\boldsymbol{r} - \boldsymbol{r}_n\right), \tag{2.16}$$

where $*$ denotes convolution. Thus

$$\mathcal{F}\{\rho(\boldsymbol{r})\} = F(\boldsymbol{q}) \mathcal{F}\left\{ \sum_{n=1}^{N} \delta\left(\boldsymbol{r} - \boldsymbol{r}_n\right) \right\}, \tag{2.17}$$

where we have defined the *structure factor* $F(\boldsymbol{q})$, which represents the amplitude and phase of scattering of the charge density distribution of the unit cell,

$$F(\boldsymbol{q}) = \int_{\text{cell}} \rho_{\text{cell}}(\boldsymbol{r}) \mathrm{e}^{-i\boldsymbol{q}\cdot\boldsymbol{r}} \mathrm{d}V. \tag{2.18}$$

If the lattice vectors $\boldsymbol{r}_n$ can be written as integer multiples of the translation vectors $\boldsymbol{a}_1$, $\boldsymbol{a}_2$ and $\boldsymbol{a}_3$, then the Fourier transform of the delta functions in equation (2.17) can be written

$$\begin{aligned}
&\mathcal{F}\left\{\sum_{h=0}^{H}\sum_{k=0}^{K}\sum_{l=0}^{L}\delta\left(\boldsymbol{r}-h\boldsymbol{a}_1-k\boldsymbol{a}_2-l\boldsymbol{a}_3\right)\right\} \\
&= \sum_{h=1}^{H}\mathrm{e}^{-ih\boldsymbol{q}\cdot\boldsymbol{a}_1}\sum_{k=1}^{K}\mathrm{e}^{-ik\boldsymbol{q}\cdot\boldsymbol{a}_2}\sum_{l=1}^{L}\mathrm{e}^{-il\boldsymbol{q}\cdot\boldsymbol{a}_3} \\
&= \exp\left\{\frac{-i\boldsymbol{q}\cdot\left[(H-1)\boldsymbol{a}_1+(K-1)\boldsymbol{a}_2+(L-1)\boldsymbol{a}_3\right]}{2}\right\} \\
&\quad\cdot\left(\frac{\sin\left(H\boldsymbol{q}\cdot\boldsymbol{a}_1/2\right)}{\sin\left(\boldsymbol{q}\cdot\boldsymbol{a}_1/2\right)}\right)\left(\frac{\sin\left(K\boldsymbol{q}\cdot\boldsymbol{a}_2/2\right)}{\sin\left(\boldsymbol{q}\cdot\boldsymbol{a}_2/2\right)}\right)\left(\frac{\sin\left(L\boldsymbol{q}\cdot\boldsymbol{a}_3/2\right)}{\sin\left(\boldsymbol{q}\cdot\boldsymbol{a}_3/2\right)}\right).
\end{aligned} \tag{2.19}$$

When H, K and L becomes large, the last three factors will result in sharp spikes when $\boldsymbol{q}$ satisfies $\boldsymbol{q}\cdot\boldsymbol{a}_1 = 2\pi h$, $\boldsymbol{q}\cdot\boldsymbol{a}_2 = 2\pi k$, $\boldsymbol{q}\cdot\boldsymbol{a}_3 = 2\pi l$, for some integers h, k and l. This happens when

$$\boldsymbol{q} = \boldsymbol{g}_{hkl} \equiv \underbrace{2\pi\frac{\boldsymbol{a}_2\times\boldsymbol{a}_3}{\boldsymbol{a}_1\cdot\boldsymbol{a}_2\times\boldsymbol{a}_3}}_{\boldsymbol{b}_1}h + \underbrace{2\pi\frac{\boldsymbol{a}_3\times\boldsymbol{a}_1}{\boldsymbol{a}_2\cdot\boldsymbol{a}_3\times\boldsymbol{a}_1}}_{\boldsymbol{b}_2}k + \underbrace{2\pi\frac{\boldsymbol{a}_1\times\boldsymbol{a}_2}{\boldsymbol{a}_1\cdot\boldsymbol{a}_2\times\boldsymbol{a}_3}}_{\boldsymbol{b}_3}l, \tag{2.20}$$

meaning that the diffraction pattern of an ideal crystal will be sharp peaks located at the *reciprocal lattice vectors*, $\boldsymbol{g}_{hkl}$. Here, we have also defined the *reciprocal translation vectors*, $\boldsymbol{b}_1$, $\boldsymbol{b}_2$ and $\boldsymbol{b}_3$. The condition in equation (2.20) is formally called the *Laue condition* [39]. $\boldsymbol{g}_{hkl}$ is orthogonal to the set of planes denoted (hkl), as introduced in section 2.2. The distance, *d-spacing*, between two parallel planes in the set (hkl) is therefore

$$d_{hkl} = \frac{2\pi n}{|\boldsymbol{g}_{hkl}|} \tag{2.21}$$

where n is an integer. Note that a real space vector $[hkl]$ (see equation (2.7)) is not always parallel with a reciprocal space vector $\boldsymbol{g}_{hkl}$ defined in equation (2.20). This is because $\boldsymbol{b}_1$, $\boldsymbol{b}_2$ and $\boldsymbol{b}_3$ in general is not parallel with $\boldsymbol{a}_1$, $\boldsymbol{a}_2$ and $\boldsymbol{a}_3$.

When observing a diffraction pattern, one sees the intensity at each reciprocal vector q,

$$\begin{aligned}
I(\boldsymbol{q}) &= |\mathcal{F}\{\rho(\boldsymbol{r})\}|^2 \\
&= |F(\boldsymbol{q})|^2\left|\mathcal{F}\left\{\sum_{n=1}^{N}\delta\left(\boldsymbol{r}-\boldsymbol{r}_n\right)\right\}\right|^2. \\
&= |F(\boldsymbol{q})|^2\left(\frac{\sin\left(H\boldsymbol{q}\cdot\boldsymbol{a}_1/2\right)}{\sin\left(\boldsymbol{q}\cdot\boldsymbol{a}_1/2\right)}\right)^2\left(\frac{\sin\left(K\boldsymbol{q}\cdot\boldsymbol{a}_2/2\right)}{\sin\left(\boldsymbol{q}\cdot\boldsymbol{a}_2/2\right)}\right)^2\left(\frac{\sin\left(L\boldsymbol{q}\cdot\boldsymbol{a}_3/2\right)}{\sin\left(\boldsymbol{q}\cdot\boldsymbol{a}_3/2\right)}\right)^2.
\end{aligned} \tag{2.22}$$

where the results from equations (2.17) and (2.19) have been used. This means that one does not observe the phase of the diffracted electrons, only their amplitude.

Just as we divided the lattice into unit cells in equation (2.16), it also common to divide the unit cells further into individual atoms by writing the charge density in each cell as convolution of

the charge densities associated with each atom and a delta function for their position. The measure of the amplitude of the electron wave scattered from every atom is called the *atomic-scattering factor*, and is given by

$$f(\boldsymbol{q}) = \int_{\text{atom}} \rho(\boldsymbol{r}) \mathrm{e}^{-i\boldsymbol{q}\cdot\boldsymbol{r}} \mathrm{d}V, \tag{2.23}$$

It is similar to $F(\boldsymbol{q})$, but is associated only with one atom instead of one unit cell.

Written in terms of the atomic scattering factor, the structure factor evaluated at a reciprocal lattice vector $\boldsymbol{g}_{hkl}$ is

$$F(\boldsymbol{g}_{hkl}) = \sum_{i=1}^{N} f_i(\boldsymbol{g}_{hkl}) \mathcal{F}\left\{\delta(\boldsymbol{r} - \boldsymbol{r}_i)\right\}(\boldsymbol{g}_{hkl}) = \sum_{i=1}^{N} f_i(\boldsymbol{g}_{hkl}) \mathrm{e}^{-2\pi i(hx_i + ky_i + lz_i)}, \tag{2.24}$$

where the sum runs over the N atoms in the unit cell, atom i has position $\boldsymbol{r}_i = x_i\boldsymbol{a}_1 + y_i\boldsymbol{a}_2 + z_i\boldsymbol{a}_3$ and atomic scattering factor f_i. Therefore, $F(\boldsymbol{g}_{hkl})$ can be interpreted as the sum of the $f_i(\boldsymbol{g}_{hkl})$ terms from all the i atoms in the unit cell multiplied by a phase factor $\mathrm{e}^{-2\pi i(hx_i+ky_i+lz_i)}$. Intensities in the DPs, which are related to $F(\boldsymbol{g}_{hkl})$ as in equation (2.22), can be zero for certain (hkl) planes. This is called the *extinction rules*, and can be identified through analyzing $F(\boldsymbol{g}_{hkl})$ of each crystal structure.

It should be noted that the ideal Laue condition in equation (2.20) that we have worked with so far holds only for ideal cases, meaning a small deviation from that is inevitable in reality. This results in intensity in the DP even when the condition is not met exactly. How far we deviate from the exact condition is measured by a vector in reciprocal space, $\boldsymbol{s}$, called the *excitation error* or the *deviation vector*, such that equation (2.20) becomes

$$\boldsymbol{q} = \boldsymbol{g}_{hkl} + \boldsymbol{s}. \tag{2.25}$$

2.4 Materials

In section 2.4.1, short history and various properties of aluminium is examined. As mentioned shortly in section 2.1, aluminium is welded to other metals in the sample studied in this thesis. The three other relevant metals, copper, titanium and steel, are described in sections 2.4.2–2.4.4 together with how they react with Al.

2.4.1 Aluminium

Aluminium (Al) is one of the most abundant metallic element on earth [45]. In the first decade of the nineteenth century, Sir Humphrey Davy proposed the existence of Al which was then successfully isolated by Hans Christian Oersted in 1825. After approximately 60 years, in 1886, Paul Heroult and Charles M. Hall, independent from each other, developed the extraction method of Al from its most important and prolific source, bauxite [46]. The method consists firstly of extracting alumina (Al_2O_3) from its ore and reducing it in molten cryolite (Na_3AlF_6). Thereafter, further refinement is done using electrolytic processes to obtain Al-metal with around 99.9% purity. The process in total requires major amounts of electrical power. With large hydro power resources, Norway is a suitable place for aluminium production, where it started as far back as 1916 in Høyanger [47].

Al has atomic number 13 in the periodic table and has atomic mass 26.98 u where u is the atomic mass constant [48]. Al has face centered cubic (fcc) crystal structure with lattice parameter $a = 4.049$ Å at room temperature [49]. It is important to remember that lattice parameters depend on temperature and pressure. The fcc metals are ductile, formable and have

high toughness at low temperatures [46]. The fcc structure exhibits cubic symmetry and it has, for the case of Al, space group number 225 which is denoted using Hermann-Mauguin symbols as $Fm\bar{3}m$ [50, 51]. In this simple notation, F means face centered, m means mirror plane and $\bar{3}$ means a three-fold rotoinversion axis. The density of Al is fairly small at 2.7 g/cm^3, corresponding to approximately one third of the density of steel, giving it the property of being light weight. Al forms a thin oxide layer when exposed to air. In addition, Al typically has impressive thermal and electrical conductivity, but Al-alloys can be developed to have high electrical resistivity [45].

Al in its purest form is weak, making it less viable for use in the industries. Therefore it is common to strengthen Al by alloying it with elements such as copper, manganese, magnesium, silicon and zinc [46]. Different Al alloys are tailored to different application areas.

Aluminium alloys are conveniently characterized into two major categories, *casting alloys* that are directly casted into the final shape and *wrought alloys* that are deformed, forged extruded or rolled after initial making [45]. According to the international aluminium alloy designation system, casting alloys are identified with the labeling $yxx.x$ while wrought alloys are identified with $yxxx$ [52]. In both of these labeling systems, the first digit y indicates the main alloying element. For wrought alloys, and the trailing digits written as x denote modifications and amount of alloying elements. It is similar for casting alloys with the difference that the last decimal x indicates the form of the product. Among the large number of possible Al alloys, those in the $6xxx$ series are especially relevant for this study. $6xxx$ alloys have magnesium (Mg) and silicon (Si) as the principle alloying elements and are wrought and heat-treatable with good machinability and weldability.

The mechanical properties of the alloys are sometimes altered by exposing them to different conditions. The type of experienced treatment is precisely identified with a single letter and a number, this notation is called *temper designation*. One such treatment is *age hardening* (precipitation hardening), which has been designated the letter "T" followed by a digit identifying the basic heat treatment [46]. Age hardening has the purpose of strengthening and hardening alloys with formation of extremely small *precipitates* of a second phase within the original phase matrix, achieved through appropriate heat treatment and aging over a period of time [53]. Precipitates function as barriers for the dislocation movements. Among the various age hardening treatments, there is the possibility of letting the alloys age naturally in room temperature after a solution heat-treatment. This is denoted as T4 [8] and is the treatment that is relevant for the present study.

Another mechanism similar to age hardening that strengthens the alloys using interaction between the particles and dislocations within the matrix is *dispersion-strengthening*. In this process, a high density of fine particles of a very hard and inert material, termed *dispersoids*, are dispersed into the metals or metal alloys [53]. Due to dispersoids being nonreactive with the matrix phase, the strengthening effect is retained at elevated temperatures and for extended time periods, which is not the case with the precipitates of constituent phases.

It is common to have an oxide layer on metals pre-welding. This phenomena is especially prominent in Al alloys which have Al_2O_3 on their surface initially. This acts as a barrier to produce a bond [54]. Welding processes have to be effective enough to break this layer to achieve oxide-free surfaces to be welded.

2.4.2 Copper

Copper (Cu) exists in various forms in nature, such as native copper and copper oxides, carbonates and silicates, and the primary sources are low-grade deposits of copper sulfide ores [55]. Copper and copper alloys have wide variety of usage due to them being ductile, malleable, antimicrobial, having excellent thermal and electrical conductivity, and having good corrosion resistance [56].

Cu has atomic number 29 in the periodic table and has atomic mass 63.546 u [48]. Cu has fcc crystal structure with lattice parameter $a = 3.615$ Å at room temperature [49]. The properties of the fcc structure have already been discussed while introducing aluminium in section 2.4.1. Shorty summarized, Cu also has cubic symmetry and space group $Fm\bar{3}m$ which is number 225. The density of Cu is 8.9 g/cm^3 [56], which is fairly large compared to the density of Al.

Pure copper is known to be a soft metal, however various mechanical properties can be achieved through alloying, as in the case with Al. Based on the Unified Numbering System for metals and alloys, copper alloys are designated with a five-digit number preceded by the letter "C", where the digits depend on the alloys composition. The designations C10100 to C79900 are used for wrought alloys and C80100 to C99900 are used for casting alloys [57]. As in the case with Al, many processes exist to produce different tempers in copper and copper alloys. Among these, there exists a process called *cold work*, which is controlled mechanical operations for changing the form or cross section of a product and for producing a strain-hardened product at temperatures below the recrystallization temperature [58]. Cold worked copper is designated with a letter "H" followed by two digits. Among these, H02 is the notation used for the half-hard condition relevant for this study [59].

2.4.3 Titanium

The most important sources of titanium (Ti) are ilmenite ($FeTiO_3$) and rutile (TiO_2). The density of Ti is 4.5 g/cm^3, which is in the middle between that of Al and Cu. Ti has the highest strength to density ratio, but is limited in usage due to its high price. The high price is mainly a result of Ti's high reactivity with oxygen which creates the need for vacuum or inert atmosphere during production. This exact reason is also why Ti has good corrosion resistance since its is protected by a stable and adherent oxide surface layer that occurs immediately when exposed to air. Compared to Al, Ti is much more resistant to high temperatures, meaning that temperature can get much higher for Ti compared to Al before mechanical properties start to degrade.

Ti has atomic number 22 in the periodic table and has atomic mass 47.88 u [48]. Ti has hexagonal close packed (hcp) crystal structure in its α phase with lattice parameters $a = 2.950$ Å and $c = 4.686$ Å at room temperature [49]. However, when temperature exceeds approximately 882 °C, Ti exhibits a phase transformation into its β phase with a body centered cubic (bcc) crystal structure [60]. The hcp structure corresponds to space group nr. 194 which is $P6_3/mmc$, while bcc structure corresponds to space group nr. 229 which is $Im\bar{3}m$ [50, 51].

Ti is readily available in relatively pure form that contain small amount of impurity elements, and these are called *commercially pure (CP)* Ti. The CP-Ti are classified into several *grades* depending on their corrosion resistance, ductility, and strength. The oxygen content in CP-Ti vary from 0.18%, at grade 1, to 0.40%, at grade 4, affecting the metal's yield stress level. Also, the iron (Fe) content in CP-Ti vary from 0.20%, at grade 1, to 0.50%, at grade 4 [60]. Ti is also available in alloyed form. Commercial titanium alloys are classified into three groups, which differ in their mechanical properties depending on the alloying element [60]. Ti alloys can further be exposed to different hardening mechanisms, such as solid solution hardening, strengthening by a high dislocation density, boundary hardening and precipitation hardening.

2.4.4 Steel

Steel is one of these most used materials in the world, with its great strength, toughness, machinability, weldability, formability, corrosion resistance and fatigue resistance. Iron (Fe) is the base material of steel, making up high percentage of the composition [61]. In the specimen examined in this thesis, carbon steel is used and it is a type of steel that contain iron of over 90% [61].

Fe is alloyed with carbon (C) and other elements to create different types of steel with varying strengths and other properties, such as oxidation or corrosion.

Fe has atomic number 26 in the periodic table and has density 7.86 g/cm^3 [50]. Fe has at least three allotropes occurring naturally in bulk form. At low temperatures ($<\sim$800 °C), α (called ferrite) occurs at lower pressures ($<\sim$ 100 kbar) while ϵ occurs at pressures higher than the range in which α occurs [62]. The third one is called γ (also called austenite), and it appears at higher temperatures than which α and ϵ occur [62]. Also, δ is the designation used for α at higher temperatures ($>\sim$1200 °C) [62]. α has bcc crystal structure with lattice parameter $a = 2.866$ Å, γ has fcc with $a = 3.647$ Å, ϵ has hcp with $a = 2.465$ Å and $c = 4.050$ Å and δ has bcc with $a = 2.932$ Å [50].

The other elements in steel, e.g. C or manganese (Mn), take up a preferential position within the respective crystal structures as per their atomic size, and form solid solution [61]. Solid solution formed in steel causes increase of mechanical strength, electrical resistivity and decrease in plasticity in the steel. Steel that is an alloy of only Fe and C is called plain carbon steel, while steel containing other alloying elements in addition is called alloy steels. Plain carbon steel is broadly grouped, depending on their carbon content, into low-carbon steel (0.15 % − 0.25 % C), medium-carbon steel (0.25 % − 0.60 % C) and high-carbon steel (0.60 % − 1.00 % C) [61].

In the sample being studied in the present thesis, *dual phase steel* is present. Dual phase steel is low-carbon steel that is thermomechanically processed to have better formability. They consist of approximately $75 - 85$ vol% ferrite (αFe) and the rest being a mixture of martensite, lower bainite, and retained austenite (γFe) [63]. Martensite and bainite are some of the microstructural phases that are generated by decomposition of austenite. Dual phase steel has a low yield to tensile strength ratio, and high tensile strength and work hardening rate [64].

2.4.5 Intermetallic compounds

When joining metals, formation of *intermetallic compounds (IMCs)* can sometimes occur at the interface between two metals. The existence of IMCs means that the metals have managed to get close enough together to bond to each other under right amount of pressure and heat. This is desirable in a joint. However, it is generally known that these IMC layers in large portions tend to be deleterious to the joint quality [65, 66]. This is due to the fact that they are usually hard and brittle and therefore act as stress concentration factors that aid fractures and crack-propagation at the interface if present in large amounts [67]. This naturally reduces the lifetime of the joint. In other words, having a thin, continuous and uniform layer of IMC means that an essential requirement for good bonding has been fulfilled [68]. However, a thick IMC layer is undesirable because of the mostly brittle nature of IMCs which may degrade the reliability of the joints. IMCs can be observed and identified by e.g. electron microscopy with techniques such as imaging, selected area diffraction and energy-dispersive spectroscopy, as was done in this thesis.

In this thesis, interactions between Al and the three base metals in the examined joint, Cu, Ti and steel, are of interest. The interaction between metals can be studied through *binary phase diagrams*, which present map of temperature versus composition. The equilibrium IMCs at various temperatures and composition are shown in such diagrams. In sections 2.4.5.1–2.4.5.3, we will look at such phase diagrams and deduce which IMCs are possible to have formed in the joint examined in this thesis. As mentioned in section 2.1.2, the joint being studied is made using HYB method and experiences a maximum temperature of around 400 °C lasting for only a few seconds during making. It is important to keep in mind that these are only the equilibrium phases and the HYB process happens so fast that there can be produced some metastable phases which the phase diagrams do not inform about. Furthermore, in the same sections, we will look at findings from previous research in terms of discovered IMCs in the joints made using different

joining techniques, and in terms of their results from mechanical testing. There are not much past research that has been done on the joints made with HYB since it is a fairly new method.

2.4.5.1 Aluminium-Copper

A binary phase diagram of Al and Cu is shown in figure 2.4 [69]. It can be observed from the Al-Cu phase diagram that the equilibrium IMCs that can be formed at around 400 °C are Al_2Cu (θ), AlCu (η_2), $Al_3Cu_{4-\delta}$ (ζ_2), Al_4Cu_9 (rhombic) (δ) and Al_4Cu_9 (γ_1). These IMCs have their structural information listed in table 2.1 [69–72].

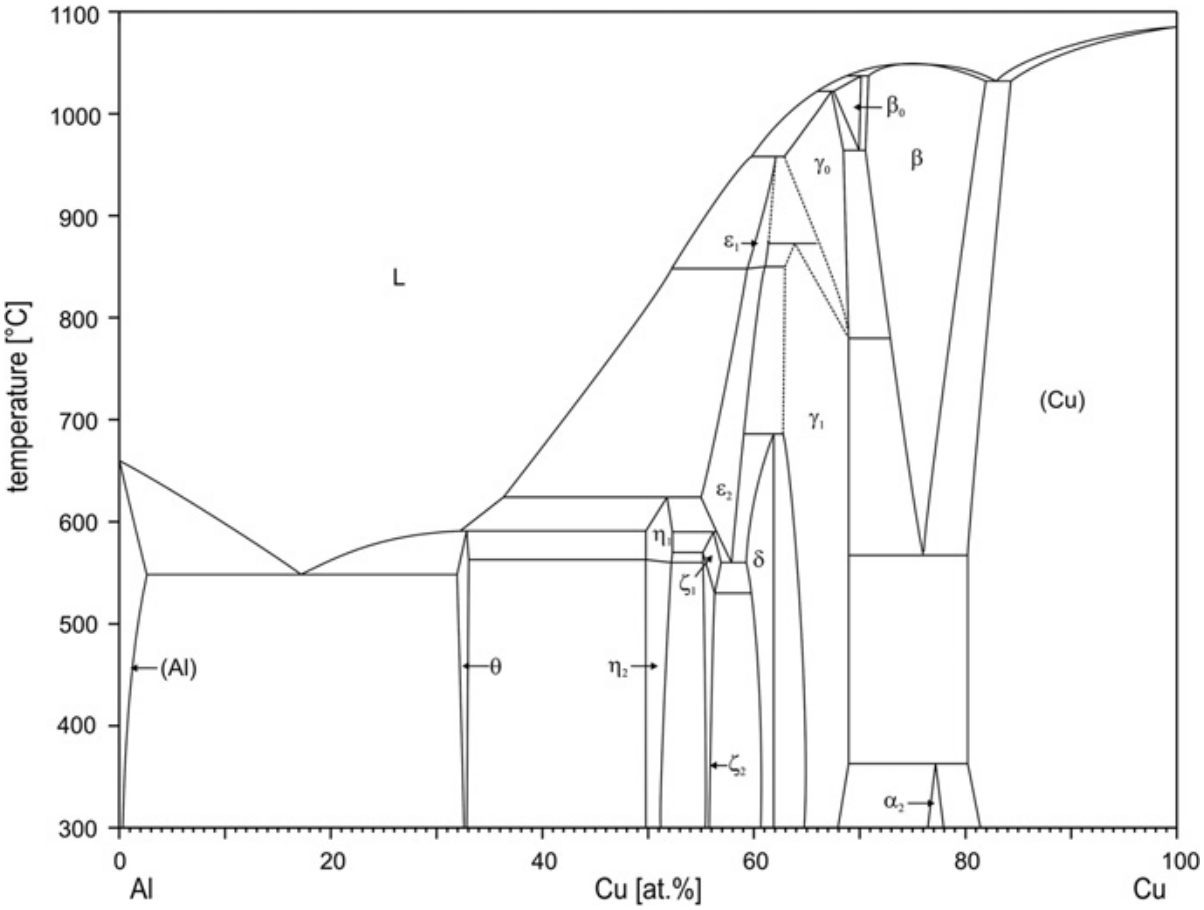

Figure 2.4: *The Al-Cu phase diagram. Figure taken from [69].*

Table 2.1: *The composition, the space group, the space group number (nr.) and the lattice parameters at room temperature of the equilibrium phases in the Al-Cu system that can be formed at temperatures around* 400 °C.

Composition	Space group	nr.	Lattice parameters	Reference
Cu	$Fm\bar{3}m$	225	$a = b = c = 3.615$ Å $\alpha = \beta = \gamma = 90°$	[70]
Al_2Cu	$I4/mcm$	140	$a = b = 5.949$ Å $c = 4.821$ Å $\alpha = \beta = \gamma = 90°$	[71]
AlCu	$C12/m1$	12	$a = 11.973$ Å $b = 4.061$ Å $c = 6.807$ Å $\alpha = \gamma = 90°$ $\beta = 124.882°$	[71]
$Al_3Cu_{4-\delta}$	$Imm2$	44	$a = 4.0972$ Å $b = 7.0313$ Å $c = 9.9793$ Å $\alpha = \beta = \gamma = 90°$	[69]
Al_4Cu_9 (r)	$R3m$	160	$a = b = c = 8.7066$ Å $\alpha = 89.74°$ $\beta = \gamma = 90°$	[69]
Al_4Cu_9	$P\bar{4}3m$	215	$a = b = c = 8.7023$ Å $\alpha = \beta = \gamma = 90°$	[72]

In addition to examination of the formation of the different Al-Cu IMCs during welding, much research has also been done in the past to evaluate the properties of the discovered IMCs. The IMCs that are most commonly formed at the Al-Cu interface are Al_4Cu_9, Al_2Cu and AlCu [67, 73–80]. Generally, the expected sequence of IMC formation in Al-Cu joints is Al_2Cu, Al_4Cu_9, AlCu, and so on [76]. Therefore most of the previous research have reported on these three IMCs, especially the first two. The hardness measurement-results from past research, similar to what has been described in section 2.1.3.1, indicate that the hardness of these three IMCs are in the following order, from the most to the least hardest, AlCu > Al_4Cu_9 > Al_2Cu [67]. The presence of such IMCs generally causes rise in hardness at the Al-Cu interface [74]. Examining the fracture mechanism at the joint interface in the past research has resulted in the conclusion that the thickening of these three IMCs promotes crack propagation and damage bond strength [76]. However, when present in thin layers, Al_2Cu and Al_4Cu_9 contribute to excellent bonding strength, bondability and tensile strength [74, 77]. This means that the IMCs layers are not necessarily damaging to the quality of the joint as long as their thickness is controlled to a micro scale.

Many different solid-state joining techniques have been used in the past to join aluminium and copper together. They include friction welding [73, 81–83], friction stir welding [74, 79, 80, 84], impact welding such as explosive welding [85–87] and diffusion bonding [75]. These joining methods have been introduced in section 2.1.1.

After performing friction welding, Sahin reported formation of Al_4Cu_9, AlCu and Al_2Cu [73]. Dalgaard et al., who also performed friction welding, reported formation of $AlCu_2$ and Al_2Cu that in total had a thickness less than 2 µm on average [83]. The thicknesses of the IMCs were reported to increase substantially when additional heat-treatments were performed after welding [83].

After performing friction stir welding, Tan et al. reported formation of Al_4Cu_9, Al_2Cu_3 and Al_2Cu [74]. They show images where Al_4Cu_9, Al_2Cu_3 and Al_2Cu seem to have been formed with

thicknesses that are approximately 0.5 µm, 0.2 µm and 0.4 µm, respectively.

After performing explosive welding, Athar and Tolaminejad reported formation of Al_2Cu [85], while Amani and Soltanieh reported formation of a non-equilibrium composition not identifiable from the phase diagram before post-welding treatment [88]. Naturally, the formation of IMCs during explosive welding, like in other welding methods, depends to some degree on the process parameters.

After performing diffusion bonding, Calvo et al. reported formation of Al_4Cu_9, AlCu and Al_2Cu [75]. They also report that to avoid voids at the joining interface, the metals have to be highly polished prior to joining and require high temperature and long times during joining. For example, they show that when increasing joining time from 16 h to 72 h at around 460 °C, the voids shrink or get eliminated with growth of IMC layers. Thicknesses of the IMC layers were different depending on temperature and time. An example can still be given of a typical process that operated at 440 °C for 129 h, which produced the average thicknesses 10 µm, 3.5 µm and 18 µm for Al_4Cu_9, AlCu and Al_2Cu, respectively.

2.4.5.2 Aluminium-Titanium

A binary phase diagram of Al and Ti is shown in figure 2.5 [89]. The phases that are present at around 500 °C continues to be relevant for temperatures around 400 °C also. It can be observed that the equilibrium IMCs that can be formed at 400 °C are Ti_3Al, TiAl, $TiAl_2$ and $TiAl_3$. $TiAl_3$ has two stable phases under equilibrium called $D0_{22}$ and $L1_2$. Ti will be present in α phase. The structural information of these phases is listed in table 2.2 [90–92].

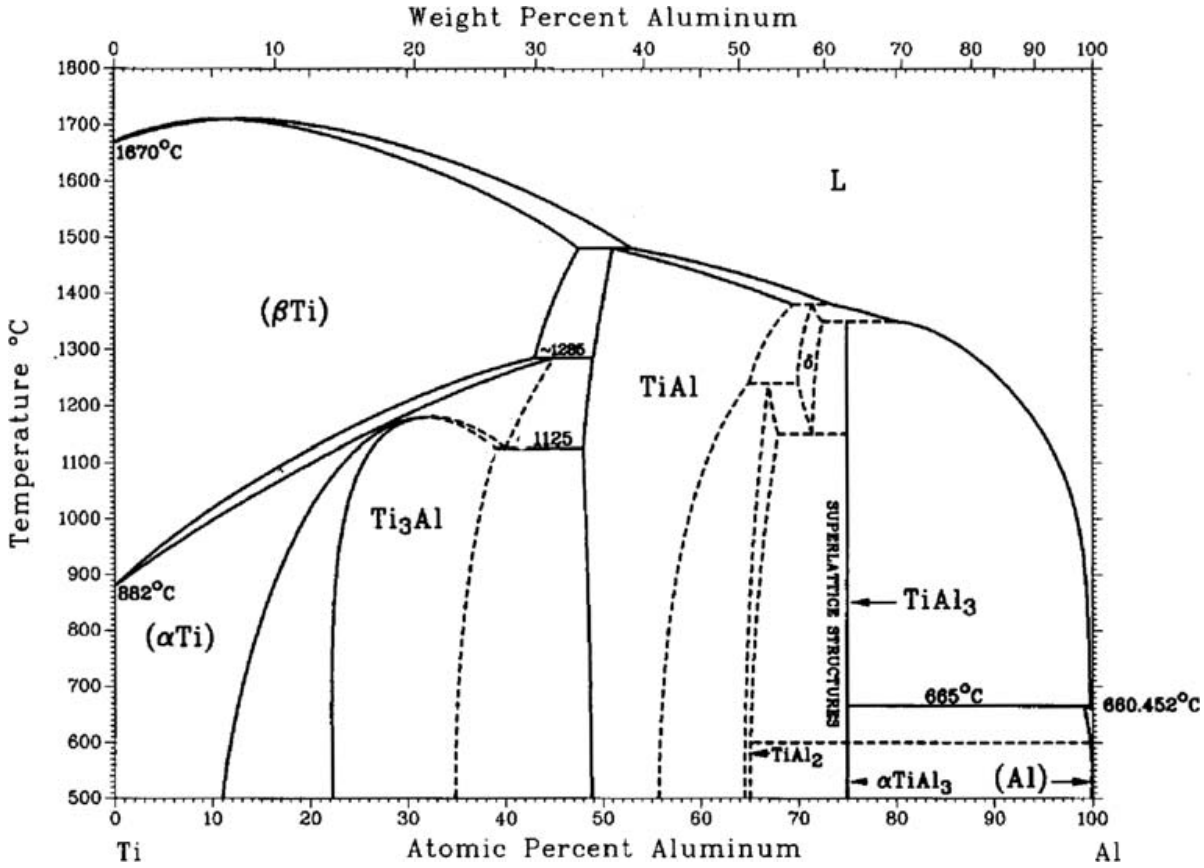

Figure 2.5: *The Al-Ti phase diagram. Figure taken from [89].*

Table 2.2: *The composition, the space group, the space group number (nr.), and the lattice parameters at room temperature of the equilibrium phases in the Al-Ti system that can be formed at temperatures around* 400 °C.

Composition	Space group	nr.	Lattice parameters	Reference
αTi	$P6_3/mmc$	194	$a = b = 2.950$ Å $c = 4.681$ Å $\alpha = \beta = 90°$ $\gamma = 120°$	[90]
Ti_3Al	$P6_3/mmc$	194	$a = b = 5.793$ Å $c = 4.623$ Å $\alpha = \beta = 90°$ $\gamma = 120°$	[91]
TiAl	$P4/mmm$	123	$a = b = 2.829$ Å $c = 4.071$ Å $\alpha = \beta = \gamma = 90°$	[91]
$TiAl_2$	$I4_1/amd$	141	$a = b = 3.976$ Å $c = 24.360$ Å $\alpha = \beta = \gamma = 90°$	[92]
$TiAl_3$-$D0_{22}$	$I4/mmm$	139	$a = b = 3.847$ Å $c = 8.621$ Å $\alpha = \beta = \gamma = 90°$	[93]
$TiAl_3$-$L1_2$	$Pm\bar{3}m$	221	$a = b = c = 3.981$ Å $\alpha = \beta = \gamma = 90°$	[93]

The Al-Ti IMC that is most commonly formed at the Al-Ti interface is $TiAl_3$ [94–99]. This could be due to the fact that $TiAl_3$ is the most thermodynamically and kinetically favorable [100]. $TiAl_3$ is usually developed in a thin layer making the measuring of its hardness using Vickers test described in section 2.1.3.1 not viable [94, 98]. However, Vickers test is still useful in measuring how the hardness of the base metals have change closer to the joint interface. In Al-Ti joints, it has been reported that both Al and Ti seem to have larger hardness closer to the interface with the reason being possible plastic deformation during welding [98]. With a thin layer of IMC, tensile test on Al-Ti joints reveal high tensile strength and ductility [94, 101], however that depends on the thickness of the IMC. In the IMC layer is thick, it has been reported that that would cause the joint to fracture in the IMC layer and favor cracks and voids in the proximity to the interface [96, 97, 102, 103].

Another important factor to be addressed is the presence of Si in the Al alloy used in this thesis. It has been mentioned in section 2.4.1 that the Al alloy relevant for this study is in the $6xxx$ series, meaning that it has Mg and Si as the principle alloying elements. It has been reported in the past that Si diffuses to the interface and enriches there during welding of Ti and Al alloys, and has a significant effect on the formation of IMCs [104]. Gathering of Si at the interface can lead to Si substituting Al atoms of $TiAl_3$, making it $Ti(Al,Si)_3$, and suppressed the formation of brittle binary Al-Ti binary phases [95].

Many different solid-state joining techniques have been used in the past to join aluminium and titanium together. They include friction welding [94], friction stir welding [96], explosive welding [98] and diffusion bonding [99]. These joining methods have been introduced in section 2.1.1.

After performing friction welding, Kim and Fuji reported formation of $TiAl_3$ in the extremely narrow region along the interface [94]. They managed to increase the thickness of the IMC with post-welding heat treatment. Through mechanical testings they concluded that the thickness of

IMCs should be below 5 µm to avoid deterioration of tensile strength and ductility.

After performing friction stir welding, Zhao et al. reported formation of mostly $TiAl_3$ and also TiAl at few places [96]. Aonuma and Nakata reported only detection of $TiAl_3$ on the friction stir welded joint interface and reported that the thickness of the IMC layer was very thin [105].

After performing explosive welding, Fronczek et al. reported formation of $TiAl_3$, $TiAl_2$, TiAl and Ti_3Al at the joint interface [98]. These IMCs were not present in continuous layer but rather in small nodes. However, post-joining heat treatment aided growth of $TiAl_3$ into a continuous layer.

After performing diffusion bonding, Enjyo et al. reported formation of $TiAl_3$ at the joint interface [99]. As in the other processes, the thickness of the IMC increased with increase in certain welding parameters. In this case, the thickness of the IMC increased with welding time at constant temperature and thicknesses up to 10 µm did not reduce the joint strength.

2.4.5.3 Aluminium-Iron

As has been mentioned earlier, the TEM studies in this thesis involving identification of IMCs have been done on the Al-Cu and Al-Ti interfaces only. Nevertheless, short information about Al-Fe IMCs is given in this section for the sake of completeness.

A binary phase diagram of Al and Fe is shown in figure 2.6 [106]. It can be seen from the Al-Fe phase diagram that the equilibrium IMCs that can be formed at 400 °C are Fe_3Al, FeAl, $FeAl_2$, Fe_2Al_5 and $FeAl_3$. The structural information of these phases is listed in table 2.3 [43, 107–110].

The solid-state joining techniques used in the previous research to join Al and steel together include friction welding [54], friction stir welding [111, 112], impact welding such as explosive welding [113] and diffusion bonding [114]. As in the previous cases with other metals, the formation of Al-Fe phases also is important in forming an effectual connection between the two metals, but excessive amounts of IMCs results in brittleness, lower joint-strength and fractures [54, 111, 115].

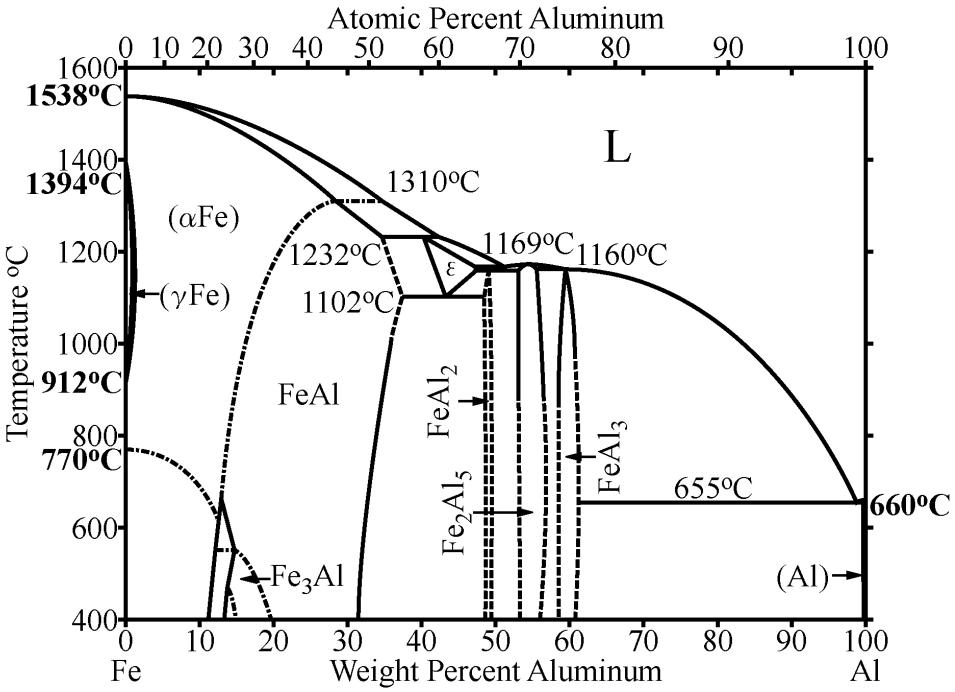

Figure 2.6: *The Al-Fe phase diagram. Figure taken from [106].*

Table 2.3: *The composition, the space group, the space group number (nr.), and the lattice parameters at room temperature of the equilibrium phases in the Al-Fe system that can be formed at temperatures around* 400 °C.

Composition	Space group	nr.	Lattice parameters	Reference
Fe_3Al	$Fm\bar{3}m$	225	$a = b = c = 5.790$ Å	[107]
			$\alpha = \beta = \gamma = 90°$	
FeAl	$Pm\bar{3}m$	221	$a = b = c = 2.910$ Å	[108]
			$\alpha = \beta = \gamma = 90°$	
$FeAl_2$	$P1$	1	$a = 4.880$ Å	[109]
			$b = 6.460$ Å	
			$c = 8.800$ Å	
			$\alpha = 87.87°$	
			$\beta = 74.41°$	
			$\gamma = 83.10°$	
Fe_2Al_5	$Cmcm$	63	$a = 7.657$ Å	[43]
			$b = 6.409$ Å	
			$c = 4.227$ Å	
			$\alpha = \beta = \gamma = 90°$	
$FeAl_3$	$C2/m$	12	$a = 15.490$ Å	[110]
			$b = 8.080$ Å	
			$c = 12.480$ Å	
			$\alpha = \gamma = 90°$	
			$\beta = 107.72°$	

2.5 Transmission Electron Microscope

The oldest type microscope is *optical microscope (OM)* that uses visible light and a set of lenses to magnify the object being examined. Unlike OM, electron microscopes use electrons and a set of magnetic coils and deflectors and apertures to obtain characterization of materials beyond the goal of magnification only. Examples for electron microscopes include *transmission electron microscope (TEM)*, discussed in this section, and *scanning electron microscope (SEM)*, discussed in section 2.6. TEM's versatility, complexity and efficiency makes it arguably the most powerful tool for material characterization purposes. In this section, we will get familiar with TEM and all the subsections are mostly based on the book, **Transmission Electron Microscopy, by D. B. Williams and C. B. Carter (2009)** [116]. Other sources that have been used will be cited along the way.

2.5.1 Electron-matter interaction in TEM

Electrons are one type of ionizing radiation which releases wide range of secondary radiation when interacting with the specimen. In electron microscopes these secondary signals are utilized to analyse the specimen. Among all secondary signals, the ones that are of special interest for TEM work in this study are shown in figure 2.7. The characteristic X-rays are used in *energy-dispersive spectroscopy (EDS)*, and will be examined in section 2.5.5. The *direct beam* corresponds to the electrons that remain undeviated with respect to the direction of the incident beam after passing through the specimen. The *inelastically and elastically scattered electrons* are, respectively, electrons that are scattered with and without loss of energy. Elastically scattered electrons are the major source of contrast in TEM images and create much of the intensity in *diffraction patters (DP)*. Inelastically scattered electrons give rise to x-rays and other useful signals to help characterize the chemistry of the specimen even better.

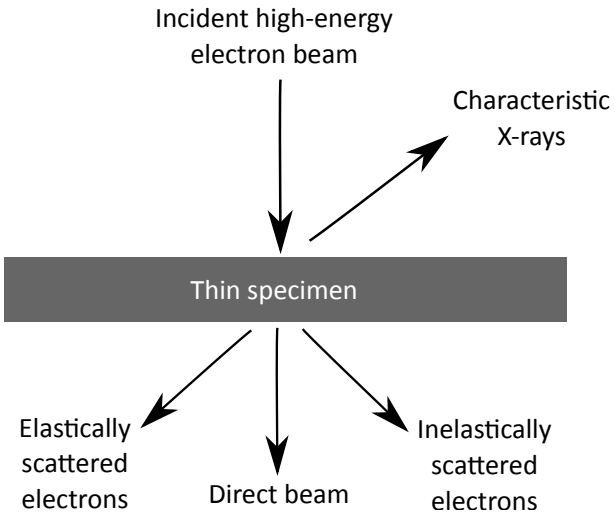

Figure 2.7: *Some of the signals that are examined in TEM, which stem from interaction between a high-energy beam of electrons with a thin specimen. The figure is adapted from [116].*

The importance of scattering lies in the fact that it is the essence of imaging in TEM or any other electron microscopy. Nothing can be seen in the images without the scattering of the electrons by the specimen. The *scattering cross section* of an atom, σ_{atom}, when divided by the area of the atom the electron interacts with, is representative of the probability for the scattering to occur. In TEM, apertures are used to limit the electrons that arrives at the detector

by blocking electrons that have scattered above an angle θ. Therefore a quantity of interest for TEM studies is the angular distribution of the scattering from an atom, the *differential cross section* which in terms of the scattering angle θ is

$$\frac{\mathrm{d}\sigma_{\mathrm{atom}}}{\mathrm{d}\Omega} = \frac{1}{2\pi \sin\theta} \frac{\mathrm{d}\sigma_{\mathrm{atom}}}{\mathrm{d}\theta} \ . \tag{2.26}$$

The differential cross section is related to the atomic form factor presented in equation (2.23) by

$$|f(\boldsymbol{q})|^2 = \frac{\mathrm{d}\sigma}{\mathrm{d}\Omega}. \tag{2.27}$$

For a specimen containing N such atoms, the total scattering cross section will naturally be

$$\sigma_{\mathrm{total}} = N\sigma_{\mathrm{atom}} = \frac{N_0 \sigma_{\mathrm{atom}} \rho}{A}, \tag{2.28}$$

where N_0 is Avogadro's number (mol^{-1}), A is the atomic weight of the scattering atoms in the specimen (kg mol^{-1}) which has density ρ (kg m^{-3}). Further, the probability of scattering from the specimen is given by

$$\sigma_{\mathrm{total}} t = N\sigma_{\mathrm{atom}} = \frac{N_0 \sigma_{\mathrm{atom}} (\rho t)}{A}, \tag{2.29}$$

where the product ρt is called the *mass thickness* of the specimen.

Electrons behave both as waves and particles. Therefore, their momentum p can be related to their wavelength λ through Planck's constant h as

$$\lambda = \frac{h}{p}. \tag{2.30}$$

This equation tells us that by adjusting the momentum, one can vary the wavelength, thus the energy, of the electrons. In TEM, momentum of the electrons is controlled through adjustment of the potential drop V through which they are accelerated. Through conversion of potential energy eV into kinetic energy $\frac{m_e v^2}{2}$ during this process, a certain velocity, thus momentum $p = m_e v$ is gained. Here, m_e is the electron mass, v is the velocity and e is the elementary charge.

It is, at this point, important to acknowledge the relativistic effects. At a working voltage greater than 100 kV in TEM, which is the case during this study, electrons will have velocity higher than half the speed of light c. This can be calculated from

$$eV = \gamma \frac{m_e v^2}{2} = \frac{1}{\sqrt{1 - \frac{v^2}{c^2}}} \frac{m_e v^2}{2}, \tag{2.31}$$

which gives $v \approx 0.55c$ when $V = 100$ kV. This means that relativistic effects must be taken into account. With that in mind, equation (2.30) can be written as

$$\lambda = \frac{h}{\sqrt{2 m_e e V (1 + \frac{eV}{2 m_e c^2})}}. \tag{2.32}$$

2.5.2 Diffraction in TEM

The concept of diffraction, together with the Laue condition, was established in section 2.3. We will now proceed to derive Bragg's law using these information, which will be useful in defining the concept of camera length in TEM.

We defined earlier $\boldsymbol{q} = \boldsymbol{k}_f - \boldsymbol{k}_i$ where $\boldsymbol{k}_i$ is the incoming wavevector and $\boldsymbol{k}_f$ is the scattered wavevector. Using this, the Laue condition in equation (2.20) can be rewritten as

$$\begin{aligned} \boldsymbol{g}_{hkl} &= \boldsymbol{k}_f - \boldsymbol{k}_i \\ |\boldsymbol{k}_f - \boldsymbol{g}_{hkl}|^2 &= |\boldsymbol{k}_i|^2 \\ |\boldsymbol{k}_f|^2 - 2\boldsymbol{k}_f \cdot \boldsymbol{g}_{hkl} + |\boldsymbol{g}_{hkl}|^2 &= |\boldsymbol{k}_i|^2 . \end{aligned} \tag{2.33}$$

As most of the diffraction originate from elastic scattering, vi assume the elastic scattering condition $|\boldsymbol{k}_f|^2 = |\boldsymbol{k}_i|^2$ and get

$$\begin{aligned} |\boldsymbol{g}_{hkl}|^2 &= 2\boldsymbol{k}_f \cdot \boldsymbol{g}_{hkl} \\ |\boldsymbol{g}_{hkl}|^2 &= 2\,|\boldsymbol{k}_f|\,|\boldsymbol{g}_{hkl}| \sin\theta \\ \left(\frac{2\pi n}{d_{hkl}}\right)^2 &= 2\left(\frac{2\pi}{\lambda}\right)\left(\frac{2\pi n}{d_{hkl}}\right)\sin\theta, \end{aligned} \tag{2.34}$$

where we have used $k = 2\pi/\lambda$ and equation (2.21), and θ is the angle the scattered wavevector makes with the atomic plane causing it which is illustrated in figure 2.8. Rearranging this expression gives us the *Bragg's law*

$$2d_{hkl} \sin\theta = n\lambda, \tag{2.35}$$

which for small angles, as is the case in TEM, and $n = 1$ gives

$$\lambda/d \approx 2\theta. \tag{2.36}$$

Figure 2.8 is an illustration of the geometrical concept of the *camera length* L as being the distance between the specimen and the viewing screen. In TEM, L is controlled by adjusting the strength of a lens.

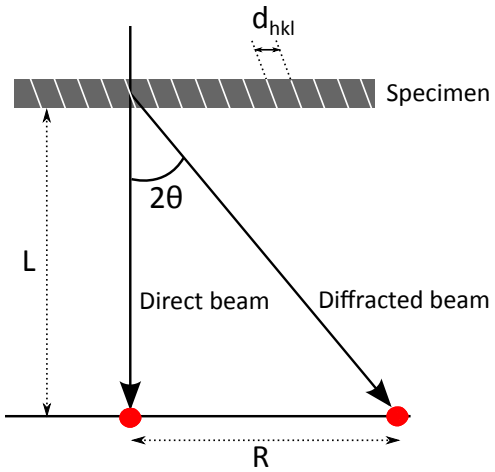

Figure 2.8: *Figure illustrating the geometrical concept of the camera length L. Also shown in the figure are the distance between the direct beam and a scattering maximum R and the angle the scattered wavevector makes with the direct beam 2θ.*

From this figure, we get the relation

$$\frac{R}{L} = \tan 2\theta \approx 2\theta, \tag{2.37}$$

where R is the distance between the direct beam and a scattering maximum in the observed pattern. Finally, combining equation (2.36) and equation (2.37), one gets

$$d_{hkl}R_{hkl} = \lambda L. \tag{2.38}$$

The value of λ can be calculated using equation (2.32). When keeping the λ and L constant, if d_{hkl} is known for one diffraction spot, one can find the same quantity of another spot through the relation

$$d_{h_1k_1l_1}R_{h_1k_1l_1} = d_{h_2k_2l_2}R_{h_2k_2l_2}. \tag{2.39}$$

Here, all the quantities are in absolute value. As L requires calibration before being used in indexing through equation (2.38), it is sometimes more convenient to use equation (2.39).

2.5.3 TEM hardware

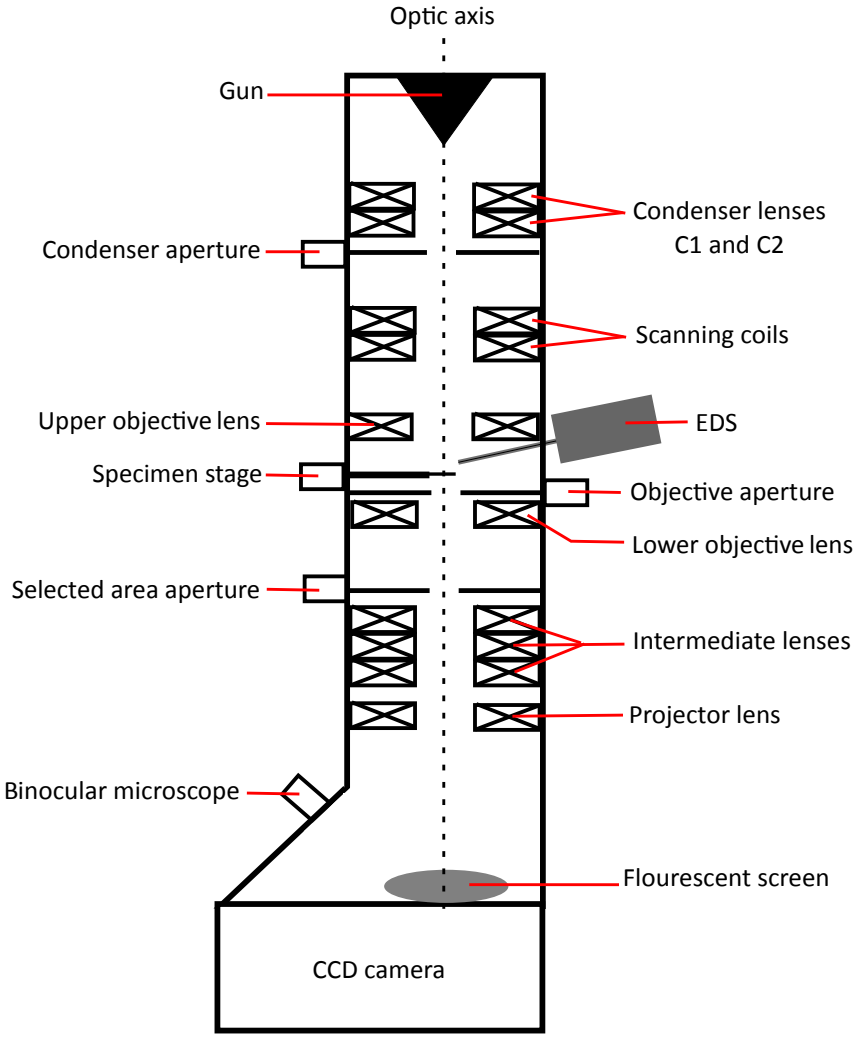

Figure 2.9: *A simplified sketch of a TEM column. The gun and the condenser lenses have the responsibility of generating and directing the electron beam, the scanning coils propagates the beam so scanning can be done in STEM mode, the objective lenses form images and DP of the specimen in the stage, the EDS detector detects X-rays, and the intermediate and projector lenses directs the image or DP further to be viewed by the flourescent screen or imaged by the CCD camera. Apertures work to select the parts of the beam that is desired.*

A simplified sketch of a typical *TEM column* is shown in figure 2.9 where the most important components are annotated. Among other things, TEM column comprises of several different apertures and different electromagnetic lenses, where the latter are coils of wire in which current flows. TEM column can conveniently be divided into three main parts: *the illumination system*, *the objective lens and stage*, and *the imaging system*.

The illumination system consists of the gun and the condenser lenses. The uppermost element indicated in figure 2.9 is the *gun* responsible for generating the electron beam. There are two main types of electron sources that can be inside a gun, a thermionic source or a field emission source. *Thermionic source* uses the principle that by heating up the filament material sufficiently by supplying it with energy, its electrons will manage to overcome the natural barrier and leak out from the surface. *Field-emission source (FEG)* achieves more monochromatic electrons than thermionic sources, and it is done by application of a large voltage on the fine tip of the source thus lowering the work-function barrier sufficiently for electrons to be ejected.

After the electrons are emitted from the gun, they illuminate the specimen either as a *convergent beam* or as a *parallel beam*. These are the two principal modes of the illumination system. The *condenser lenses*, C1 and C2, and the *upper objective lens* positioned right below the gun in figure 2.9 have the responsibility of achieving these modes. Both the parallelness and the convergence of the beam are almost never complete. The convergent beam mode is standard for e.g. STEM which will be discussed in section 2.5.6. The parallel beam is essential in getting the best classical *diffraction-contrast imaging* and the sharpest *selected-area DP (SADP)* formation. The C1 and C2 lenses image the source at the front focal plain of the upper objective lens, creating a parallel beam of electrons at the specimen plane. To get a more parallel beam, a *condenser aperture*, as shown in figure 2.9, can be inserted right below the condenser lenses to block the electrons hitting the specimen with large angles with respect to the optic axis. Figure 2.10 is a ray diagram describing this process.

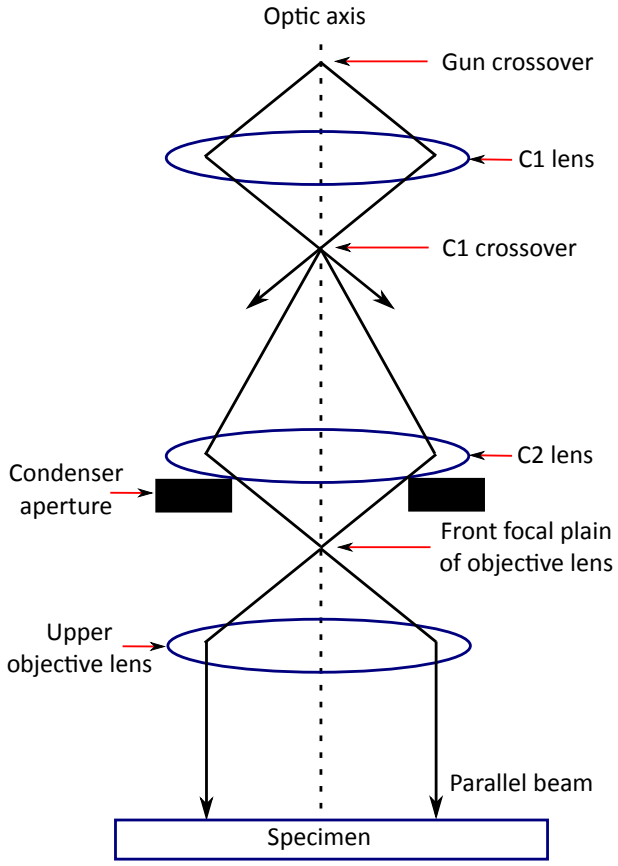

Figure 2.10: *C1 and C2 condenser lenses image the source at the front focal plain of the upper objective lens, creating a parallel beam of electrons at the specimen plane. Figure adapted from [116].*

As mentioned earlier, the lenses in TEM are electromagnetic coils, and they make it easy to manipulate the electron beam in different ways. One can do operations such as translating the beam laterally on the specimen or tilting the beam an angle from the optic axis by varying the current that flows through the coils. This generates local magnetic field $\boldsymbol{B}$ inside the coils and the impact force $\boldsymbol{F}$ from this on the electrons with velocity $\boldsymbol{v}$ and electric charge $q = -e$ is

$$\boldsymbol{F} = -e\,(\boldsymbol{v} \times \boldsymbol{B})\,. \tag{2.40}$$

As $\boldsymbol{v}$ of the electrons are never completely parallel to the optical axis, the dependence of $\boldsymbol{F}$ on the cross product between $\boldsymbol{v}$ and $\boldsymbol{B}$ tells us that the electrons will follow a helical trajectory down the column. This leads to the consequence that the quality of the beam is the better the closer it is to the optical axis. Thus, it is beneficial to insert a condenser aperture to obtain a higher quality beam at the expense of the total electron current. It is also important to keep in mind the usual defects that can accompany the lenses, such as aberration and astigmatism, and try to minimize them through use of different techniques such as use of apertures and use of wobbling.

Further down the column in figure 2.9 are the upper and the lower *objective lenses* which are the most important lenses in TEM. They are responsible for forming images and DPs. The separation of upper and lower objective lenses gives the possibility of inserting both specimen, objective aperture and EDS device in between these lenses. The position of the specimen is called the *stage*. By exciting the upper objective lens, one can produce both broad beam for TEM or fine beam for AEM and STEM. Separating the objective lens to two pieces also makes it easy to perform various tasks with the specimen holder. The specimen can be moved up and down (z direction) and be tilted in two perpendicular directions (x and y directions), all within the limits

of that particular TEM. The specimen can also be heated, cooled or undergo other treatments. When performing tilting of the specimen, it is ideal to fix the height of the specimen on the optic axis so the same objective-lens current, thus a fixed objective-lens magnification can be used. To obtain this aim, we define a reference plane, called *eucentric plane*, which is normal to the optic axis. If a specimen lies on this plane, the point of the specimen positioned on the optic axis will not move laterally when being tilted around the holder axis.

It is usual practice to equip TEM with *EDS device* to detect X-rays, as in figure 2.9. EDS devices are usually also present in SEM which we will examine in section 2.6. The physics behind X-rays themselves are discussed in common in section 2.5.5. The EDS device is constituted of three main parts, the detector, the processing electronics and the computer. One of the most common detectors is *Si-drift detector (SDD)*. When an X-ray hits the detector, thousands of electrons and holes proportional to the energy of the X-ray are generated and constitutes a minor charge pulse. A reverse bias is applied to separate the electrons and holes, and to measure the electron pulse. The processing electronics process this charge pulse further. The pulse is first converted to a voltage which gets amplified by a *field-effect transistor (FET)*. Thereafter, the signal is assigned to the correct energy channel in the storage system and shown in the computer display. The computer controls the whole process from the beginning.

Going further down the TEM column in figure 2.9, one meets the *selected-area diffraction aperture (SAD aperture)* using which one can create SADP. As the name suggests, one selects the area of interest using SAD aperture. This is done by inserting it in the image plane of the objective lens which is a plane conjugate with the specimen.

The imaging system, towards the lower part of the TEM column in figure 2.9, then uses lenses like *intermediate* and *projector lenses* to magnify the image or the DP and focus them onto the flourescent viewing screen, to be viewed with or without the binocular microscope, or the CCD camera.

2.5.4 Imaging and diffraction procedures in TEM

To produce images in TEM by working in image mode, the intermediate lens is adjusted so that its object plane is the image plane of the objective lens. This way, an image gets projected down to the flourescent viewing screen or the CCD camera. However, if diffraction mode is desired, the imaging-system lenses must be readjusted so that the *back focal plane (BFP)* of the objective lens acts as the object plane for the intermediate lens. This way, the DP gets projected onto the viewing screen or the CCD camera. By selecting certain area of your specimen using SAD aperture, as explained in section 2.5.3, DP of only that area, SADP, can be generated.

By utilizing the combination of the objective aperture and the obtained DP, one can perform the two most basic imaging operations in TEM. The first one is *bright field (BF)* imaging obtained by selecting the direct beam in the DP. This is done by placing the objective aperture into the BFP of the objective lens and adjusting it to select the direct beam on the optic axis. *Dark field (DF)* imaging, contrary to BF imaging, is obtained by only selecting the electrons that have been scattered. This time, objective aperture is adjusted to select one or multiple of the diffracted spots in the DP. Due to the fact that electrons farther away from the optic axis suffer more from aberrations and astigmatism, it is rather preferred to set the objective aperture on the optic axis and shift the desired scattered electrons to the optic axis thus get selected by the objective aperture. This conventional way to do DF imaging is called *centered dark-field (CDF)* imaging. All in all, the role of the objective aperture is useful as one can select, in similar fashion, certain DP spots that correspond to a specific material in a multi-material sample to highlight only that material in the image.

TEM is such a powerful tool, one can even obtain atomic resolution images. This mode of

operation is called *high resolution TEM (HRTEM)*, achieved by strongly magnifying the image using the intermediate lenses. It is important to not use objective aperture in this mode as all beams should be allowed to contribute to the images in order to obtain the optimal resolution.

No matter what kind of imaging is done, a good contrast is always desired. Contrast is defined as the relative difference in intensity between two adjacent areas, $C = \frac{I_2 - I_1}{I_1} = \frac{\Delta I}{I_1}$, and is caused by the scattering of the electrons as mentioned in section 2.5.1. When getting scattered by the specimen, the electron beam changes both its amplitude and phase. Both factors contribute to the contrast of the image. *Amplitude contrast* can further be divided into two main types, *mass-thickness contrast*, which is due to electrons interacting more with material with higher mass, and *diffraction contrast*, which occurs because the specimen is not uniformly thin thus diffracts differently from one place to another. *Phase-contrast* is caused by scattered electron beams with different phases interfering with each other.

2.5.5 Energy-Dispersive Spectroscopy in TEM

When electrons are scattered inelastically after interacting with the specimen, two different kinds of X-rays are produced. The first type is a continuous radiation called the *bremsstrahlung X-rays*, which are released when an electron gets decelerated by the electrostatic interaction with the nucleus and loses its kinetic energy in terms of a ejected photon. In TEM, this is considered as the unwanted background radiation which does not contain as useful information as the second type of X-rays that is produced, namely the *characteristic X-rays* used in EDS as mentioned in figure 2.7. As the name suggests, characteristic X-rays are unique for the type of element that causes the scattering of the electron and reflects the possible energy level in the atom, and therefore function as a powerful tool for elemental analysis. They are emitted when an atom ionized by the electrons returns to the ground state. In order to isolate the characteristic X-rays in a X-ray spectrum, the bremsstrahlung radiation is subtracted from the spectrum. The resulting spectrum then shows characteristic peaks which can be further explained through a simple model proposed by Niels Bohr in 1913 [117]. This model proposes atoms to be consisting of a small and dense nucleus and orbitals of electrons surrounding circulating the nucleus. The orbitals correspond to different energy levels and transitioning from one to the other requires a corresponding energy exchange. Starting from the innermost orbital, they are named K, L, M etc., and transitioning between them causes emissions which have been given the names as indicated in figure 2.11. For instance, transitioning from the L orbital to the K orbital produces a K_α emission.

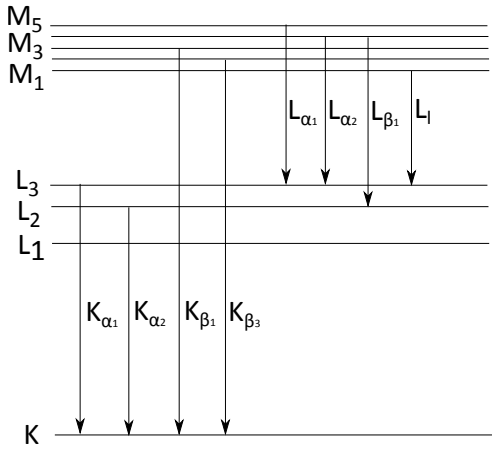

Figure 2.11: *Some of the transitions that give rise to the emission lines in a X-ray spectrum. Figure adapted from [118].*

In TEM, due to the specimens being thin, absorption and flourescence effects are not highly significant. To quantify the weight fractions, C_A and C_B, of two elements A and B in a binary material, the *Cliff-Lorimer ratio method* (1975) [119]

$$\frac{C_\mathrm{A}}{C_\mathrm{B}} = k_\mathrm{AB}\frac{I_\mathrm{A}}{I_\mathrm{B}} \tag{2.41}$$

can be used where I_i is the measured characteristic X-ray intensity of element i and k is a sensitivity factor that varies depending on the specimen, TEM and EDS device. k for different pairs of elements satisfy

$$k_\mathrm{AB} = \frac{k_\mathrm{AC}}{k_\mathrm{BC}} \tag{2.42}$$

and, in TEM, is related only to the atomic-number correction factor (Z). Weight fractions C are also called *weight percentage (wt%)* and can be converted into *atomic percentage (at%)* through

$$\mathrm{at\%}A = \frac{(\mathrm{wt\%}A)/(\text{at. wt. } A)}{(\mathrm{wt\%}A)/(\text{at. wt. } A) + (\mathrm{wt\%}B)/(\text{at. wt. } B)}, \tag{2.43}$$

where at. wt. stands for *atomic mass*. This relationship can be extended to more than two elements by taking into account all the elements in the denominator.

2.5.6 Scanning Transmission Electron Microscope hardware and imaging

As mentioned in section 2.5.3, *Scanning Transmission Electron Microscope (STEM)* operates in the convergent beam mode where the beam functions as a probe to localize the signals. A probe can be produced by adjusting the condenser lenses and the upper objective lens. This probe is then used to scan over the whole area of interest while propagating parallel to the optic axis. This is accomplished by tilting the beam twice with two sets of *scanning coils*, seen in figure 2.9. By addressing a sequence of discrete (x,y) positions on the specimen and measuring the interaction of the electron beam with each positions, intensities of the signal of interest from every position can be recorded. This gives rise to the resulting image where the variations in the detected intensities produces contrast in the image.

To facilitate the STEM mode in TEM, in addition to the scanning coils, there are also additional STEM detectors and necessary circuitry present. Bright field and dark field imaging have been discussed in relation to TEM in section 2.5.4. Similar techniques are used also in STEM. By positioning a circular electron detector centered on the optic axis below the sample, as shown in figure 2.12, the electrons scattered almost parallel to the optic axis can be detected, which results in an BF STEM image. In contrast, if an annular detector with larger radius is centered on the optic axis below the sample, also as shown in figure 2.12, the electrons that have been scattered with higher angles can be detected. This detector is called *annular dark field (ADF)* detector. By adjusting the camera length using the intermediate lenses, electrons with different scattering angles can be detected by ADF detector. When using a short camera length, thus detecting electrons scattered at high angles, the image produced is called *high-angle annular dark field (HAADF)* image. HAADF is not affected by coherent interference between different atomic columns and illustrates the difference in atomic number, namely Z-contrast. EDS scans can be performed in combination with STEM in order to acquire spectra of characteristic X-rays for each pixel the probe scans.

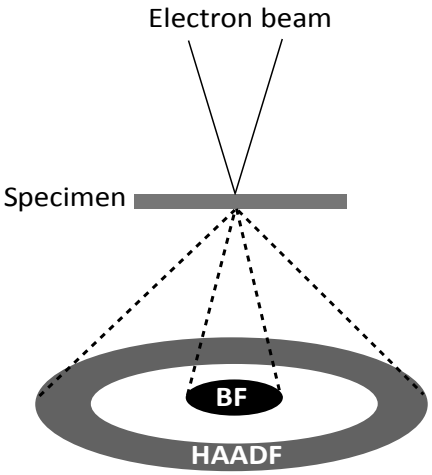

Figure 2.12: *In STEM, a convergent electron beam is scanned over the specimen and the transmitted signal is detected by a bright field (BF) detector or a high-angle annular dark field (HAADF) detector. Figure adapted from [120].*

2.6 Scanning Electron Microscope

In this section, we will get familiar with SEM and all the subsections are mostly based on the book, **Scanning Electron Microscopy and X-Ray Microanalysis by J. I. Goldstein et al. (2018)** [121]. Other sources that have been used will be cited along the way.

2.6.1 Electron-matter interaction in SEM

In contrast to TEM, the specimens in SEM are much thicker, causing the interaction volume of electrons to be much larger. This further means that the secondary signals that are of interest in a SEM study are to some degree different from the ones that are examined in TEM (see figure 2.7). Some of the signals that are produced when the electron beam interacts with the specimen in SEM are shown in figure 2.13 together with the part of the interaction volume they originate from. When incident electrons scatter inelastically, they can collide and eject weakly bound electrons from the material which have been given the name *secondary electrons (SE)*. The incident beam electrons have much higher energy than the ionization energy of the weakly bound atomic electrons, therefore the ejected SEs obtain a small transfer of kinetic energy. This further results in the fact that only the SEs generated close to the surface manage to propagate through the specimen and get detected, as shown in figure 2.13. The *backscattered electrons (BSE)*, from figure 2.13, originate from further inside the specimen and depend on the atomic number Z of the materials. BSEs are generated when some of the incident beam electrons gets affected by the attractive force from the nucleus of the atoms. This force, sometimes, causes incident electrons to circle around the nucleus and change their direction of propagation. After getting scattered elastically in this way multiple times, the electrons finally escape through the surface of the specimen. While experiencing multiple scatterings, the BSEs travel further into the specimen than the detected SEs, until sufficient impact has been made for them to change direction. The last secondary signal shown in figure 2.13 is the characteristic X-rays discussed in section 2.5.5. This signals can come from the whole interaction volume. The extra factors to consider when analyzing the X-ray spectra generated in SEM, compared to TEM, are discussed in section 2.6.3.

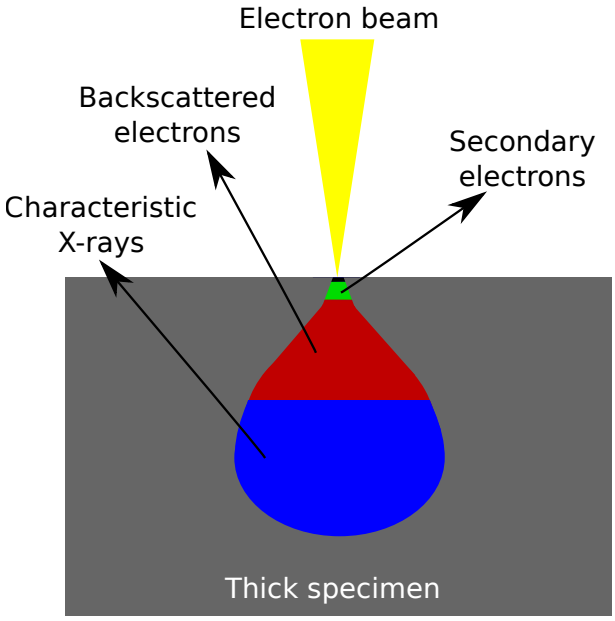

Figure 2.13: *Some of the signals that are examined in SEM, which stem from interaction between a beam of electrons with a thick specimen. The different signals, BSE, SE and X-ray, originate from different parts of the interaction volume. Figure adapted from [120].*

2.6.2 SEM hardware and imaging

Figure 2.14 is a simplified sketch of a SEM column.

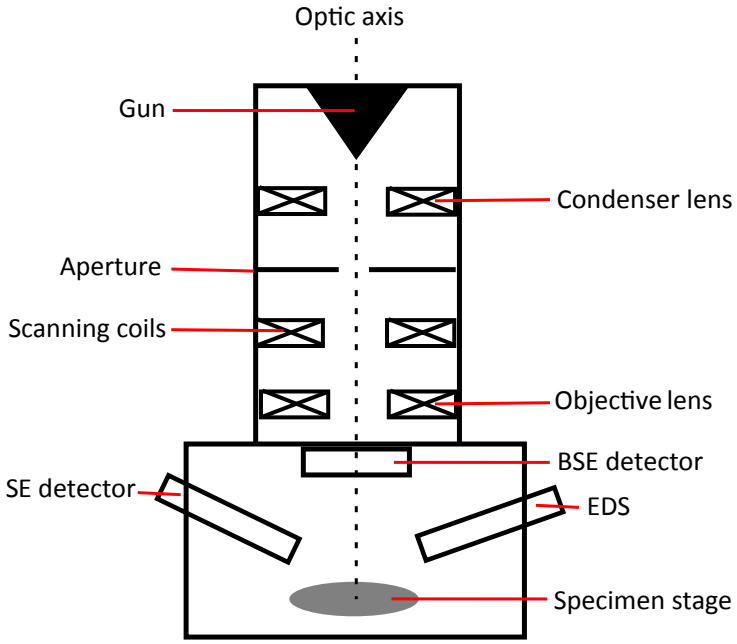

Figure 2.14: *A simplified sketch of a SEM column. The gun and the condenser lens have the responsibility of generating and directing the electron beam, the objective lens form images of the specimen in the stage, the EDS detector detects X-rays, the BSE detector detects back-scattered electrons, and the SE detector detects secondary electrons. Aperture work to select the parts of the beam that is desired.*

Comparing it to figure 2.9, it can be seen that a SEM column resembles very much the upper

part of a TEM column ending at the specimen stage. The components of SEM, mostly, have the same function as the components in TEM with the same name, and TEM hardware have been thoroughly explained in section 2.5.3. SEM has a gun which produces electron beam which is further manipulated in different ways by electro-magnetic lenses and apertures in the similar way as described for TEM. Similar to the STEM discussed in section 2.5.6, the electron beam is scanned over the specimen in SEM using scanning coils shown in figure 2.14. The scanning procedure is in principle the same as in STEM where electron intensity corresponding to each pixel is measured and processed into an image.

Unlike TEM where the specimens have limited possibility to move along the direction of the optic axis, the specimens in SEM can move much more in that direction (formally called the *working distance (WD)*) to alter the optimized resolution for different signals depending on the position of the detector.

2.6.3 Energy-Dispersive Spectroscopy in SEM

The basic principles of X-rays are explained section 2.5.5. Due to the higher thickness of SEM specimens compared to TEM specimens, larger counts of the characteristic X-rays is created and detected. This is beneficial if the region of interest in the specimen is large and uniform since this increases the accuracy of the results. However, if an excellent spacial resolution is required due the presence of different IMCs with small regions, SEM might not be the best tool for that. This can be explained by looking at the interaction volume from which the characteristic X-rays stem from in SEM in figure 2.13. The whole "light bulb" like volume is responsible for production of characteristic X-rays even though the incident beam electrons only pass through a much smaller region in the surface of the specimen. This means that signals are obtained from a wider and deeper region than what is intended, causing a bad spacial resolution.

Remember from section 2.5.5 that for TEM specimens, the absorption and flourescence effects are not highly significant due to the specimens being thin. This is not the case anymore. The first disadvantage of having a thicker specimen is the photoelectric absorption X-ray photons can experience while passing through the specimen. This happens when an X-ray whose energy exceeds the binding energy of an atomic orbital transfers this energy to a bound electron, thus emitting the electron with kinetic energy equal to the difference between the original energy of the X-ray and the binding energy of the orbital. In this process, the X-ray is annihilated and will not be detected. The photoelectric absorption process is quantified by the absorption coefficient μ which determines the intensity of the detected beam I after the initial X-ray intensity I_0 has traveled through a thickness x of the material, which gives the relation

$$I = I_0 \mathrm{e}^{-\mu x}. \tag{2.44}$$

The second disadvantage with thicker specimens is the X-ray flourescence. This is actually a consequence of photoelectric absorption. After the absorption follows a de-excitation of the atoms. This process causes production of a secondary X-ray spectrum of lower energy characteristic X-rays. These secondary X-rays originate from a far greater volume then the interaction volume that generates the primary X-rays, shown in figure 2.13. This then worsens the accuracy even more. The yield of the X-ray flourescence effect varies depending on the orbital involved, and follows the trend K $>$ L $\gg$ M. This causes, for instance, the M-family X-rays to have a much lower peak to background radiation ratio, making it difficult to determine with high confidence if the M-family is excited.

Chapter

3 Materials and Experimental Methods

3.1 The Multi-Material Joint

3.1.1 The materials

A simple sketch of the multi-material joint being examined in the present study is shown in figure 3.1. The three base metals (BM) are Cu-H02, Ti-Grade 2 and HCT590 steel, and the filler

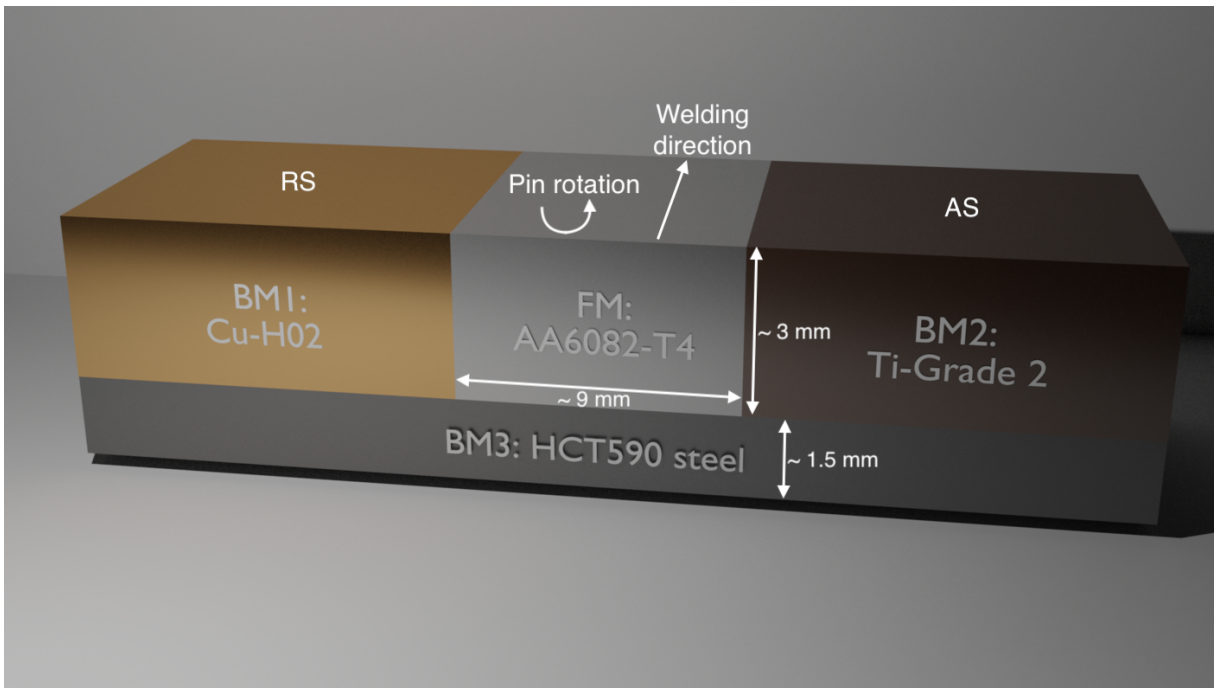

Figure 3.1: *A sketch of the multi-material joint showing the base metals (BM) Cu-H02, Ti-Grade 2 and HCT590 steel, and the filler metal (FM) AA6082-T4. The Cu and Ti plates are* ~ 3 *mm thick and the steel plate is* ~ 1.5 *mm thick. The groove between the BMs has length* ~ 9 *mm. Ti is on the advancing side (AS) and Cu is on the retreating side (RS), which is due to their positions relative to the welding direction and the pin rotation.*

metal (FM) is AA6082-T4. Their chemical compositions, given in weight percentage (wt.%), are listed in table 3.1 while their suppliers and thicknesses are listed in table 3.2.

The FM, AA6082-T4, is a filler wire with diameter 1.4 mm. The filler wire is wrought aluminium alloy from the $6xxx$ series in the T4 temper condition (explained in section 2.4.1). The filler wire was made from a DC cast billet (a bar of metal) which then was homogenized, hot extruded, cold drawn and shaved down to the final dimension [28]. Homogenization is a

Table 3.1: *The chemical compositions of the base and filler metals (BM and FM), given in weight percentage (wt.%). The BMs are Cu-H02, Ti-Grade 2 and HCT590 steel, and the FM is AA6082-T4. *For HCT590 steel, Cr corresponds to Cr+Mo and Ti corresponds to Ti+Nb.*

Materials	Si	Mg	Cu	Mn	Fe	Cr*	Zr	Ti*	B	Al	C	H	N	O	P	S	Other
AA6082-T4	1.11	0.61	0.002	0.51	0.20	0.14	0.13	0.043	0.006	97.22	–	–	–	–	–	–	0.029
Cu-H02	–	–	99.90	–	–	–	–	–	–	–	–	–	–	–	–	–	0.10
Ti-Grade 2	–	–	–	–	0.3	–	–	99.2	–	–	0.1	0.015	0.03	0.25	–	–	–
HCT590	0.75	–	–	2.50	93.50	1.40	–	0.15	–	1.50	0.15	–	–	–	0.04	0.015	–

Table 3.2: *The suppliers and thicknesses of the base metals (BM) and diameter of the filler metal (FM). The BMs include Cu-H02, Ti-Grade 2 and HCT590 steel, and the FM is AA6082-T4.*

Materials	Supplier	Thickness (mm)
AA6082-T4	Hybond AS	1.4 (diameter)
Cu-H02	Astrup	3
Ti-Grade 2	BAOTi	3
HCT590	Benteler	1.5

treatment by which the composition or structure of the wire is made uniform [122]. Homogenizing conditions for the filler wire consisted of a heating rate of approximately 200 °C/h, a holding time of 2 h 15 min at 540 °C and a cooling rate of approximately 300 °C/h. Hot extrusion, which has also been applied to the FM, is a process where a preheated billet is placed inside the press container, which is then pressed by a ram through the extrusion die, to finally get out the desired profile [123]. When being cold drawn, the FM wire is pulled through a die, resulting in an elongated form with a decreased diameter [124].

The first base metal Cu-H02, BM1 in figure 3.1, is pure copper that has been cold worked into half-hard condition (explained in section 2.4.2). The second base metal Ti-Grade 2, BM2 in figure 3.1, is CP titanium that belongs to the classification grade 2 due to its composition (explained in section 2.4.3). The third base metal HCT590, BM3 in figure 3.1, is dual phase steel (explained in section 2.4.4).

3.1.2 HYB process parameters

The metal plates were welded together using the HYB process, described in section 2.1.2, at room temperature without any preheating. The operational parameters employed in the joining process are listed in table 3.3.

During the welding, the titanium plate was on the advancing side (AS) and the copper plate was on the retreating side (RS). This means that while the rotating pin was moving along the groove between the BMs in the welding direction (moving into or out of the paper in the sketch shown in figure 2.1), it was also rotating in a direction that makes its relative velocity to the titanium surface higher compared to its relative velocity to the copper surface. In other words, at the advancing side (Ti), the travel and rotational speed had same direction, while at the retreating side (Cu), both speeds had different directions [125].

Table 3.3: *The operational parameters employed in the HYB joining process.*

Groove width	Rotational speed	Welding speed	Spindle rotational speed	Wire feed rate	Gross heat input
8.6 mm	350 rpm	6 mm/s	350 rpm	115 mm/s	0.33 kJ/mm

3.2 Specimen Preparation for Electron Microscopy

3.2.1 SEM preparation

The preparation process started with cutting out a cross section from the multi-material joint that includes all three interfaces, Al-Cu, Al-Ti and Al-steel. The instrument and the parameters used on that instrument is presented in appendix A.1. The piece was then embedded in *epoxy* with the steps described in appendix A.2.

After being embedded in epoxy, the piece was ready to be polished to make its surface smooth for SEM examination. The polishing process started with rough polishing using silicon carbide grinding papers as described in appendix A.3, and thereafter using *diamond fine polishing*. Two more even finer polishing methods were done after this that both resulted in failure, meaning that they did not improve the condition of all four metals in the specimen and actually had adverse effects on the surface finish of some of them. See appendix A.4 for the results from these two methods, vibration polishing and oxide polishing. After the failed methods, another specimen was prepared using the exact same steps up until and including the step of diamond fine polishing.

Diamond fine polishing process consisted of four steps where different sizes of diamond particles were used. The particle sizes in the four steps were 9 µm, 3 µm, 1 µm and 0.25 µm, in that order. This order of polishing was due to the strategy that one should start polishing with the roughest polishing suited for the hardest material present in the specimen, then continue with finer polishings. The diamond particles came in suspensions that were dripped onto suitable cloths on which the metal piece was polished. The exact suspensions and cloths that were used, together with other details, such as, the polishing instrument and polishing parameters, are all listed in appendix A.5. An OM was used often to determine how long polishing time each step should take. The OM images taken after each of the diamond fine polishing process, with diamond sizes 9 µm, 3 µm, 1 µm and 0.25 µm, are shown in figures 3.2a–3.2d, respectively.

After all the polishing, the whole epoxy surface was covered with aluminium foil and carbon tape connecting the foil to the specimen surface to ensure electrical conduction. This helps to avoid overcharging the epoxy and causing periodic release of electrons which inhibit image formation. An image of the specimen in its final step, ready to be examined, is shown in figure 3.3.

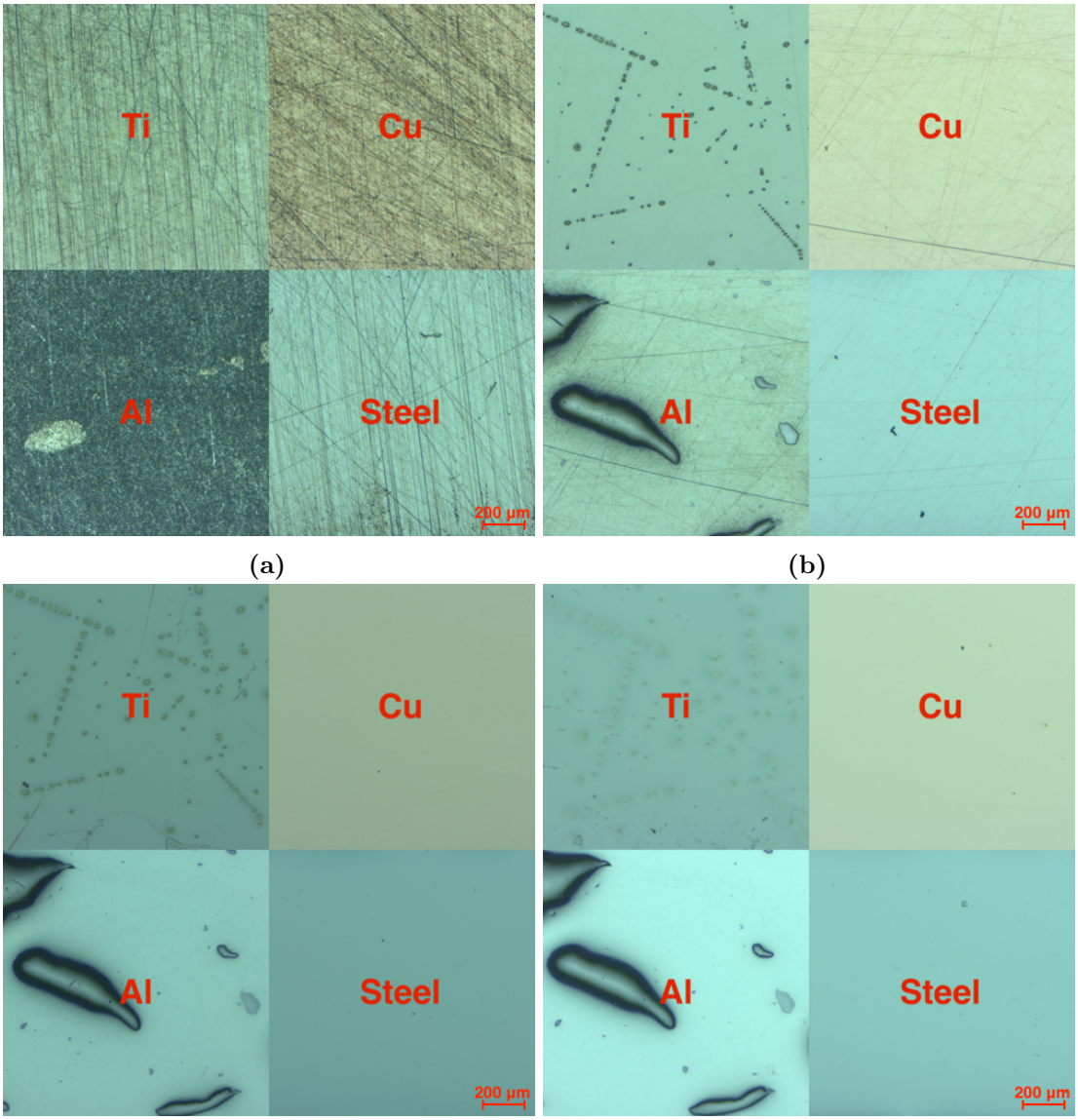

Figure 3.2: *The OM images taken after each of the diamond fine polishing process, with diamond sizes (a)* 9 µm*, (b)* 3 µm*, (c)* 1 µm *and (d)* 0.25 µm*. Some fragments from other metals can be seen in Al.*

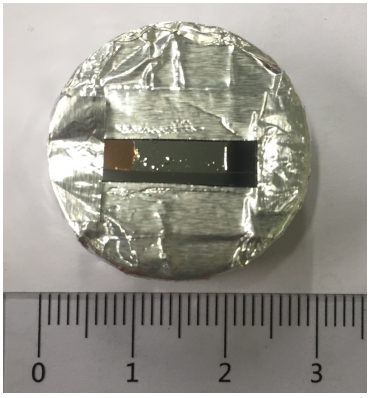

Figure 3.3: *The multi-material joint specimen embedded in epoxy. The epoxy surface has been covered with aluminium foil and carbon tape (hidden underneath Al-foil) connecting the foil to the specimen.*

3.2.2 TEM preparation

Two TEM specimens from each of the Al-Cu and Al-Ti interfaces in the SEM specimen were extracted. Their positions are shown in figure B.1. The specimens Al-Cu-nr.2 and Al-Ti-nr.1 were placed on Cu-grids, while Al-Cu-nr.1 and Al-Ti-nr.2 were placed on Mo-grids. The extraction process of the TEM specimens from the Al-Cu and Al-Ti interfaces has been documented with SEM images in appendix B that show the geometry of the TEM specimens as related to surface of the SEM-specimen in figure 3.3 and also the final shape and size of the TEM lamella.

Specimens were made using *focused ion beam (FIB)*. Site specific FIB, by using a dual-beam Helios G4 UX from FEI, was used to prepare TEM specimens. Carbon protection layers were first deposited on top of the chosen regions to avoid Ga ion-beam damage in the regions of interest. The first part of the carbon protection layer was deposited by electron-beam assisted deposition before a thicker layer was deposited by ion-beam assisted deposition. The chosen regions were cut out and transferred to dedicated half grids by standard lift-out technique. The TEM lamellae were welded onto the half grid ports by carbon on the sides. All coarse thinning was performed with 30 kV acceleration voltage for the Ga+ ions. Final thinning was performed with 5 and 2 kV acceleration voltage on either side to minimize specimen surface damage. The final width of the specimens were approximately 100 nm. A more detailed description of the workings of the FIB can be found, for example, in the paper by Giannuzzi and Stevie (1999) [126].

3.3 Electron Microscopy Characterisation

3.3.1 SEM

The SEMs used for SE and BSE imaging and EDS scans were the Zeiss SUPRA 55-VP and Zeiss ULTRA 55. Both were equipped with *Field Emission Gun (FEG)* capable of obtaining high resolution. SE and BSE imaging were done using both SEMs, and EDS scans were done using Zeiss SUPRA 55-VP with the EDS detector EDAX Octane Pro. Most of the images were taken while using a high tension (HT) voltage between 5 kV to 20 kV.

3.3.2 TEM

The TEMs used were Jeol JEM-2100 equipped with a LaB_6 thermionic source in the gun and Jeol JEM-2100F equipped with a FEG. Both TEMs had EDS detector X-Max with 80 mm^2 detector area from Oxford Instruments. The TEMs were operated at a HT of 200 kV. A Jeol

dual tilt holder was always used. BF-TEM and HAADF-STEM images, SADPs and EDS maps were taken. Jeol JEM-2100 was mainly used to take SADPs and BF TEM images, while Jeol JEM-2100F was mainly used to take HAADF-STEM images in combination with EDS scans. The regular TEM BF imaging was done while inserting an objective aperture to increase the contrast, while SAD was done with selected area apertures of different sizes inserted depending on the size of the area of interest. All diffraction data were taken using the same camera length (100 cm) for ease of comparison.

3.4 Mechanical Tests

The Vickers hardness tests were done along three trajectories that cross the three interfaces with a constant load of 1 kgf = 9.8 N, where kgf is the unit called kilogram-force. The distance between each indentation during the testing was 0.5 mm.

Tensile tests were done across the interfaces Al-Ti and Al-steel, with four specimens from each interface. All Al-Cu specimens failed during machining and could not be tensile tested. The joint examined in this thesis required tensile testing at a smaller scale than usual. The problem was solved by using a miniature tensile test technique developed by Blindheim et al. [127]. The process, described in detail in [127], produced specimens depicted in figure 3.4 which shows that the dimensions of the specimens are around the 1 mm scale. Such specimens were attempted to be made from all three interfaces between the metals, and Al-part was always at the bottom while the top of the specimens were either Cu, steel or Ti. After the specimen preparation, a specially designed split collar was used to grip the head of the specimens, at the same time as the sample was clamped to the lower part of the test machine. This is also shown in the sketch in figure 3.4. Then the specimens were exposed to a pure tensile stress until fracture, and the total displacement and the applied load were recorded. After fracturing, the specimens were examined in SEM as described in section 3.3.1.

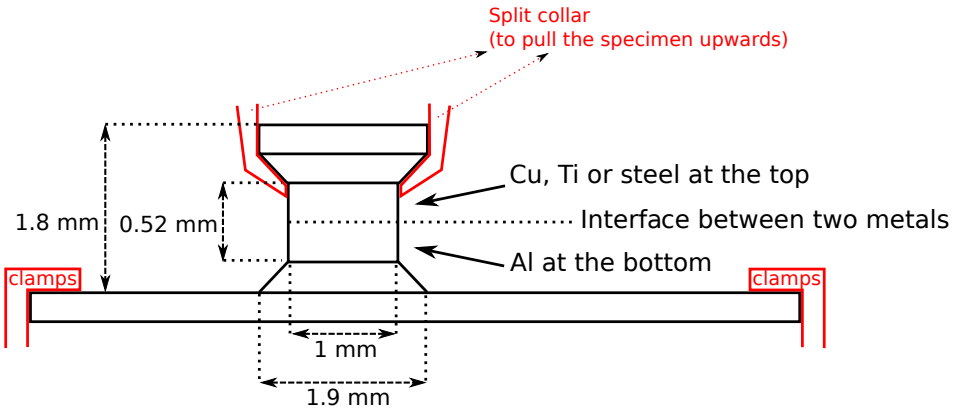

Figure 3.4: *A sketch of a tensile test specimens from the joint examined in this thesis, where Al was always at the bottom while the top of the specimens were either Cu, steel or Ti. During tensile tests, the specimens were fastened at the bottom with clamps while the top part was pulled upwards with a split collar.*

3.5 Data Analysis

3.5.1 SEM

Firstly, the SE images taken with SEM were visually examined to discover regions with interesting phenomena from the interfaces between the metals and the BM fragments in the EZ (extrusion

zone). The program *EDAX* was used to output EDS scan-data in the form of characteristic X-ray spectrum and calculated weight fractions using the Cliff-Lorimer method from equation (2.41). The results from these were used to determine the main composition of the BM-fragments in Al. SE and BSE images taken from the fracture surfaces after tensile testing were visually examined to determine where and how the fractures happened.

3.5.2 TEM

HAADF-STEM and BF-TEM images were examined visually to investigate the morphology of the IMCs at the interfaces. HAADF-STEM images complimented the EDS maps and were used to measure the thickness of the IMC layers. To index the DPs and identify the IMCs, the theory of diffraction explained in sections 2.3 and 2.5.2 was used in addition to a code that has been written in Python. These will be explained in section 3.5.2.1. The processing of the raw data from the EDS maps were done in Python using the theory from section 2.5.5, which will be explained in section 3.5.2.2.

The mean thicknesses, $\bar{x}$, of each of the observed IMC layers were calculated from measurements over 10 different places in every one of the EDS-map-sites using corresponding HAADF-STEM images. Based on the assumption that the $N = 10$ measurements, x_i where $i \in [1, 10]$, were independent, the standard error of the mean, $\delta\bar{x}$, was calculated from

$$\delta\bar{x} = \frac{1}{\sqrt{N}}\sqrt{\frac{\sum_i (x_i - \bar{x})^2}{N-1}}. \tag{3.1}$$

3.5.2.1 DP analysis

The code written in Python is presented in appendix C. The aim of this code was to faster identify the IMCs that generated each DP. The code was designed to take as input the three largest d-spacings from a DP, meaning d-spacing of the three spots in a DP that are closest to the center beam (000), as well as which IMC to test. It then produced a list of possible zone axes and the corresponding indices of the spots consistent with the input IMC and d-spacings. Further verification was then carried out manually regarding whether one of the suggested zone-axis was compatible with the rest of the DP, in which case the input IMC was a possible candidate. Doing this for all the candidate IMCs, one could quickly determine the correct indexing for the observed DP.

The d-spacings, defined by equation (2.21), were found by inserting distances measured using the program ImageJ [128], i.e. inserting number of pixels from (000) to the spots of interest, into equation (2.39) together with the corresponding information from the calibration-DPs. Calibration-DPs were from areas with pure Al, Cu or Ti where d-spacings were known. Also, the IMCs considered in the code were the candidates listed in tables 2.1 and 2.2.

The logic behind the programmatically implemented method of IMC-identification can be summarized as follows:

- The user suggests what IMC to test for and a list of the three largest d-spacings measured from the DP. These d-spacings correspond to the diffraction spots closest to the point corresponding to $(0, 0, 0)$.
- The possible theoretical values of the d-spacings for the given IMC are calculated based on the theoretical atomic configuration and extinction rules explained in section 2.3.
- The theoretical values of the d-spacings are said to match the measured values when they lie within the error-limit set by the user. A typical error-limit used in this thesis was 0.1 Å.

- Going through the list of theoretical d-spacings, the program finds sets of three that match the input.
- The three suggested indices must lie on the same diffraction plane, meaning that they are all perpendicular to the suggested zone-axis vector.
- The three suggested indices must be the ones closest to (000) and there are no other spots that could lie closer in that particular diffraction plane of the IMC being tested.
- The list of indices satisfying these criteria is further reduced by eliminating all but one group of three indices from each zone-axis. This process does not eliminate zone-axes that are equivalent by symmetry.

3.5.2.2 EDS scan analysis

Raw data from EDS scans was obtained through the program *AZTEC*. Any further processing of the raw data was done using the Python package called *HyperSpy* [129]. HyperSpy provides tools to easily facilitate the data analysis.

The analysing process started with plotting the sum spectrum, the spectrum with all the acquired signals, and identifying the characteristic peaks for different elements in the spectrum. The sum spectrum of the Al-Cu-nr.1 specimen is shown as an example in figure 3.5. Thereafter, a sum-map of all the signals were made where the contrast in the image corresponded to the intensity of the signal. This initial plot is often with pixels that are unreliable due to insufficient X-ray counts. If a pixel in the map did not have enough X-ray counts by itself, the spectrum was binned until the count at every binnded-pixel was such that each prominent energy peak in the spectrum became a well defined smooth curve. The term *binned* means to combine several pixels into one larger binned-pixel.

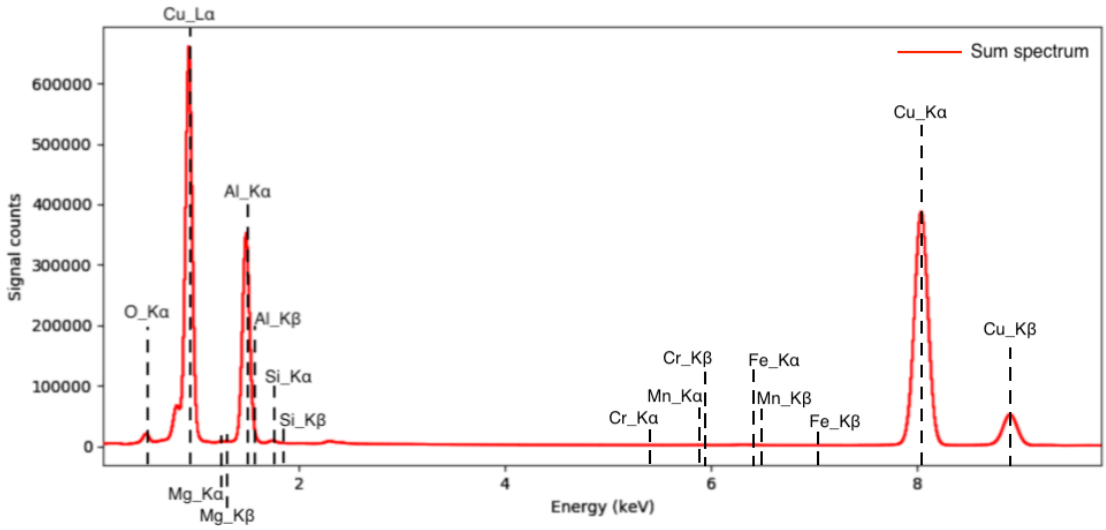

Figure 3.5: *The sum spectrum of Al-Cu-nr.1.*

In the next step, model-fitting was performed for every single spectrum corresponding to each pixel. The model-fitting consisted of a Gaussian distribution for each identified peak in the spectrum and a polynomial for the background signal. An example using Al-Cu-nr.1 is presented in figure 3.6a that shows the model that has been fitted to the signal from a pixel at the position marked in figure 3.6b.

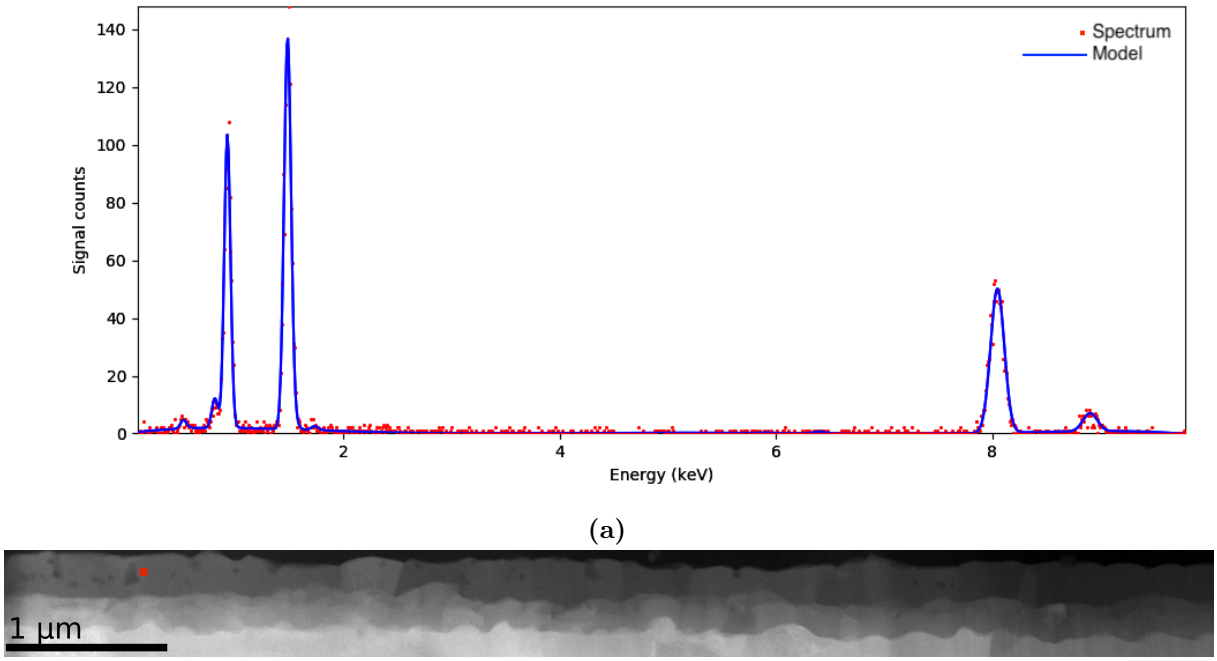

(a)

(b)

Figure 3.6: *An example of model-fitting, performed on the EDS data from Al-Cu-nr.1. (a) Model-fitting performed for the signals in a pixel at the position marked with red in (b).*

The intensities were subsequently used for EDS-quantification at each binned-pixel based on the Cliff-Lorimer method, equation (2.41). This was done to extract atomic percentage (at%) from the measured intesities. The results were then used to plot EDS-maps of at% of user-defined list of elements. The list is made based on the observed characteristic peaks from the sum spectrum. This gave, for each element, a contrast map showing the intensity distribution. The element Mo has been excluded since the Mo-signals only originate from the Mo-grid two of the specimens are mounted on.

Finally, if a layer of IMC with sufficient thickness was observed in the EDS-maps, a mask was applied to filter out the pixels that corresponded to that region. The region could then be analysed in isolation to identify the IMC. The masks were chosen based on the contrast seen in the STEM image of the examined region.

3.5.3 Mechanical tests

The initial processing and further analysis of the results from the mechanical tests used the theories presented in section 2.1.3. The measured Vickers hardness numbers HV, from equation (2.1), were plotted against the displacement along the joint to be analysed further using theory from section 2.1.3.1. The results from the tensile tests were used to make plots similar to the example shown in figure 2.2 where stress, equation (2.2), have been plotted against strain, equation (2.3). These were further analysed using theory from section 2.1.3.2.

The Vickers hardness numbers were found as the mean from 3 individual measurements at each spot. The tensile test results were used to calculate the mean UTS (ultimate tensile strength). For these two, the standard error of the mean of the measurements were calculated using equation (3.1).

Chapter

4 Results

The main objective in this thesis is to investigate the bonding mechanisms in the joint on the microscale by use of SEM, on the nanoscale by use of TEM, and investigate mechanical properties by use of several tests. As such, the results presented in this chapter have been seperated into three parts.

Part one, given in section 4.1, is the results from the SEM studies of the joint where SE-images have been presented for the purpose of giving a general overview of the joint. The focus is on gaps and deformations, differences in grain structure between the bulk and the part close to the interface and to what extent there are regions of mixing between the metals along the interface.

Part two, given in section 4.2, is the results from the TEM studies where HAADF-STEM and BF-TEM images and EDS maps are shown for each TEM-specimen. The SAD results have been indicated on the BF-images. Section 4.2 also includes tables that list the at% of the elements in the potential IMC layers as found from the EDS maps.

Part three, given in section 4.3, is the results from the mechanical tests in terms of plots of hardness values (HV) measured in Vickers hardness tests and in terms of stress-strain curves measured in tensile tests. The same section also shows SE and BSE images taken in SEM of the fracture surfaces after testile testing.

The purpose of this chapter is to present the results in a concise manner. For this reason, only a few sentences will be given to clearify the results. A thorough discussion of the observed results and their implications is given in chapter 5.

4.1 SEM characterisation

4.1.1 Gaps and deformations

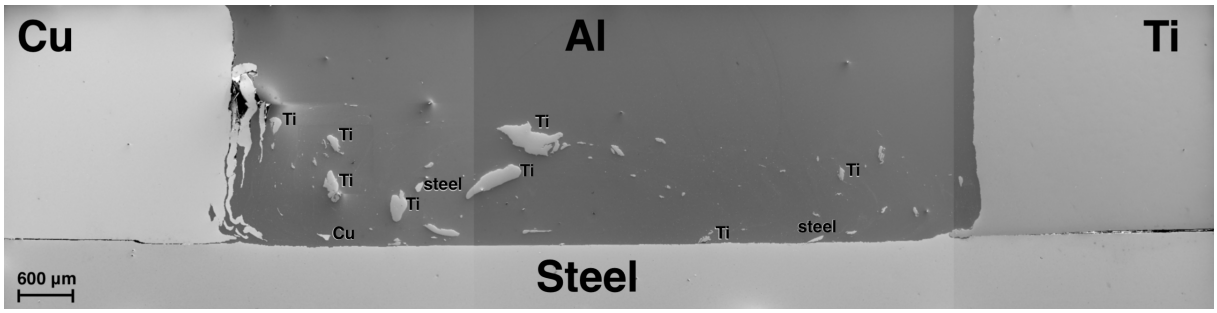

Figure 4.1: *SEM SE-image of the multi-material joint. The images were acquired using low magnification in the SE acquisition mode. The three base metals (BM), Cu-H02, Ti-Grade 2 and HCT590 steel, and the filler metal (FM) AA6082-T4 have been indicated as Cu, Ti, Steel and Al, respectively. The main element of some of the BM fragments in FM have been written with small texts besides the particles, showing that most of them are titanium.*

Figure 4.1 shows SEM SE-image that shows a general view of the multi-material joint depicted in the sketch in figure 3.1. The images are acquired using low magnification in the SE acquisition mode. The three BMs, Cu-H02, Ti-Grade 2 and HCT590 steel, and the FM, AA6082-T4 have been indicated as Cu, Ti, Steel and Al, respectively. This simplified notation will be used hereafter to refer to the metals. EDS analysis of some of the BM fragments in FM show that they are mainly Ti. This is noted using small texts beside these particles in figure 4.1. The same figure shows that Al-Cu interface is the only one among the three that exhibits large pores and deformations. Both Ti and steel has tightly bonded interface with Al.

4.1.2 Change in grain structure

To compare the grain structure in the bulk to that at the interface, SE-images with high magnification have been taken at the interfaces and bulk of the metals. To image the bulk of the metals in the multi-material joint, images have been taken approximately 1 mm into the metals. Figures 4.2a, 4.2c and 4.2e show images from the bulk of Cu, Ti and steel, respectively, while figures 4.2b, 4.2d and 4.2f show images of the same metals close to the interface with Al. There are noticeable differences between the bulk of the steel and the part close to the interface with Al, in terms of grain size. Grain size is smaller closer to the interface. Similar factors could not be observed in other BMs. Also during the SEM inspection, the Al FM looked the same close to all three interfaces and in the middle (farthest away from all three interfaces). Difference in grain size could not be observed in Al either. Therefore, only one image from the middle part of Al is given in figure 4.2g. There, one can see light colored particles in the dark Al-background which probably scattered off BMs while welding. Image of the same region taken at an even higher magnification is shown in figure 4.2h where one starts to see much smaller dispersoids inherent in the Al alloy from the filler wire. The observed phenomena in the images of Al, i.e. dispersoids and scattered particles from BMs, are expected and are not the focus of this thesis. Thus, they will not be discussed further. Some of the images in figure 4.2, especially figures 4.2a and 4.2b, show polishing stripes that are from the surface preparation and are not inherent features of the various metals.

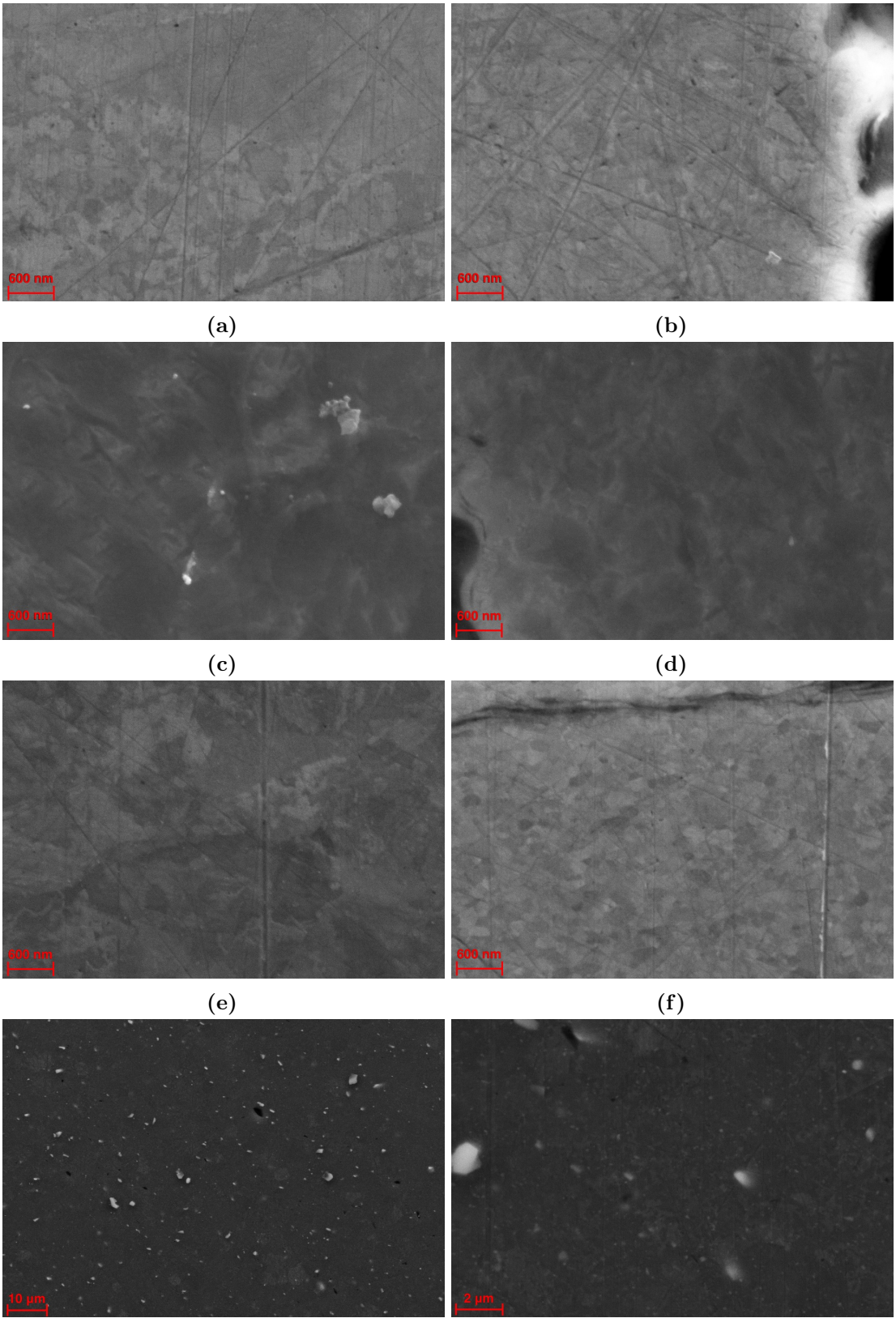

Figure 4.2: *SE-images taken in SEM of the different metals in the multi-material joint to illustrate the difference between bulk and the part close to the interface. (a) Cu bulk, (b) Cu close to interface, (c) Ti bulk, (d) Ti close to interface, (e) Steel bulk, (f) Steel close to interface, (g) Al at a lower magnification, (h) Al at a higher magnification.*

4.1.3 Mixing at the interfaces

Finally, SE-images with high magnification have been taken along all three interfaces to investigate the degree to which the metals have been mixed. The mixing is both in terms of diffusion, a prerequisite for formation of IMCs, and in terms of a swirling or weaving of the two metals.

SE-images taken in SEM from 3 representative regions will be shown from each interface. Figure 4.3 shows the places where these representative examples are taken from. However, to give an idea of the frequency of the occurrence of these regions of mixing, it should be mentioned that hundreds of similar images have been taken (but not shown in this thesis) and much more have been observed while looking at the specimen in SEM.

Figures 4.4–4.7 show, respectively, SE-images from the Al-Cu, Al-Ti and Al-Steel interfaces and from the BM fragments in Al. The images have been taken from the same areas at two different magnifications, lowest magnification images to the left and highest magnification images to the right. In the lowest magnification images, red rectangles mark the location of the highest magnified images to the right. The highest magnification images of all three interfaces and BM fragments in Al display regions with contrast (or color) that is intermediate compared to the that from each of the main metals in the joint. Hence, these images indicate that there are layers of mixing between the metals, and that the elemental contents seem relatively constant in each layer. This is highly indicative of IMCs. The number of layers varies. Some of the highest magnified images, such as figure 4.6d, seem to indicate that only one layer is present, while most of the other images seem to display more than one layers or have layers being mixed together. The multi-layer formation is especially evident in figure 4.4f which seem to show three different layers.

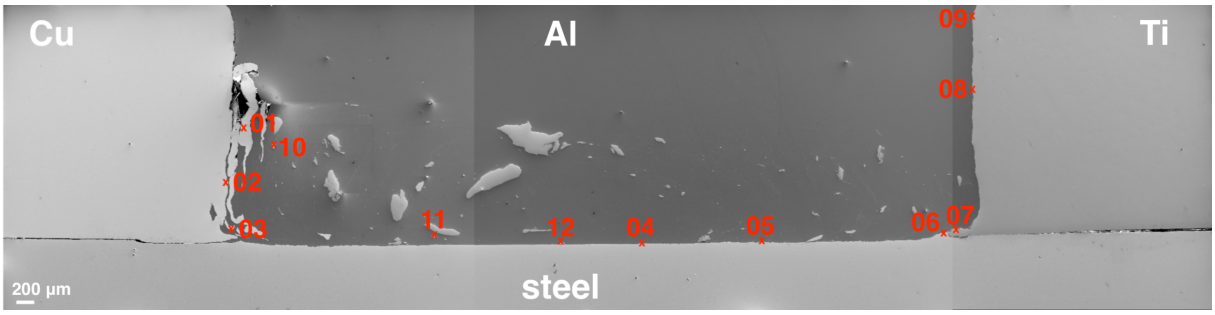

Figure 4.3: *SE-image of the whole specimen examined in SEM, showing the position of the regions with images presented in figures 4.4–4.7.*

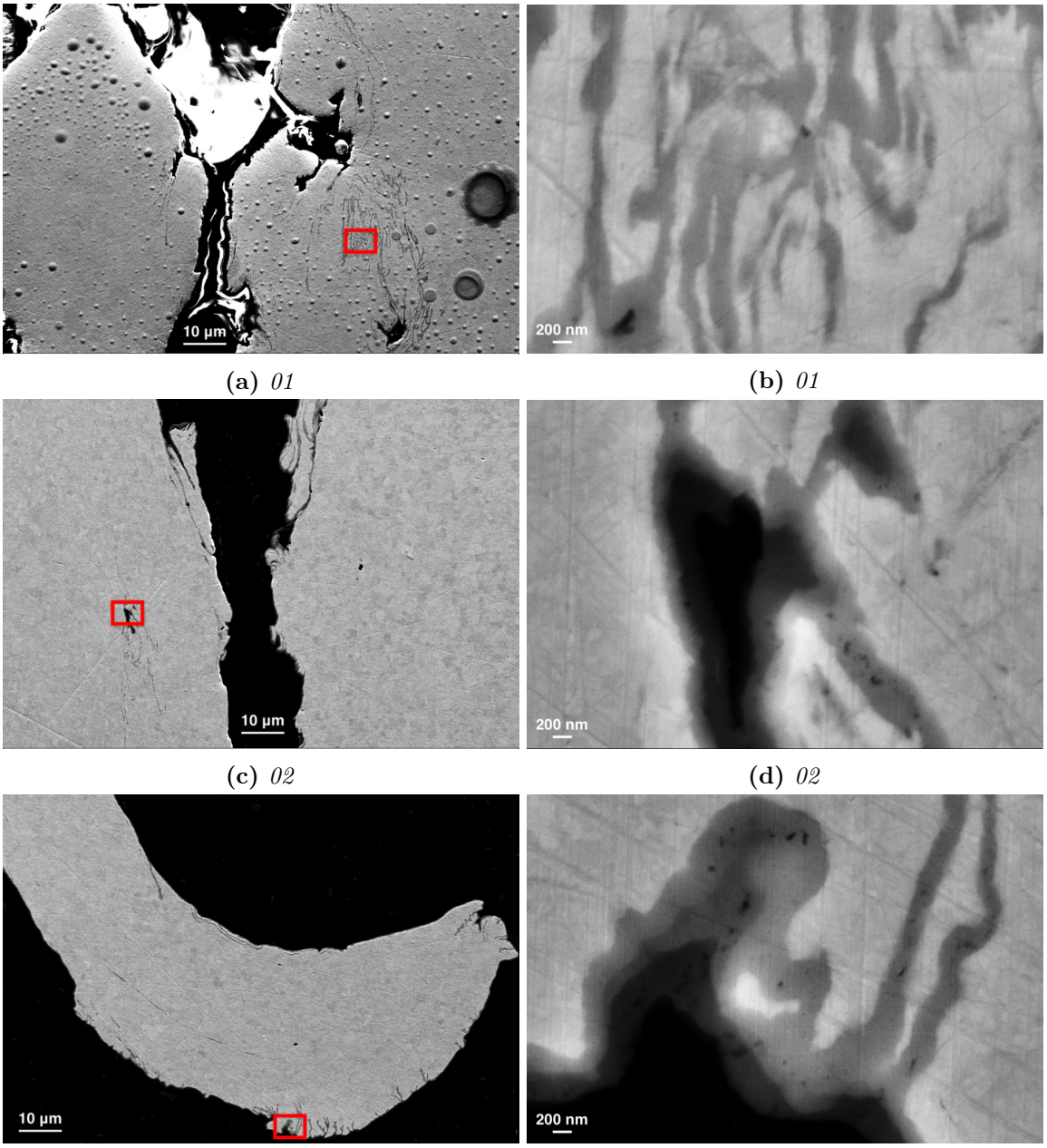

(a) *01* **(b)** *01*

(c) *02* **(d)** *02*

(e) *03* **(f)** *03*

Figure 4.4: *SE-images taken in SEM from the Al-Cu interface of the multi-material joint. Images with low magnification to the left ((a), (c), (e)) have red rectangles indicating the locations of the images with high magnification to the right ((b), (d), (f)). Subtitles indicate the position of the images as numbered in figure 4.3. (a) shows that epoxy has gathered in the gaps and has also resided on the metal surface as small droplets.*

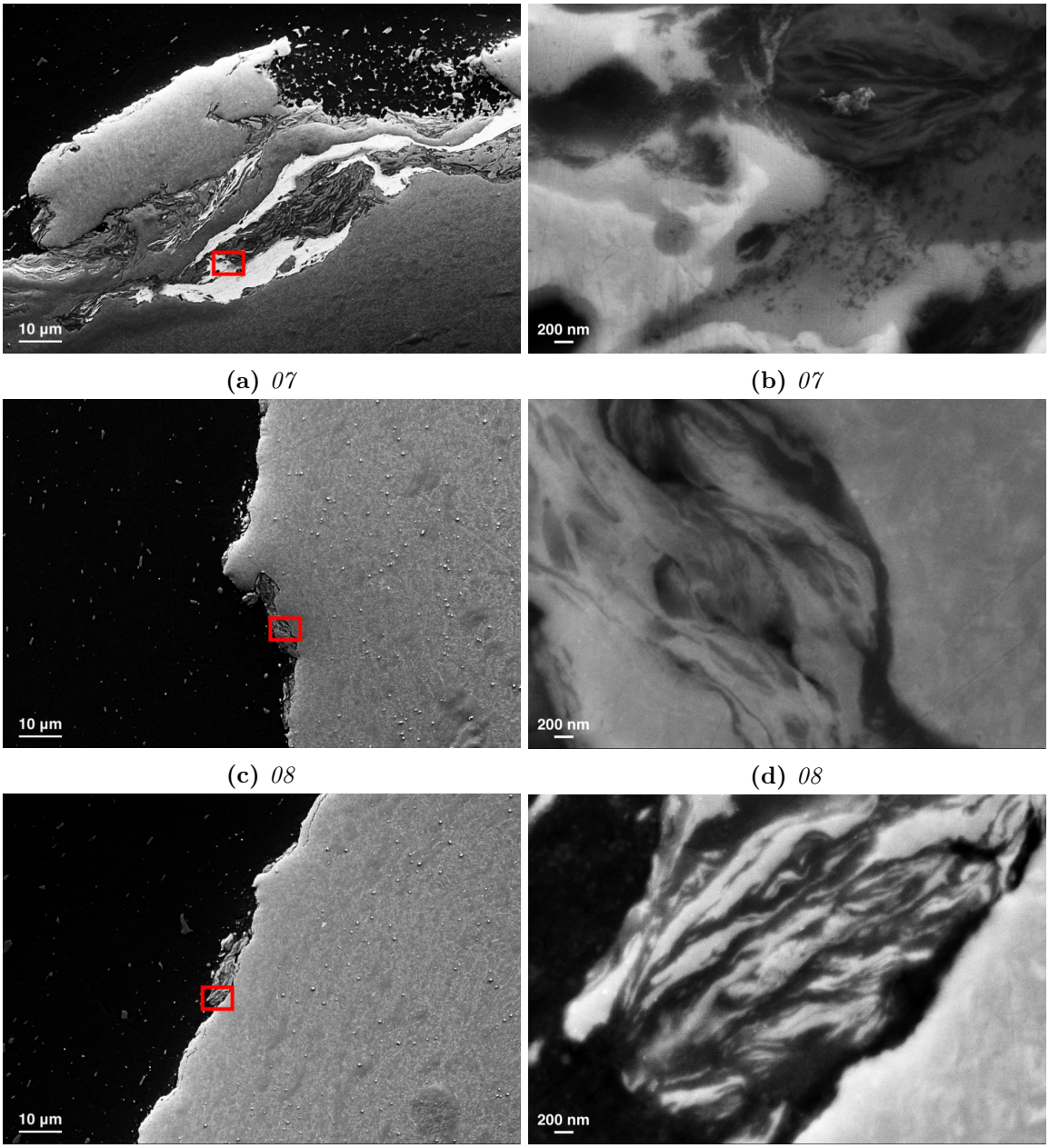

(a) *07* **(b)** *07*

(c) *08* **(d)** *08*

(e) *09* **(f)** *09*

Figure 4.5: *SE-images taken in SEM from the Al-Ti interface of the multi-material joint. Images with low magnification to the left ((a), (c), (e)) have red rectangles indicating the locations of the images with high magnification to the right ((b), (d), (f)). Subtitles indicate the position of the images as numbered in figure 4.3.*

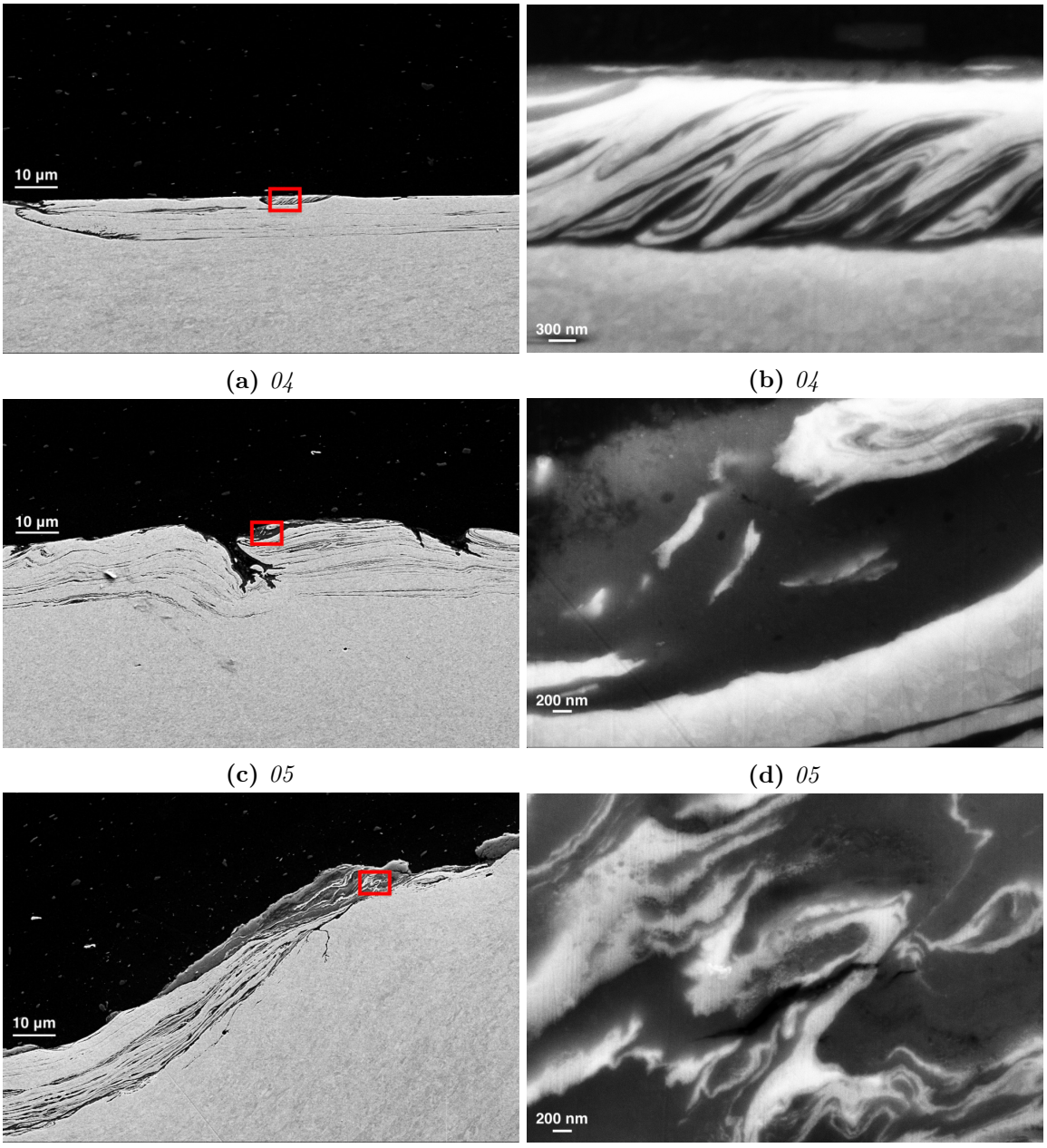

(a) *04* **(b)** *04*

(c) *05* **(d)** *05*

(e) *06* **(f)** *06*

Figure 4.6: *SE-images taken in SEM from the Al-steel interface of the multi-material joint. Images with low magnification to the left ((a), (c), (e)) have red rectangles indicating the locations of the images with high magnification to the right ((b), (d), (f)). Subtitles indicate the position of the images as numbered in figure 4.3.*

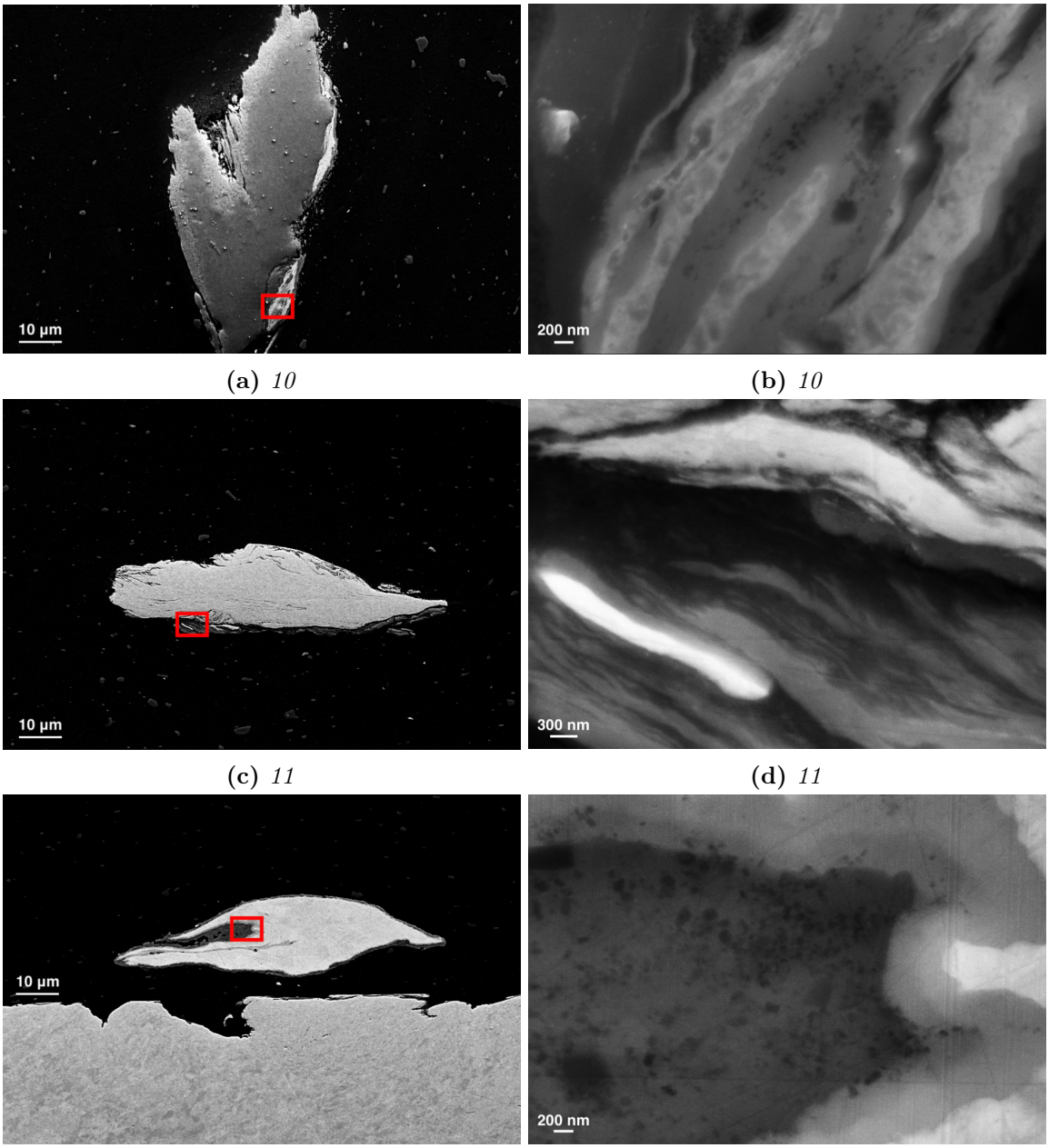

(a) *10* **(b)** *10*

(c) *11* **(d)** *11*

(e) *12* **(f)** *12*

Figure 4.7: *SE-images taken in SEM from the BM fragments that have fallen into Al of the multi-material joint. Images with low magnification to the left ((a), (c), (e)) have red rectangles indicating the locations of the images with high magnification to the right ((b), (d), (f)). Subtitles indicate the position of the images as numbered in figure 4.3.*

4.2 TEM characterisation

The purpose of the TEM results presented here is to identify possible IMCs that are present in regions of mixing at the interface, found in section 4.1.3, and to investigate their morphologies and thicknesses. This is achieved by EDS mapping and SADPs. There are two TEM-specimens from the Al-Cu interface, Al-Cu-nr.1 and Al-Cu-nr.2, and two from the Al-Ti interface, Al-Ti-nr.1 and Al-Ti-nr.2.

4.2.1 Al-Cu-nr.1

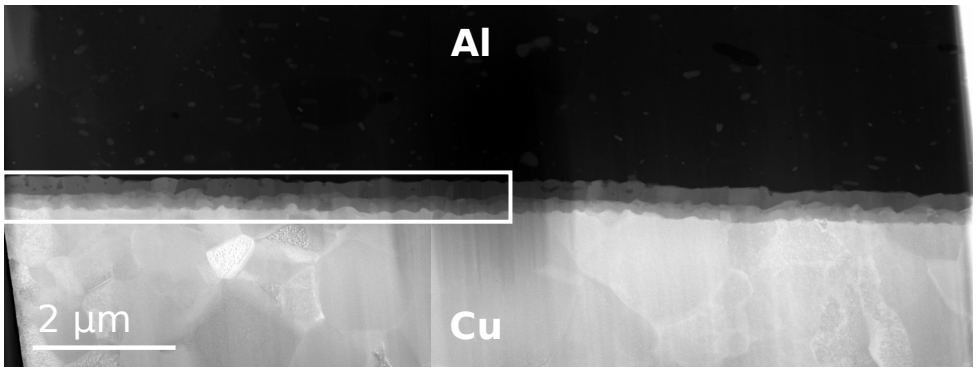

(a)

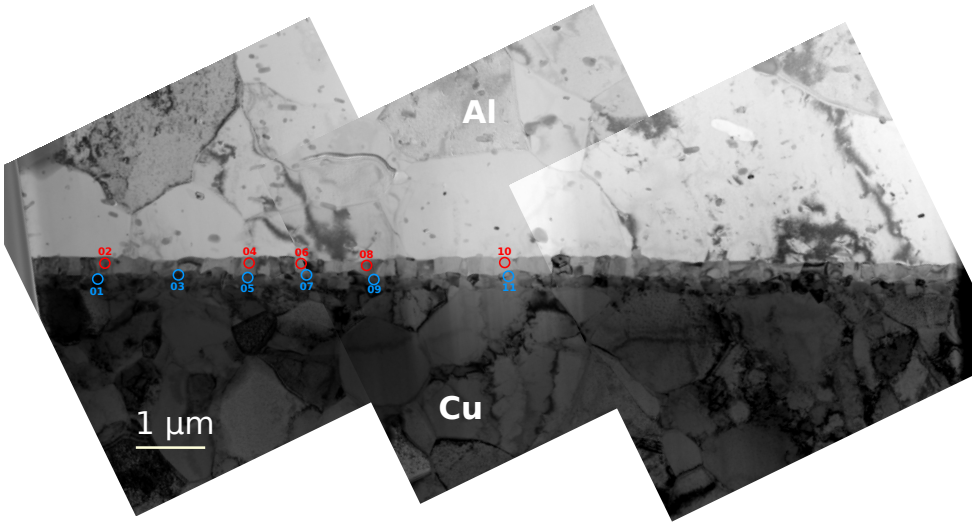

(b)

Figure 4.8: *(a) HAADF-STEM and (b) BF-TEM images taken of the specimen Al-Cu-nr.1. The rectangle in (a) shows the locations of the EDS site. (b) shows all the regions where SADPs have been taken from and identified. Each numbered region has been indicated using a circle which symbolizes the SA-aperture used. The colors of the circles mean that the DPs taken from that region have been identified to be from the following IMCs: blue means Al_4Cu_9 and red means Al_2Cu.*

Figure 4.8a shows the HAADF-STEM image of Al-Cu-nr.1 which is the notation used in this thesis to denote the first specimen taken from the Al-Cu interface. Regions with intermediate contrast (color) can be seen between the regions with pure Al, which is shown with dark contrast, and pure Cu, which has a light contrast. This is in agreement with the SEM results presented in section 4.1.3 and indicate the formation of IMCs between Al and Cu. Similar phenomena can also be seen in the other specimens shown in the later sections. Figure 4.8b shows the BF-TEM image of the same specimen. In figure 4.8b, all the regions where SADPs have been taken and used to identify the crystal structure, have been numbered and indicated using a circle which symbolizes the SA-aperture used. Remember, the region inside the SA-aperture is the region contributing to the DP. The colors of the circles mean that the DPs taken from that region have been identified to be from the following IMCs: blue means Al_4Cu_9 and red means Al_2Cu. For each identified IMC, two SADPs taken from different zone-axes is given as examples here in figure 4.9, where the IMC each SADPs correspond to have been written on the upper right corner of each image while the zone axis, z, have been written on the upper left corner. The whole list of SADPs are

presented in the same way in figures D.1 and D.2 in appendix D.

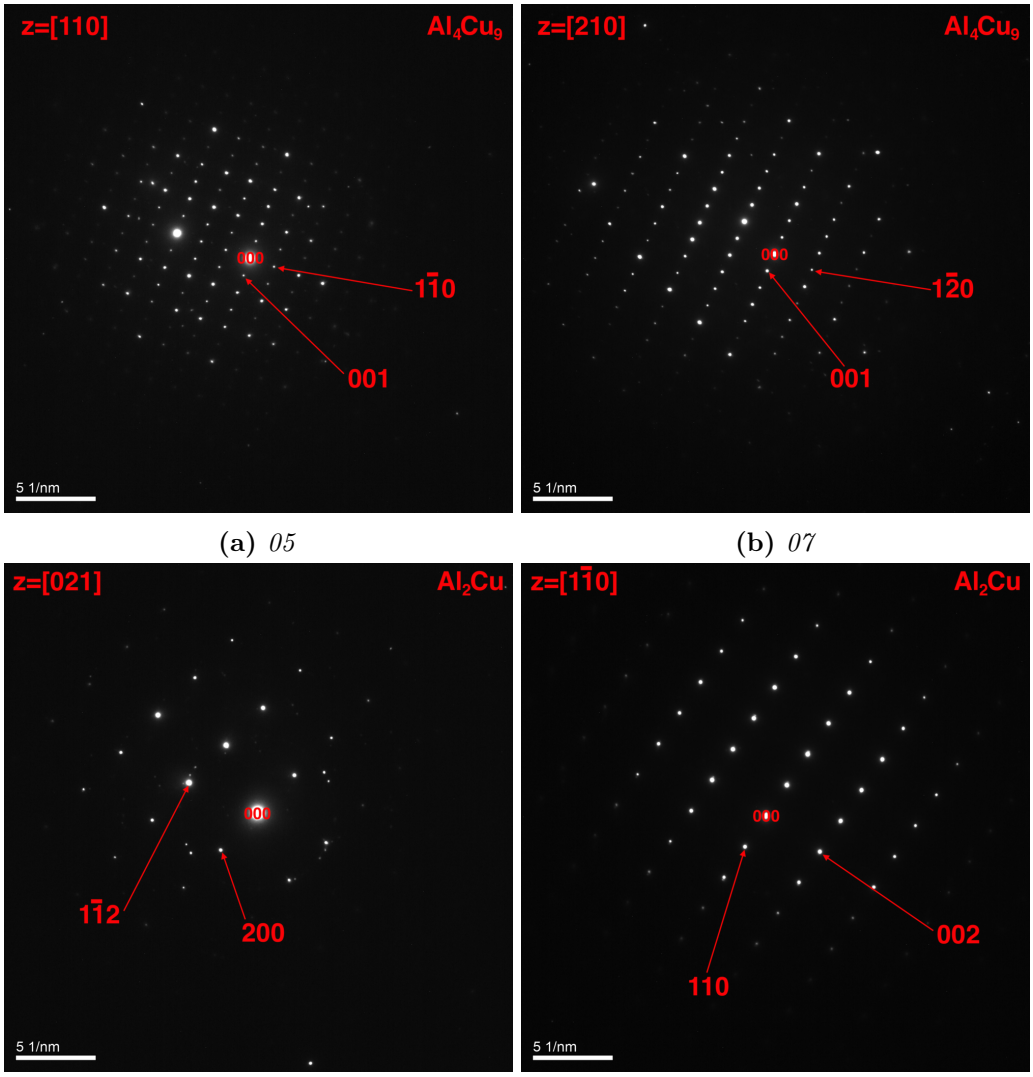

(a) *05* **(b)** *07*

(c) *06* **(d)** *08*

Figure 4.9: *Some of the SADPs taken from Al-Cu-nr.1. The IMCs the SADPs correspond to have been written on the upper right corner of each image while the zone axis, z, have been written on the upper left corner. The numbers in the subtitles indicate which numbered-region in figure 4.8b each DP is taken from.*

The EDS maps showing the at% of the elements in a site in Al-Cu-nr.1 are shown in figures 4.10b–4.10i for the elements Al, Cu, O, Cr, Fe, Mg, Mn, and Si, respectively. The EDS site location is indicated in figure 4.8a using a rectangle. The HAADF-STEM image of that site is shown in figure 4.10a. Two potential IMC layers have been observed and filtered out from the map data using the masks in figures 4.10j and 4.10k. Table 4.1 lists the measured at% of the different elements in those layers.

The thickness of each IMC layer has been estimated by use of the HAADF-STEM image in figure 4.8a. The mean thicknesses, $\bar{x}$, and corresponding standard errors, $\delta\bar{x}$, are shown in table 4.2. Table 4.2 also shows the ratio between the at% of Cu and Al in the IMC layers, which have been calculated using the data from table 4.1.

Table 4.1: *The at% of the elements in the potential Al-Cu IMC layers in Al-Cu-nr.1, selected with masks shown in figures 4.10j and 4.10k. The at% are given to the nearest whole number.*

	Al	Cu	O	Cr	Fe	Mg	Mn	Si
at% in layer 1	65	29	5	0	0	1	0	1
at% in layer 2	36	59	5	0	0	0	0	0

Table 4.2: *The ratio between the at% of Cu and Al in the IMC layers in Al-Cu-nr.1 and the mean thicknesses, $\bar{x}$, of those layers together with the corresponding standard errors, $\delta\bar{x}$. The thicknesses are measured from the HAADF-STEM image in figure 4.8a.*

Layer	$\frac{\text{at\% Cu}}{\text{at\% Al}}$	$\bar{x}$ (nm)	$\delta\bar{x}$ (nm)
1	0.45	221	16
2	1.64	189	10

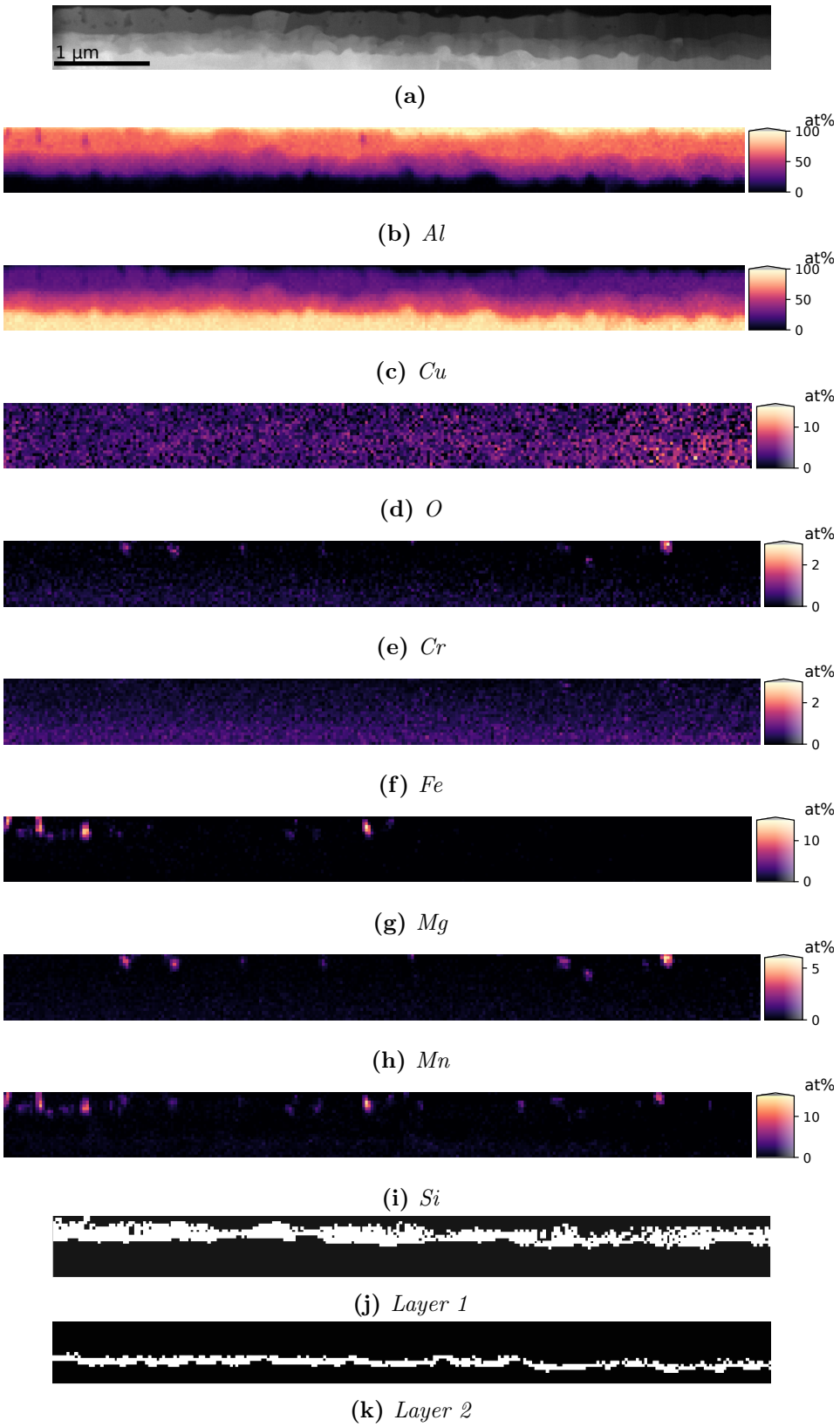

(a)

(b) *Al*

(c) *Cu*

(d) *O*

(e) *Cr*

(f) *Fe*

(g) *Mg*

(h) *Mn*

(i) *Si*

(j) *Layer 1*

(k) *Layer 2*

Figure 4.10: *A site in Al-Cu-nr.1. (a) HAADF-STEM image, (b)-(i) EDS maps showing the at% of the elements Al, Cu, O, Cr, Fe, Mg, Mn, and Si, respectively, and (j)-(l) masks applied to filter out the potential IMC layers.*

4.2.2 Al-Cu-nr.2

(a)

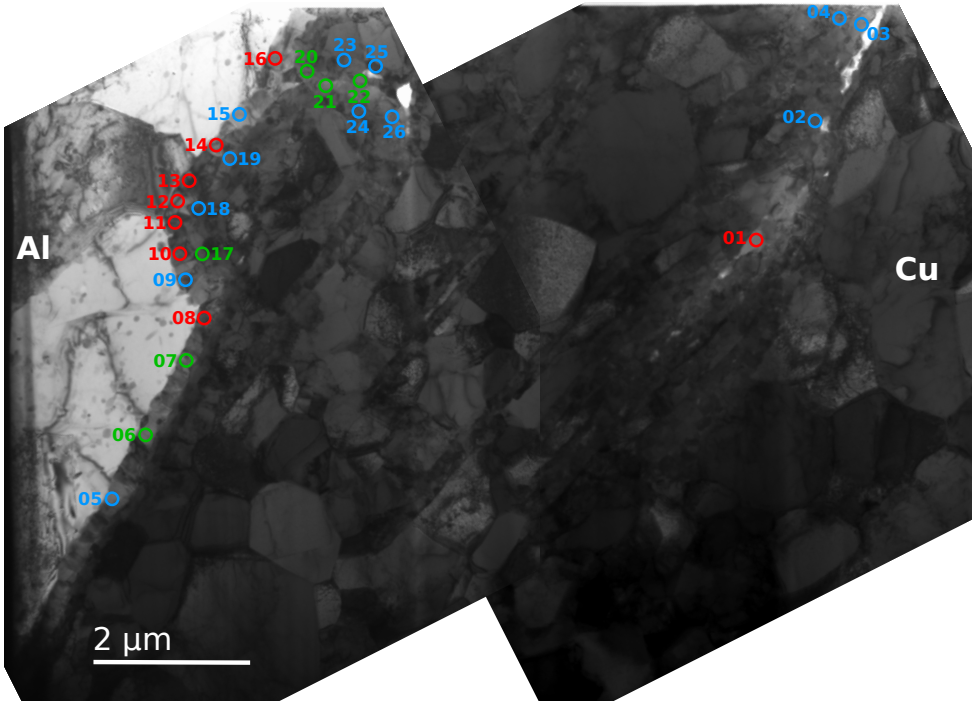

(b)

Figure 4.11: *(a) HAADF-STEM and (b) BF-TEM images taken of the specimen Al-Cu-nr.2. (a) shows the locations of the EDS sites 1-3. (b) shows all the regions where SADPs have been taken from and identified. Each numbered region has been indicated using a circle which symbolizes the SA-aperture used. The colors of the circles mean that the DPs taken from that region have been identified to be from the following IMCs: blue means Al_4Cu_9, red means Al_2Cu and green means $AlCu$.*

Figure 4.11a shows the HAADF-STEM image of Al-Cu-nr.2 which is the notation used in this thesis to denote the second specimen taken from the Al-Cu interface. Figure 4.11b shows the BF-TEM image of the same specimen. Both figures seem to show presence of IMC layers between Al and Cu. In figure 4.11b, all the regions where SADPs have been taken and used to identify the crystal structure, have been numbered and indicated using a circle which symbolizes the SA-aperture used. The colors of the circles mean that the DPs taken from that region have been identified to be from the following IMCs: blue means Al_4Cu_9, red means Al_2Cu and green means AlCu. For each identified IMC, two SADPs taken from different zone-axes is given as examples here in figure 4.12, where the IMC each SADPs correspond to have been written on the upper right corner of each image while the zone axis, z, have been written on the upper left corner. The whole list of SADPs are presented in the same way in figures E.1–E.4 in appendix E.

The EDS maps have been taken from three different sites in Al-Cu-nr.2: site 1, site 2 and site 3 indicated in figure 4.11a. The maps are presented here and discussed later in section 5.2.1.2. The EDS maps showing the at% of the elements in *site 1* are shown in figures 4.13b–4.13f and 4.14a–4.14c for the elements Al, Cu, O, Cr, Fe, Mg, Mn, and Si, respectively. The HAADF-STEM image of site 1 is shown in figure 4.13a. The same image with different image contrast, to show the grains in Al, is shown in figure 4.15. Three potential IMC layers have been observed and filtered out from the map data using the masks in figures 4.14d–4.14f. Table 4.3 lists the measured at% of the different elements in those layers.

The EDS maps showing the at% of the elements in *site 2* are shown in figures 4.16b–4.16i for the elements Al, Cu, O, Cr, Fe, Mg, Mn, and Si, respectively. The HAADF-STEM image of site 2 is shown in figure 4.16a. Two potential IMC layers have been observed and filtered out from the map data using the masks in figures 4.16j and 4.16k. Table 4.4 lists the measured at% of the different elements in those layers.

The EDS maps showing the at% of the elements in *site 3* are shown in figures 4.17b–4.17i for the elements Al, Cu, O, Cr, Fe, Mg, Mn, and Si, respectively. The HAADF-STEM image of site 3 is shown in figure 4.17a. Three potential IMC layers have been observed and filtered out from the map data using the masks in figures 4.17j–4.17l. Table 4.5 lists the measured at% of the different elements in those layers.

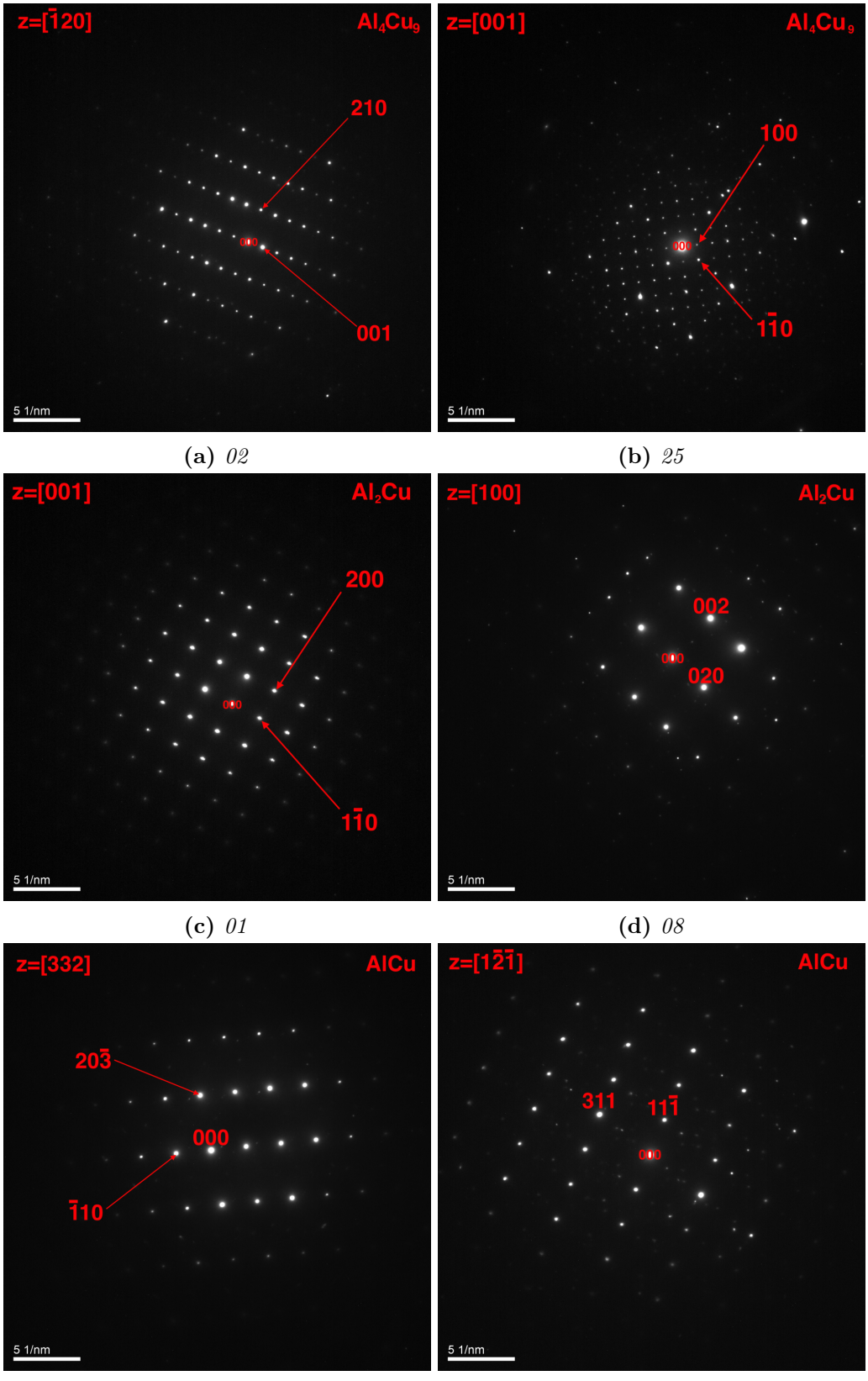

(a) *02* **(b)** *25*

(c) *01* **(d)** *08*

(e) *07* **(f)** *21*

Figure 4.12: *Some of the SADPs taken from Al-Cu-nr.2. The IMCs the SADPs correspond to have been written on the upper right corner of each image while the zone axis, z, have been written on the upper left corner. The numbers in the subtitles indicate which numbered-region in figure 4.11b each DP is taken from.*

Table 4.3: *The at% of the elements in the potential Al-Cu IMC layers in site 1 in Al-Cu-nr.2, selected with masks shown in figures 4.14d–4.14f. The at% are given to the nearest whole number.*

	Al	Cu	O	Cr	Fe	Mg	Mn	Si
at% in layer 1	63	31	4	0	0	1	0	1
at% in layer 2	39	55	5	0	0	0	0	0
at% in layer 3	27	68	5	0	0	0	0	0

Table 4.4: *The at% of the elements in the potential Al-Cu IMC layers in site 2 in Al-Cu-nr.2, selected with masks shown in figures 4.16j and 4.16k. The at% are given to the nearest whole number.*

	Al	Cu	O	Cr	Fe	Mg	Mn	Si
at% in layer 1	65	30	3	0	0	1	0	1
at% in layer 2	34	62	4	0	0	0	0	0

Table 4.5: *The at% of the elements in the potential Al-Cu IMC layers in site 3 in Al-Cu-nr.2, shown in figures 4.17j–4.17l. The at% are given to the nearest whole number.*

	Al	Cu	O	Cr	Fe	Mg	Mn	Si
at% in layer 1	57	37	3	0	0	1	0	1
at% in layer 2	41	53	5	0	0	1	0	1
at% in layer 3	20	75	4	0	0	0	0	0

The thickness of each IMC layer has been estimated by use of the HAADF-STEM image in figure 4.11a. The mean thicknesses, $\bar{x}$, and corresponding standard errors, $\delta\bar{x}$, are shown in table 4.6. Table 4.6 also shows the ratio between the at% of Cu and Al in the IMC layers in the three sites in Al-Cu-nr.2, which have been calculated using the data from tables 4.3–4.5.

Table 4.6: *The ratio between the at% of Cu and Al in the IMC layers in the three sites in Al-Cu-nr.2 and the mean thicknesses, $\bar{x}$, of those layers together with the standard errors of the mean thicknesses, $\delta\bar{x}$. The thicknesses are measured from the HAADF-STEM image in figure 4.11a.*

Site	Layer	$\frac{\text{at\% Cu}}{\text{at\% Al}}$	$\bar{x}$ (nm)	$\delta\bar{x}$ (nm)
1	1	0.49	307	31
1	2	1.41	146	21
1	3	2.52	294	49
2	1	0.46	250	12
2	2	1.82	168	9
3	1	0.66	260	22
3	2	1.29	254	39
3	3	3.75	407	59

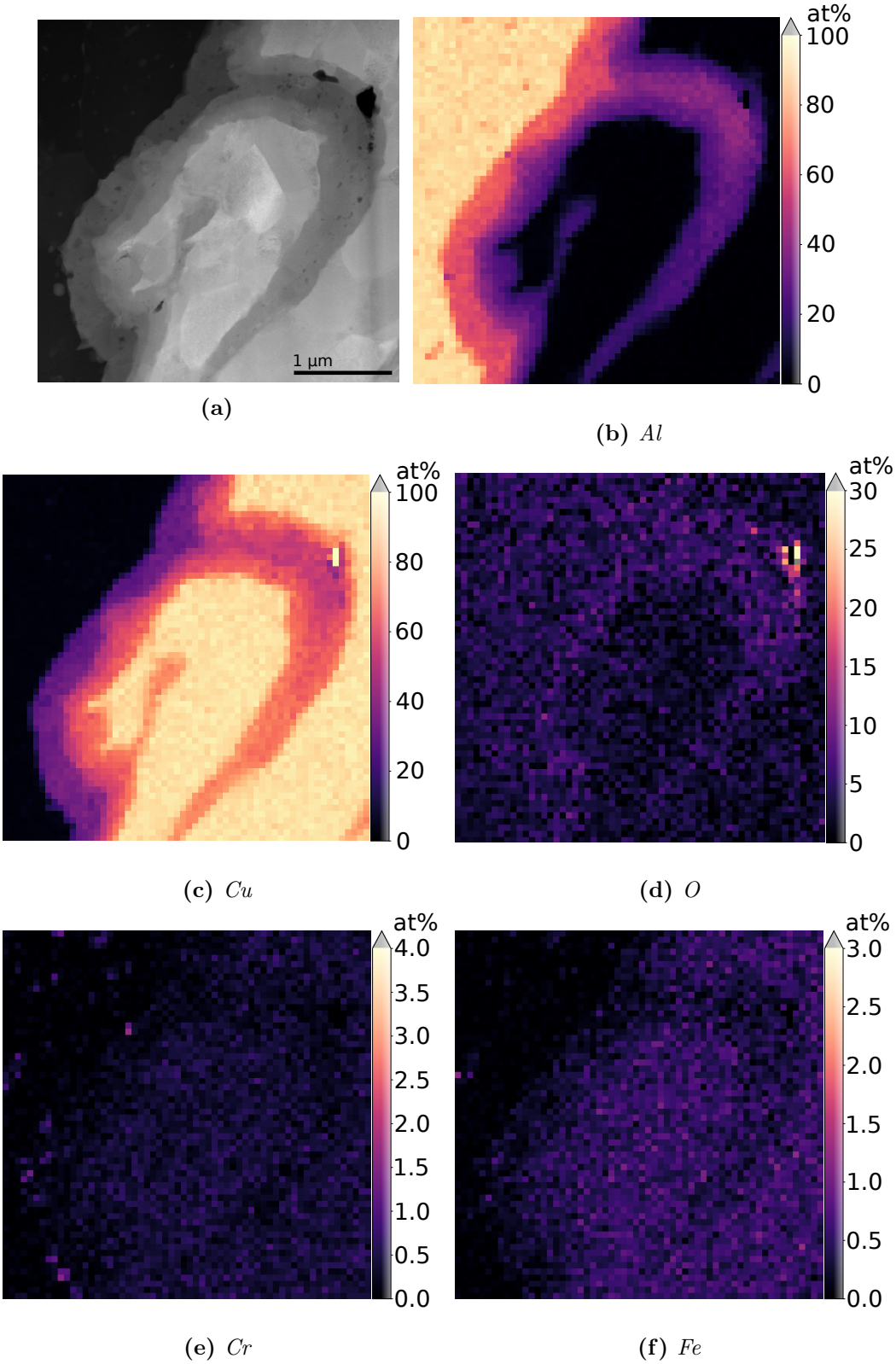

(a) **(b)** *Al* **(c)** *Cu* **(d)** *O* **(e)** *Cr* **(f)** *Fe*

Figure 4.13: ***Part 1: Site 1*** *in Al-Cu-nr.2. (a) HAADF-STEM image, (b)-(i) EDS maps showing the at% of the elements Al, Cu, O, Cr, Fe, Mg, Mn, and Si, respectively, and (j)-(l) masks applied to filter out the potential IMC layers.*

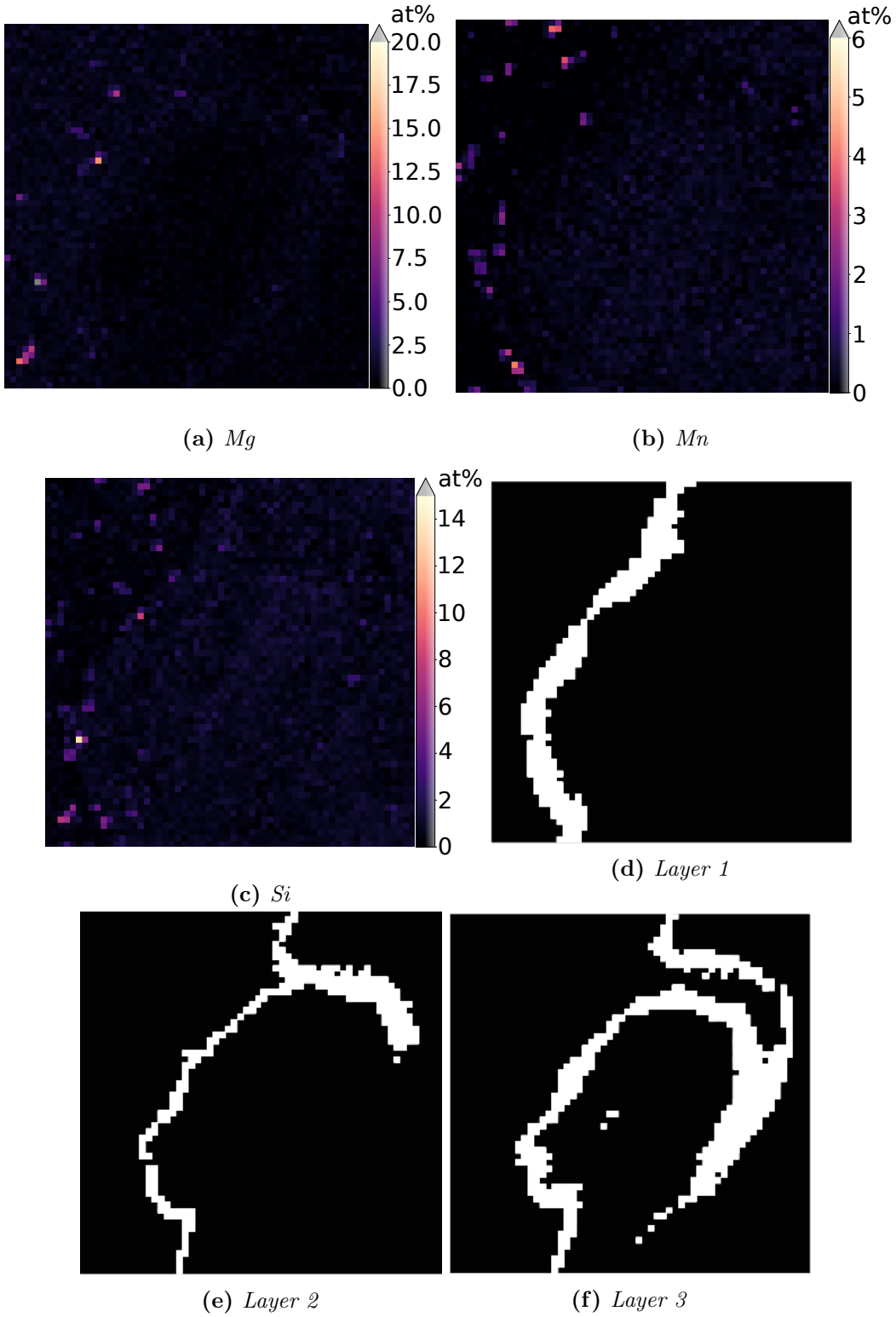

(a) *Mg* **(b)** *Mn*

(c) *Si* **(d)** *Layer 1*

(e) *Layer 2* **(f)** *Layer 3*

Figure 4.14: ***Part 2: Site 1*** *in Al-Cu-nr.2. (a) HAADF-STEM image, (b)-(i) EDS maps showing the at% of the elements Al, Cu, O, Cr, Fe, Mg, Mn, and Si, respectively, and (j)-(l) masks applied to filter out the potential IMC layers.*

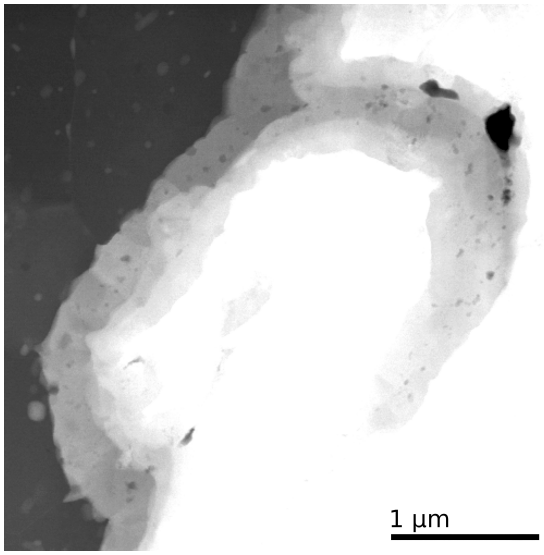

Figure 4.15: *HAADF-STEM image of **site 1** in Al-Cu-nr.2.*

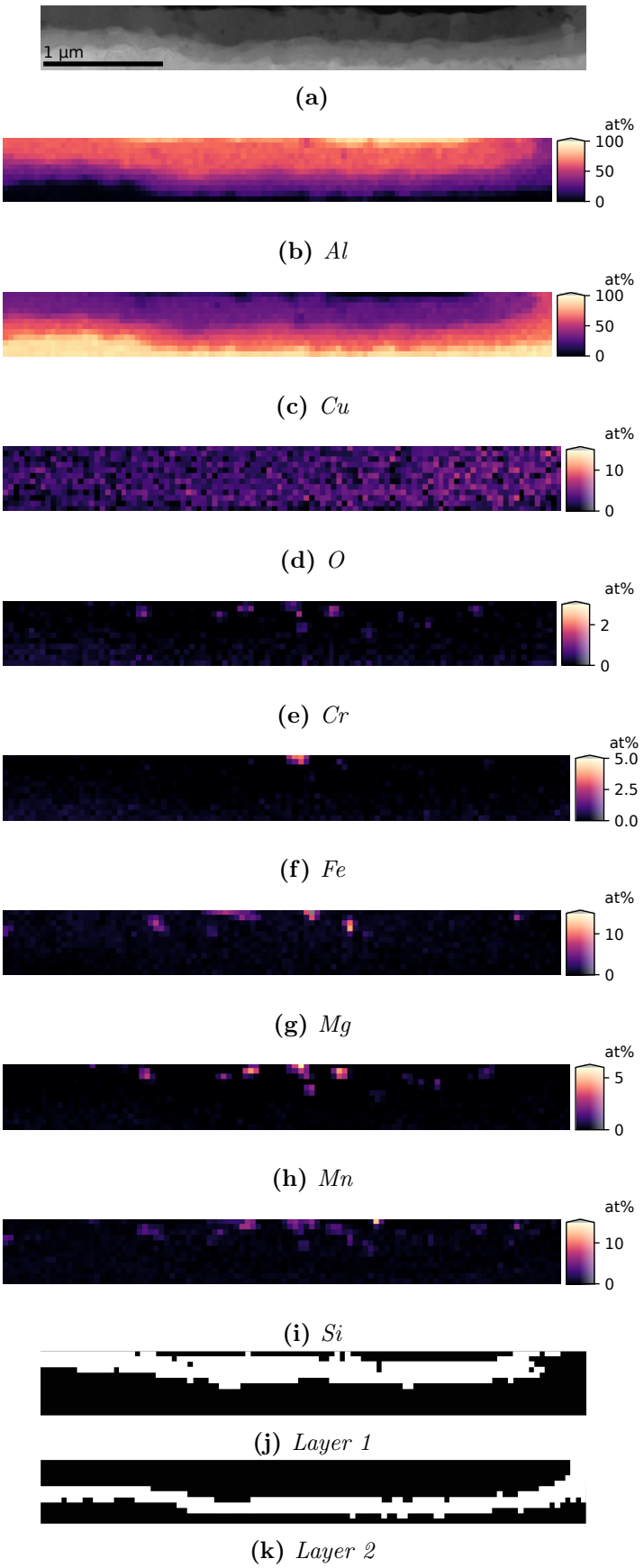

Figure 4.16: ***Site 2*** *in Al-Cu-nr.2. (a) HAADF-STEM image, (b)-(i) EDS maps showing the at% of the elements Al, Cu, O, Cr, Fe, Mg, Mn, and Si, respectively, and (j)-(l) masks applied to filter out the potential IMC layers.*

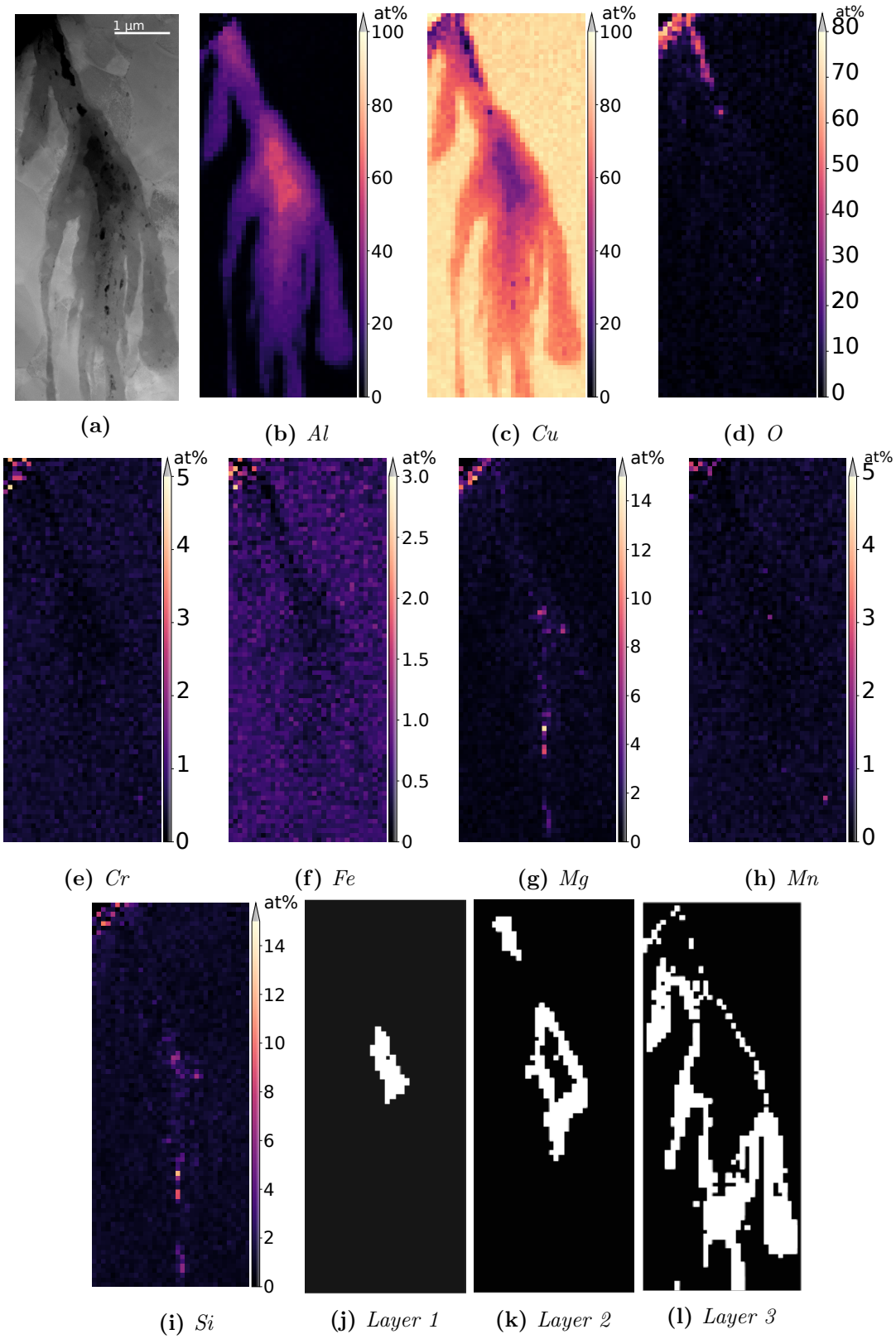

(a) **(b)** *Al* **(c)** *Cu* **(d)** *O*

(e) *Cr* **(f)** *Fe* **(g)** *Mg* **(h)** *Mn*

(i) *Si* **(j)** *Layer 1* **(k)** *Layer 2* **(l)** *Layer 3*

Figure 4.17: ***Site 3*** *in Al-Cu-nr.2. (a) HAADF-STEM image, (b)-(i) EDS maps showing the at% of the elements Al, Cu, O, Cr, Fe, Mg, Mn, and Si, respectively, and (j)-(l) masks applied to filter out the potential IMC layers.*

4.2.3 Al-Ti-nr.1

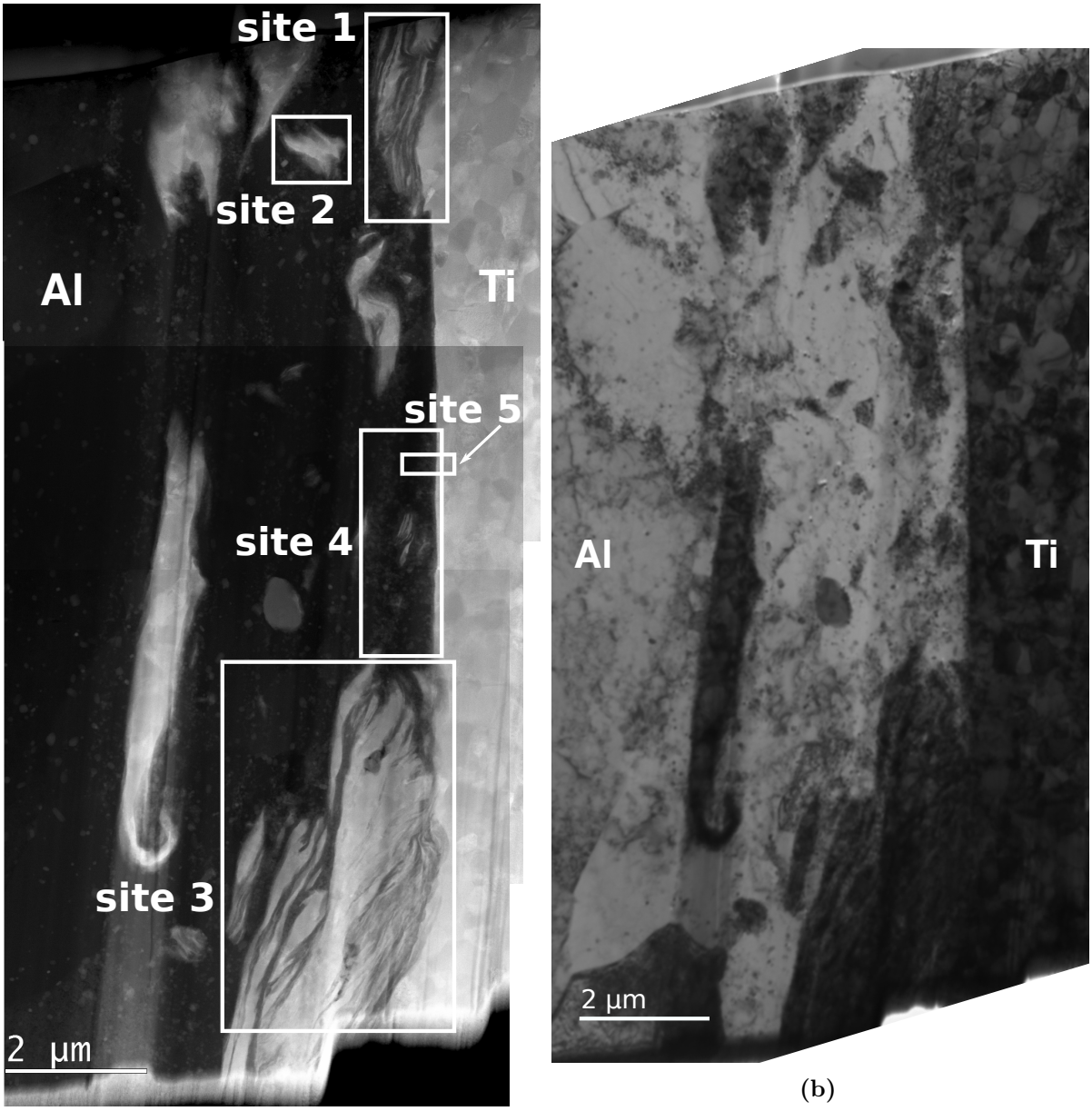

Figure 4.18: *(a) HAADF-STEM and (b) BF-TEM images taken of Al-Ti-nr.1. (a) shows the locations of the EDS sites 1-3.*

Figure 4.18a shows the HAADF-STEM image of Al-Ti-nr.1 which is the notation used in this thesis to denote the first specimen taken from the Al-Ti interface. Figure 4.18b shows the BF-TEM image of the same specimen. These images firstly show that Al and Ti have mixed together in large regions resembling a combination of mechanical interlocking and IMC formation, e.g. site 1 and site 3 in figure 4.18a. Zooming into the middle part of the Al-Ti-nr.1, i.e. region around site 4 and site 5 in figure 4.18a, one gets the image shown in figure 4.19. It can be seen in that image, a possible IMC layer along the interface between Al and Ti much thinner than the Al-Cu IMC layers seen above. From the HAADF-STEM image in figure 4.19, the mean

thicknesses of this layer at the interface have been estimated to be $\bar{x} = 53 \pm 5$ nm.

The regions where there are possibly IMCs present were extremely narrow with small and overlapping grains. Due to this, attempts to do SAD or layerwise filtering of the EDS data at those regions did not produce identification of the compositions at those regions. Two examples for SADPs taken from such regions are shown in figure 4.20. In those images, in addition to the strong reflections corresponding to pure Ti, one can also see reflections closer spaced together that do not match any of the main elements at hand (e.g. Al, Ti, Si). This indicates that there are IMCs present, even though their crystal structure and composition remains unknown.

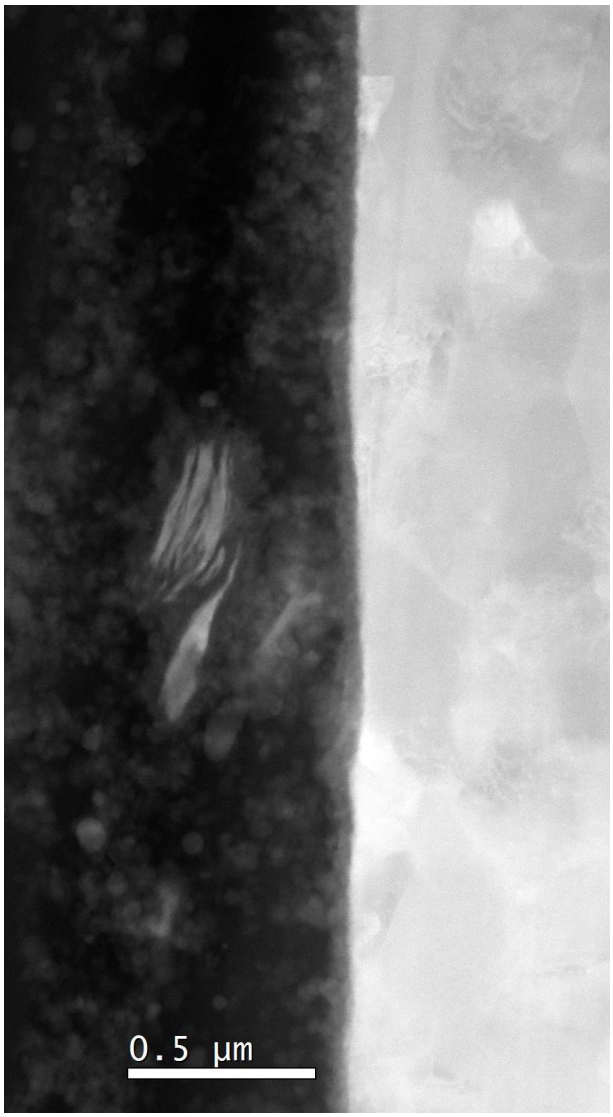

Figure 4.19: *HAADF-STEM image taken at a higher maginification of the middle part of Al-Ti-nr.1 shown in figure 4.18a.*

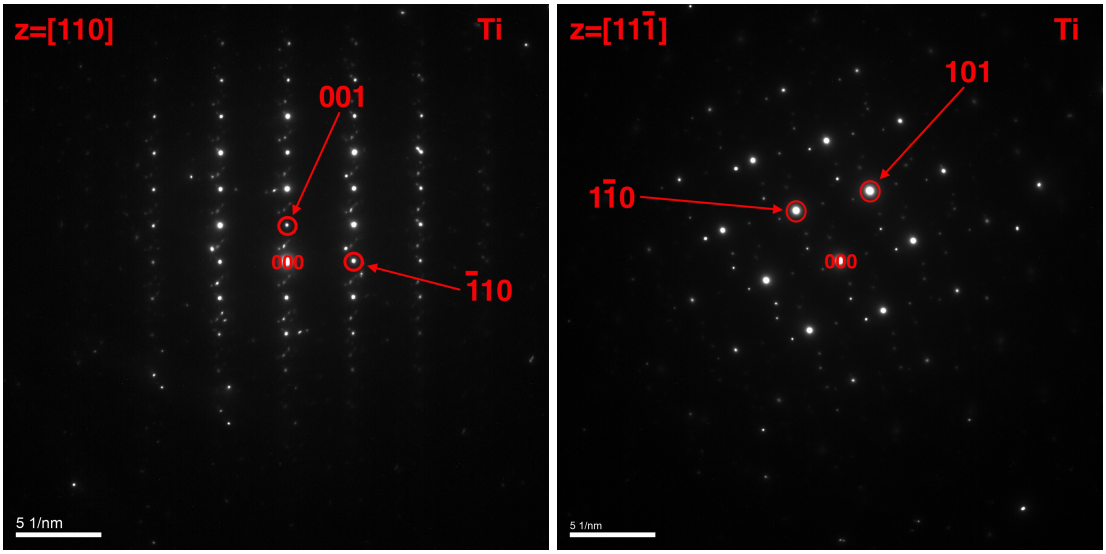

(a) **(b)**

Figure 4.20: *SADPs taken from the interface region of Al-Ti-nr.1 where there seemed to be IMC formation.*

The EDS maps have been taken from five different sites in Al-Ti-nr.1: site 1 to site 5 as indicated in figure 4.18a. For *site 1*, the HAADF-STEM image is shown in figure 4.21a and the EDS maps showing the at% are shown in figures 4.21b–4.21j for the elements Al, Ti, O, Cr, Fe, Mg, Mn, Si and Cu, respectively. For *site 2*, the HAADF-STEM image is shown in figure 4.22a and the EDS maps showing the at% are shown in figures 4.22b–4.22j for the same elements. For *site 3*, the HAADF-STEM image is shown in figure 4.23a and the EDS maps showing the at% are shown in figures 4.23b–4.23j for the same elements. For *site 4*, the HAADF-STEM image is shown in figure 4.24a and the EDS maps showing the at% are shown in figures 4.24b–4.24j for the same elements. For *site 5*, the HAADF-STEM image is shown in figure 4.25a and the EDS maps showing the at% are shown in figures 4.25b–4.25j for the same elements.

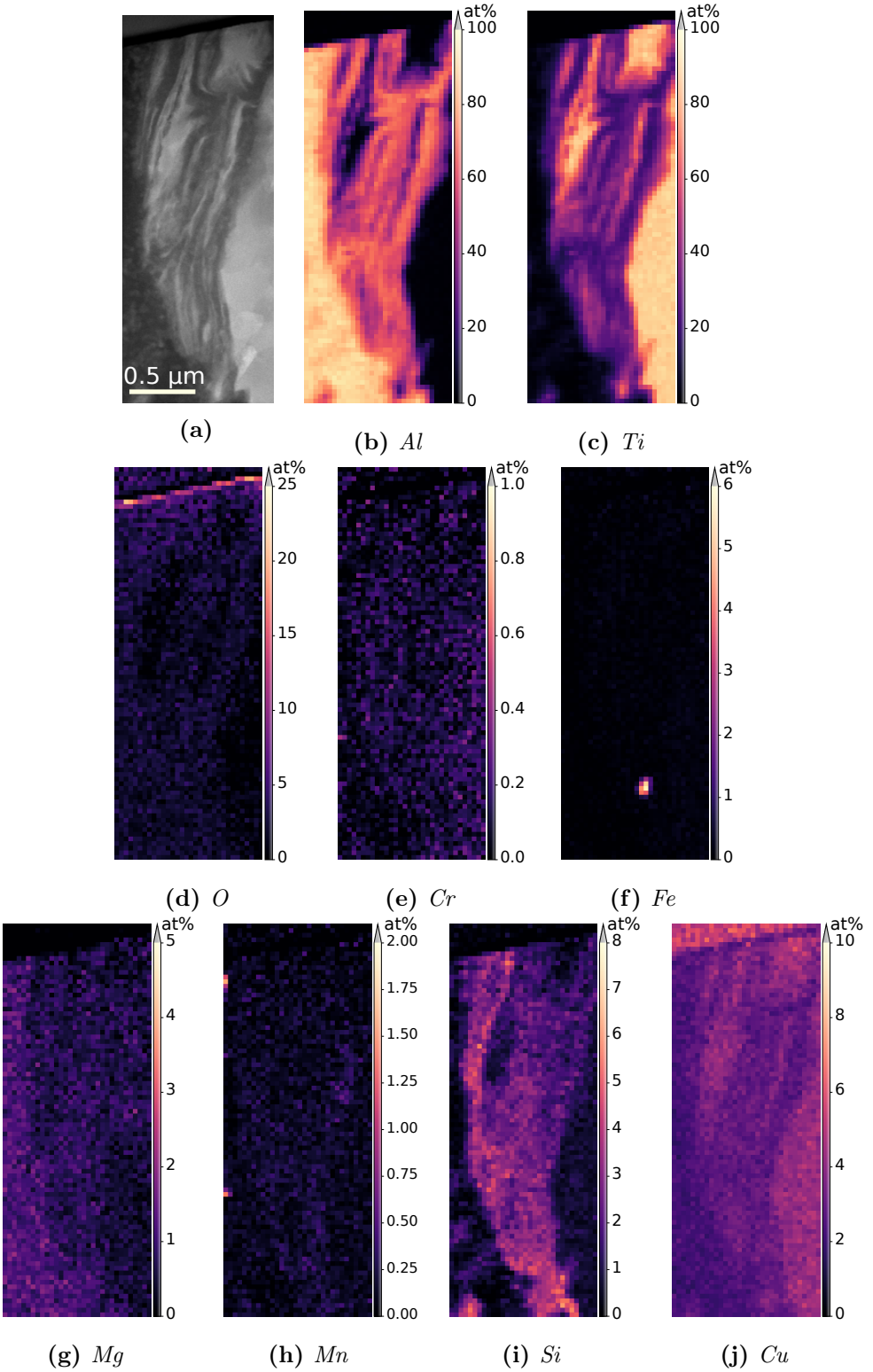

Figure 4.21: ***Site 1*** *in Al-Ti-nr.1. (a) HAADF-STEM image, (b)-(j) EDS maps showing the at% of the elements Al, Ti, O, Cr, Fe, Mg, Mn, Si and Cu, respectively.*

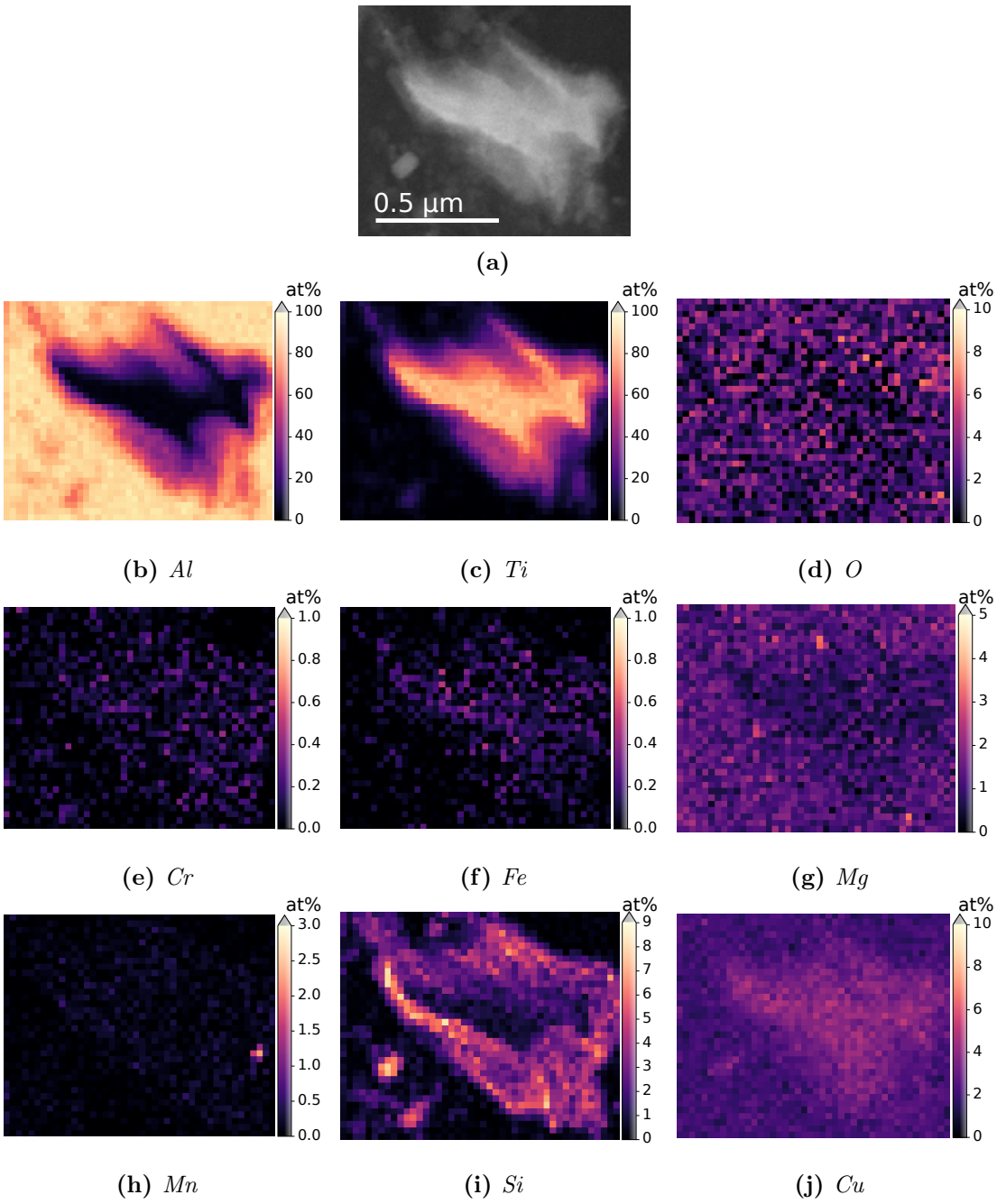

Figure 4.22: ***Site 2*** *in Al-Ti-nr.1. (a) HAADF-STEM image, (b)-(j) EDS maps showing the at% of the elements Al, Ti, O, Cr, Fe, Mg, Mn, Si and Cu, respectively.*

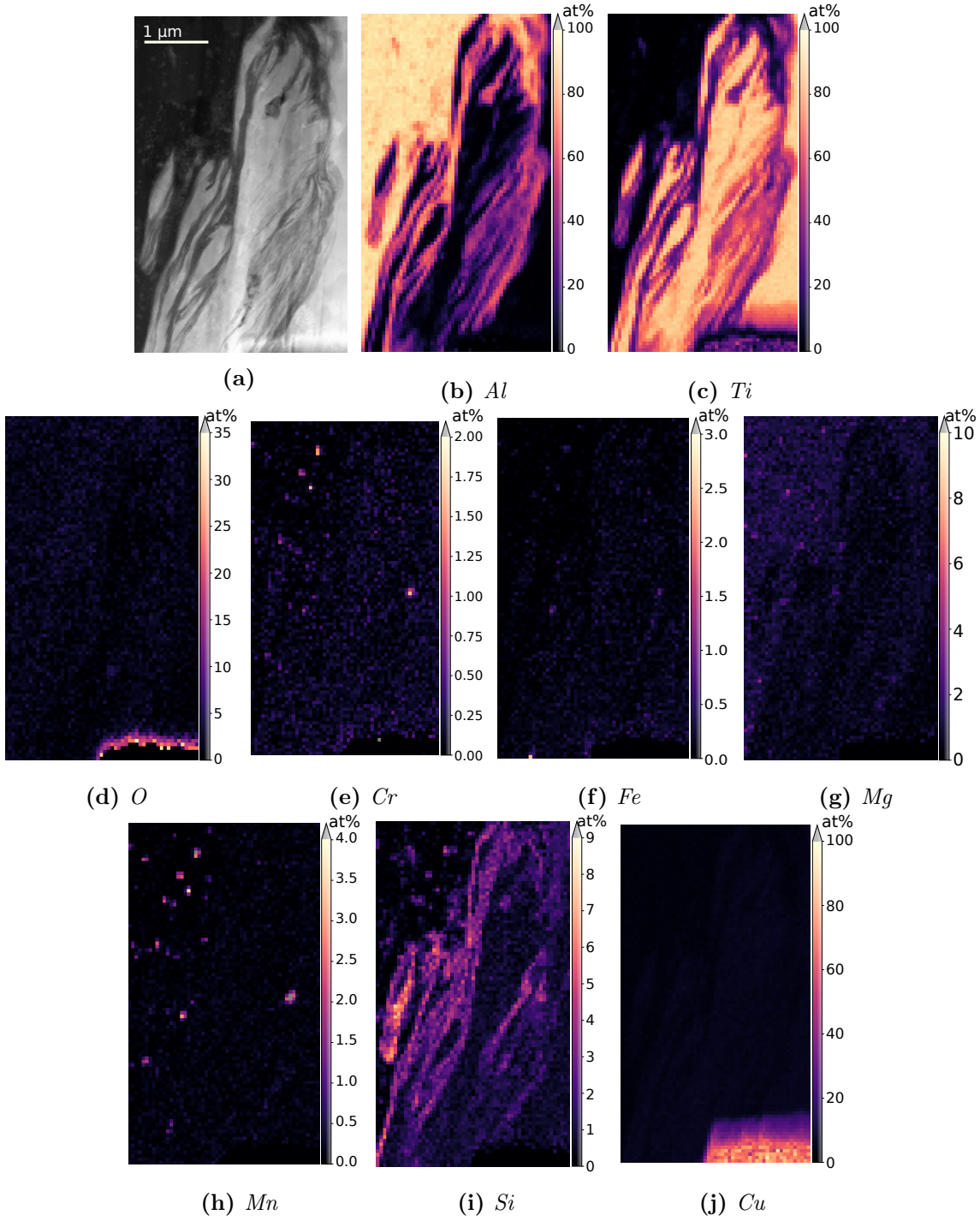

Figure 4.23: ***Site 3*** *in Al-Ti-nr.1. (a) HAADF-STEM image, (b)-(j) EDS maps showing the at% of the elements Al, Ti, O, Cr, Fe, Mg, Mn, Si and Cu, respectively.*

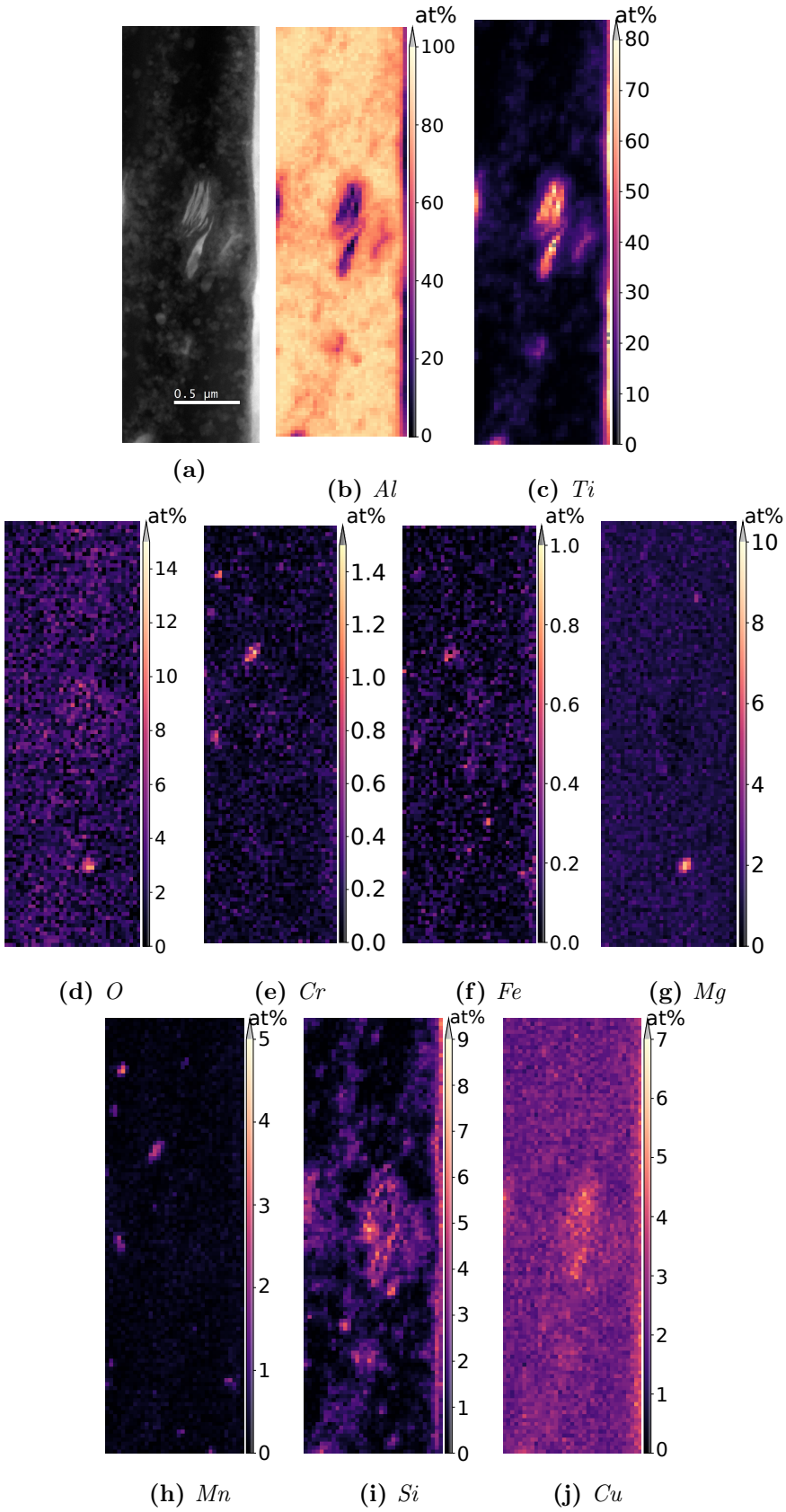

(a) **(b)** *Al* **(c)** *Ti*

(d) *O* **(e)** *Cr* **(f)** *Fe* **(g)** *Mg*

(h) *Mn* **(i)** *Si* **(j)** *Cu*

Figure 4.24: ***Site 4*** *in Al-Ti-nr.1. (a) HAADF-STEM image, (b)-(j) EDS maps showing the at% of the elements Al, Ti, O, Cr, Fe, Mg, Mn, Si and Cu, respectively.*

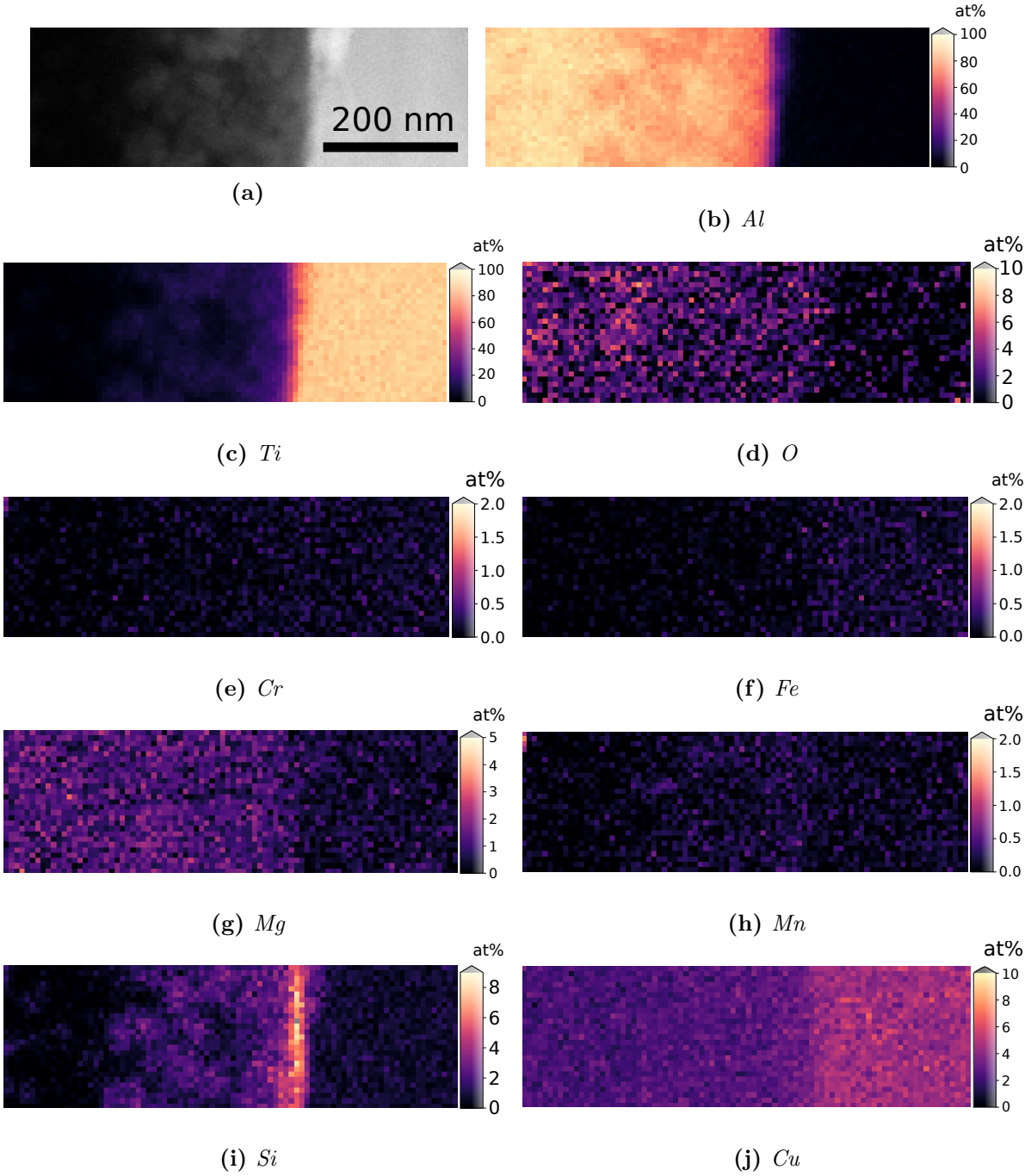

Figure 4.25: ***Site 5*** *in Al-Ti-nr.1. (a) HAADF-STEM image, (b)-(j) EDS maps showing the at% of the elements Al, Ti, O, Cr, Fe, Mg, Mn, Si and Cu, respectively.*

4.2.4 Al-Ti-nr.2

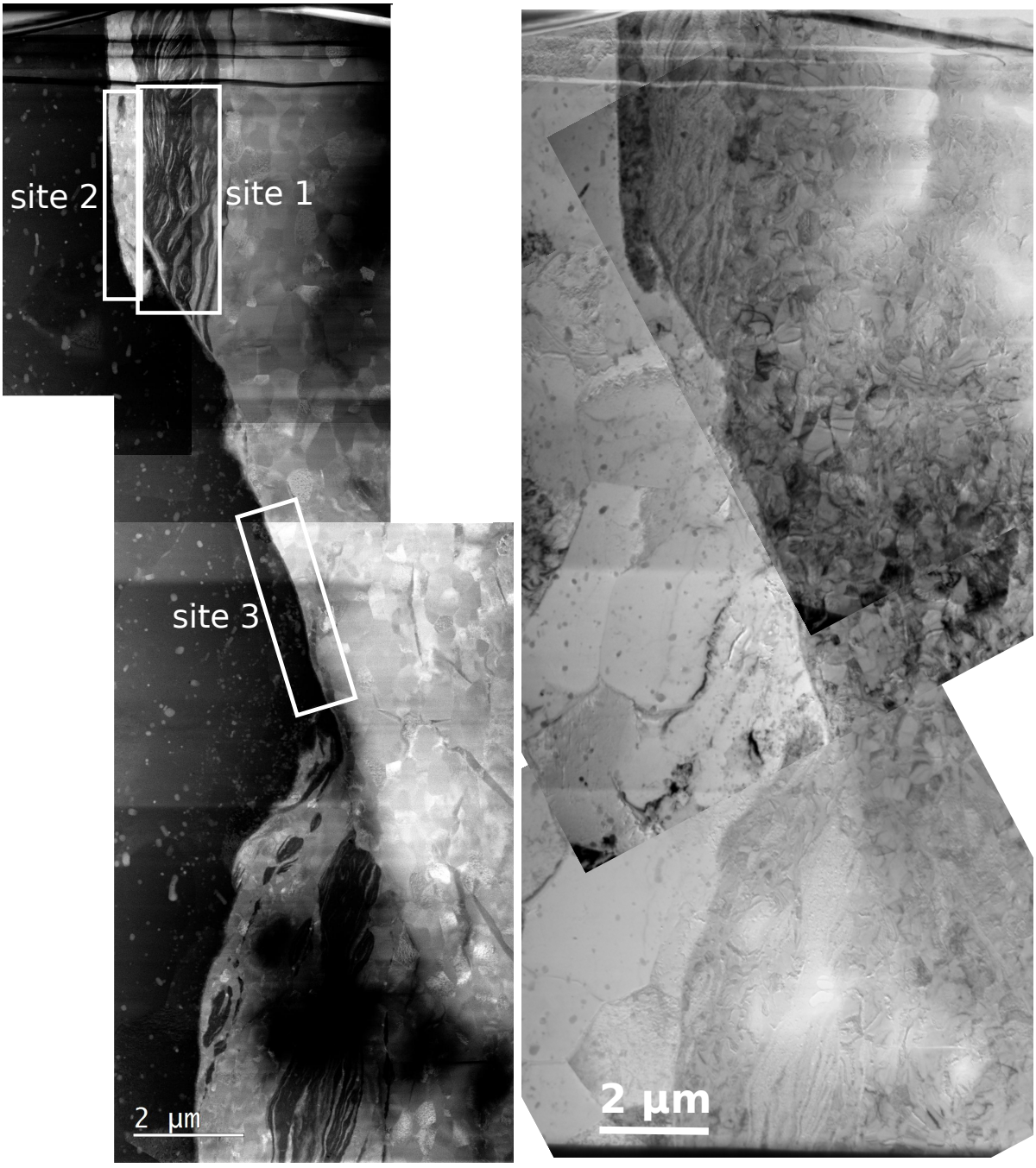

(a) (b)

Figure 4.26: *(a) HAADF-STEM and (b) BF-TEM images taken of Al-Ti-nr.2. (a) shows the locations of the EDS sites 1-3.*

Figure 4.26a shows the HAADF-STEM image of Al-Ti-nr.2 which is the notation used in this thesis to denote the second specimen taken from the Al-Ti interface. Figure 4.26b shows the BF-TEM image of the same specimen. The lower part of the images show that the specimen has holes at that region. As in the case with Al-Ti-nr.1, here one also sees Al and Ti being mixed together in large regions, e.g. in site 1 in figure 4.26a. One also sees a narrow potential IMC

layer at the interface, which can more clearly be seen in the higher maginification image shown in figure 4.27 of the interface region around site 3 in figure 4.26a. From the HAADF-STEM image in figure 4.27, the mean thicknesses of this layer at the interface have been estimated to be $\bar{x} = 48 \pm 5$ nm.

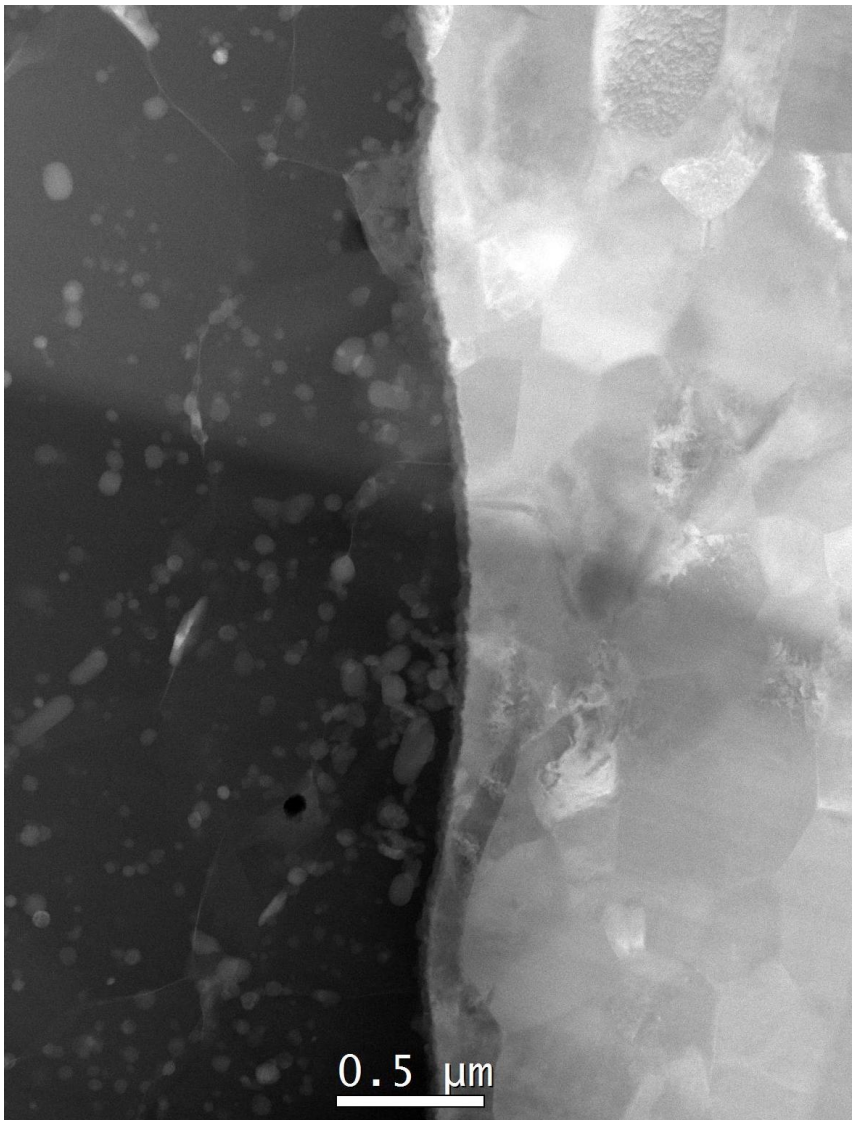

Figure 4.27: *HAADF-STEM image taken at a higher maginification of the middle part of Al-Ti-nr.1 shown in figure 4.26a.*

The EDS maps have been taken from three different sites in Al-Ti-nr.2: site 1, site 2 and site 3 indicated in figure 4.26a. For *site 1*, the HAADF-STEM image is shown in figure 4.28a and the EDS maps showing the at% are shown in figures 4.28b–4.28j for the elements Al, Ti, O, Cr, Fe, Mg, Mn, Si and Cu, respectively. For *site 2*, the HAADF-STEM image is shown in figure 4.29a and the EDS maps showing the at% are shown in figures 4.29b–4.29j for the same elements. For *site 3*, the HAADF-STEM image is shown in figure 4.30a and the EDS maps showing the at% are shown in figures 4.30b and 4.30d–4.30k for the same elements. Due to the regions where there seem to be IMCs present being extremely narrow with small and overlapping grains, SAD or layerwise filtering of the EDS data at those regions were not possible.

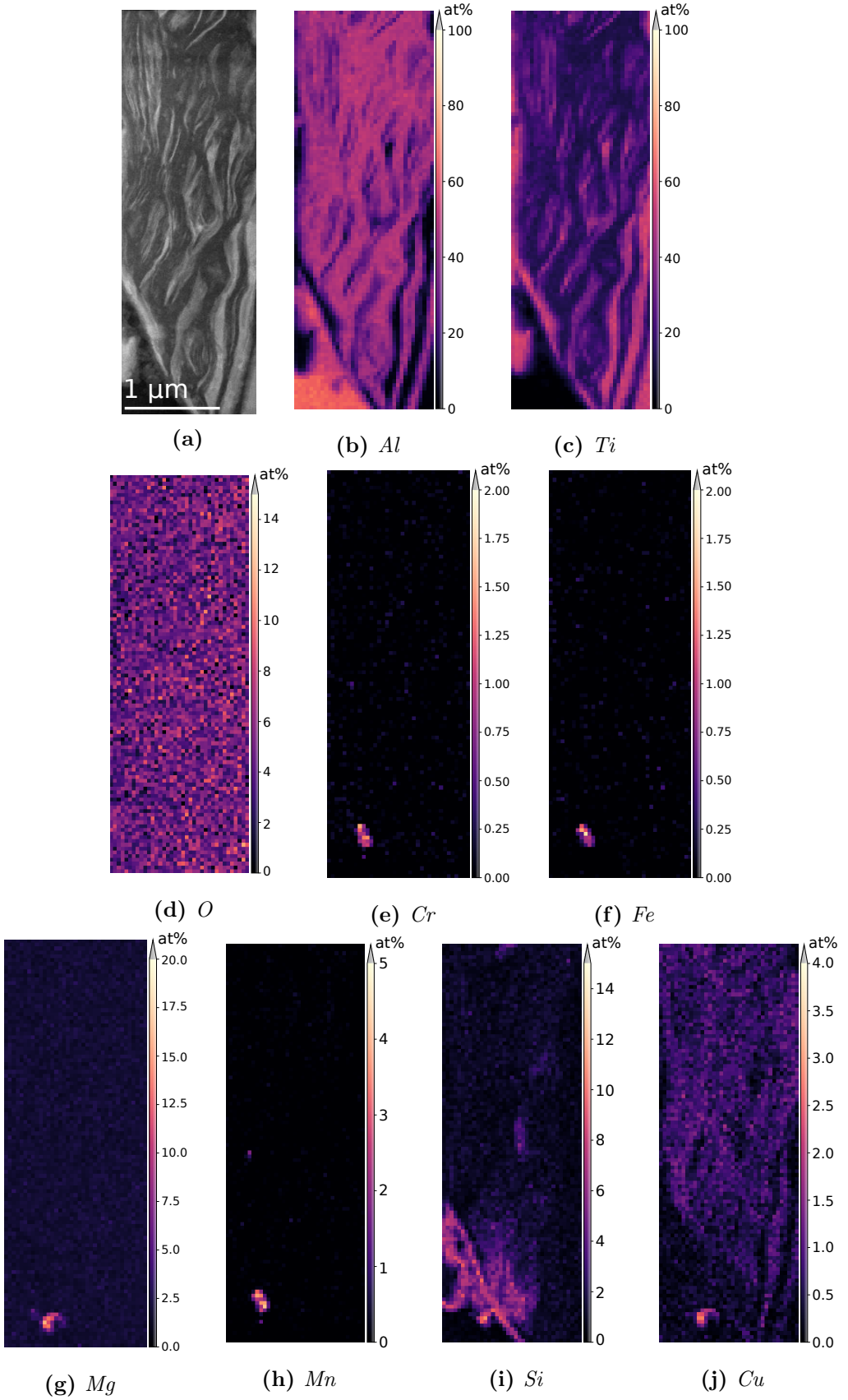

Figure 4.28: ***Site 1*** *in Al-Ti-nr.2. (a) HAADF-STEM image, (b)-(j) EDS maps showing the at% of the elements Al, Ti, O, Cr, Fe, Mg, Mn, Si and Cu, respectively.*

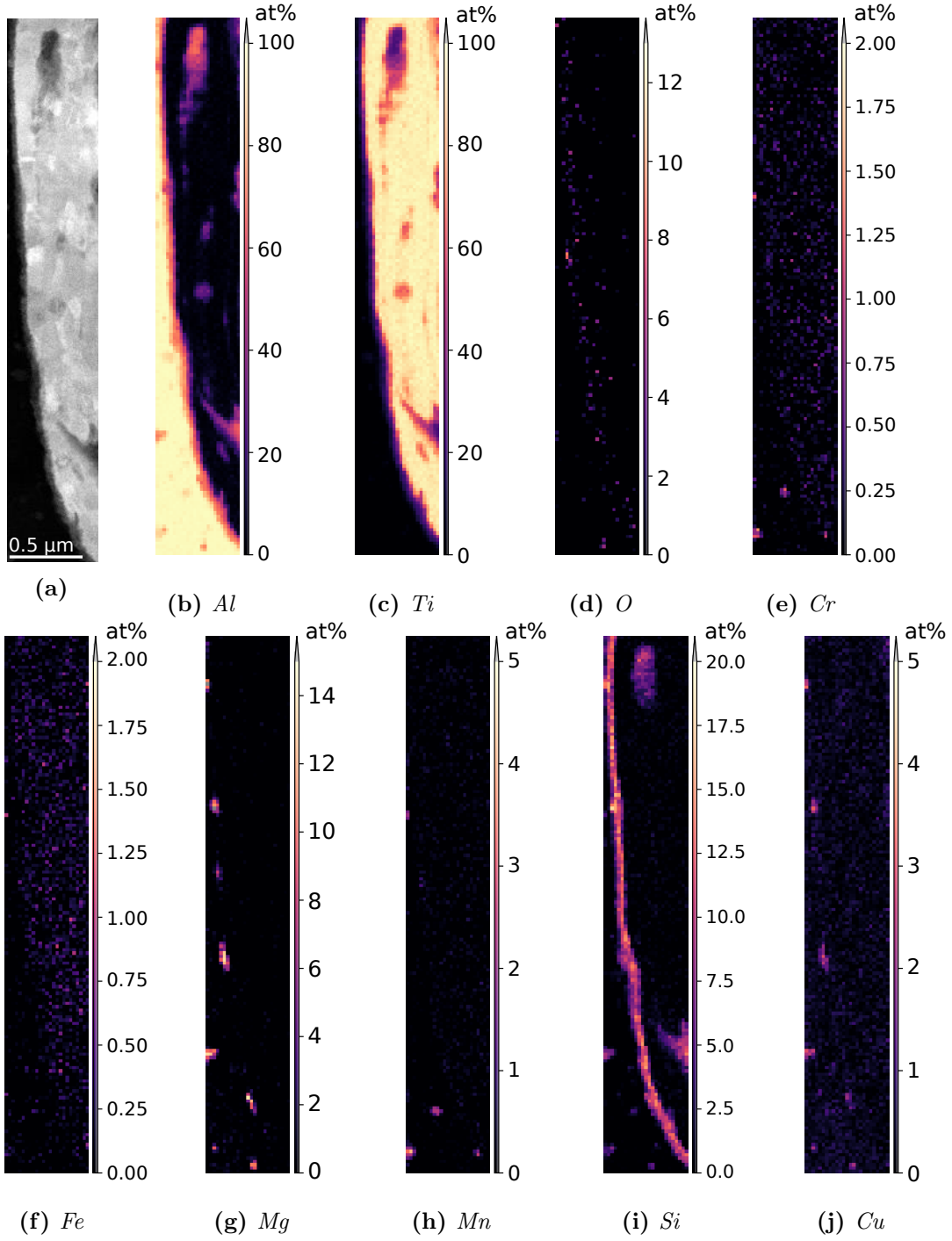

Figure 4.29: ***Site 2*** *in Al-Ti-nr.2. (a) HAADF-STEM image, (b)-(j) EDS maps showing the at% of the elements Al, Ti, O, Cr, Fe, Mg, Mn, Si and Cu, respectively.*

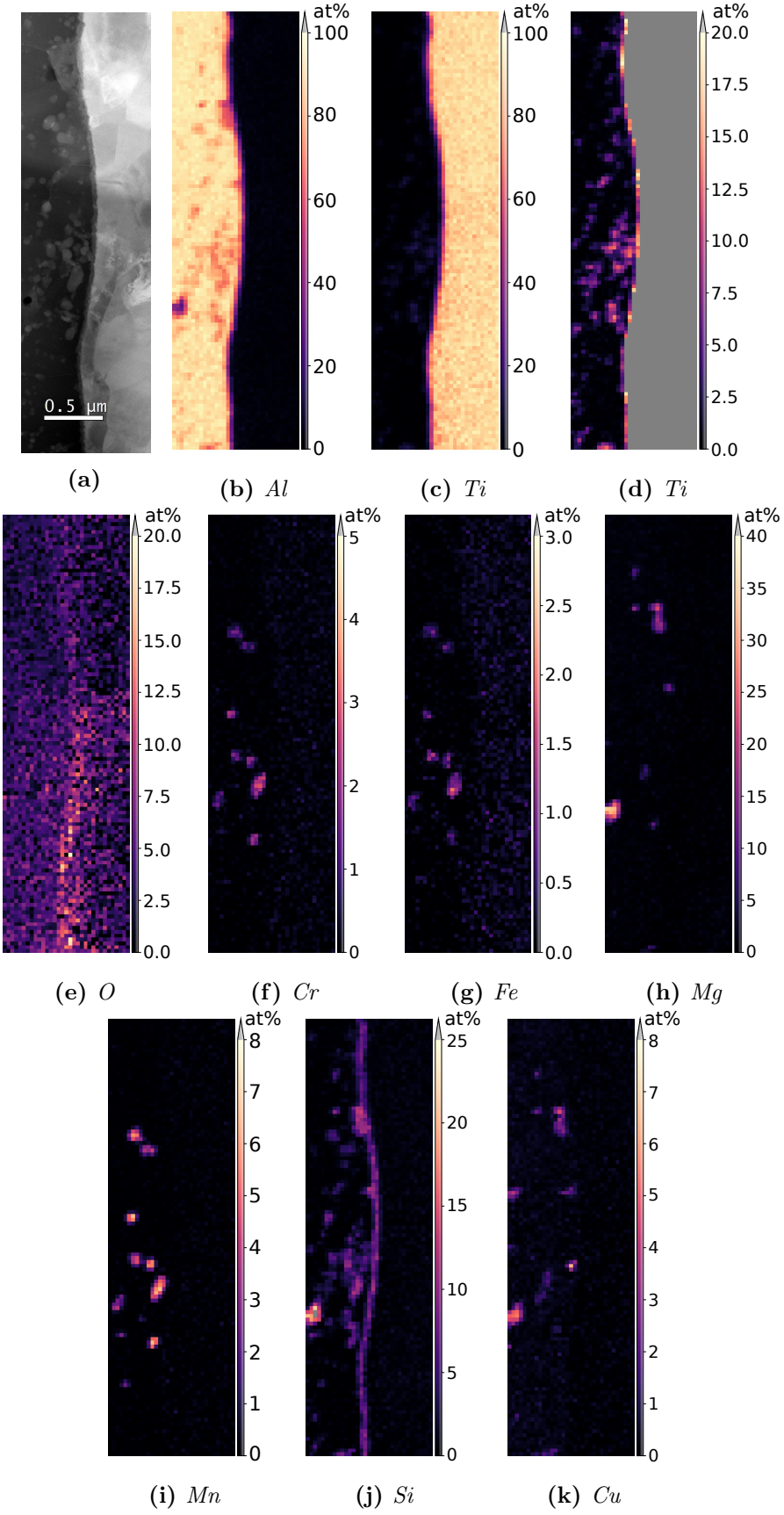

Figure 4.30: ***Site 3*** *in Al-Ti-nr.2. (a) HAADF-STEM image, (b)-(j) EDS maps showing the at% of the elements Al, Ti, O, Cr, Fe, Mg, Mn, Si and Cu, respectively.*

4.3 Mechanical tests

4.3.1 Vickers hardness test

The Vickers hardness test was performed along the three trajectories as illustrated in figure 4.31. Figure 4.31 also shows how displacement along the trajectories are measured along the axes x and y. The measured Vickers hardness numbers HV have been plotted against x or y along trajectories 1 to 3, in figures 4.32a–4.32c. All three base metals of the joint, Cu, Ti and steel, seem to have gained higher hardness closer towards the interface, while Al seem to display uniform hardness everywhere.

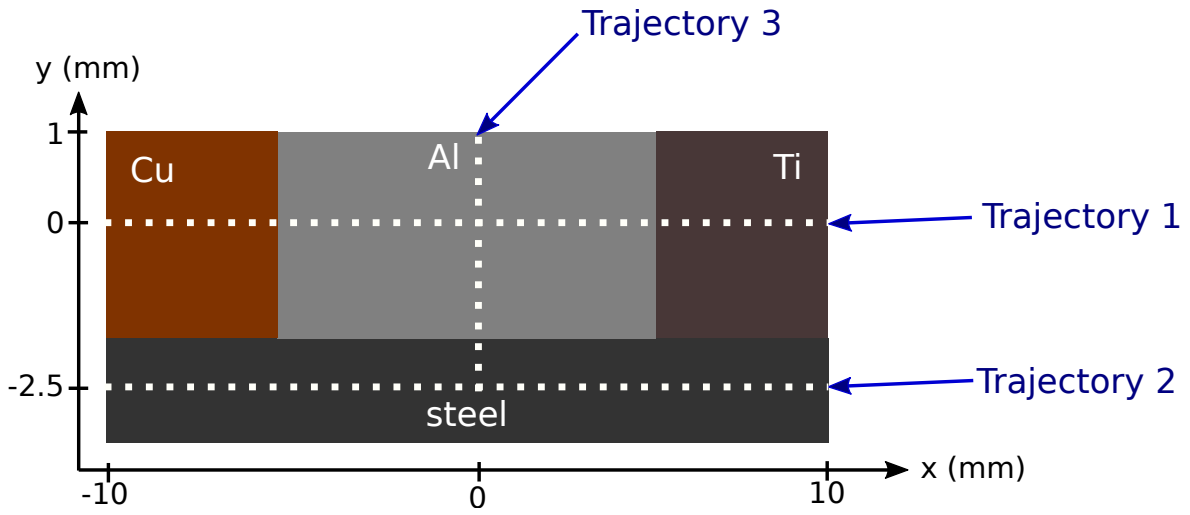

Figure 4.31: *The Vickers hardness test was performed along trajectories 1-3 that cross the interfaces of the joint.*

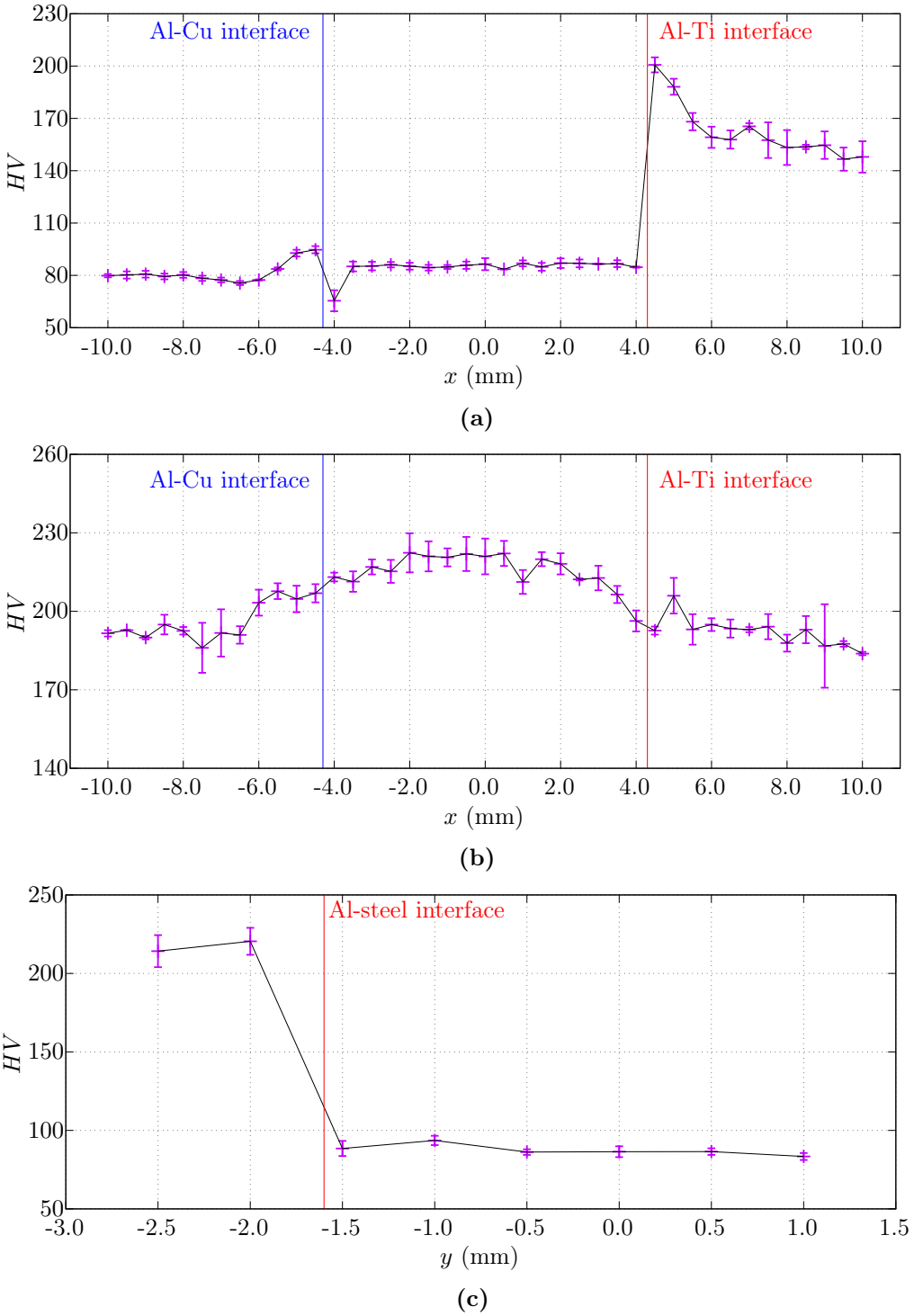

Figure 4.32: *Vickers hardness numbers HV measured along (a) trajectory 1, (b) trajectory 2 and (c) trajectory 3 in figure 4.31. Vertical lines have been plotted to indicate the approximate position of the interfaces between the metals.*

4.3.2 Tensile test

Based on the assumption that the tensile test specimens had initial dimensions as listed in figure 3.4, the original cross sectional area of the specimens was 0.79 mm^2 and the original length

was 0.55 mm. Using these quantities, the engineering stress-strain curves have been calculated from the tensile test measurements and are shown in figure 4.33a for Al-Ti specimens 1-4 and in figure 4.33b for Al-steel specimens 1-4. For the specimens from the Al-Cu interface, all of them broke during machining, meaning that they broke during the process of making the specimens before tensile testing. From the results in section 4.3.2, it can be calculated that the mean UTS (as defined in section 2.1.3.2) of the Al-Ti specimens is 305 ± 1 MPa and the mean UTS of the Al-steel specimens is 266 ± 21 MPa.

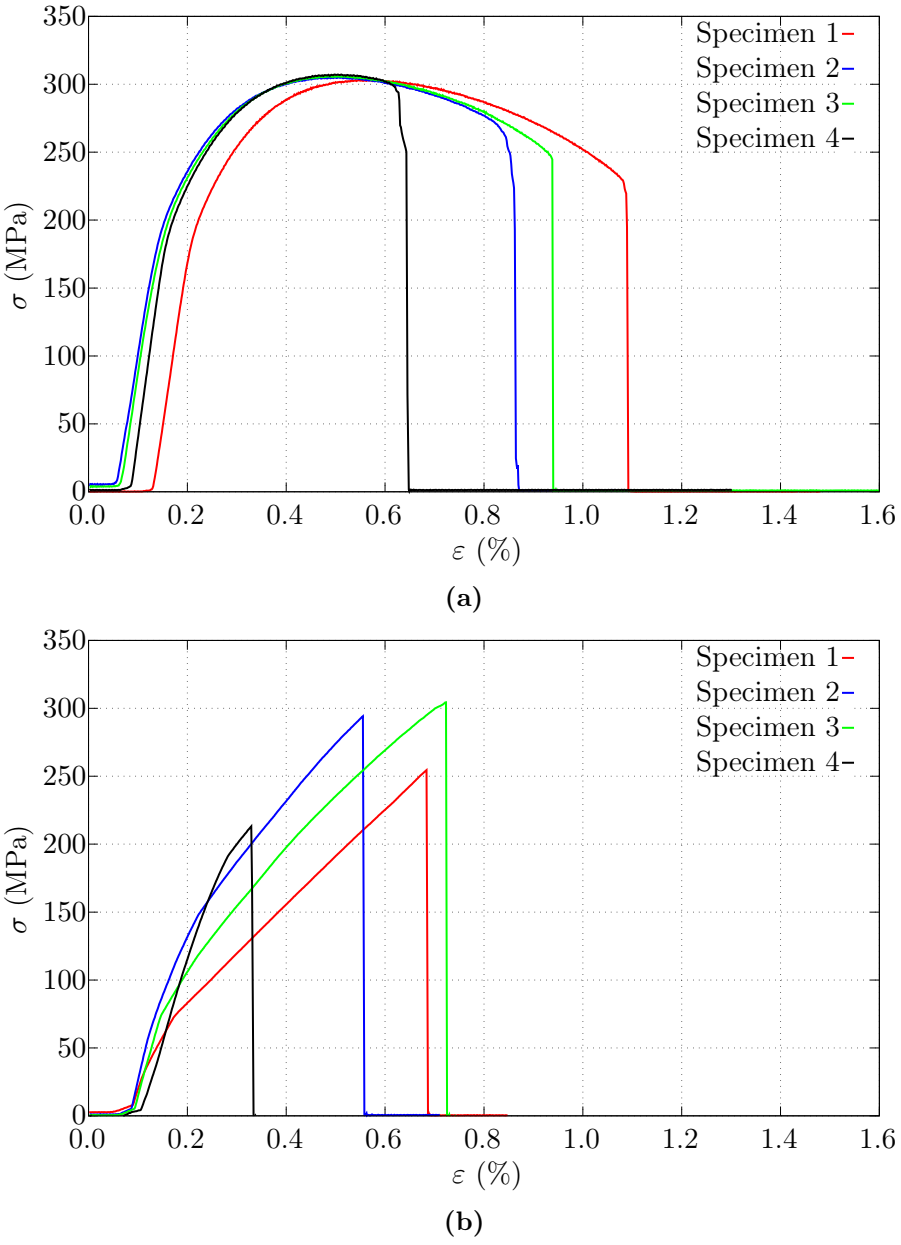

Figure 4.33: *Strain ε and stress σ measured during tensile tests of (a) Al-Ti specimens 1-4 and (b) Al-steel specimens 1-4.*

Tensile testing terminated when the specimens broke. Each Al-Ti and the Al-steel specimen broke into *top and bottom pieces*. The SE and BSE images, taken in SEM, of the fracture surfaces of Al-Ti specimen 1 are shown in figure 4.34, while the BSE images of Al-steel specimen

1 are shown in figure 4.35. These images show the surfaces of both the top and the bottom pieces of the broken tensile test specimens. Similarly, the images of Al-Ti specimens 2-4 are shown in figures F.1–F.3 in appendix F, while the images of Al-steel specimens 2-4 are shown in figures G.1–G.3 in appendix G. Images from specimens 2-4 from both interfaces display similar characteristics as the first specimen from either interface. The stress-strain curves and the SEM images combine to show that the Al-Ti specimens underwent elastic deformation and subsequent plastic deformation, which includes necking, before fracturing well within Al. On the other hand, Al-steel specimens fractured sharply without plastic deformation at the interface between Al and steel.

Although the Al-Cu specimens did not survive machining, the surfaces of four remaining bottom pieces were still examined in SEM. BSE and SE images of Al-Cu specimen 1 are shown in figure 4.36 while the similar images from Al-Cu specimens 2-4 are presented in, respectively, figures H.1–H.3 in appendix H. The surfaces of the specimens are covered in black dots resembling dirt which are most likely remnants of the different fluids used during machining. At high magnification, the surfaces are mostly smooth, without e.g. dimples as seen in the Al-Ti specimens or possible IMCs as seen in the Al-steel specimens. It can be deduced from this that the breakage of the potential specimens happened during making due to presence of pores.

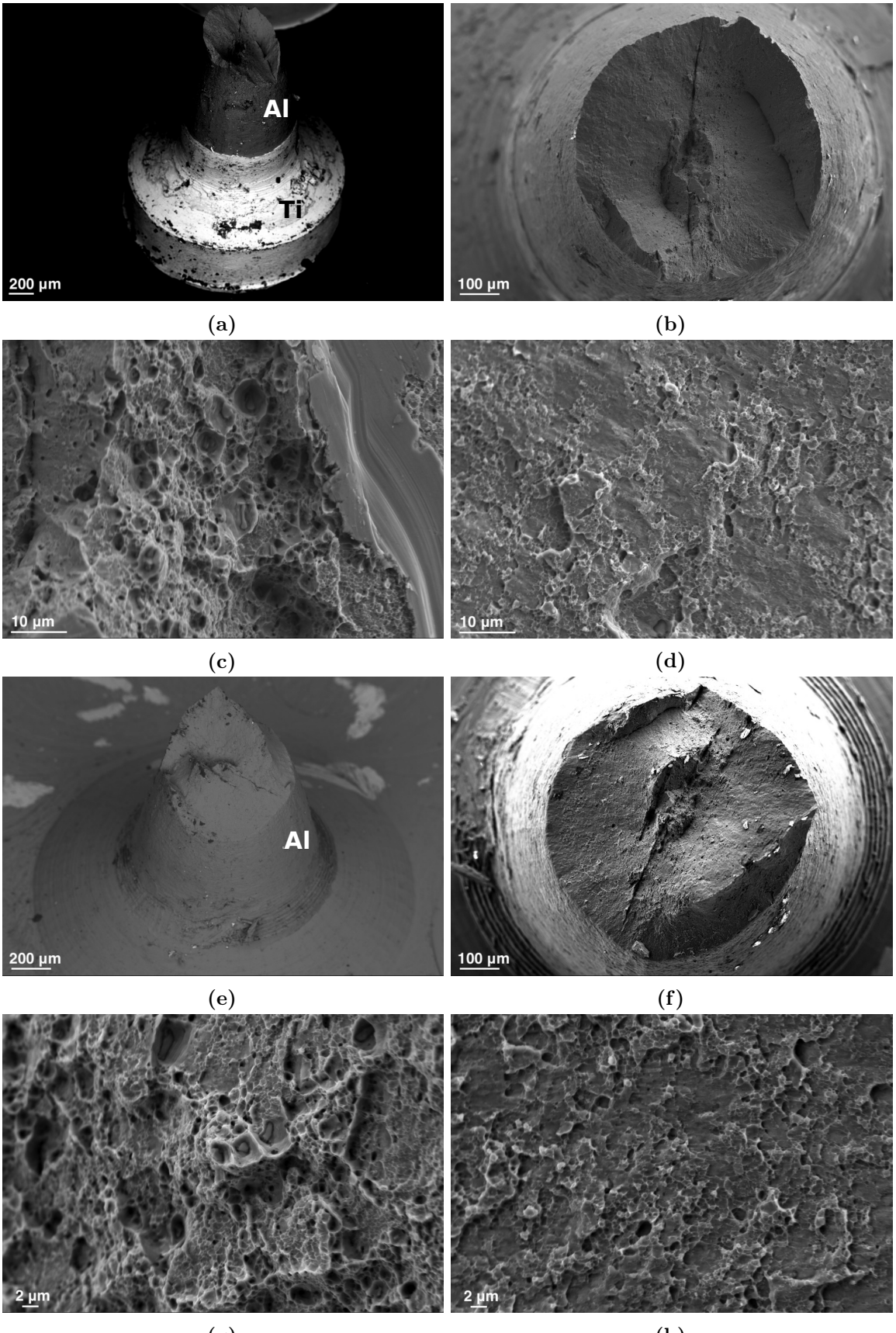

Figure 4.34: *(a) BSE and (b)-(d) SE images of the top piece of specimen 1 from the Al-Ti interface, and (e) BSE and (f)-(h) SE images of the bottom piece of the same specimen.*

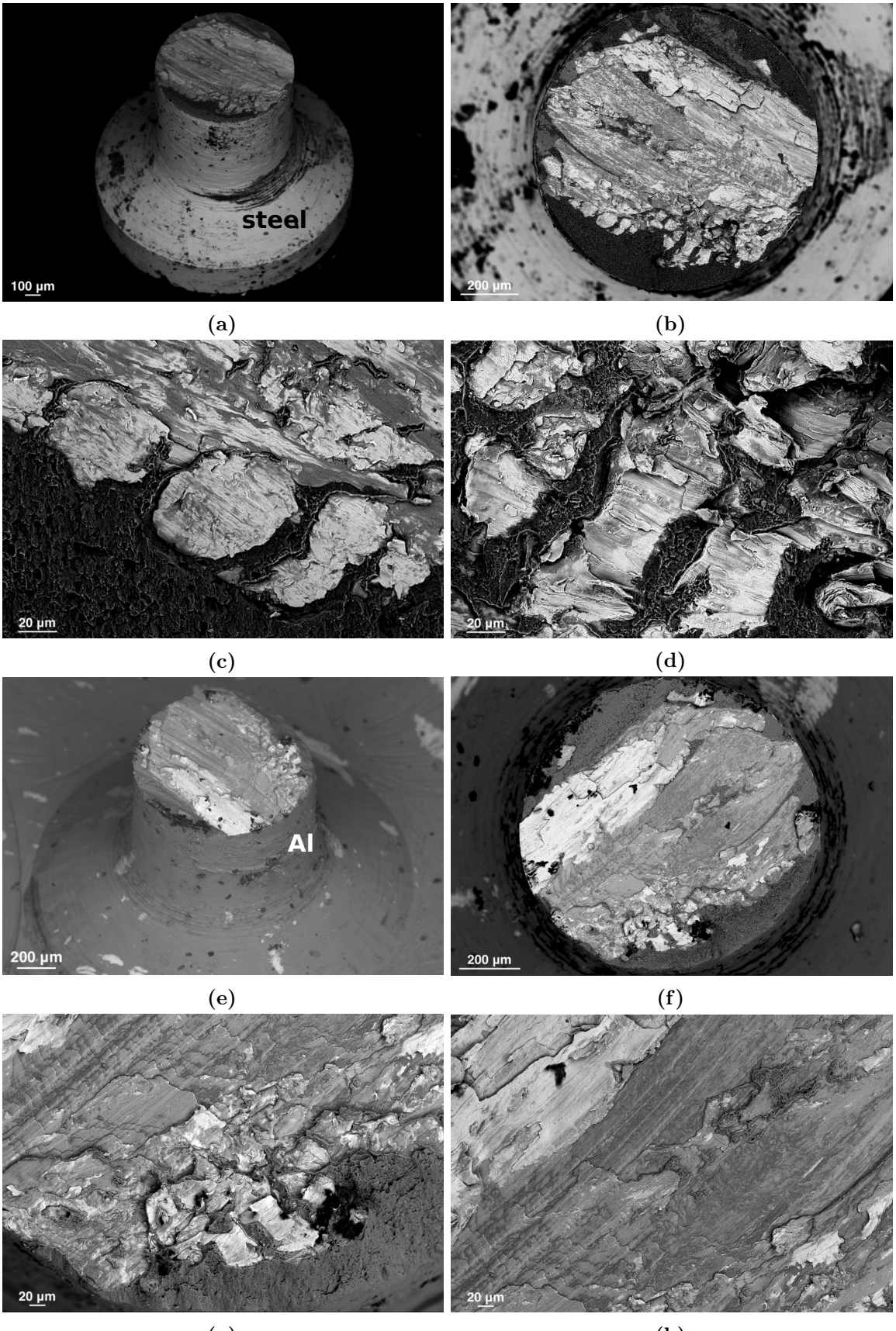

Figure 4.35: *BSE images of (a)-(d) the top piece and (e)-(h) the bottom piece of specimen 1 from the Al-steel interface.*

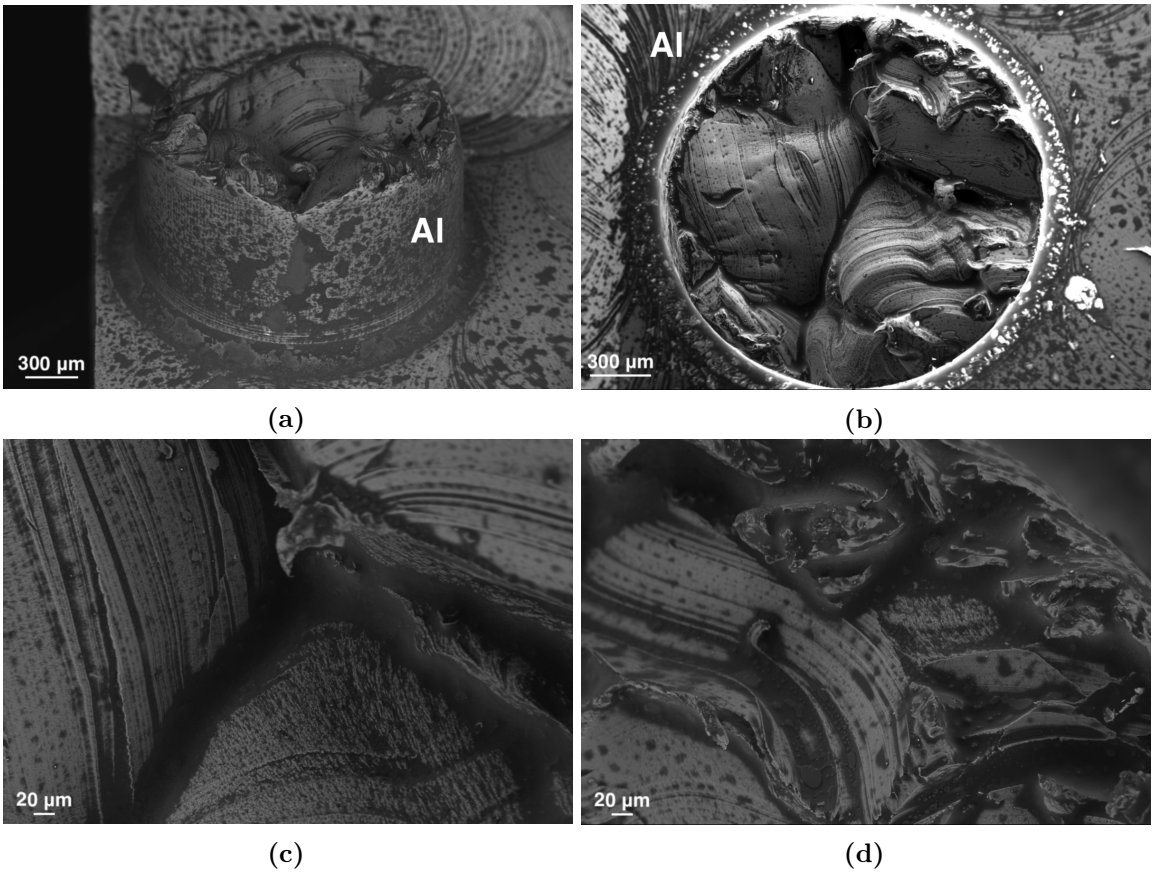

Figure 4.36: *(b) SE and (a), (c) and (d) BSE images of the bottom piece of specimen 1 from the Al-Cu interface.*

Chapter

5 Discussion

In this chapter, the results presented in chapter 4, their origin and their implications are discussed based on the background theory presented in chapter 2. In alignment with the threefold nature of the thesis structure, the discussion is split into three parts. First is the microscale features studied using SEM, second is the observation of mixing at the interface in SEM and the identification of the corresponding IMCs in TEM, and third is the mechanical properties investigated by hardness and tensile tests. The three parts are combined and summarized in the conclusion presented in chapter 6.

5.1 SEM characterisation

5.1.1 Gaps and deformations

This section concerns the findings from section 4.1.1 that revealed the following. Al-Cu interface is the only one among the three interfaces that exhibits large pores and deformations. The BM fragments that have been mixed into Al during welding are mostly Ti. Steel has tightly bonded interface, as does Ti, but steel does not have many loose fragments in Al.

Firstly, it can be observed from Figure 4.1 that the Al-Cu interface has significantly more gaps and deformations than the other interfaces. This means that the welding is more sound and sturdy between Al and Ti and between Al and steel in this joint compared to the weld between Al and Cu. The observed phenomena could be due to the placement of the metals during welding. As mentioned in section 3.1.2, Ti was on the advancing side and the Cu was on the retreating side during welding. During such welding mechanism, the advancing side is normally bonded the best, since the relative velocity between extrusion pin and the base metal is higher, leading to a stronger shear force and higher temperature that aids the bonding. This means that if Cu was placed on the advancing side rather than the retreating side, the joint interface Al-Cu might have been better and, in the same way, the Al-Ti interface might have had more gaps and deformations.

From mere visual observation of figure 4.1, one would expect the BM fragments that have mixed into Al to originate from Cu, as Al-Cu is the most deformed interface. However, this was proven wrong from the results of the EDS scans which showed that they are, for the most part, from Ti. This means that the smoothness of the Al-Ti interface compared to that of Al-Cu is not because Ti was less affected, but rather that everything that came off loose from Ti got dragged all the way into the Al while deformations from Al-Cu remained close to the interface. A plausible explanation for this could again be the fact that Ti was placed on the advancing side during welding. Compared to Cu, due to the higher relative velocity with the extrusion pin experienced by Ti, more of the looser parts from the Ti-surface got separated from the bulk and got dragged into Al. This could contribute to bringing the Al closer to the Ti-BM, thus avoiding pore formation due to these deformed parts being in the way as can be seen with the case of Cu as discussed above. Another possible explanation for the difference could be that

Cu has higher ductility than Ti causing it to undergo plastic deformation more than Ti. This could be the reason Cu is easier permanently deformed at the interface, while Ti is more prone to fracturing into small fragments rather than changing its shape with plastic deformation. The Vickers hardness result in figure 4.32a, discussed in section 5.3.1, supports this claim as it shows a lower hardness in Cu compared to in Ti. The higher hardness of Ti means that it was more resistant to plastic deformation caused by the indentation made during Vickers test. As ductility is a measure of material's ability to undergo plastic deformation, it can be deduced that Cu is indeed more ductile than Ti.

Steel has tightly bonded interface as Ti but do not have many loose fragments in Al. The steel used in this joint have a high hardness-level, which could be the reason it did not shed many loose fragments into Al. Aside from its mechanical properties, steel's placement could have contributed to its bonding to Al. The rotating pin in the extruder, illustrated in figure 2.1, points down towards the steel while rotating. The steel part experiences rotation on the plane of its surface while Cu and Ti experiences a perpendicular rotation to their surfaces. This means that, in contrast to the situation with Cu and Ti, any loose steel-bits that is detached from the steel surface is not dragged away from the interface by the motion of the extruder pin.

Moreover, it is important to keep in mind that the condition of the surface of the metals plates (Cu, Ti and steel) before the welding is not known. It is not known if the surface of the plates were equally smooth to start with. A rough surface is normally desired during welding to achieve large contact-area. If there were differences in the roughness of the surfaces from the beginning, then this might or might not have affected the circumstances observed after the welding. The effects would depend on the types of metals and welding conditions. Therefore, it is crucial to keep in mind the unknown initial conditions when considering the arguments given above for the different observations.

5.1.2 Difference in grain structure

This section concerns the findings from section 4.1.2 that revealed noticeable difference between the bulk of the steel and the part of steel next to the interface with Al. Similar effects could not be observed in other BMs during the SEM inspection.

In section 4.1.2, a comparison between the bulk (approximately 1 mm into the metals) and the part that is right next to the interface of each BM in the multi-material joint have been displayed through SE-images. From figures 4.2a–4.2d, it is not possible to observe any difference in the bulk versus the part close to the interface in either Cu or Ti BMs. However, in steel, a significant grain refinement into small grains close to the welding interface can be observed when comparing the images in figure 4.2f and figure 4.2e. The reason could be that the steel used during welding is more easily affected compared to the other BMs due to its material properties. Another explanation could be that the surface of the steel might have experienced more impact force during the welding process, resulting in the grains getting crushed into smaller sizes than what is the case in the bulk. The experienced larger impact force would be due to the fact that steel was placed at the bottom during welding and got extruded Al pushed towards its surface with higher impact, as illustrated in figure 2.1.

Regarding the structure of the Al part of the joint, it was reported in the results that the Al part seemed to have uniform appearance over the whole surface, meaning that differences, if any, could not be observed during the SEM study. The uniformity of the Al over the whole surface area in the joint could be due to the flexible performance of Al when under stress during welding because of its good ductility and malleability.

There can be several alternative explanations for not observing significant difference in the bulk and the part next to the interface for Cu, Ti and Al. Firstly, the results could be due

to the inadequacy of the instrument, SEM, when used for SE-imaging. A different technique, e.g. electron backscatter diffraction, could be performed in SEM to examine the grain structure. Otherwise, another instrument, such as TEM, that can image grains of Al more clearly could be used instead for this investigation purpose. It has been seen in the TEM studies carried out to investigate the IMCs in this thesis that TEM is able to image the grain structures of the metals, see e.g. figure 4.11. Secondly, the fact that SEM images in this thesis cannot show the grain structures could be due to the polishing methods used. The specimen for SEM was prepared using mechanical polishing. The specimens intended for TEM were prepared using FIB, and SEM-images were taken simultaneously during preparation, as can be seen in appendix B. These images clearly show the grain structure. This possibly mean that the FIB polishing can produce better polished surfaces than the mechanical polishing. In addition, after mechanical polishing, the SEM specimen might have oxidized significantly on its surface before imaging, deteriorating the image quality. After performed FIB polishing in vacuum, the specimen were taken image of before being exposed to air. In other words, the mechanical polishing and subsequent exposure of the specimen to air before imaging might have produced images with insufficient quality for the purpose of studying the grain structures. Thirdly, the images that were meant to be from the bulk regions of the metals were only approximately 1 mm into the metals. To be able to examine the true unaffected-zone of the metals, it may be that the examination of the bulk regions should have been carried out even further into the metals. From the hardness measurements that is discussed later in section 5.3.1, one can see that the images of the bulk regions should be taken at at least 2 mm into the metals in order to avoid the work-hardened zone of the metals.

5.2 TEM characterisation

The SEM studies presented in section 4.1.3 show that regions with mixing of the metals are common along all three interfaces and surrounding the BM fragments in Al, as shown in figures 4.4–4.7. These regions are prime candidates for IMCs and metallic interlocking. TEM studies revealed that IMCs are indeed present. As explained in section 2.4.5, IMCs are desirable in thin layers which indicate bonding between the metals, but as the layers increase in thickness the hard and brittle nature of IMCs start to dominate, making the joint-interface prone to fractures. The results from examining the two TEM-specimens from the Al-Cu interface are discussed in section 5.2.1, while the results from examining the two TEM-specimens from the Al-Ti interface are discussed in section 5.2.2.

Some features are common for all four specimens. The HAADF-STEM images of the specimens correctly show Al with darker contrast and Cu or Ti (respectively for Al-Cu specimens or Al-Ti specimens) with lighter contrast on a grey-scale. This is as expected because Cu/Ti has a higher atomic number than Al causing more electrons to be scattered at high angles by the nucleus, which further leads to greater scattered-signal to be generated and detected by the HAADF detector. Greater signal is then converted into brighter contrast in the images. In between the regions with pure Al with dark contrast and pure Cu/Ti with light contrast, regions with approximately constant contrast intermediate between that of Al and Cu/Ti, which indicate possible IMC formation, can be seen in all four specimens.

There are also several common features that can be observed in the EDS maps of the four specimens.[1] Oxygen tend to give significant signals over the entire surface of the specimens. Different elements oxidize to different levels. Surface oxidation of the TEM lamellae (not the oxidation on the interface between the metals) is an expected phenomenon and does not contribute to the analysis of the weld quality. Surface oxidation will thus not be discussed further. Other

[1] Always remember to check the scale-bar in the EDS maps.

interesting phenomena observed in the O-maps are discussed with examples below. Another significant source of signals in the EDS maps that do not need extra attention, is the high signals from Cu originating from the grid and the Cu-rings placed on top of the grids in the specimen holder in TEM. Note that Cu-rings were used to secure all the specimens and Al-Cu-nr.2 and Al-Ti-nr.1 were placed on Cu-grids while Al-Cu-nr.1 and Al-Ti-nr.2 were placed on Mo-grids. Signals from Mo have been excluded in the results as Mo is not present in the specimen itself.

It is common to observe dispersoids in the EDS maps as small dots. Dispersoids are inherent in the Al FM and are expected to show up in the EDS maps. It should also be mentioned that the maps of Fe can show a weak signal originating from the pole pieces that sit right above and below the specimen and are part of the objective lens system shown in figure 2.9. These pole pieces are composed of mainly Fe and small amounts of other elements. Electrons in the beam or electrons that have scattered to the sides after hitting the specimen might have excited these elements in the pole pieces, resulting in the weak signals in the maps. Furthermore, Cu and Ti have heavier atomic nucleus than Al, meaning that they will manage to scatter more electrons than Al easier excite Fe in the pole piece. This difference can sometimes be seen in the Fe-maps.

5.2.1 Al-Cu

Firstly, TEM characterisation of Al-Cu-nr.1 is considered, in section 5.2.1.1, which is the simplest and will act as a suitable introduction for the other specimens. Thereafter, a similar discussion of Al-Cu-nr.2 will follow, in section 5.2.1.2. A combined discussion is given in the end, in section 5.2.1.3, which focuses on evaluations of the discovered IMCs.

5.2.1.1 Al-Cu-nr.1

In Al-Cu-nr.1, two distinct layers of IMCs have been formed on the border between Al and Cu (see figure 4.8a). The upper and lower IMC layers in the image have been called layer 1 and layer 2, respectively, in connection with the EDS studies discussed below. The SADPs taken from places in layer 1 corresponded to that of Al_2Cu while SADPs from layer 2 corresponded to that of Al_4Cu_9, as indicated in figure 4.8b. It is indeed reasonable that the IMC layer closest to Al (layer 1) is rich in Al while the IMC layer closest to Cu (layer 2) is rich in Cu. Almost all of the SADPs were taken from more than one zone axis, making the identification of the IMCs more reliable. Additionally, complementary EDS scans were performed.

EDS results of Al-Cu-nr.1, shown in figure 4.10, support the findings from the SADP-analysis. The map of Al, in figure 4.10b, and the map of Cu, in figure 4.10c, both display a two-layer structure where the at% of the element is different. Going from top to the bottom in these two maps, one sees that the at% of Al decreases while the at% of Cu increases. This finding confirms that there are indeed two distinct IMC layers that have been formed uniformly along the interface between Al and Cu. Furthermore, this finding confirms that the top layer, layer 1, has higher Al percentage, and the bottom layer, layer 2, has higher Cu percentage. Comparing the ratio between the at% of Cu and the at% of Al in these two layers, that are listed in table 4.2, with the most possible candidates listed in table 2.1, it can be said that EDS results suggest the IMC in layer 1 to be Al_2Cu, and the IMC in layer 2 to be Al_3Cu_4 or Al_4Cu_9.

When evaluating the validity of the EDS results, it should be kept in mind that the masks applied to the total signal to filter out each presumed IMC-layer, shown in figures 4.10j and 4.10k, may have included signals from regions outside those exact layers. It is also possible that within what seems (from images), to be a layer composed of one single type of IMC, there may exist several different types of IMCs that are similar in composition. This is especially the case with the next Al-Cu specimen, Al-Cu-nr.2, as can be seen from its SAD results shown in figure 4.11b. During EDS analysis, the mask applied to filter out one such layer outputs the total at% of the

different elements included in that mask and thus does not distinguish each grain within the mask by itself. Therefore it is important to evaluate the EDS results in combination with the SAD results. Evaluating these EDS results together with the SAD results that were done at many different places and produced the same IMC-suggestion along each layer, it is reasonable to conclude that, for Al-Cu-nr.1, layer 1 at the top is Al_2Cu and layer 2 at the bottom is Al_4Cu_9. This conclusion has been listed in table 5.1 in an organized manner together with the similar conclusions from the other Al-Cu specimen.

An important trait of an IMC that is critical for the performance of the joint is its thickness, as remarked earlier. It is desirable to have the IMC layer uniformly formed over the whole interface between the two parent metals with as small thickness as possible. Both layer 1 and 2 expand smoothly over the whole Al-Cu interface in the specimen, indicating that the two parent metals have managed to bond over the whole interface without certain spots being omitted. The narrow thicknesses of both of the layers contribute positively in addition. The mean thicknesses of the layers, stated in table 4.2, as well as with other properties of the discovered IMCs, is discussed further through comparison with previous research in section 5.2.1.3.

Looking at the other EDS maps, it can be observed that maps of Cr, Fe, Mg, Mn and Si in figures 4.10e–4.10i display presence of dispersoids in the IMC layer closest to Al. All of these elements are alloying elements in the Al-FM used in the making of the joint, therefore they should indeed be present in the dispersoids in Al. One interesting thing to note is that several dispersoids are concentrated in the Al-rich IMC layer layer 1 and not in the Cu-rich IMC layer, layer 2. This could mean that the original interface between Al and Cu was probably right between layer 1 and layer 2, and that layer 1 grew into Al, which has dispersoids, while layer 2 grew into Cu from the original interface. The dispersoids play a strengthening role in the original Al-FM because they limit the movement of lattice defects. Their presence in the IMC layer could therefore mean that they contribute to the strength of the IMCs. EDS map of O in figure 4.10d does not display any evident oxide layer which could mean that the welding process managed to remove the oxide layer that is always present at the Al surface prior to welding. Being able to remove the oxide layer adds positively to the ability of the welding method in bringing the pure parent metals together with high friction to develope sufficiently high temperature at the interface to facilitate bonding.

5.2.1.2 Al-Cu-nr.2

Although Al-Cu-nr.2, shown in figure 4.11a, appear to be more complex than Al-Cu-nr.1, discussed above in section 5.2.1.1, they display several similar features. Like Al-Cu-nr.1, the interface between the main Al part and the main Cu part of the specimen in Al-Cu-nr.2 display uniformly formed IMC layers that span over the whole interface. In addition, almost everywhere at the interface, the IMCs seem to have formed in two distinct layers, as was also the case in Al-Cu-nr.1. Most (7 out of 12) of the SADPs taken from the numbered places that lie in the IMC layer closest to Al (numbered as 05-16 in figure 4.11b) match Al_2Cu. The rest of the SADPs match Al_4Cu_9 and AlCu. As mentioned earlier, it is expected that the Al-rich IMC, Al_2Cu, dominates the IMC layer that lies closest to Al. SADPs of those places that lie a little bit further in at the interface (places numbered 17-19 in figure 4.11b) match Al_4Cu_9 and AlCu. In addition to the interface IMC layers, Al-Cu-nr.2 has also formed IMCs further into Cu. SADPs from these regions (numbered 01-04 and 20-26 in figure 4.11b) correspond mostly to Al_4Cu_9 and AlCu.

Unlike the diffraction study results from Al-Cu-nr.1, the Al-Cu-nr.2 interface IMC layers display a wider variety of IMCs within each layer whereas Al-Cu-nr.1 had only one type of IMC in each layer. This could be related to the fact the interface is more deformed in Al-Cu-nr.2 compared to that in Al-Cu-nr.1. This plastic deformation points to more redistribution of material during welding, which is a possible explanation for why the layers are less homogeneous and why

IMCs have migrated further into Cu.

The EDS scans have been done at three different sites in Al-Cu-nr.2, figures 4.13, 4.14, 4.16 and 4.17. Several different features that have been observed and discussed earlier with Al-Cu-nr.1, in section 5.2.1.1, can be found here also. As in Al-Cu-nr.1, dispersoids are present in the Al-rich IMC layers only, that lie closest to the bulk of Al. It has been discussed above (section 5.2.1.1) that this might contribute to strengthening of these IMC layers and also indicate that the original interface between Al and Cu was probably between these dispersoid-containing layers and the adjacent IMC layers.

The O-map from site 1 in figure 4.13d display a thin oxide-layer along the edge of the IMC layer that lies closest to Al. This means that the oxide layer in this part of the specimen has not been removed, however oxide layer at other places in the specimen could have been broken so that Al could have seeped through and managed to form IMC with Cu. Upon closer inspection of figure 4.13d in combination with the HAADF-STEM image in figure 4.15, one also sees excess oxygen along grain boundaries in Al. This could mean that the welding conditions potentially gave rise to intergranular corrosion within the Al close to the joined interface. Corrosion can have degraded the properties, such as the strength, of Al. The O-map from site 3 in figure 4.17d shows a collection of O towards the top of the map where Al concentration seem to be significant also, indicating Al-oxide.

Site 2 (figure 4.16) has characteristics most similar to Al-Cu-nr.1 where it shows two IMC layers. This becomes extra apparent in the maps of Al and Cu. The ratio between the at% of Cu and the at% of Al in these two layers, that are listed in table 4.6, have been compared with the most possible candidates listed in table 2.1. The conclusion that can be made from this, with the aid of the previous experience with the other Al-Cu specimen and the SAD analysis, is that IMC in layer 1 here is probably Al_2Cu, and layer 2 is probably Al_4Cu_9. The same procedure has been executed for site 1 (figures 4.13 and 4.14) and site 3 (figure 4.17) which display a more complex structure, as there seems to have been formed three IMC layers rather than two. The suggested IMCs in all of these regions have been listed in table 5.1. The mean thicknesses of these layers stated in table 4.6, together with the other properties of the discovered IMCs, is discussed further through comparison with previous research in section 5.2.1.3.

5.2.1.3 Combined evaluation

The suggested IMCs in the specimens Al-Cu-nr.1 and Al-Cu-nr.2, after discussions in sections 5.2.1.1 and 5.2.1.2, have been listed in table 5.1. The mean thicknesses $\bar{x}$ of these IMCs, from tables 4.2 and 4.6, have been regiven in table 5.1 for ease of comparison and discussion. The suggestions for IMCs are trustworthy since both SAD and EDS analysis gave similar results, strengthening the conclusions. Among the two methods, EDS analysis has higher chance of contributing to errors as it is a semi-quantitative technique which can have high percentage of errors that depend highly on the specific elements that are quantified. Therefore, as seen above, at% ratios found from EDS analysis can deviate from the exact ratios expected from the concluded IMCs after comparison with SADP results. Nonetheless, the EDS studies have been proven to be useful in confirming the composition of the IMCs suggested by SADPs in the Al-Cu specimens discussed above. The EDS studies have also been useful in discovering that dispersoids from Al filler metal are present in the Al-rich IMC layers only, possibly strengthening those layers. This finding also helped to deduce that the original interface between Al and Cu was probably between these dispersoid-containing layers and their adjacent IMC layers. Furthermore, EDS studies revealed that the oxide layer at the interface between Al and Cu seem to have been removed at most places and initiated beneficial IMC formation. However, there were also evidence, from EDS maps, of corrosion within Al close to the interface, which can degrade the properties of Al.

Table 5.1: *The suggested IMCs in the specimens Al-Cu-nr.1 and Al-Cu-nr.2 and their mean thicknesses $\bar{x}$. The suggestions were made based on SAD and EDS analysis.*

Specimen	Site	Layer	IMC	$\bar{x}$ (nm)
Al-Cu-nr.1		1	Al_2Cu	221 ± 16
Al-Cu-nr.1		2	Al_4Cu_9	189 ± 10
Al-Cu-nr.2	1	1	Al_2Cu	307 ± 31
Al-Cu-nr.2	1	2	AlCu	146 ± 21
Al-Cu-nr.2	1	3	Al_4Cu_9	294 ± 49
Al-Cu-nr.2	2	1	Al_2Cu	250 ± 12
Al-Cu-nr.2	2	2	Al_4Cu_9	168 ± 9
Al-Cu-nr.2	3	1	Al_2Cu	260 ± 22
Al-Cu-nr.2	3	2	AlCu	254 ± 39
Al-Cu-nr.2	3	3	Inconclusive	407 ± 59

From previous research it is known that IMCs that are most commonly formed at the Al-Cu interface are Al_4Cu_9, Al_2Cu and AlCu [67, 73–80] (see section 2.4.5.1). Different welding methods than HYB have resulted in the formation of these IMCs, such as friction welding, friction stir welding, explosive welding and diffusion bonding. The findings presented in this thesis support the claim that these are the most common Al-Cu IMCs. Like the other Al-Cu IMCs, these three are hard and brittle, meaning they can promote crack propagation if present in thick layers but be excellent to the bonding strength if present in thin layers.

In the Al-Cu specimens, Al_2Cu were formed in layers with an average thickness 260 ± 43 nm, Al_4Cu_9 were formed in layers with an average thickness 217 ± 51 nm, and AlCu were formed in layers with an average thickness 200 ± 44 nm. Summing together the IMC thicknesses at each site in table 5.1 gives that the total combined average thickness of IMCs is $\bar{x}_{\text{total}} = 525 \pm 22$ nm. Site 3 in Al-Cu-nr.2 has been excluded from the calculation of $\bar{x}_{\text{total}}$ because the IMC in third layer is inconclusive. Note that not all the examined sites have all three layers of IMCs.

$\bar{x}_{\text{total}} = 525 \pm 22$ nm can be compared to cases where similar Al-Cu IMCs have been formed using different welding techniques than HYB. $\bar{x}_{\text{total}}$ is less than the 2000 nm thickness reported after friction welding by Dalgaard et al. [83], the 1100 nm thickness reported after friction stir welding by Tan et al. [74], and also the 31.5 µm thickness formed after a typical diffusion bonding process by Calvo et al. [75]. The reason for this could be the higher welding temperatures used in friction welding, friction stir welding and diffusion bonding than that used in HYB (see section 2.1.1 for details on these methods). The highest welding temperature of HYB is approximately 400 °C. The thickness created by diffusion bonding is exceptionally high compared to the measured $\bar{x}_{\text{total}}$. This could be the result of much longer bonding time diffusion bonding has, which for the case of 31.5 µm thickness given above was 129 hours, compared to the few seconds of HYB.

The findings here mean that HYB generally manages to keep the thickness of the Al-Cu IMCs much less than the other common solid state methods. HYB manages to achieve bonding between Al and Cu through IMCs at the interface at the same time as it manages to avoid forming too thick IMC layers which would deteriorate the joint quality by being brittle and crack-prone. If the entire Al-Cu interface was the same to the two specimens examined in TEM, i.e. without pores and with continuous and uniform IMC layers between the two metals, the quality of the joint would be excellent. However, SEM results revealed earlier presence of large gaps and pores in the interface between Al and Cu. The damage caused by those pores is reflected in the mechanical testing which is discussed in section 5.3.

5.2.2 Al-Ti

The Al-Ti specimens, Al-Ti-nr.1 and Al-Ti-nr.2, are considered in combination in this section. Examining the images of the Al-Ti specimens, clear differences can be spotted between the Al-Ti interfaces and the interfaces examined earlier of the Al-Cu specimens. The Al-Cu specimens had uniform and continuous IMC layers along the whole interface with significant thickness so as to get noticed at once through visual examination of the low magnification images. In the Al-Ti specimens one sees both mixing between the metals happening in large and messy regions and also in thin layers at the interface which can be seen at higher magnification.

Unlike with Al-Cu specimens, it was not possible to identify IMCs from SAD or layerwise filtering of the EDS data at the regions with the possibility to contain IMCs in the Al-Ti specimens. This is due to those region being extremely narrow with small and overlapping grains. Even the smallest SA-aperture available in the TEM used was too large to isolate the regions of interest. Potential IMCs between Al and Ti were listed in table 2.2 in the theory-chapter. Nonetheless, two attempts to capture DPs from such regions have been shown in figure 4.20. There, in addition to strong reflections corresponding to pure Ti, one can also see reflections closer spaced together that do not match any of the main elements at hand, such as Al, Ti, Si. These reflections could have originated from IMCs. The EDS maps from regions with potential IMCs tend to show high concentration of both Al, Ti and Si. This could have simply been due to overlapping or intermixing (without IMC formation) of these elements at those regions, but the DPs shown in figure 4.20 gives credence to the existence of Al-Si-Ti IMCs. Si, which is an alloying element in Al-alloy FM, could have diffused to the interface during welding of Al and Ti. The temper condition of the Al FM used to make the examined joint was T4. In this temper condition, the alloying elements in Al, such as Si in this case, can be found both in the form of dispersoids and also in solid solution in the Al matrix. The latter can more easily travel to the interface between Al and Ti and contribute to formation of IMCs. This could be what has happened at the Al-Ti interface of the joint in this thesis. In the paper by Sun et al. [95], they suggest that Si can manage to substitute Al atoms in the Al-Ti IMCs, which can suppress further development of the brittle Al-Ti IMCs. This could be one possible explanation for why the regions with possible IMCs are very thin.

EDS maps have been taken from several different sites in both specimens. As earlier with Al-Cu specimens, signals from dispersoids can be observed as small dots in some of the EDS maps. These dispersoids close to the Al-Ti interface seem to be randomly placed in Al as before the welding, therefore they do not need extra discussion.

In the Al-Ti specimens shown in figures 4.18 and 4.26, one noticeable feature is that Al and Ti have mixed together in large regions, such as in site 1 and site 3 in Al-Ti-nr.1 (figure 4.18a) and site 1 in Al-Ti-nr.2 (figure 4.26a). These three sites resemble a combination of mechanical interlocking and IMC formation. Through mechanical interlocking, Al and Ti can hold together mechanically. Metaphorically speaking, it is as if Al and Ti are holding hands without fusing together. Both mechanical interlocking and IMC formation contributes positively to holding the metals together, and thus also to the weld strength.

The EDS maps from site 1 and 3 in Al-Ti-nr.1 and site 1 in Al-Ti-nr.2, are given in figures 4.21, 4.23 and 4.28, respectively. There are places in these sites where both Al and Ti seem to be present. In addition, Si seem to have gathered in those places. The presence of both Al, Ti and Si indicates formation of Al-Si-Ti IMCs. The thickness of such places in these large mixing regions could not be measured since the exact location of the IMC layers could not be pinpointed from the images.

In the SEM studies above, loose Ti-fragments in Al were observed on the large scale. Similar but smaller Ti-fragments can be observed with a higher magnification in TEM, in figures 4.18

and 4.26. Site 2 in Al-Ti-nr.1 (figure 4.18a) is one such fragment. The EDS maps of this site, shown in figure 4.22, confirms that the main body of the fragment is Ti. At the edges of the fragment, there are both contributions from Al, Ti and Si. This phenomenon is the same as observed above in the large mixing regions and suggests Al-Si-Ti IMC formation.

Figures 4.19 and 4.27 show high magnification images of the part of the interface of the Al-Ti specimens where there are no formation of large mixing regions discussed above. Looking closely, one can observe a thin layer of mixing right at the boundary between the two main metals Al and Ti, suggesting the possible formation of IMC. The mean thickness of the layers in the two specimen are similar and have been found from those images to be $\bar{x} = 53 \pm 5$ nm and $\bar{x} = 48 \pm 5$ nm, giving an average of $\bar{x} = 51 \pm 4$ nm. Such regions have been investigated with EDS at sites 4 and 5 in Al-Ti-nr.1 (figure 4.18a) and site 3 in Al-Ti-nr.2 (figure 4.26a). Sites 4 and 5 in Al-Ti-nr.1 partially overlaps. A thin, uniform and continuous IMC layer between Al and Ti, that give high signals in the Al, Si and Ti maps, can be most clearly seen in the EDS maps of site 5 in Al-Ti-nr.1 in figure 4.25 and site 3 in Al-Ti-nr.2 in figure 4.30. As in the case of large mixing regions discussed above, this suggests that there is an Al-Si-Ti IMC layer at the boundary between Al and Ti. These layers are again too narrow to be examined using SAD and layerwise EDS analysis, therefore identification of the Al-Si-Ti IMC composition could not be done here, but remain an interesting prospect for further work.

Another interesting feature revealed from the EDS maps in these regions is the following, which can be most clearly seen in the EDS maps of site 4 in Al-Ti-nr.1 in figure 4.24 and site 3 in Al-Ti-nr.2 in figure 4.30. In addition to the usual dispersoids in Al, there are also spots in the Al constituting of Al, Ti and Si. These could once again be Al-Si-Ti IMCs, and they probably contribute positively to the strength of the region around the weld interface. This is similar to the role dispersoids play in the Al FM.

Site 2 in Al-Ti-nr.2 in figure 4.29 has a similar IMC layer between Al and Ti as those observed in the other sites discussed above. However, in addition to the signals from Al, Ti and Si, the EDS maps here also show concentration of O at this layer, indicating that the oxides have not been removed totally here.

It has been mentioned above that the IMC layers that have been observed to have formed in the middle between Al and Ti have an average thickness of $\bar{x} = 51 \pm 4$ nm. This is much smaller than IMC layer thicknesses typically produced with other solid state methods. Al and Ti have been joined together in the past using different solid state welding techniques than HYB before, such as friction welding, friction stir welding, explosive welding and diffusion bonding (see section 2.4.5.2). After all these welding methods, $TiAl_3$ is the IMC that has almost always been reported to have formed. Kim and Fuji performed friction welding, yielding $TiAl_3$ with thicknesses between approximately 5 µm and 50 µm [94]. They suggested 5 µm as an upper limit in order to avoid deterioration of tensile strength and ductility. $\bar{x} = 51 \pm 4$ nm of the specimens examined in this thesis is much less than this limit. $\bar{x}$ is also much smaller than the 10 µm limit suggested by Enjyo et al., who performed diffusion bonding [99]. Both the friction welding and the diffusion bonding methods have higher welding temperatures than HYB, and diffusion bonding has much longer welding time than HYB (see section 2.1.1 for details on these methods). These could be the reasons HYB produced IMCs with much smaller thickness than the thicknesses resulted from these two welding methods.

The findings here mean that HYB generally manages to produce Al-Ti welds with IMC layers that have thickness much less than that produced with the other common solid state methods. HYB manages to achieve bonding between Al and Ti through mechanical interlocking and IMCs at the interface at the same time as it manages to avoid forming too thick IMC layers which would have deteriorated the joint quality by being brittle and crack-prone. The quality of the Al-Ti interface in the examined joint, as well as the other two interfaces, are examined further

through mechanical tests which is discussed in the next section, section 5.3.

5.3 Mechanical tests

5.3.1 Vickers hardness test

The purpose of the Vickers hardness test is to evaluate the hardness of the joint, especially around the heat-affected zone (HAZ) close to the interfaces. Figure 4.32a shows the HV values measured during Vickers hardness test done along trajectory 1. Trajectory 1 starts at Cu and crosses the interfaces Al-Cu and Al-Ti before reaching Ti, as shown in the illustration in figure 4.31. The leftmost and the rightmost part of the curve are over the regions well inside Cu and Ti. Here, the HV values should approach that of the metals before welding. As expected, Ti turns out to be much harder metal than Cu, as can be seen from the almost double as large HV values it has. This, as mentioned above, can help explain why the Al-Cu interface is more deformed than the Al-Ti interface. Cu is more amenable to plastic deformations, while Ti is less deformed but instead has loose fragments that has been detached from the interface.

When moving closer to the interface with Al, which is at around $x \approx -4.5$ mm for Cu and around $x \approx 4.5$ mm for Ti, both metals have higher HV values. This is expected, since the pressure experienced at the interface during welding increases the dislocation density in the metal and causes dislocation entanglement, making movement of dislocations more difficult and resulting in a harder metal near the interfaces. This process is called work-hardening [131], also called cold working. At $x = -0.4$ mm, a sudden drop in the HV can be seen in the curve. This was most likely due to a pore at the Al-Cu interface since this interface displayed many pores in the SEM-images. The HV values over the whole Al region, approximately $x \in [-4.5, 4.5]$ mm, are stable around a value right above $HV = 80$ and do not increase when closing in on the interfaces at the two ends. This could mean that the whole Al region is equally hard and strong. That Al is more homogeneous in strength is reasonable, since all of the Al experienced similar conditions when it was pressed through the extrusion pin during welding.

Figure 4.32b shows the HV values measured during the Vickers hardness test along trajectory 2, which spans over steel only, as illustrated in figure 4.31. The part of steel that meets Al lies approximately in the range $x \in [-4.5, 4.5]$ mm in the figure. In this region, a clear increase in the HV can be observed compared to that outside of this region. This suggests that steel was work-hardened during welding due to the pressure exerted on its surface by the FM and the extrusion pin. With this, it can be concluded that all three base metals of the joint, Cu, Ti and steel, have been work hardened close to the interface. This means that Cu, Ti and steel have become stronger and have achieved higher resistance to deformation towards the interface, which further helps to make the weld stronger.

Figure 4.32c shows the HV values measured along trajectory 3 which starts at steel and crosses the Al-steel interface before going well into Al, as shown in figure 4.31. No valid information about steel can be extracted from this figure since there are only two measurement points inside steel. The HV values inside Al, $y \in [-1.5, 1.0]$ mm, matches those seen in figure 4.32a and do not shown any significant increase towards the interface with steel. This supports the claim that the whole Al region seems to be equally hard and strong.

It should be mentioned that the hardness of the IMCs cannot be measured from the Vickers hardness test results. This is firstly because the distance between each indentation during the testing was 0.5 mm, which is much larger than the IMC thicknesses. It is therefore highly unlikely that the position of the indentation made during the Vickers hardness test correspond to the location of an IMC. Even if the positions were to coincide, this test is still much too crude to properly measure hardness of the interfacial IMCs. This is because the diagonal length of the

indentations should be 20 µm or larger to avoid measurement inaccuracy [132]. This is several orders of magnitude too large, since the thickness of the IMCs formed in the examined joint is on the 100 nm scale. This means that the indentations cannot make an accurate measurement of the hardness of an IMC without involving the surrounding metal.

5.3.2 Tensile test

This section starts by addressing the engineering stress-strain curves in section 4.3.2, before providing a discussion around the fracture surfaces examined in SEM.

First, compare the example shown in figure 2.2 with the engineering stress (σ) - strain (ε) curves in figures 4.33a and 4.33b of the Al-Ti specimens and the Al-steel specimens, respectively. The Al-Ti specimens seem to have followed all the steps described in the example while the Al-steel specimens broke off early. This shows the ductile nature of the Al-Ti specimens since they underwent elastic deformation and subsequent plastic deformation, which includes necking, before fracturing. The necking of these specimens means that at one point during stretching of the specimens, the strain focused on a weak point and caused local deformation which lead to fracture at that point. Necking can be seen clearly in the SEM images of Al-Ti specimens, as discussed below. On the other hand, the Al-steel specimens are of a more brittle nature as they fracture sharply without plastic deformation. The mean UTS of the Al-Ti specimens was found earlier to be 305 ± 1 MPa and the same of the Al-steel specimens was found to be 266 ± 21 MPa. Although these mean UTS values differ they are not too far apart, which means that both the Al-Ti and the Al-steel interfaces seem to have similar strength. However, the Al-Ti interface of the joint has the upper hand in being more ductile hence tolerant towards being stretched and deformed, compared to the Al-steel interface.

The top piece of Al-Ti specimen 1 in figure 4.34a shows that the fracture happened well within Al. This means that the bonding mechanisms at the interface, such as IMCs and mechanical bonding, were strong enough to not be the source of fracture. The fractured spot in Al experienced necking before breaking. This can be seen more clearly in figure 4.34e, which shows that the original cylindrical shape of the specimen became more conical. The fracture surfaces, seen in figures 4.34b and 4.34f, has only one metal, Al, on the whole surface as expected. When zooming further into these fracture surfaces, shown in figures 4.34c, 4.34d, 4.34g and 4.34h, dimples at the surface become apparent indicating that region to be ductile. The same findings are also true for the remaining three Al-Ti specimens shown in figures F.1–F.3. These findings support the observation from the stress-strain curve discussed above and confirm that Al-Ti interface has both ductile and strong bond, making the quality of the joint excellent at that interface.

Both the top piece, figure 4.35a, and the bottom piece, figure 4.35e, of Al-steel specimen 1 show that the fracture happened at the interface between Al and steel. These images show no signs of necking as the specimens kept their original cylindrical shape. The large scale BSE images of the fracture surfaces in figures 4.35b and 4.35f have darker regions towards the edges of the surfaces and grey and white regions towards the middle. The dark regions are probably Al while the grey and white regions in the middle seems to probably be a mix between steel and IMCs. At higher magnification, in figures 4.35c, 4.35d, 4.35g and 4.35h, it can be seen that the fracture through the dark regions with Al were ductile in nature while the lighter regions with possibly steel or IMCs show large patches with smooth surfaces indicating brittle fracture. The other three Al-steel specimens in figures G.1–G.3 also show similar characteristics as the first specimen.

The dual phase steel used in this joint is steel with high strength, hardness and brittleness, making it susceptible to defects. This means that this type of steel is sensitive to cracks on the interface and breaks easily. This could explain why the fracture happened on the interface.

The fact that there seems to be remnants of both Al, steel and IMCs on the fracture surfaces, supports the claim that there was bonding between the metals at the interface. Otherwise, the fracture surfaces after being teared apart would have contained mostly only Al or only steel. These findings support the observation from the stress-strain curve discussed earlier, namely that the Al-steel specimens have a brittle but sound bonding.

The last interface in question is Al-Cu, and figure 4.36 shows Al-Cu specimen 1. The surface of the specimen is mostly smooth and non-flat. Al-Cu specimens 2-4 in figures H.1–H.3 show similar characteristics. Combining this result with the previously know properties of the Al-Cu interface from the SEM-studies, the most probable explanation for the breaking of the Al-Cu specimens during machining process, which is the process of preparing specimens for tensile testing, is presence of pores. The TEM studies of the Al-Cu specimens suggested that, at the nanoscale, the two metals are able to create bonding through IMCs after being welded with HYB. Therefore, the Al-Cu interface would have achieved strong bonding if the interface did not have macroscopic porosity. It is therefore important to understand why gaps and pores are created at the Al-Cu interface. If the HYB welding could be done without creating such gaps, it would likely be of much benefit to the quality of the joint. The presence of pores and gaps could be a consequence of the material properties of Cu, but it could also be due to Cu being on the retreating side during welding. Investigating a joint created with Cu on the advancing side would therefore be of much interest for future work.

Chapter

6 Conclusion

The aim of this thesis was to better understand the properties of a multi-material joint made from the new and innovative Hybrid Metal Extrusion & Bonding (HYB) method. This was done in three steps: using SEM to investigate microscale characteristics near the interface, using TEM to investigate nanoscale formation of intermetallic compounds (IMCs) at the interface and using mechanical tests to examine mechanical properties. The joint was made of four different metals that are widely used in the industry, namely aluminium, copper, titanium and steel. The three base metals plates, Cu-H02, Ti-Grade 2 and HCT590 steel, were joined together in one passing by using Al filler metal AA6082-T4. Because of time constraints and the fact that Al-steel joint made with HYB is being studied elsewhere, the focus of the TEM study used to characterize IMCs was put on the Al-Cu and Al-Ti interfaces.

The Al-Cu interface of the joint was the only interface among the three that displayed macroscopic pores and deformations in the initial SEM investigation. This could be due to the mechanical properties of Cu, but it could also be a consequence of the placement of Cu in the welding process. The pores could in principle also be a result of the initial conditions of the Cu interface. Effort should be put into uncovering the origin of the pores, since whether or not the placement of base metals affects joint properties is important to know. The Al-Cu interface was also shown to have developed bonding through IMCs, through examination of two different specimens in TEM. It was discovered that IMCs formed in two or three layers that uniformly spanned the whole Al-Cu interface. The total combined average thickness of the Al-Cu IMCs was 525 ± 22 nm, which is much less than the thickness of Al-Cu IMCs reported in studies of other welding techniques. It is preferable for the quality of the joint that IMCs are formed, since it means that the metals are joined on the atomic scale. It is also advantageous that the IMCs are thin because IMCs tend to be brittle and prone to crack easily. SADP and EDS analysis revealed the IMCs to be mostly Al_4Cu_9 and Al_2Cu, and also AlCu in some places. Vickers hardness tests showed that parts of Cu close to the interface with Al had work hardened and became stronger. Due to macroscopic pores, tensile test specimens from the Al-Cu interface could not be made without breaking during machining. That is, despite the strong bond evidenced by the IMCs, the macroscopic pores and gaps rendered the interface vulnerable.

The Al-Ti interface of the joint had no significant pores and displayed close bonding between the two metals at the interface, as revealed by the initial SEM investigation. SEM studies also showed that Ti was affected by the welding process as many fragments from Ti loosened and got mixed into Al. The Vickers hardness measurements showed that parts of Ti close to the interface with Al was work hardened, as a result of Ti experiencing pressure during welding. EDS studies in TEM revealed that Al and Ti were mixed at some places on the interface in large regions indicating both mechanical interlocking and Al-Si-Ti IMC formation. In other places without formation of such large mixing regions, a Al-Si-Ti IMC layer seem to have formed with extremely narrow thickness along the interface between the Al and Ti bulk. The average thickness of such IMC layer were found to be 51 ± 4 nm. The IMC thicknesses were much less than those formed with other welding techniques used to join Al and Ti. Due to their thickness and the fact that

the grains at those regions where small and overlapping, SAD or layerwise EDS analysis could not be used to determine the composition of the IMCs. Tensile tests showed a high strength of the Al-Ti interface with UTS reaching 305 ± 1 MPa. During tensile testing, the Al-Ti specimens underwent elastic deformation and subsequent plastic deformation, which include necking, before fracturing well within Al. The findings combine to confirm that Al-Ti interface of the joint had a both ductile and strong bond, making the quality of the joint excellent at that interface.

The Al-steel interface of the joint, as in the case of Al-Ti, had no significant pores and seemed to display close bonding between the two metals at the interface, as revealed by the initial SEM investigation. SEM studies also revealed noticeably smaller grains of steel closer to the interface with Al. Vickers hardness tests supported this by showing that steel was work hardened, as a result of experienced pressure on its surface during welding. IMC formation and mechanical interlocking seemed to have happened on the interface in images taken in SEM. Remnant of these IMCs seemed to be present on the fracture surfaces examined in SEM after tensile testing. The UTS of the Al-steel specimens reached 266 ± 21 MPa, indicating high strength. The Al-steel specimens had sharp fracture at the interface without undergoing plastic deformation. The results combine to conclude that the Al-steel interface managed to develop a brittle but sound bonding.

All in all, HYB managed to achieve bonding between the metals with mostly positive outcomes. The Al-Ti and Al-steel interfaces display significant strength where bonding seemed to have happened through both IMCs and mechanical interlocking. The Al-Cu interface show uniform bonding through IMC at the microscopic level, however its quality is deteriorated by macroscopic pores. All the IMCs formed in the examined joint seem to be thinner than what was formed with other common solid state welding methods, which avoids deteriorating the joint quality due to IMCs being brittle and crack-prone. The results in this thesis are promising for HYB as a viable and robust welding technique. HYB should be pursued further as a way to create the high-performance and lightweight multi-material structures that could bring us one step closer to a more energy efficient future.

Chapter

7 Future Work

There are several topics for future work that could be explored to supplement the investigation of the four-metal joint carried out in this thesis. There are also other future work that could strengthen the general knowledge about the welds produced by the HYB method even further. The suggestions for both of these are given in this chapter.

One important question that came out as a result of this thesis is whether the deterioration of the Al-Cu interface through the formation of macroscopic pores could have been avoided by having Cu on the advancing side during welding. It is of great interest to know whether the pores are simply a result initial conditions or the mechanical properties of Cu, or if it is in fact a result of the placement of metals chosen during welding. If the nature of HYB is such that the bond on the retreating side is more prone to pores and deformations regardless of the metals used, then that is a valuable information that should inform the choice of placement. Making new joints with HYB where the position of the metals have been exchanged could give an answer to this. In general, when making new joints for the purpose of a better understanding HYB, the initial conditions should be monitored in order to facilitate a better comparison. This includes the properties such as the surface roughness of the metals, which can be measured prior to welding.

For the joint examined in this thesis, the future work should consider the examination of the Al-steel interface in TEM, as this was omitted in this thesis. Investigation of IMC formation and determination of the IMC composition should be carried out in TEM through imaging, SAD and EDS. The IMCs at the Al-Ti interface was too thin to be identified through SAD and EDS. For such thin IMCs, one could use another technique in TEM called scanning precession electron diffraction (SPED). SPED consists of precessing a probe over the selected area and recording diffraction patterns at each probe position [133]. Using a very small probe size (typically 1-2 nm), diffraction patterns from IMCs could be collected without being affected by the surroundings.

To measure the hardness of all the IMCs formed in the joint, a nanohardness testing should be used rather than the Vickers test used in this thesis. This is because the size of the indentations used in the Vickers test is too large to probe the hardness of the IMCs. The depth of indentation in nanohardness testing is less than about 50 nm and the indentation diameter is smaller than about 150 nm [134], which are numbers that lie on the same scale as the in the thicknesses of the IMCs measured in this thesis.

Examining the change in grain structure of the metals would help to understand better the impacts HYB has on the metals. To examine the change in grain structure of the metals in the regions close to the interfaces and the bulk regions, imaging in SEM after mechanical polishing has been seen in this thesis to be an insufficient technique. One reason was argued to be that the images of bulk region were not taken far enough into the metals. Such images should be taken at at least 2 mm into the metals to avoid the work-hardened zone of the metals. Prior to imaging, FIB polishing should be performed after mechanical polishing in order to display the grain structures in the metals better. Also, the SEM images should be taken right after FIB polishing and before exposing the specimen to air to avoid oxidation of its surface.

To obtain an even better study of the grain structure, future work is advised to perform

electron backscatter diffraction (EBSD) in SEM. EBSD is a technique used to obtain structural organization of the material using the Kikuchi diffraction patterns [135]. Using EBSD, one can map the grain orientations and obtain information on the grain structures. If the grains are very small, it is beneficial to perform TEM studies. However, the TEM specimens are much smaller than what can be studied in SEM, and the latter thus gives a better statistics. Relevant TEM studies are imaging or the SPED method mentioned earlier. Like EBSD, SPED can also be used produce information on the grain structures by mapping the grain orientations.

Bibliography

[1] K. Martinsen, S. Hu, and B. Carlson. "Joining of dissimilar materials". In: *CIRP Annals* 64.2 (2015), pp. 679–699 *Cited on page 1.*

[2] N. Sakundarini et al. "Optimal multi-material selection for lightweight design of automotive body assembly incorporating recyclability". In: *Materials & Design* 50 (2013), pp. 846–857 *Cited on page 1.*

[3] C. for Automotive Research. *Automotive Technology: Greener Products, Changing Skills. Lightweight Materials & Forming Report.* 2011 *Cited on page 1.*

[4] W. Cai et al. "A state-of-the-art review on solid-state metal joining". In: *Journal of Manufacturing Science and Engineering* 141.3 (2019) *Cited on pages 1, 4, 5, 7.*

[5] L. Sandnes et al. "Exploring the hybrid metal extrusion and bonding process for butt welding of Al–Mg–Si alloys". In: *The International Journal of Advanced Manufacturing Technology* 98.5-8 (2018), pp. 1059–1065 *Cited on pages 2, 6.*

[6] E. Ruska. "The development of the electron microscope and of electron microscopy". In: *Reviews of modern physics* 59.3 (1987), p. 627 *Cited on page 2.*

[7] F. C. Campbell. *Joining: Understanding the Basics.* ASM International, 2011 *Cited on page 4.*

[8] Ø. Grong. "Recent advances in solid-state joining of aluminum". In: *Welding journal* 91.1 (2012), pp. 26–33 *Cited on pages 4, 6, 14.*

[9] O. Myhr et al. "Modeling of microstructure evolution, residual stresses and distortions in 6082-T6 aluminum weldments". In: *Welding Journal New York* 77 (1998), 286–s *Cited on page 4.*

[10] O. Myhr and Ø. Grong. "Process modelling applied to 6082-T6 aluminium weldments-II. Applications of model". In: *Acta Metallurgica et Materialia* 39.11 (1991), pp. 2703–2708 *Cited on page 4.*

[11] O. Myhr et al. "Modelling of the microstructure and strength evolution in Al–Mg–Si alloys during multistage thermal processing". In: *Acta Materialia* 52.17 (2004), pp. 4997–5008 *Cited on page 4.*

[12] O. Myhr and Ø. Grong. "Novel modelling approach to optimisation of welding conditions and heat treatment schedules for age hardening Al alloys". In: *Science and technology of welding and joining* 14.4 (2009), pp. 321–332 *Cited on page 4.*

[13] American Welding Society C6 Committee on Friction Welding. *Recommended Practices for Friction Welding.* 1st ed. American Welding Society, 2009 *Cited on page 5.*

[14] W.-Y. Li et al. "Microstructure characterization and mechanical properties of linear friction welded ti-6al-4v alloy". In: *Advanced Engineering Materials* 10.1-2 (2008), pp. 89–92 *Cited on page 5.*

[15] A. R. McAndrew et al. "A literature review of Ti-6Al-4V linear friction welding". In: *Progress in Materials Science* 92 (2018), pp. 225–257 *Cited on page 5.*

[16] W. M. Thomas et al. *Friction welding*. US Patent 5,460,317. Google Patents, Oct. 1995 *Cited on page 5.*

[17] R. S. Mishra and Z. Ma. "Friction stir welding and processing". In: *Materials science and engineering: R: reports* 50.1-2 (2005), pp. 1–78 *Cited on page 5.*

[18] G. R. Cowan, J. J. Douglass, and A. H. Holtzman. *Explosive bonding*. US Patent 3,137,937. June 1964 *Cited on page 5.*

[19] A. Vivek et al. "Vaporizing foil actuator: A tool for collision welding". In: *Journal of Materials Processing Technology* 213.12 (2013), pp. 2304–2311 *Cited on page 5.*

[20] G. S. Daehn and J. C. Lippold. *Low-temperature laser spot impact welding driven without contact*. US Patent 8,084,710. Dec. 2011 *Cited on page 5.*

[21] B. Gulenc. "Investigation of interface properties and weldability of aluminum and copper plates by explosive welding method". In: *Materials & Design* 29.1 (2008), pp. 275–278 *Cited on page 5.*

[22] B. Crossland and J. Williams. "Explosive welding". In: *Metallurgical Reviews* 15.1 (1970), pp. 79–100 *Cited on page 5.*

[23] Y. Qu. "Temperature distribution across the explosive welding interface". In: *Combustion, Explosion, and Shock Waves* 47.1 (2011), pp. 123–127 *Cited on page 5.*

[24] N. F. Kazakov. *Diffusion bonding of materials*. Pergamon Press, 1985 *Cited on page 5.*

[25] K. Aydın, Y. Kaya, and N. Kahraman. "Experimental study of diffusion welding/bonding of titanium to copper". In: *Materials & Design* 37 (2012), pp. 356–368 *Cited on page 6.*

[26] S. Kolukisa. "The effect of the welding temperature on the weldability in diffusion welding of martensitic (AISI 420) stainless steel with ductile (spheroidal graphite-nodular) cast iron". In: *Journal of Materials Processing Technology* 186.1-3 (2007), pp. 33–36 *Cited on page 6.*

[27] Ø. Grong. *Method and device for joining of metal components, particularly light metal components*. US Patent 7,131,567. Google Patents, Nov. 2006 *Cited on page 6.*

[28] L. Sandnes et al. "Assessment of the Mechanical Integrity of a 2 mm AA6060-T6 Butt Weld Produced Using the Hybrid Metal Extrusion & Bonding (HYB) Process–Part II: Tensile Test Results". In: *Procedia Structural Integrity* 17 (2019), pp. 632–642 *Cited on pages 6, 35.*

[29] F. Abbatinali et al. "Mechanical Characterization and Crack Growth Path Analysis of a Hybrid Metal Extrusion & Bonding (HYB) Joint of AA6082-T6 Aluminium Alloy and S355 Structural Steel". In: 6th International Conference on Crack Paths, Italy. 2018 *Cited on page 6.*

[30] Ø. Grong, L. Sandnes, and F. Berto. "A status report on the hybrid metal extrusion & bonding (HYB) process and its applications". In: *Material Design & Processing Communications* 1.2 (2019), e41 *Cited on page 6.*

[31] R. L. Smith and G. Sandly. "An accurate method of determining the hardness of metals, with particular reference to those of a high degree of hardness". In: *Proceedings of the Institution of Mechanical Engineers* 102.1 (1922), pp. 623–641 *Cited on page 7.*

[32] T. Sugimoto and T. Kawaguchi. "Development of an automatic Vickers hardness testing system using image processing technology". In: *IEEE transactions on industrial electronics* 44.5 (1997), pp. 696–702 *Cited on page 7.*

[33] N. Saba, M. Jawaid, and M. Sultan. "1 - An overview of mechanical and physical testing of composite materials". In: *Mechanical and Physical Testing of Biocomposites, Fibre-Reinforced Composites and Hybrid Composites*. Ed. by M. Jawaid, M. Thariq, and N. Saba. Woodhead Publishing Series in Composites Science and Engineering. Woodhead Publishing, 2019, pp. 1–12 *Cited on page 7.*

[34] I. Faridmehr et al. "Correlation between engineering stress-strain and true stress-strain curve". In: *American Journal of Civil Engineering and Architecture* 2.1 (2014), pp. 53–59 *Cited on pages 8, 9.*

[35] E. Hearn. *Mechanics of Materials 1, An Introduction to the Mechanics of Elastic and Plastic Deformation of Solids and Structural Materials*. 3rd ed. Elsevier, 1997 *Cited on page 8.*

[36] Y. Z. Ma, D. Sobernheim, and J. R. Garzon. "Glossary for Unconventional Oil and Gas Resource Evaluation and Development". In: *Unconventional Oil and Gas Resources Handbook*. Elsevier, 2016, pp. 513–526 *Cited on page 8.*

[37] A. P. Mouritz. *Introduction to aerospace materials*. Elsevier, 2012 *Cited on page 8.*

[38] P. Vincent. "The necking and cold-drawing of rigid plastics". In: *Polymer* 1 (1960), pp. 7–19 *Cited on page 8.*

[39] C. Kittel. *Introduction to solid state physics*. 8th ed. John Wiley & Sons, Inc, 2005 *Cited on pages 9, 12.*

[40] C. Giacovazzo et al. *Fundamentals of Crystallography*. 3rd ed. Oxford University Press, 2011 *Cited on pages 9–11.*

[41] J. M. Zuo and J. C. Spence. *Advanced transmission electron microscopy*. Springer New York, 2017 *Cited on page 10.*

[42] A. Jostsons and J. Napier. *Crystallographic techniques and data for transmission electron microscopy of zirconium*. Australian Nuclear Science and Technology Organisation, 1970 *Cited on page 10.*

[43] A. Griger, V. Stefaniay, and T. Turmezey. "Crystallographic Data and Chemical Compositions of Aluminium-Rich Al–Fe Intermetallic Phases". In: *Z. Metallkd.* 77.1 (1986), pp. 30–35 *Cited on pages 10, 21, 22.*

[44] D. J. Griffiths. *Introduction to quantum mechanics*. 2nd ed. Cambridge University Press, 2017 *Cited on page 11.*

[45] J. R. Davis et al. *ASM specialty handbook, Aluminum and aluminum alloys*. ASM International Materials Park, OH, 1993, pp. 207–216 *Cited on pages 13, 14.*

[46] G. Mathers. *The welding of aluminium and its alloys*. Woodhead publishing, 2002 *Cited on pages 13, 14.*

[47] R. Solheim. "Dialect development in a melting pot: The formation of a new culture and a new dialect in the industrial town of Høyanger". In: *Nordic Journal of Linguistics* 32.2 (2009), pp. 191–206 *Cited on page 13.*

[48] J. De Laeter. "Atomic weights of the elements 1987". In: *Journal of physical and chemical reference data* 17.4 (1988), pp. 1791–1793 *Cited on pages 13, 15.*

[49] G. Chiarotti, ed. *Physics of Solid Surfaces - Structure*. Vol. Volume 24A. Springer-Verlag Berlin Heidelberg, 1993 *Cited on pages 13, 15.*

[50] P. Eckerlin and H. Kandler. *Structure data of elements and intermetallic phases*. Ed. by K.-H. Hellwege and A. M. Hellwege. Vol. 6. Springer, 1971 *Cited on pages 14–16.*

[51] H. Wonderatschek and U. Müller. *International Tables for Crystallography: Volume A1: Symmetry Relations Between Space Groups*. Springer, 2004 *Cited on pages 14, 15.*

[52] A. Association et al. "International alloy designations and chemical composition limits for wrought aluminum and wrought aluminum alloys". In: *Teal Sheets* (2009) *Cited on page 14.*

[53] W. D. Callister and D. G. Rethwisch. *Materials science and engineering: an introduction*. 8th ed. John wiley & sons New York, 2010 *Cited on page 14.*

[54] M. Yılmaz, M. Çöl, and M. Acet. "Interface properties of aluminum/steel friction-welded components". In: *Materials Characterization* 49.5 (2002), pp. 421–429 *Cited on pages 14, 21.*

[55] G. Atwood and C. Curtis. *Hydrometallurgical process for the production of copper*. US Patent 3,785,944. United States Patent Office, 1974 *Cited on page 14.*

[56] C. D. Association et al. *The Copper Advantage: A Guide to Working with Copper and Copper Alloys* *Cited on pages 14, 15.*

[57] G. Parker. *Encyclopedia of materials: science and technology*. Elsevier, 2001 *Cited on page 15.*

[58] J. R. Davis et al. *Copper and copper alloys*. ASM international, 2001 *Cited on page 15.*

[59] A. B601-18a. *Standard Classification for Temper Designations for Copper and Copper Alloys—Wrought and Cast*. ASTM International, 2018 *Cited on page 15.*

[60] G. Lütjering and J. C. Williams. *Titanium*. 2nd ed. Springer Science & Business Media, 2007 *Cited on page 15.*

[61] S. Mandal. *Steel Metallurgy: Properties, Specifications and Applications*. McGraw Hill Professional, 2015 *Cited on pages 15, 16.*

[62] H. Bhadeshia and R. Honeycombe. *Steels: microstructure and properties*. Butterworth-Heinemann, 2017 *Cited on page 16.*

[63] M. Rashid. "Dual phase steels". In: *Annual Review of Materials Science* 11.1 (1981), pp. 245–266 *Cited on page 16.*

[64] S. Flachstahl. *HTC590X+Z, dual-phase steel for cold forming*. 2017 *Cited on page 16.*

[65] J. Madeni, S. Liu, and T. Siewert. "Intermetallics formation and growth at the interface of tin-based solder alloys and copper substrates". In: *2nd International Brazing and Soldering Conference (ISBC), San Diego, California. NIST*. Vol. 9. Citeseer. 2003 *Cited on page 16.*

[66] K. Ikeuchi et al. "Effect of interfacial reaction layer on bond strength of friction-bonded joint of Al alloys to steel". In: *Transactions of JWRI* 34.1 (2005), pp. 1–10 *Cited on page 16.*

[67] K. S. Lee et al. "Evaluation of intermediate phases formed on the bonding interface of hot pressed Cu/Al clad materials". In: *Metals and Materials International* 22.5 (2016), pp. 849–855 *Cited on pages 16, 18, 91.*

[68] T. Laurila, V. Vuorinen, and J. Kivilahti. "Interfacial reactions between lead-free solders and common base materials". In: *Materials Science and Engineering: R: Reports* 49.1-2 (2005), pp. 1–60 *Cited on page 16.*

[69] N. Ponweiser, C. L. Lengauer, and K. W. Richter. "Re-investigation of phase equilibria in the system Al–Cu and structural analysis of the high-temperature phase η1-Al1- δCu". In: *Intermetallics* 19.11 (2011), pp. 1737–1746 *Cited on pages 17, 18.*

[70] L. Huey-Lin and P. Duwez. "Solid solutions of rhodium with copper and nickel". In: *Journal of the Less Common Metals* 6.3 (1964), pp. 248–249 *Cited on pages 17, 18.*

[71] Y.-c. Su et al. "Thermodynamic analysis and experimental research on Li intercalation reactions of the intermetallic compound Al2Cu". In: *Solid State Ionics* 177.5-6 (2006), pp. 507–513 *Cited on pages 17, 18.*

[72] S. Westman. "Refinement of the r-CugA] 4 Structure". In: *Acta Chemica Scandinavica* 19.6 (1965), pp. 1411–1419 *Cited on pages 17, 18.*

[73] M. Sahin. "Joining of aluminium and copper materials with friction welding". In: *The International Journal of advanced Manufacturing technology* 49.5-8 (2010), pp. 527–534 *Cited on pages 18, 91.*

[74] C. Tan et al. "Microstructural evolution and mechanical properties of dissimilar Al–Cu joints produced by friction stir welding". In: *Materials & Design* 51 (2013), pp. 466–473 *Cited on pages 18, 91.*

[75] F. Calvo et al. "Special features of the formation of the diffusion bonded joints between copper and aluminium". In: *Journal of materials science* 23.6 (1988), pp. 2273–2280 *Cited on pages 18, 19, 91.*

[76] C.-Y. Chen, H.-L. Chen, and W.-S. Hwang. "Influence of interfacial structure development on the fracture mechanism and bond strength of aluminum/copper bimetal plate". In: *Materials transactions* 47.4 (2006), pp. 1232–1239 *Cited on pages 18, 91.*

[77] J. Li et al. "Interfacial microstructures and thermodynamics of thermosonic Cu-wire bonding". In: *IEEE Electron Device Letters* 32.10 (2011), pp. 1433–1435 *Cited on pages 18, 91.*

[78] R. Pelzer et al. "Growth behavior and physical response of Al-Cu intermetallic compounds". In: *2014 IEEE 16th Electronics Packaging Technology Conference (EPTC)*. IEEE. 2014, pp. 372–377 *Cited on pages 18, 91.*

[79] P. Xue et al. "Enhanced mechanical properties of friction stir welded dissimilar Al–Cu joint by intermetallic compounds". In: *Materials science and engineering: A* 527.21-22 (2010), pp. 5723–5727 *Cited on pages 18, 91.*

[80] P. Hema and M. Reddaiah. "Impact of Process Parameters on The Friction Stir Butt Welded Aa6061–Cu Joint Strength". In: *International Journal of Research in Advent Technology* 7.4 (2019) *Cited on pages 18, 91.*

[81] W.-B. Lee, K.-S. Bang, and S.-B. Jung. "Effects of intermetallic compound on the electrical and mechanical properties of friction welded Cu/Al bimetallic joints during annealing". In: *Journal of Alloys and Compounds* 390.1-2 (2005), pp. 212–219 *Cited on page 18.*

[82] P. Wanjara et al. "Linear friction welding of Al–Cu: Part 1–process evaluation". In: *Canadian Metallurgical Quarterly* 50.4 (2011), pp. 350–359 *Cited on page 18.*

[83] E. Dalgaard et al. "Linear friction welding of Al–Cu part 2–interfacial characteristics". In: *Canadian Metallurgical Quarterly* 50.4 (2011), pp. 360–370 *Cited on pages 18, 91.*

[84] T. Bhattacharya, H. Das, and T. Pal. "Influence of welding parameters on material flow, mechanical property and intermetallic characterization of friction stir welded AA6063 to HCP copper dissimilar butt joint without offset". In: *Transactions of Nonferrous Metals Society of China* 25.9 (2015), pp. 2833–2846 *Cited on page 18.*

[85] M. H. Athar and B. Tolaminejad. "Weldability window and the effect of interface morphology on the properties of Al/Cu/Al laminated composites fabricated by explosive welding". In: *Materials & Design* 86 (2015), pp. 516–525 *Cited on pages 18, 19.*

[86] M. Asemabadi, M. Sedighi, and M. Honarpisheh. "Investigation of cold rolling influence on the mechanical properties of explosive-welded Al/Cu bimetal". In: *Materials Science and Engineering: A* 558 (2012), pp. 144–149 *Cited on page 18.*

[87] S. Chen et al. "Atomic diffusion behavior in Cu-Al explosive welding process". In: *Journal of Applied physics* 113.4 (2013), p. 044901 *Cited on page 18.*

[88] H. Amani and M. Soltanieh. "Intermetallic phase formation in explosively welded Al/Cu bimetals". In: *Metallurgical and Materials Transactions B* 47.4 (2016), pp. 2524–2534 *Cited on page 19.*

[89] J. C. Schuster and M. Palm. "Reassessment of the binary aluminum-titanium phase diagram". In: *Journal of phase equilibria and diffusion* 27.3 (2006), pp. 255–277 *Cited on page 19.*

[90] G. E.A. et al. "Variations en fonction de la concentration en oxygène des paramètres cristallins de la solution solide interstitielle Ti-O". In: *Comptes Rendus des Seances de l'Academie des Sciences, Serie C: Sciences Chimiques 277* (1973) *Cited on pages 19, 20.*

[91] S. Sridharan and H. Nowotny. "Studies in the ternary system Ti-Ta-Al and in the quaternary system Ti-Ta-Al-C". In: *Zeitschrift fuer Metallkunde* 74 (1983), pp. 468–472 *Cited on pages 19, 20.*

[92] K. Schubert et al. "Einige Strukturdaten metallischer Phasen (7)". In: *Naturwissenschaften* 49.3 (1962), pp. 57–57 *Cited on pages 19, 20.*

[93] H. Hu et al. "Structural stability, mechanical properties and stacking fault energies of TiAl3 alloyed with Zn, Cu, Ag: First-principles study". In: *Journal of Alloys and Compounds* 666 (2016), pp. 185–196 *Cited on page 20.*

[94] Y.-C. Kim and A. Fuji. "Factors dominating joint characteristics in Ti–Al friction welds". In: *Science and technology of welding and joining* 7.3 (2002), pp. 149–154 *Cited on pages 20, 93.*

[95] Q. Sun et al. "Microstructural characterization and mechanical properties of Al/Ti joint welded by CMT method—Assisted hybrid magnetic field". In: *Materials & Design* 116 (2017), pp. 316–324 *Cited on pages 20, 92.*

[96] H. Zhao et al. "Interfacial microstructure and mechanical properties of Al/Ti dissimilar joints fabricated via friction stir welding". In: *Journal of Alloys and Compounds* 789 (2019), pp. 139–149 *Cited on pages 20, 21.*

[97] G. Casalino and M. Mortello. "Modeling and experimental analysis of fiber laser offset welding of Al-Ti butt joints". In: *The International Journal of Advanced Manufacturing Technology* 83.1-4 (2016), pp. 89–98 *Cited on page 20.*

[98] D. Fronczek et al. "Structural properties of Ti/Al clads manufactured by explosive welding and annealing". In: *Materials & Design* 91 (2016), pp. 80–89 *Cited on pages 20, 21.*

[99] T. Enjyo et al. "Diffusion welding of aluminum to titanium". In: *Transactions of JWRI* 6.1 (1977), pp. 123–130 *Cited on pages 20, 21, 93.*

[100] M.-S. Chu and S.-K. Wu. "Interreactions of TiAl3 Thin Film on Bulk γ-TiAl and on Bulk α2-Ti3Al Alloys at 700—1000 degrees Celsius". In: *Materials Transactions* 45.4 (2004), pp. 1290–1298 *Cited on page 20.*

[101] M. Aonuma and K. Nakata. "Effect of calcium on intermetallic compound layer at interface of calcium added magnesium–aluminum alloy and titanium joint by friction stir welding". In: *Materials science and engineering: B* 173.1-3 (2010), pp. 135–138 *Cited on page 20.*

[102] A. Wu et al. "Interface and properties of the friction stir welded joints of titanium alloy Ti6Al4V with aluminum alloy 6061". In: *Materials & Design* 71 (2015), pp. 85–92 *Cited on page 20.*

[103] Z. Chen and S. Yazdanian. "Microstructures in interface region and mechanical behaviours of friction stir lap Al6060 to Ti–6Al–4V welds". In: *Materials Science and Engineering: A* 634 (2015), pp. 37–45 *Cited on page 20.*

[104] S.-H. Chen et al. "Si diffusion behavior during laser welding-brazing of Al alloy and Ti alloy with Al-12Si filler wire". In: *Transactions of Nonferrous Metals Society of China* 20.1 (2010), pp. 64–70 *Cited on page 20.*

[105] M. Aonuma and K. Nakata. "Dissimilar metal joining of 2024 and 7075 aluminium alloys to titanium alloys by friction stir welding". In: *Materials transactions* 52.5 (2011), pp. 948–952 *Cited on page 21.*

[106] H. Ozaki and M. Kutsuna. "Dissimilar metal joining of zinc coated steel and aluminum alloy by laser roll welding". In: *Welding processes* 2 (2012), pp. 33–53 *Cited on pages 21, 22.*

[107] E. Popiel et al. "Investigation of Fe3- xVxAl alloys with DO3 type structure by X-ray, magnetostatic and Mössbauer effect methods". In: *Journal of the Less Common Metals* 146 (1989), pp. 127–135 *Cited on pages 21, 22.*

[108] S. H. Mahmood, M. A. Awawdeh, and A. S. Saleh. "Structural and Mössbauer studies of the alloy system FeAl1- x Nb x". In: *Journal of applied physics* 73.10 (1993), pp. 5663–5665 *Cited on pages 21, 22.*

[109] A. Van der Kraan and K. Buschow. "The 57Fe Mössbauer isomer shift in intermetallic compounds of iron". In: *Physica B+ C* 138.1-2 (1986), pp. 55–62 *Cited on pages 21, 22.*

[110] J. G. Barlock and L. F. Mondolfo. "Structure of Some Aluminum-Iron-Magnesium-Manganese-Silicon Alloys". In: *Zeitschrift fur Metallkunde* 66.10 (1975), pp. 605–611 *Cited on pages 21, 22.*

[111] A. Elrefaey et al. "Characterization of aluminum/steel lap joint by friction stir welding". In: *Journal of materials engineering and performance* 14.1 (2005), pp. 10–17 *Cited on page 21.*

[112] W.-B. Lee et al. "Interfacial reaction in steel–aluminum joints made by friction stir welding". In: *Scripta Materialia* 55.4 (2006), pp. 355–358 *Cited on page 21.*

[113] Y. Li et al. "Morphology and structure of various phases at the bonding interface of Al/steel formed by explosive welding". In: *Microscopy* 49.1 (2000), pp. 5–16 *Cited on page 21.*

[114] M. K. Karfoul, G. J. Tatlock, and R. T. Murray. "The behaviour of iron and aluminium during the diffusion welding of carbon steel to aluminium". In: *Journal of materials science* 42.14 (2007), pp. 5692–5699 *Cited on page 21.*

[115] G. Casalino et al. "Effects of laser offset and hybrid welding on microstructure and IMC in Fe–Al dissimilar welding". In: *Metals* 7.8 (2017), p. 282 *Cited on page 21.*

[116] D. B. Williams and C. B. Carter. *Transmission Electron Microscopy. A Textbook for Materials Science*. 2nd ed. Springer US, 2009 *Cited on pages 23, 28.*

[117] N. Bohr. "On the constitution of atoms and molecules". In: *The London, Edinburgh, and Dublin Philosophical Magazine and Journal of Science*. 6th ser. 26 (1913) *Cited on page 30.*

[118] A. Thompson et al. *X-Ray Data Booklet*. Lawrence Berkeley National Laboratory, University of California, Berkeley, 2009 *Cited on page 30.*

[119] G. Cliff and G. Lorimer. "The quantitative analysis of thin specimens". In: *Journal of Microscopy, Wiley Online Library* 103.2 (1975), pp. 203–207 *Cited on page 31.*

[120] B. Fultz and J. M. Howe. *Transmission Electron Microscopy and Diffractometry of Materials*. 4th ed. Springer Science & Business Media, 2013 *Cited on pages 32, 33.*

[121] J. I. Goldstein et al. *Scanning Electron Microscopy and X-Ray Microanalysis*. 4th ed. Springer, 2018 *Cited on page 32.*

[122] M. L. De Castro and F. Priego-Capote. "Ultrasound-assisted preparation of liquid samples". In: *Talanta* 72.2 (2007), pp. 321–334 *Cited on page 36.*

[123] E. Tempelman, H. Shercliff, and B. N. van Eyben. *Manufacturing and design: understanding the principles of how things are made*. Elsevier, 2014 *Cited on page 36.*

[124] A. Markopoulos, I. Pressas, and D. Manolakos. "Manufacturing processes of shape memory alloys". In: *Materials Forming and Machining*. Elsevier, 2016, pp. 155–180 *Cited on page 36.*

[125] A. R. Raja, M. K. Yusufzai, and M. Vashista. *Characterization of advancing and retreating weld of friction stir welding of aluminium*. 2016 *Cited on page 36.*

[126] L. A. Giannuzzi and F. A. Stevie. "A review of focused ion beam milling techniques for TEM specimen preparation". In: *Micron* 30.3 (1999), pp. 197–204 *Cited on page 39.*

[127] J. Blindheim et al. "On the mechanical integrity of AA6082 3D structures deposited by hybrid metal extrusion & bonding additive manufacturing". In: *Journal of Materials Processing Technology* (2020) *Cited on page 40.*

[128] C. A. Schneider, W. S. Rasband, and K. W. Eliceiri. "NIH Image to ImageJ: 25 years of image analysis". In: *Nature methods* 9.7 (2012), pp. 671–675 *Cited on page 41.*

[129] F. de la Peña et al. *hyperspy/hyperspy: HyperSpy v1.5.2*. Version v1.5.2. Sept. 2019. DOI: 10.5281/zenodo.3396791 *Cited on page 42.*

[130] B. P. Epps and E. M. Krivitzky. "Singular value decomposition of noisy data: noise filtering". In: *Experiments in Fluids* 60.8 (2019), p. 126.

[131] V. Kain. "Stress corrosion cracking (SCC) in stainless steels". In: *Stress Corrosion Cracking*. Elsevier, 2011, pp. 199–244 *Cited on page 94.*

[132] M. Lindegren. "Hardness Testing and Specimen Preparation". In: *Struers Application notes* (2017) *Cited on page 95.*

[133] J. S. Barnard, D. N. Johnstone, and P. A. Midgley. "High-resolution scanning precession electron diffraction: Alignment and spatial resolution". In: *Ultramicroscopy* 174 (2017), pp. 79–88 *Cited on page 99.*

[134] G. Sundararajan and M. Roy. *Encyclopedia of materials: science and technology*. Elsevier, 2001 *Cited on page 99.*

[135] M. de Assumpção Pereira-da-Silva and F. A. Ferri. "Scanning Electron Microscopy". In: *Nanocharacterization Techniques*. Elsevier, 2017, pp. 1–35 *Cited on page 100.*

[136] Struers. *MD System, The unique consumables for materialographic grinding and polishing.* 2018 *Cited on page 111.*

Appendix

A Details on specimen preparation for SEM

A.1 Cutting

"Struers Accutom-50" was used to cut out a cross-section from the multi-material joint with the operational parameters listed in table A.1.

Table A.1: *The operational parameters used with Struers Accutom - 50 to cut the multi-material joint.*

Wheel	Speed	Feed	Force	Rotation	Water
452CA	2700 rpm	0.030 mm/s	Medium	Off	On

A.2 Embedding in epoxy

The piece cut out from the joint was embedded in epoxy in the following steps. Firstly, a holder of suitable size to mold the epoxy was smeared with silicon inside for ease of removal of the epoxy after it has hardened. Thereafter, 5 g resin and 1 g hardener were stirred together in a cup for 2-3 minutes and left still for 5 minutes. The specimen was placed in the holder smeared with silicon, after which the mixture was poured into the same holder. This holder was then left in a fume hood for at least 12 hours to harden.

A.3 Rough polishing details

The polishing process of the specimen, to make its surface smooth, started with a rough polishing using silicon carbide grinding papers with grain sizes (in terms of diameter) 15.3 µm and 6.5 µm, with approximately one minute each in that order. The instrument used for this was "Struers Rotopol-20". Water rinsing was used during polishing and the rotation speed was 150 rpm.

A.4 Unsuccessful polishing methods

The two methods that did not work well for all of the four metals in the joint are *vibration polishing* and *oxide polishing*. The diamond fine polishing was redone in between these two methods. The OM optical images from the same region of the specimen, both right before either methods were used and right after each of the methods were used, are shown in figure A.1. All other parts of the surface of the specimen were also examined carefully using OM. The vibration polishing was done for one hour and the oxide polishing was done for one minute. As neither methods manage to polish all four metals equally well, they were deemed unsuitable for this particular joint.

A.5 Diamond fine polishing

The specimen underwent diamond fine polishing using the instrument "Struers Tegramin-30". Diamond fine polishing process consisted of four steps, with three different types of polishing cloths [136] (same type in the last two steps) and four different diamond suspensions from Struers, listed in table A.2. Table A.2 also lists the sizes of the diamond particles in each suspension and the polishing time for each step. The explanation for the long polishing times is that the marks on the surface of the titanium were more resistant to polishing than that in other metals. The polishing was done in the order listed in the table. The rotation speed of both the holder and the plate were 150 rpm and they were rotated in the same direction.

Table A.2: *The polishing cloths and diamond suspensions used during diamond fine polishing.*

Diamond size (µm)	Polishing cloth	Diamond suspension	Time (min)
9	MD-Largo	Largo	3
3	MD-Mol	Mol-B3	20
1	MD-Nap	Nap-R1	15
0.25	MD-Nap	Nap-1/4	20

It should also be mentioned that in-between each polishing step, the specimen was rinsed firstly with water then cleaned in ultrasonic cleanser while being submerged in ethanol for five minutes and dried using a hair blower. The equipment was also washed in-between each step and separate polishing cloth was used specifically for every step.

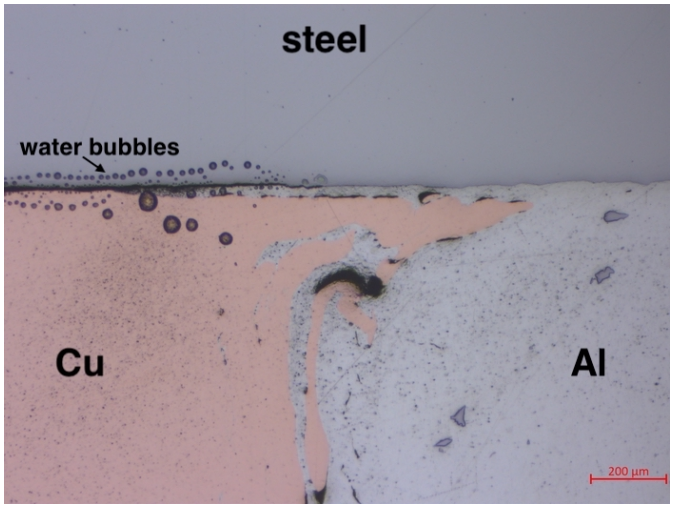

(a)

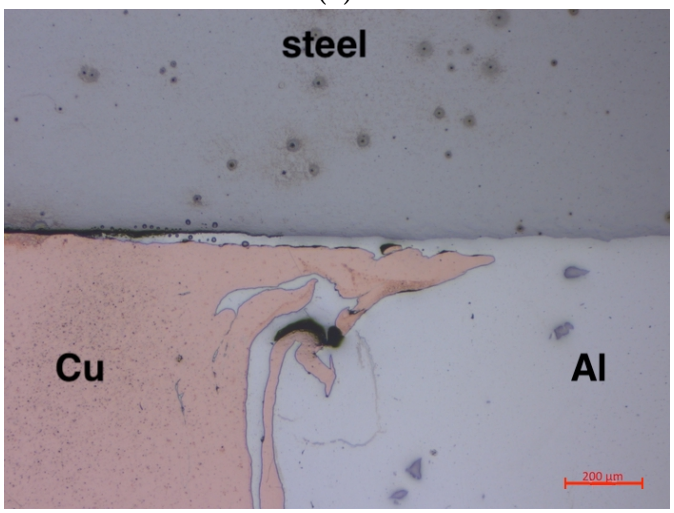

(b)

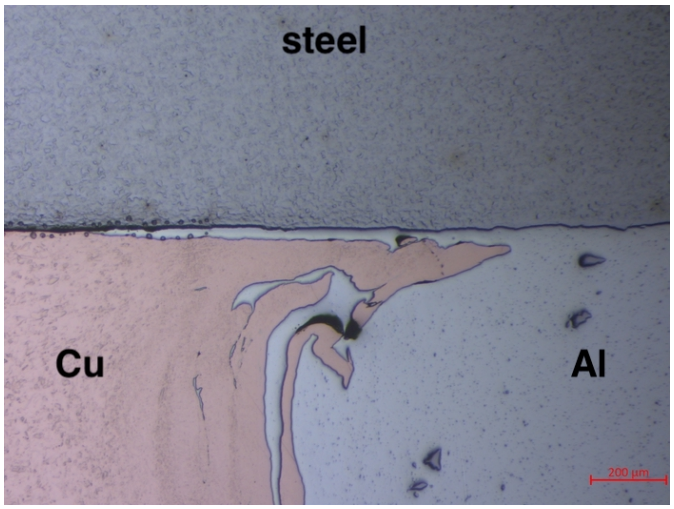

(c)

Figure A.1: *The OM optical images from the same region of the specimen, (a) right before either methods were used, (b) right after vibration polishing and (c) right after oxide polishing.*

Appendix

B Details on specimen preparation for TEM

The extraction process of the TEM specimens from the Al-Cu and Al-Ti interfaces has been done using FIB and was documented with images. Two specimens were taken from each of the Al-Cu and Al-Ti interfaces in the SEM specimen. They have been named Al-Cu-nr.1, Al-Cu-nr.2, Al-Ti-nr.1 and Al-Ti-nr.2, and their position in the SEM specimen is shown in figure B.1.

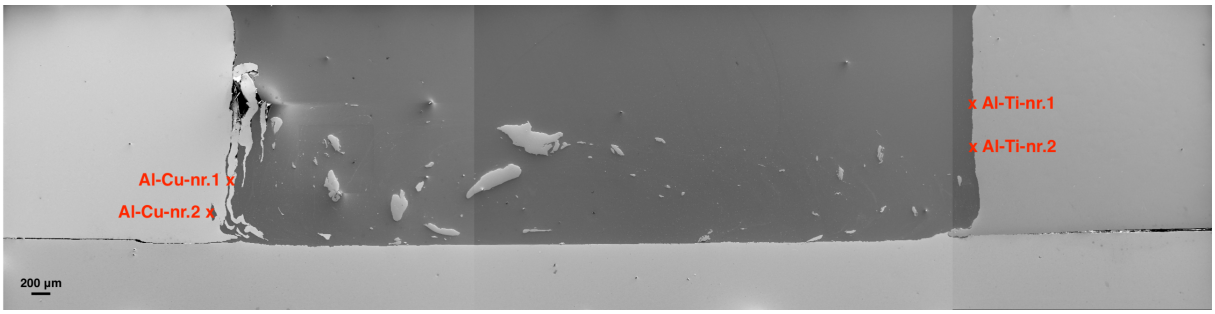

Figure B.1: *The position of the TEM specimens, Al-Cu-nr.1, Al-Cu-nr.2, Al-Ti-nr.1 and Al-Ti-nr.2.*

Figure B.2a shows the region the specimen Al-Cu-nr.2 was taken from. Figure B.2b shows Al-Cu-nr.2 after ion beam carbon deposition. This was done to protect the area of interest while attacking the area around it using ion beam. Figure B.2c shows the cut out process of the same specimen. Figure B.2d shows the same specimen placed on the FIB grid using wolfram Omniprobe lift-out needle. Figure B.2e shows the finished Al-Cu-nr.2.

The rest of the specimens were made in the same way. Figure B.3a shows the region Al-Cu-nr.1 was taken from. Figure B.3b shows the finished Al-Cu-nr.1. Figure B.4a shows the region Al-Ti-nr.1 was taken from. Figure B.4b shows the finished Al-Ti-nr.1. Figure B.5a shows the region Al-Ti-nr.2 was taken from. Figure B.5b shows the finished Al-Ti-nr.2.

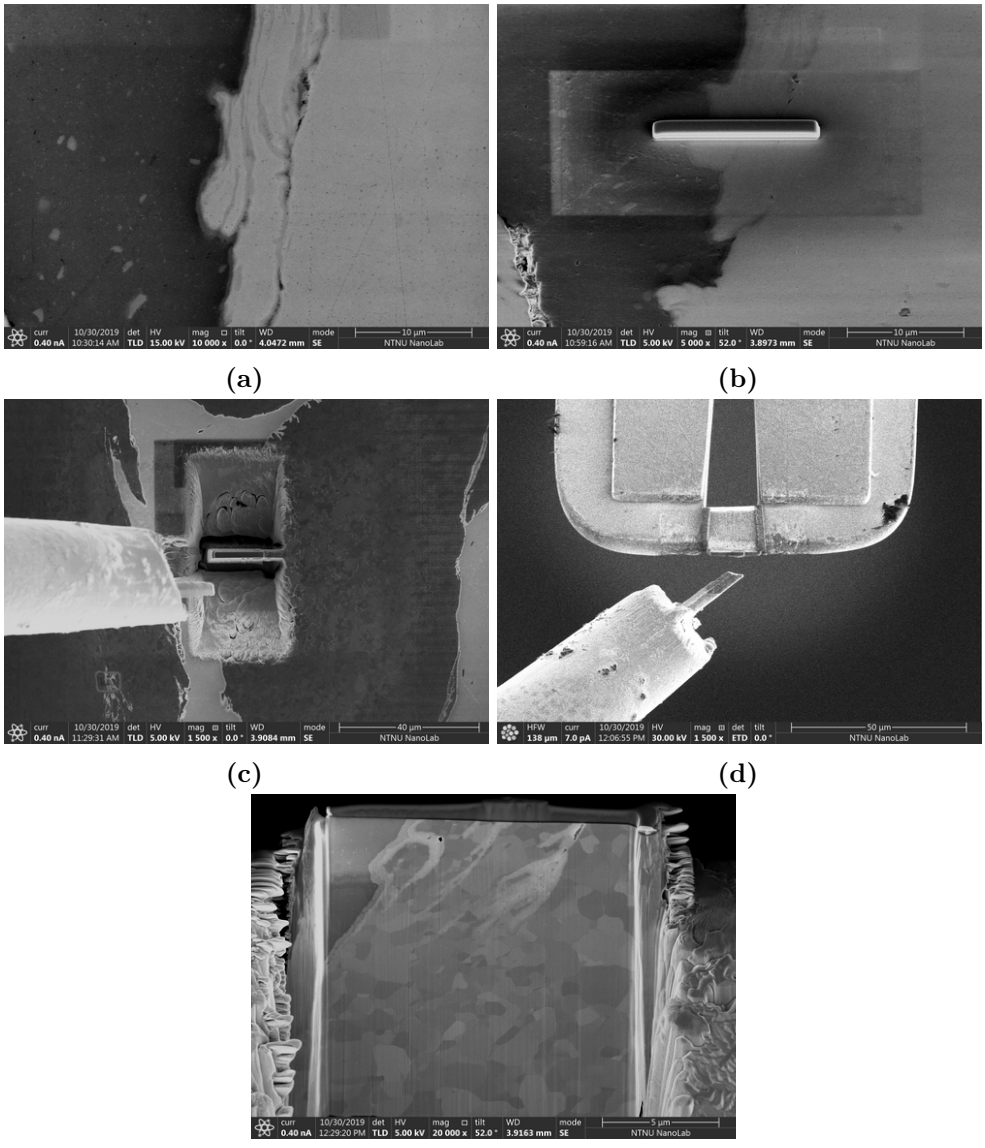

Figure B.2: *SE-images taken in SEM showing the making of the TEM specimen Al-Cu-nr.2 from the multi-material joint using FIB. (a) The location of Al-Cu-nr.2. (b) Al-Cu-nr.2 after ion beam carbon deposition. (c) The cut out process of Al-Cu-nr.2. (d) Al-Cu-nr.2 placed on a FIB grid. (e) The finished Al-Cu-nr.2.*

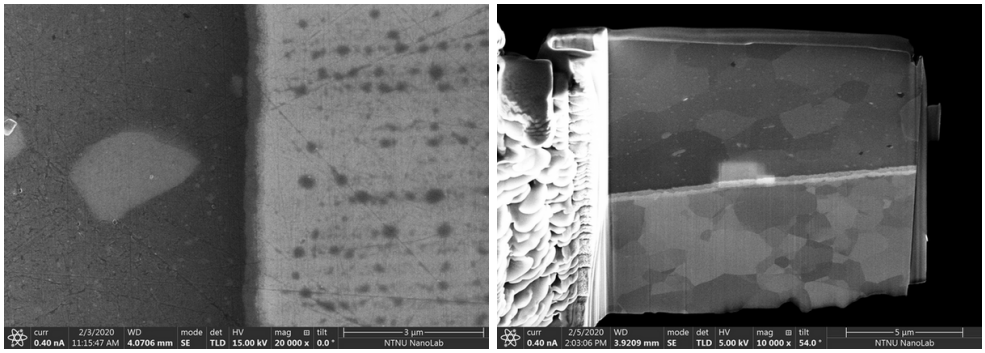

(a) **(b)**

Figure B.3: *SE-images taken in SEM of Al-Cu-nr.1 made using FIB, from the multi-material joint. (a) The location. (b) The finished product.*

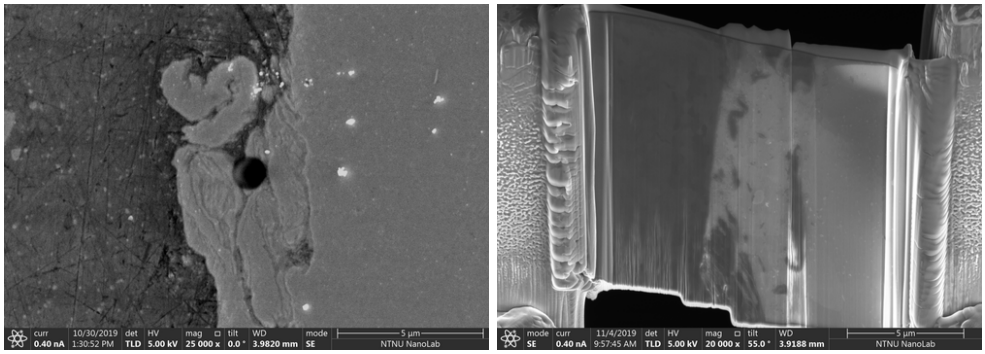

(a) **(b)**

Figure B.4: *SE-images taken in SEM of Al-Ti-nr.1 made using FIB, from the multi-material joint. (a) The location. (b) The finished product.*

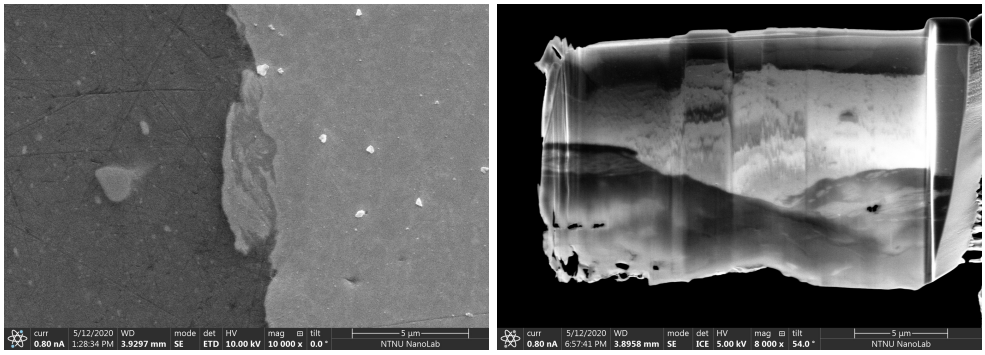

(a) **(b)**

Figure B.5: *SE-images taken in SEM of Al-Ti-nr.2 made using FIB, from the multi-material joint. (a) The location. (b) The finished product.*

Appendix

C DP-analysing code

```
### Comments from Hursanay:
### Insert into the main function "planesAndZone" the three LARGEST d-spacings from your DP and specify the range of indices you want to take into consideration. You also have to choose the phase you are interested in testing: Al, Cu, Al2Cu, AlCu, Al3Cu4d etc. (see which ones have been defined at the bottom).
### Example to run the code in terminal:
###    python   --->   exec(open("dSpacing.py").read()) --->   planesAndZone(Al4Cu9, -3, 3, 3.82, 2.4, 2.1, 0.09)

#_____________________________________________

import numpy as np
from math import gcd

def cubic(h, k, l, a):
    return a/np.sqrt(h**2 + k**2 + l**2)

def monoclinic(h, k, l, a, b, c, beta):
    return np.sin(beta)/np.sqrt(h**2/a**2 + k**2*np.sin(beta)**2/b**2 + l**2/c**2 -
        2*h*l*np.cos(beta)/(a*c))

def hexagonal(h, k, l, a, c):
    id2 = 4*(h**2 + h*k + k**2)/(3*a**2) + l**2/c**2
    return 1/np.sqrt(id2)

def tetragonal(h, k, l, a, c):
    id2 = (h**2 + k**2)/(a**2) + l**2/c**2
    return 1/np.sqrt(id2)

def orthorhombic(h, k, l, a, b, c):
    id2 = h**2/a**2 + k**2/b**2 + l**2/c**2
    return 1/np.sqrt(id2)

#gives a list of planes that match the d-spacing with the limits. (orignal design)
def listPlanes(phase, startIndex, stopIndex):
    for h in range(startIndex, stopIndex+1):
        for k in range(startIndex, stopIndex+1):
            for l in range(startIndex, stopIndex+1):
                if abs(h) + abs(k) + abs(l) > 0 and phase(h, k, l) != False:
                    print("(", h, ",", k, ",", l, ") -", phase(h,k,l))


#for this particular "phase", which planes, with indices limited by startIndex and stopIndex, have d-spacing within startIndex and stopIndex:
```

```
39 def listPlanesInterval(phase, startIndex, stopIndex, startInt, stopInt):
40     planes=[]
41     dSpac=[]
42     incl = False
43     for h in range(startIndex, stopIndex+1):
44         for k in range(startIndex, stopIndex+1):
45             for l in range(startIndex, stopIndex+1):
46                 d = phase(h, k, l)
47                 if abs(h) + abs(k) + abs(l) > 0 and d != False and d >= startInt and d
                       <= stopInt:
48                     incl = True
49                     #excluding those points in DP that have points closer to 000 that
                           lies on the same line, because the user is expected to work
                           with three points closest to 000 that are in three different
                           directions:
50                     g = gcd(gcd(h, k), l)
51                     for i in range(1, g):
52                         if phase(i*h/g, i*k/g, i*l/g) != False:
53                             incl = False
54                             break
55                     if incl:
56                         planes.append([h,k,l])
57                         dSpac.append(round(d,3))
58     return planes, dSpac
59
60
61 # given the largest three d-spacings from a DP, dSpac1 to dSpac3, find the lists of
       planes, p1 to p3, that match each d within the limit dlim. Then go through the
       lists p1-p3 to find which three planes from the three lists can be in the same
       DP. Return a list of such candidates and the corresponding zone axis z. Also
       return the calculated d-spacings, d1-d3, of each plane.
62 def planesAndZone(phase,startIndex, stopIndex, dSpac1,dSpac2,dSpac3,dlim):
63     p1,d1 = listPlanesInterval(phase, startIndex, stopIndex, dSpac1-dlim, dSpac1+dlim)
64     p2,d2 = listPlanesInterval(phase, startIndex, stopIndex, dSpac2-dlim, dSpac2+dlim)
65     p3,d3 = listPlanesInterval(phase, startIndex, stopIndex, dSpac3-dlim, dSpac3+dlim)
66     pCheck,dCheck = listPlanesInterval(phase, startIndex, stopIndex, dSpac3, dSpac3+15)
67     z=[]
68     for i in range(len(p1)):
69         for j in range(len(p2)):
70             if not np.array_equal(np.cross(p1[i], p2[j]), [0,0,0]):
71                 zTemp = np.cross(p1[i],p2[j])
72                 includeZ = False
73                 # Check if there is also a plane in p3 orthogonal to zTemp
74                 for k in range(len(p3)):
75                     if np.dot(zTemp, p3[k])==0 and not np.array_equal(np.cross(p2[j],
                           p3[k]), [0,0,0]):
76                         includeZ = True
77                         break
78                 # Check if there is already a vector parallel to zTemp in z
79                 if includeZ:
80                     for v in z:
81                         if np.array_equal(np.cross(v, zTemp), [0,0,0]):
82                             includeZ = False
83                             break
84                     for n in range(len(pCheck)):
```

```
85                      if np.dot(zTemp, pCheck[n])==0 and dCheck[n]>d3[k] and not
                            np.array_equal(np.cross(pCheck[n], p1[i]), [0,0,0]) and not
                            np.array_equal(np.cross(pCheck[n], p2[j]), [0,0,0]):
86                          includeZ = False
87                          break
88              if includeZ:
89                  gz=gcd(gcd(zTemp[0], zTemp[1]), zTemp[2])
90                  zTemp = zTemp/int(gz)
91                  z.append(zTemp)
92                  print(phase.__name__, "has following three planes in your DP:")
93                  print( p1[i], " with d = ", d1[i], "Angstrom")
94                  print( p2[j], " with d = ", d2[j], "Angstrom")
95                  print( p3[k], " with d = ", d3[k], "Angstrom")
96                  print("z = ", zTemp.astype(int), "\n")
97
98
99  #_____________________________________________
100
101 # Al:
102 def Al(h,k,l):
103     if (h % 2 == k % 2 == l % 2):
104         return cubic(h, k, l, 4.049)
105     else:
106         return False
107
108 # Cu:
109 def Cu(h,k,l):
110     if (h % 2 == k % 2 == l % 2):
111         return cubic(h, k, l, 3.615)
112     else:
113         return False
114
115 # alpha-Ti:
116 def aTi(h, k, l):
117     if (h + 2*k) % 3 == 0 and l % 2:
118         return False
119     else:
120         return hexagonal(h, k, l, 2.950, 4.681)
121
122
123 # Al-Cu phases:
124 def AlCu(h,k,l):
125     if (h + k) % 2 == 0:
126         return monoclinic(h, k, l, 11.973, 4.061, 6.807, np.pi*124.882/180)
127     else:
128         return False
129
130 def Al4Cu9R(h, k, l):
131     return hexagonal(h, k, l, 8.7066, 8.7066)
132
133 def Al4Cu9(h, k, l):
134     return cubic(h, k, l, 8.7023)
135
136 def Al2Cu(h, k, l):
137     if h == 0 or k == 0:
```

```
138         if h % 2 == 0 and k % 2 == 0 and l % 2 == 0:
139             return tetragonal(h, k, l, 5.949, 4.821)
140         else:
141             return False
142     elif (h+k+l) % 2 == 0:
143         return tetragonal(h, k, l, 5.949, 4.821)
144     else:
145         return False
146 
147 def Al3Cu4d(h, k, l):
148     if (h+k+l) % 2 == 0:
149         return orthorhombic(h, k, l, 4.0972, 7.0313, 9.9793)
150     else:
151         return False
152 
153 # Al-Ti phases:
154 def Ti3Al(h, k, l):
155     if (h + 2*k) % 3 == 0 and l % 2:
156         return False
157     else:
158         return hexagonal(h, k, l, 5.793, 4.623)
159 
160 def TiAl(h, k, l):
161     return tetragonal(h, k, l, 2.829, 4.071)
162 
163 def TiAl2(h, k, l):
164     if l==0:
165         if h % 2 or k % 2:
166             return False
167         else:
168             return tetragonal(h, k, l, 3.976, 24.360)
169     elif h==0 and k==0:
170         if l%4==0:
171             return tetragonal(h, k, l, 3.976, 24.360)
172         else:
173             return False
174     elif (h+k+l) % 2 == 0:
175         return tetragonal(h, k, l, 3.976, 24.360)
176     else:
177         return False
178 
179 def TiAl3D022(h, k, l):
180     if (h+k+l) % 2 == 0:
181         return tetragonal(h, k, l, 3.847, 8.621)
182     else:
183         return False
184 
185 def TiAl3L12(h, k, l):
186     return cubic(h, k, l, 3.981)
```

Appendix

D SADPs from Al-Cu-nr.1

Figures D.1 and D.2 show the SADPs taken from Al-Cu-nr.1. The IMC each SADPs correspond to have been written on the upper right corner of each image while the zone axis, z, have been written on the upper left corner. The numbers in the subtitles indicate which numbered-region in figure 4.8b each DP is taken from.

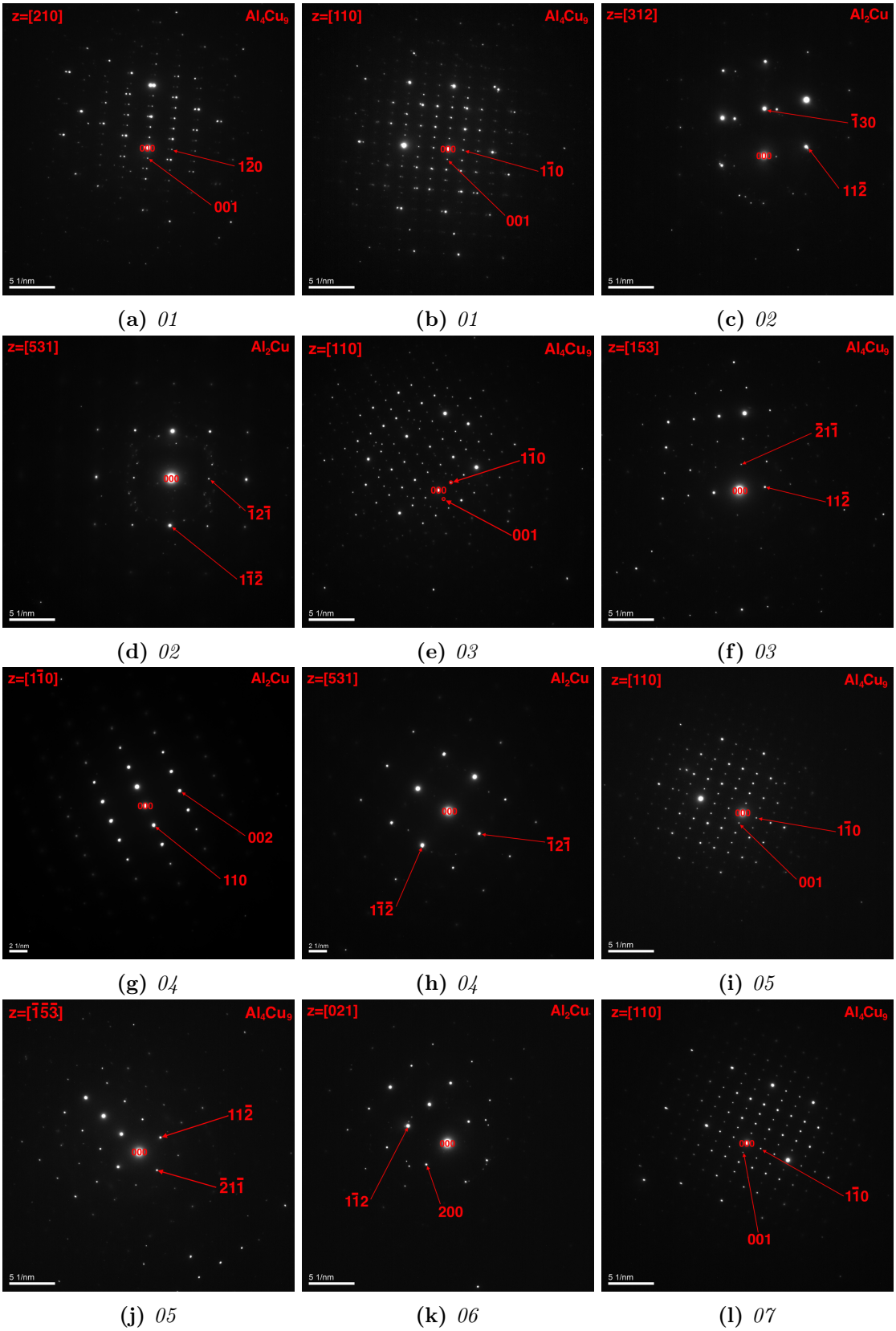

(a) *01* **(b)** *01* **(c)** *02*

(d) *02* **(e)** *03* **(f)** *03*

(g) *04* **(h)** *04* **(i)** *05*

(j) *05* **(k)** *06* **(l)** *07*

Figure D.1: ***Part 1:*** *SADPs taken from the Al-Cu-nr.1 specimen. The IMCs the SADPs correspond to have been written on the upper right corner of each image while the zone axis, z, have been written on the upper left corner. The numbers in the subtitles indicate which numbered-region in figure 4.8b each DP is taken from.*

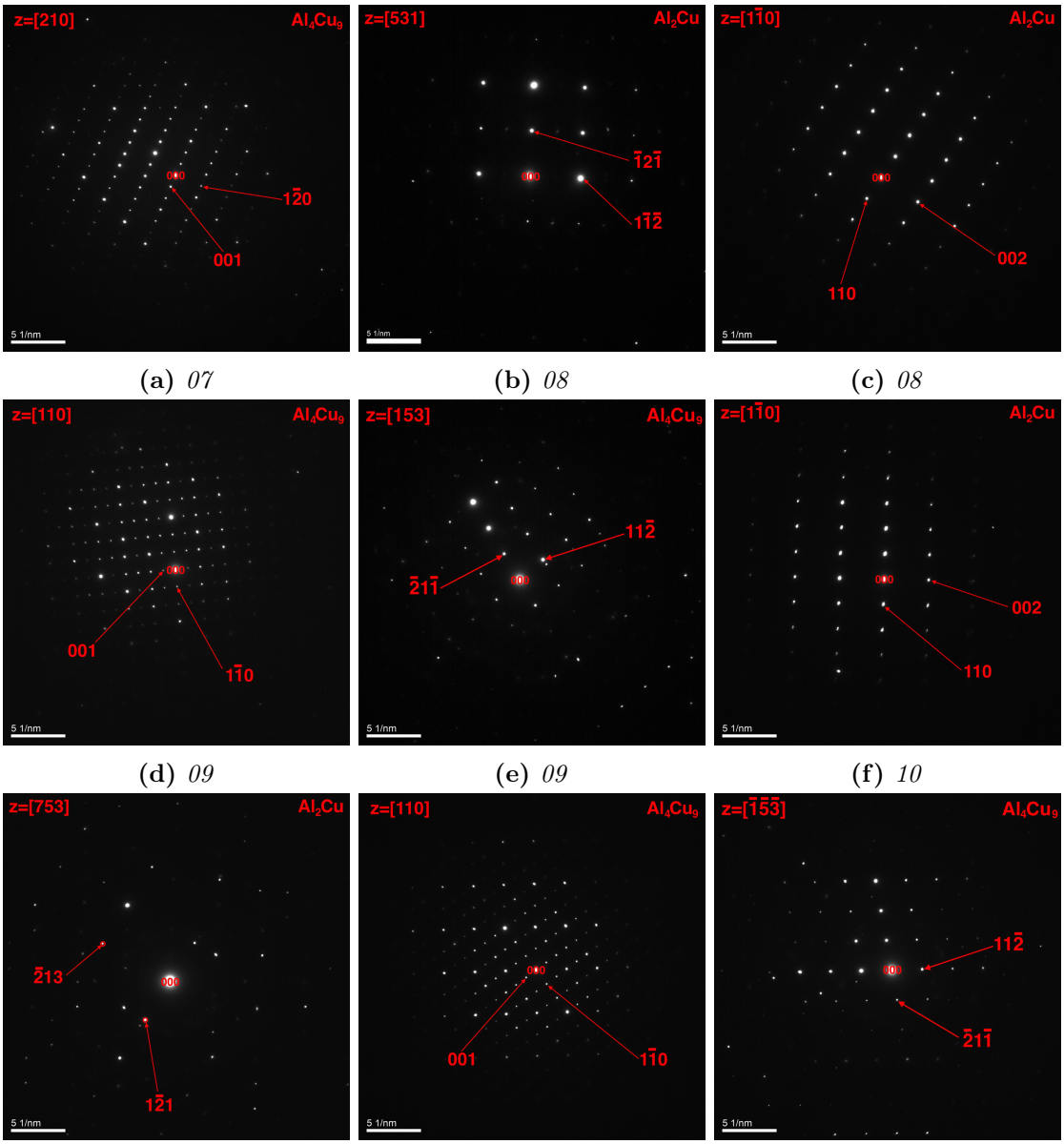

(a) *07* **(b)** *08* **(c)** *08*

(d) *09* **(e)** *09* **(f)** *10*

(g) *10* **(h)** *11* **(i)** *11*

Figure D.2: ***Part 2:*** *SADPs taken from the Al-Cu-nr.1 specimen. The IMCs the SADPs correspond to have been written on the upper right corner of each image while the zone axis, z, have been written on the upper left corner. The numbers in the subtitles indicate which numbered-region in figure 4.8b each DP is taken from.*

Appendix

E SADPs from Al-Cu-nr.2

Figures E.1–E.4 show the SADPs taken from Al-Cu-nr.2. The IMC each SADPs correspond to have been written on the upper right corner of each image while the zone axis, z, have been written on the upper left corner. The numbers in the subtitles indicate which numbered-region in figure 4.11b each DP is taken from.

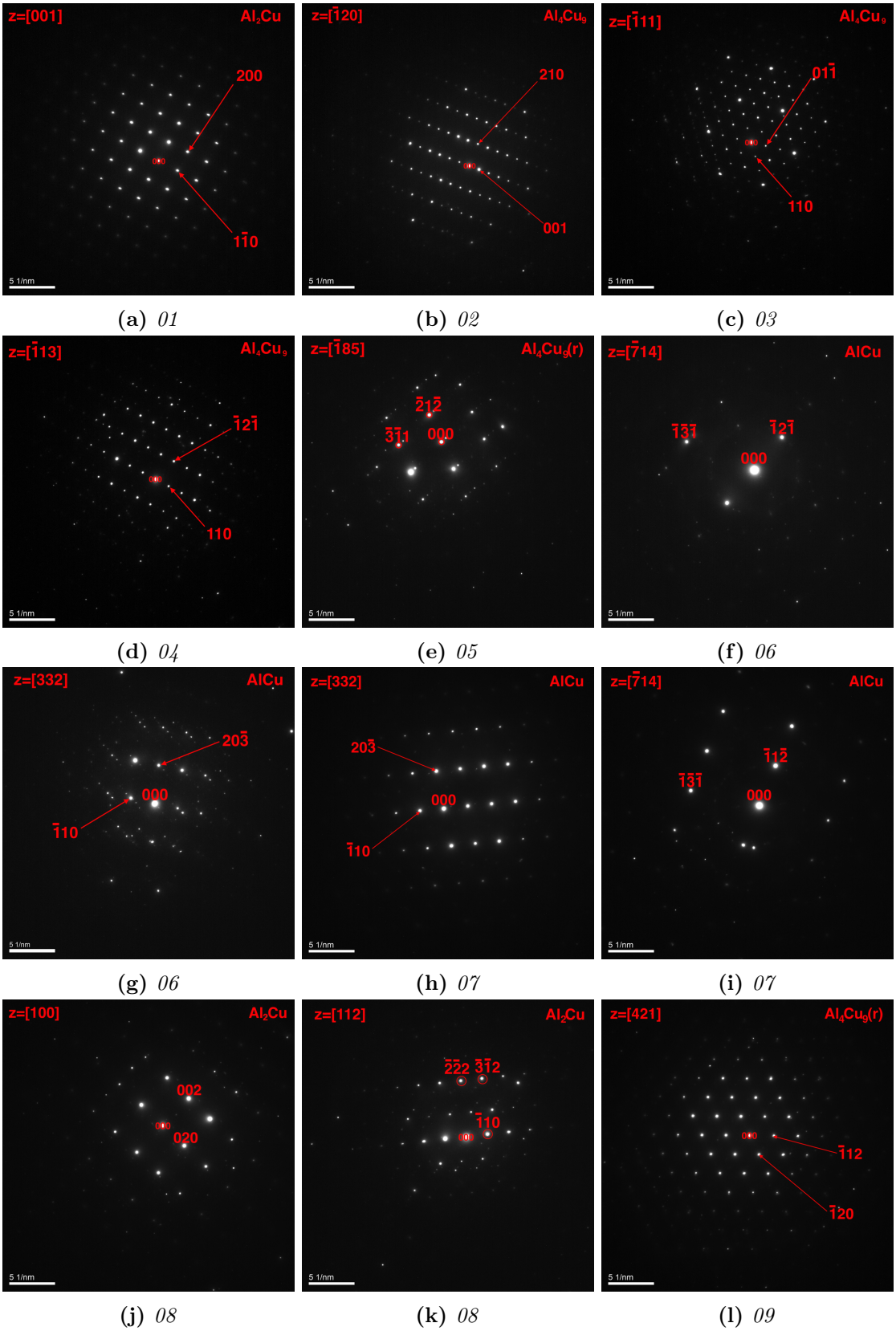

(a) *01* **(b)** *02* **(c)** *03*

(d) *04* **(e)** *05* **(f)** *06*

(g) *06* **(h)** *07* **(i)** *07*

(j) *08* **(k)** *08* **(l)** *09*

Figure E.1: ***Part 1:*** *SADPs taken from the Al-Cu-nr.2 specimen. The IMCs the SADPs correspond to have been written on the upper right corner of each image while the zone axis, z, have been written on the upper left corner. The numbers in the subtitles indicate which numbered-region in figure 4.11b each DP is taken from.*

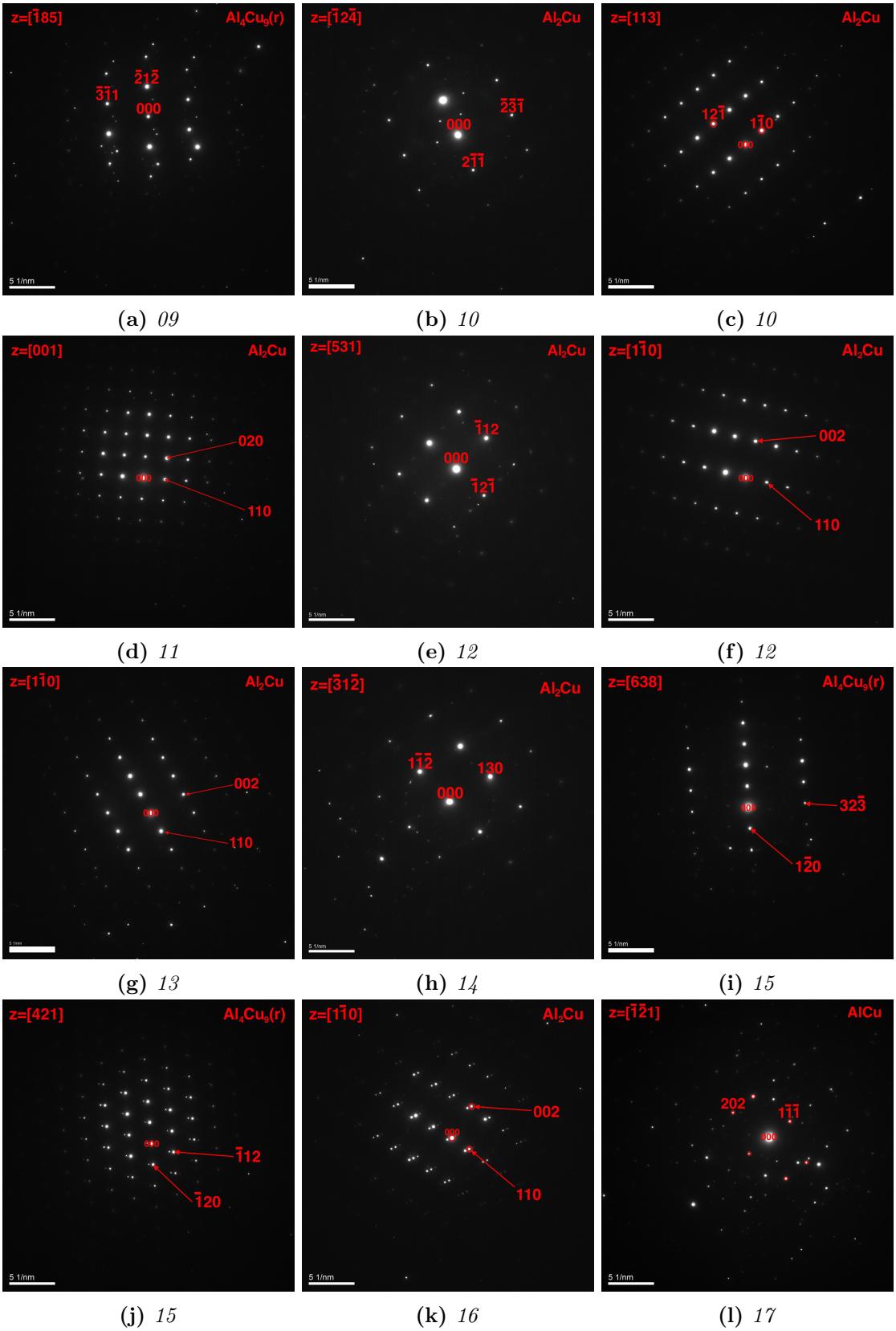

(a) *09* **(b)** *10* **(c)** *10*

(d) *11* **(e)** *12* **(f)** *12*

(g) *13* **(h)** *14* **(i)** *15*

(j) *15* **(k)** *16* **(l)** *17*

Figure E.2: ***Part 2:*** *SADPs taken from the Al-Cu-nr.2 specimen. The IMCs the SADPs correspond to have been written on the upper right corner of each image while the zone axis, z, have been written on the upper left corner. The numbers in the subtitles indicate which numbered-region in figure 4.11b each DP is taken from.*

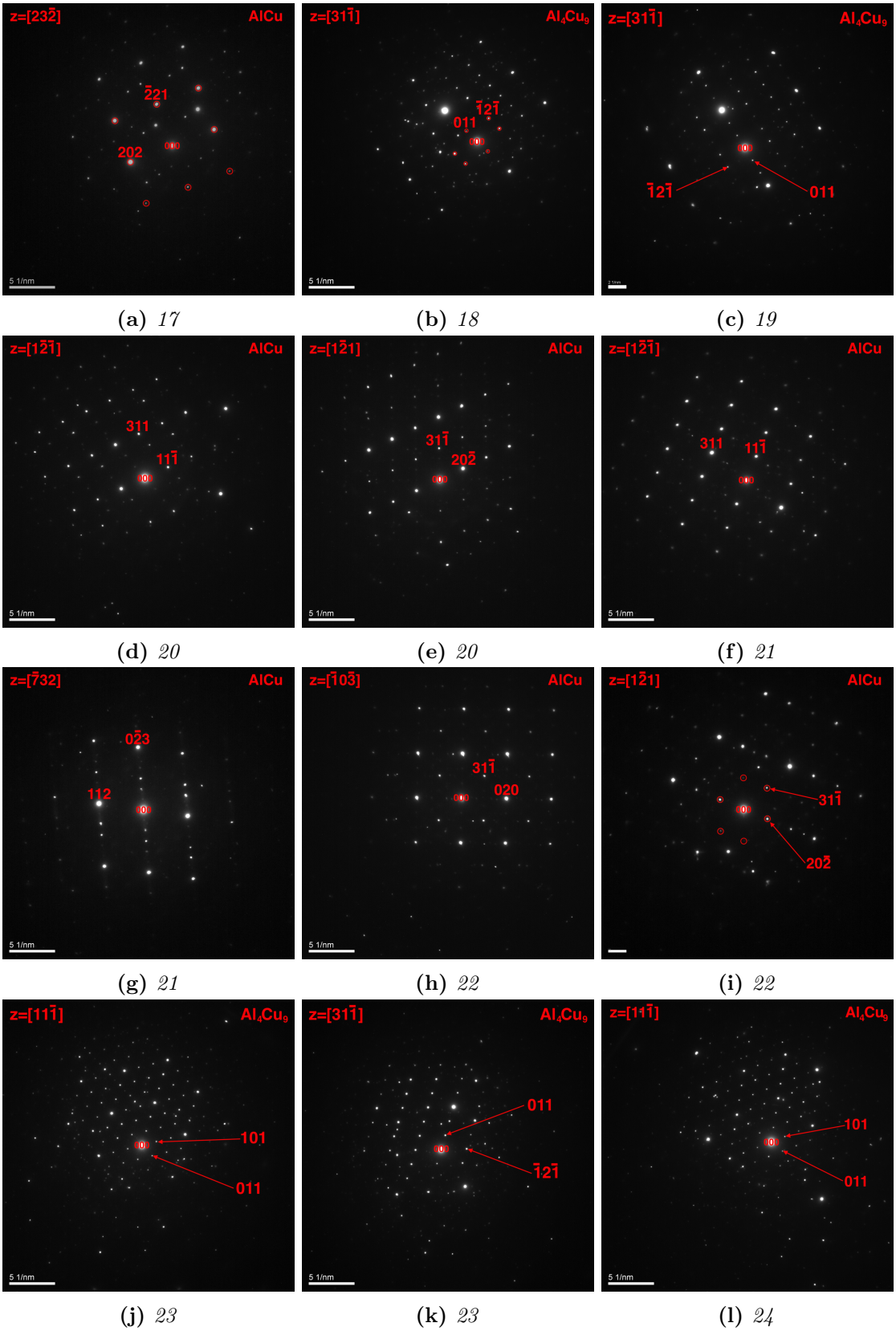

(a) *17* **(b)** *18* **(c)** *19*

(d) *20* **(e)** *20* **(f)** *21*

(g) *21* **(h)** *22* **(i)** *22*

(j) *23* **(k)** *23* **(l)** *24*

Figure E.3: ***Part 3:*** *SADPs taken from the Al-Cu-nr.2 specimen. The IMCs the SADPs correspond to have been written on the upper right corner of each image while the zone axis, z, have been written on the upper left corner. The numbers in the subtitles indicate which numbered-region in figure 4.11b each DP is taken from.*

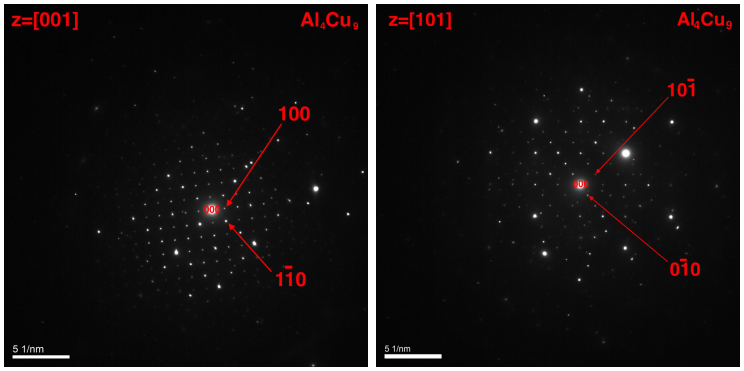

(a) *25* **(b)** *26*

Figure E.4: ***Part 4:*** *SADPs taken from the Al-Cu-nr.2 specimen. The IMCs the SADPs correspond to have been written on the upper right corner of each image while the zone axis, z, have been written on the upper left corner. The numbers in the subtitles indicate which numbered-region in figure 4.11b each DP is taken from.*

Appendix

F SEM images of Al-Ti tensile test specimens 2-4

Each Al-Ti specimen broke into top and bottom pieces. The surfaces of both the top and the bottom pieces, i.e. fracture surfaces, were examined in SEM. The SE and BSE images, taken in SEM, of the fracture surfaces of Al-Ti specimen 1 were shown earlier in figure 4.34, and the rest of the specimens, 2 to 4, are shown in figures F.1–F.3, respectively. These images show the surfaces of both the top and bottom pieces of the broken tensile test specimens.

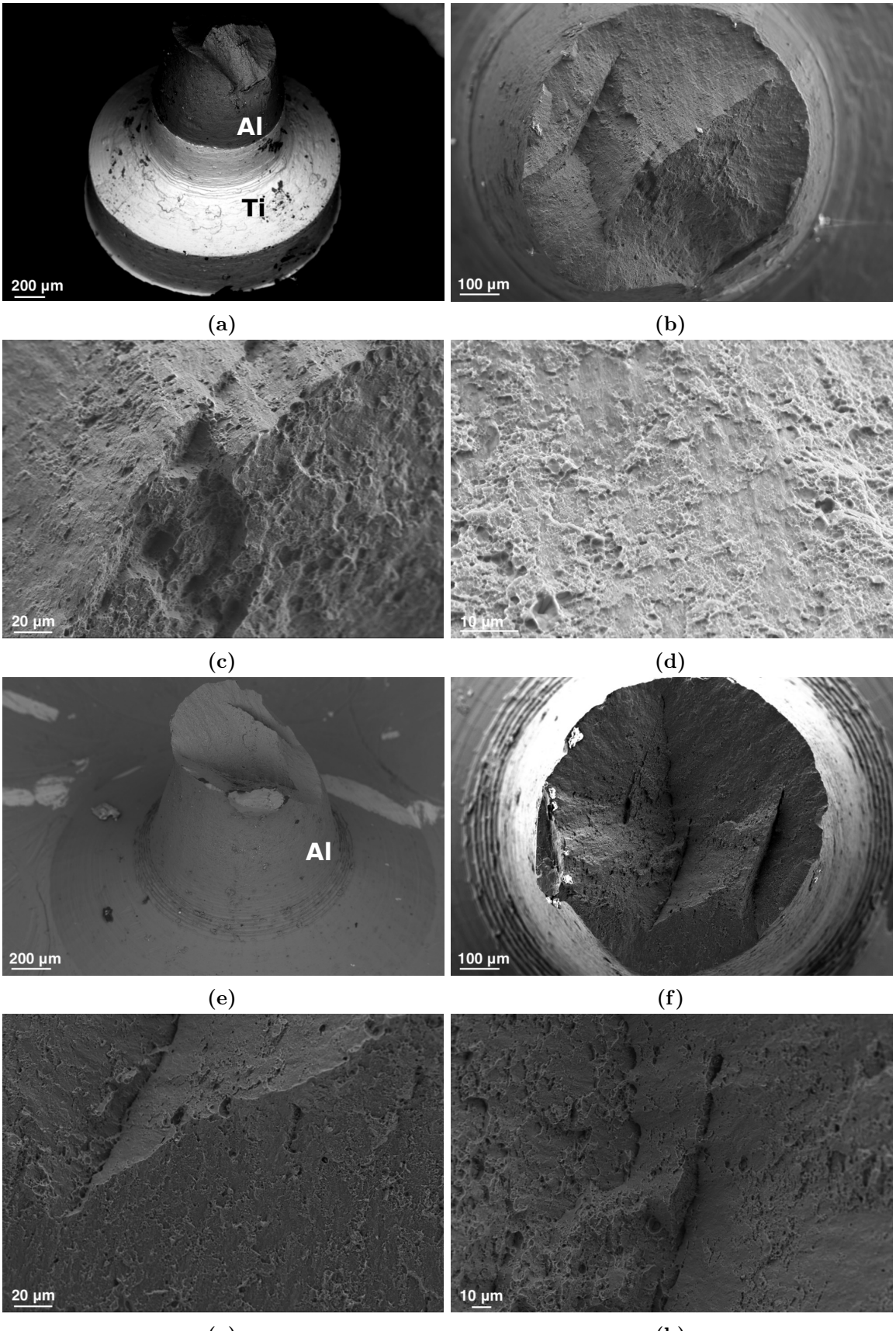

Figure F.1: *(a) BSE and (b)-(d) SE images of the top piece of specimen 2 from the Al-Ti interface, and (e) BSE and (f)-(h) SE images of the bottom piece of the same specimen.*

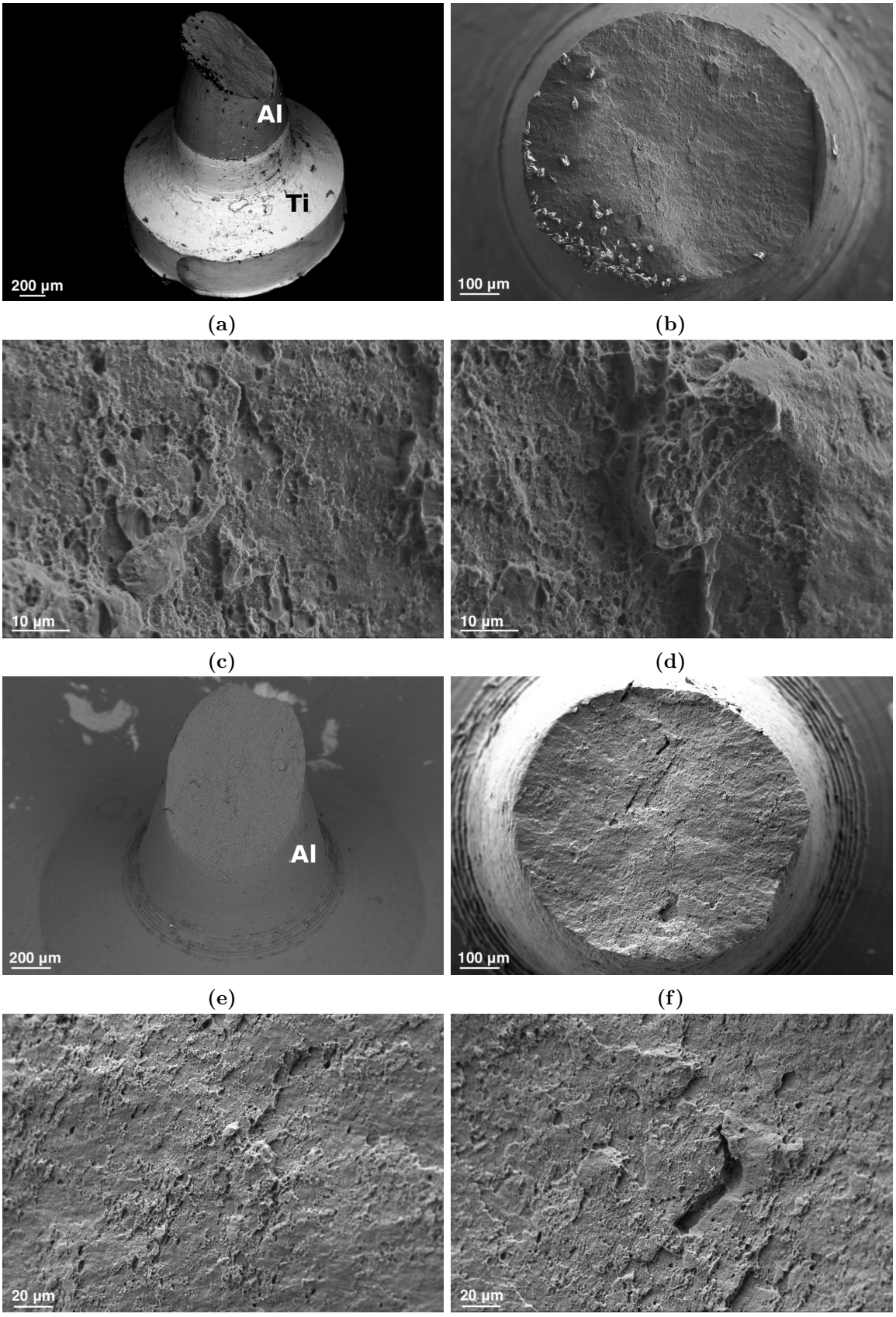

Figure F.2: *(a) BSE and (b)-(d) SE images of the top piece of specimen 3 from the Al-Ti interface, and (e) BSE and (f)-(h) SE images of the bottom piece of the same specimen.*

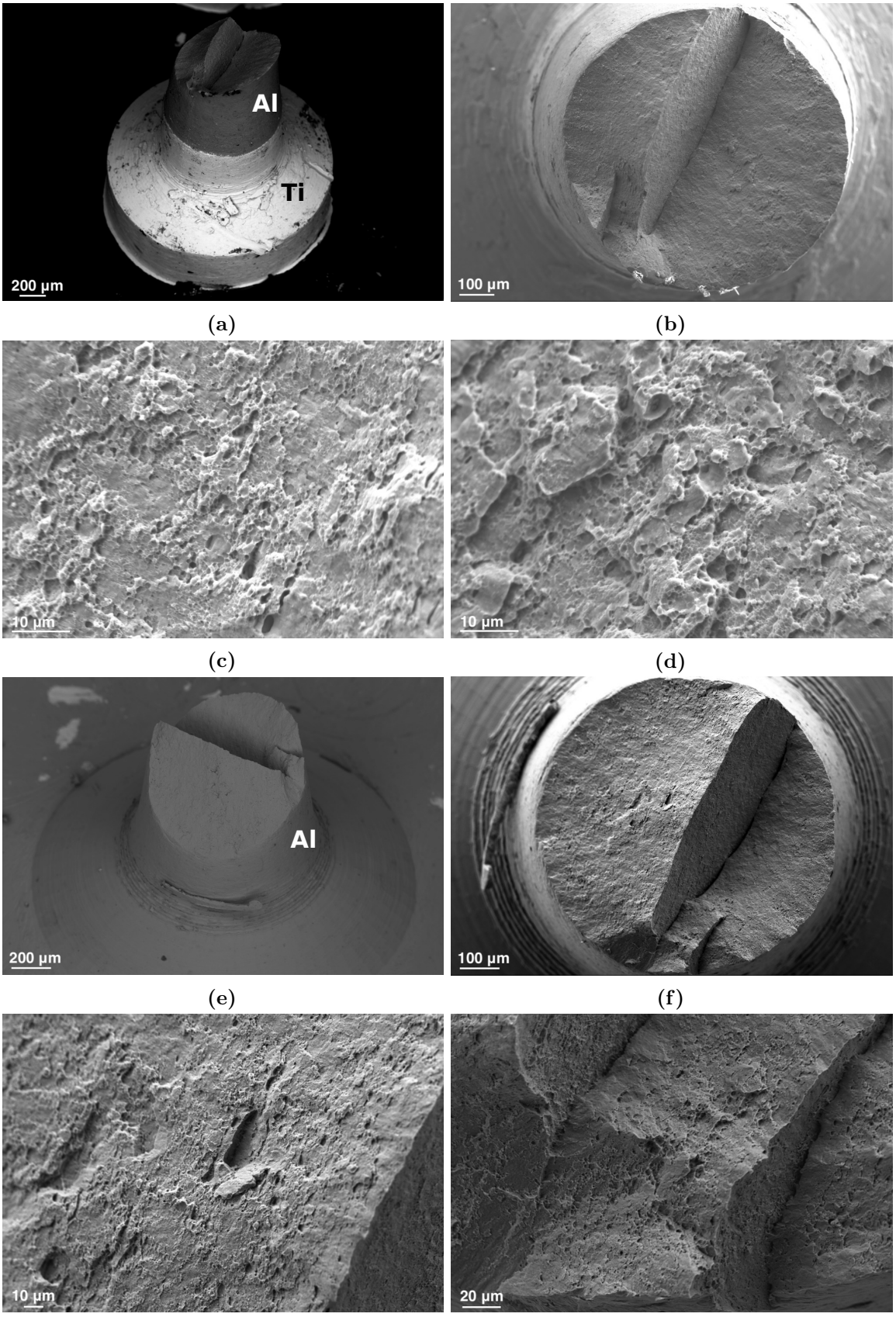

Figure F.3: *(a) BSE and (b)-(d) SE images of the top piece of specimen 4 from the Al-Ti interface, and (e) BSE and (f)-(h) SE images of the bottom piece of the same specimen.*

Appendix

G SEM images of Al-steel tensile test specimens 2-4

Each Al-steel specimen broke into top and bottom pieces. The surfaces of both the top and the bottom pieces, i.e. fracture surfaces, were examined in SEM. The BSE images, taken in SEM, of the fracture surfaces of Al-steel specimen 1 were shown earlier in figure 4.35, and the rest of the specimens, 2 to 4, are shown in figures G.1–G.3, respectively. These images show the surfaces of both the top and bottom pieces of the broken tensile test specimens.

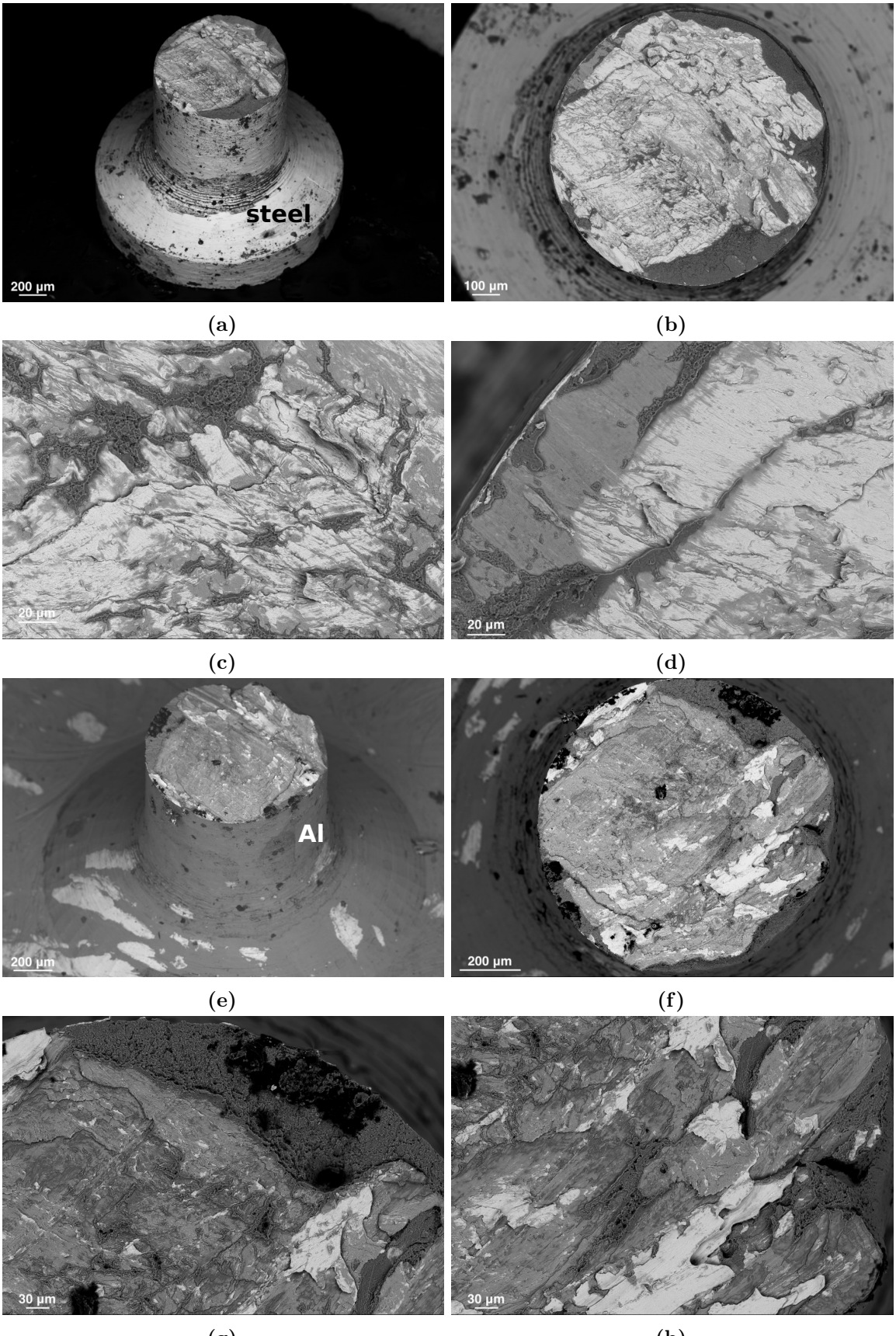

(a) **(b)**

(c) **(d)**

(e) **(f)**

(g) **(h)**

Figure G.1: *BSE images of (a)-(d) the top piece and (e)-(h) the bottom piece of specimen 2 from the Al-steel interface.*

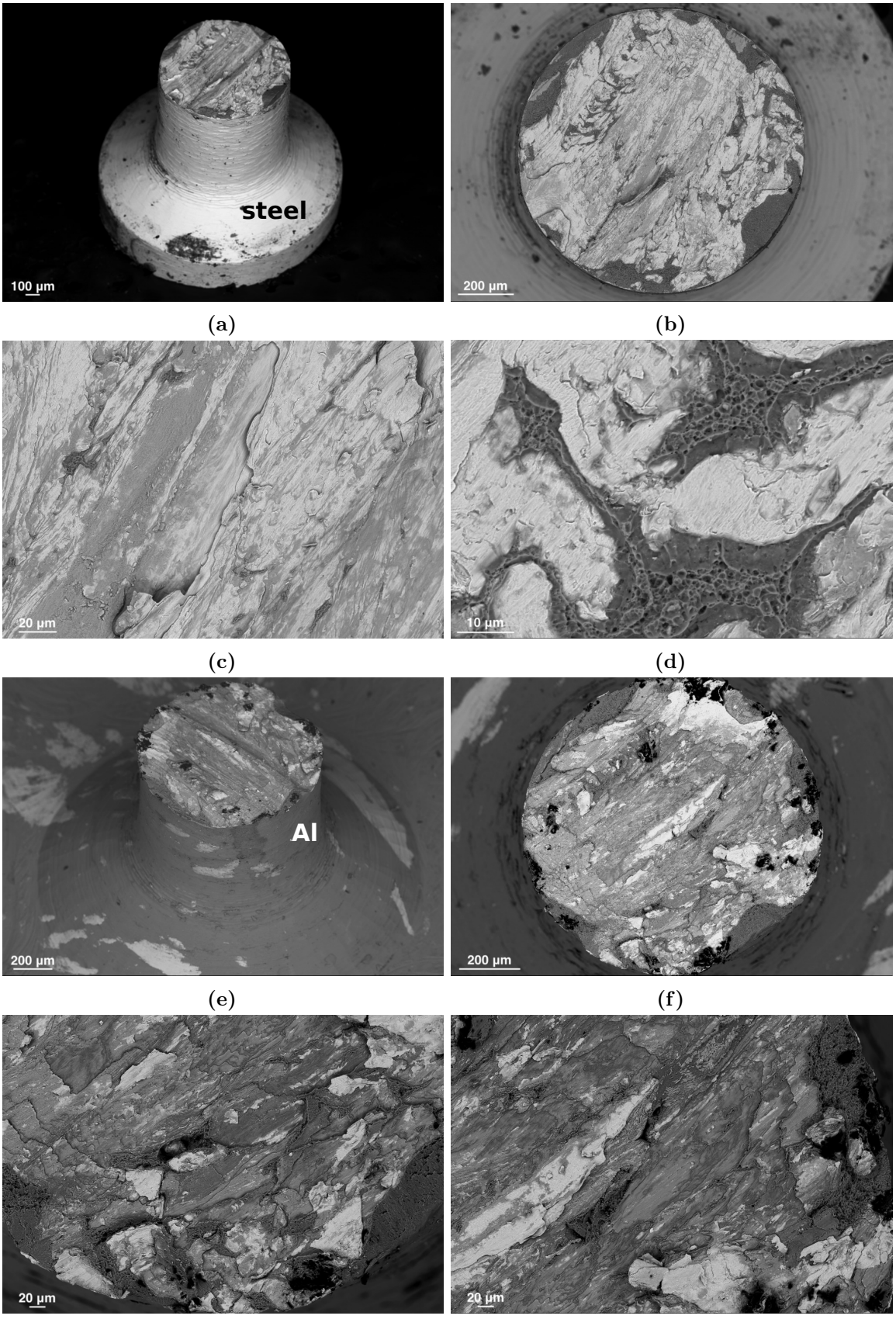

Figure G.2: *BSE images of (a)-(d) the top piece and (e)-(h) the bottom piece of specimen 3 from the Al-steel interface.*

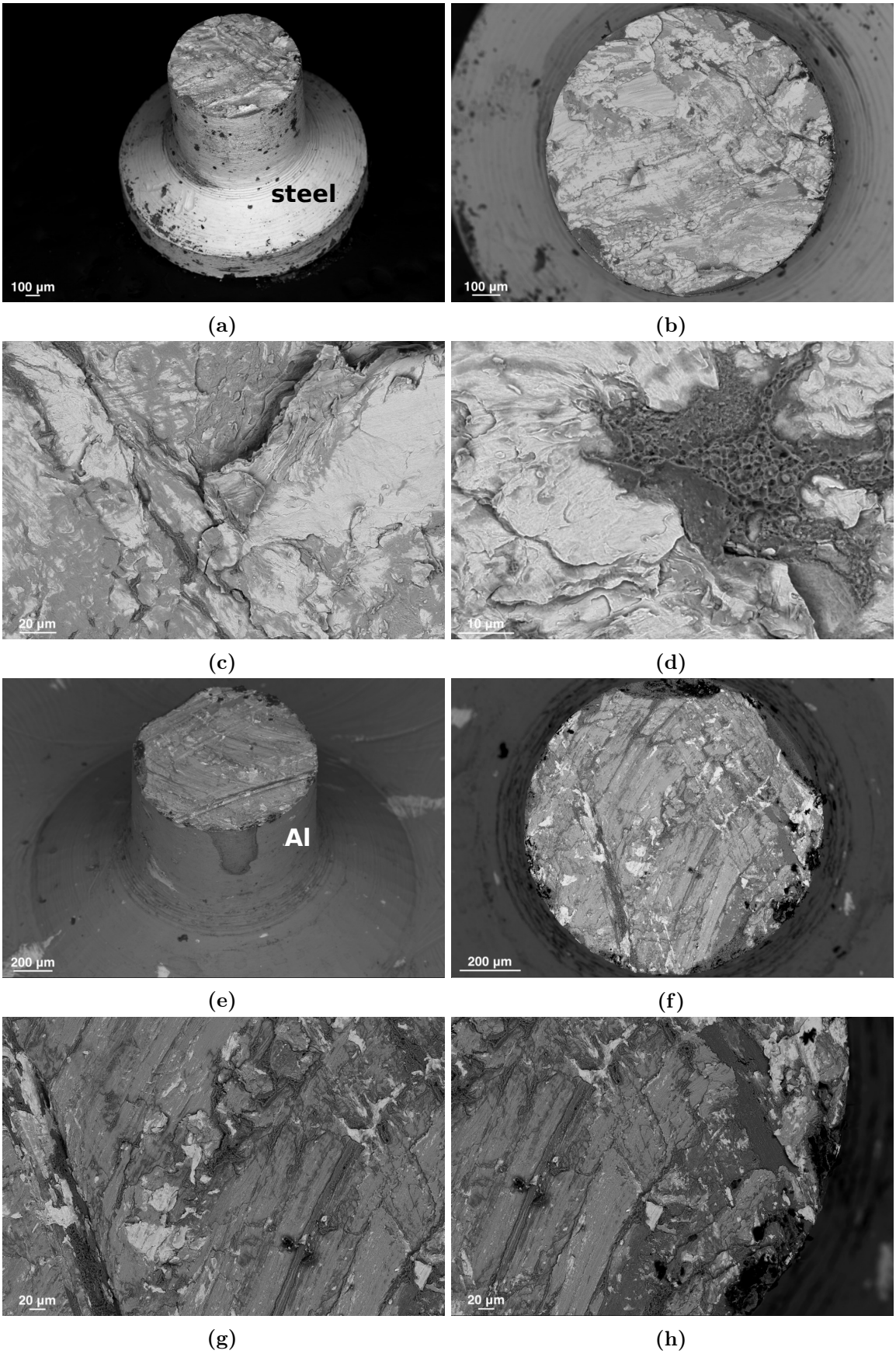

(a) **(b)** **(c)** **(d)** **(e)** **(f)** **(g)** **(h)**

Figure G.3: *BSE images of (a)-(d) the top piece and (e)-(h) the bottom piece of specimen 4 from the Al-steel interface.*

Appendix

H SEM images of Al-Cu tensile test specimens 2-4

The Al-Cu specimens did not survive machining before tensile testing, however, the surfaces of four remaining bottom pieces were still examined in SEM. BSE and SE images of Al-Cu specimen 1 were shown earlier in figure 4.36 while the similar images from Al-Cu specimens 2-4 are presented in figures H.1–H.3, respectively.

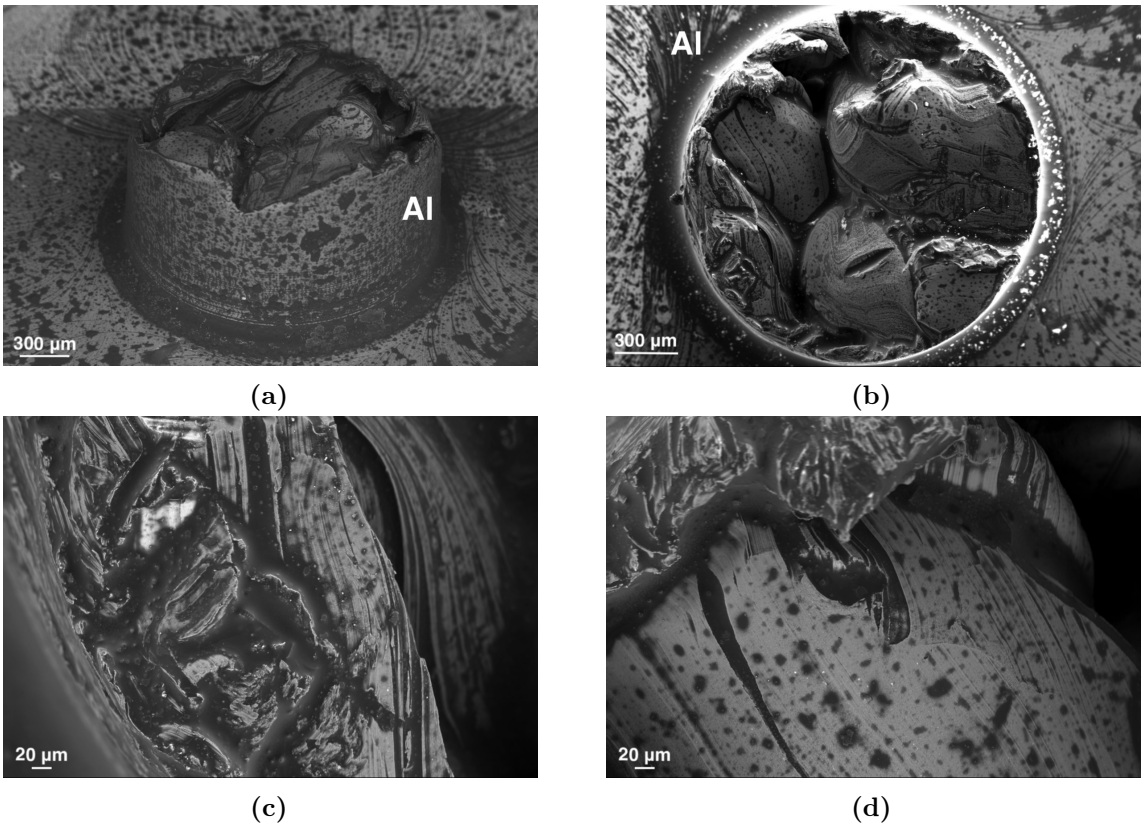

Figure H.1: *(b) SE and (a), (c) and (d) BSE images of the bottom piece of specimen 2 from the Al-Cu interface.*

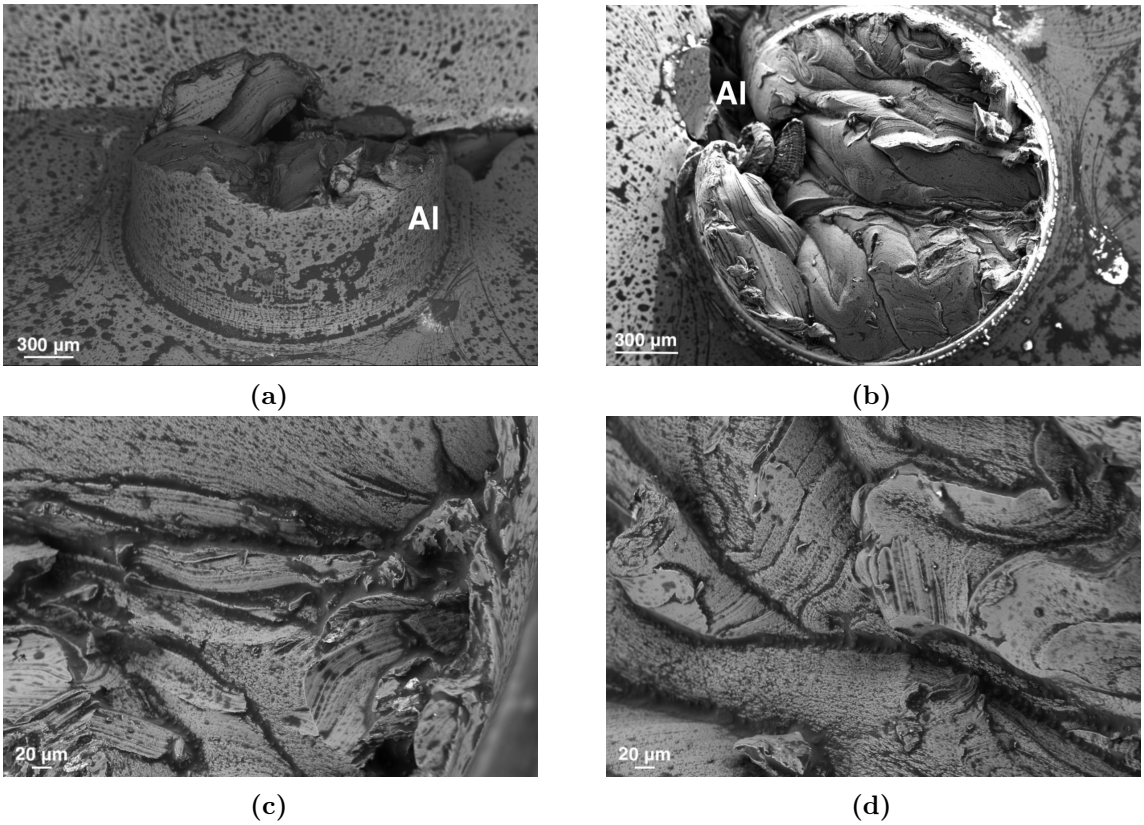

Figure H.2: *(b) SE and (a), (c) and (d) BSE images of the bottom piece of specimen 2 from the Al-Cu interface.*

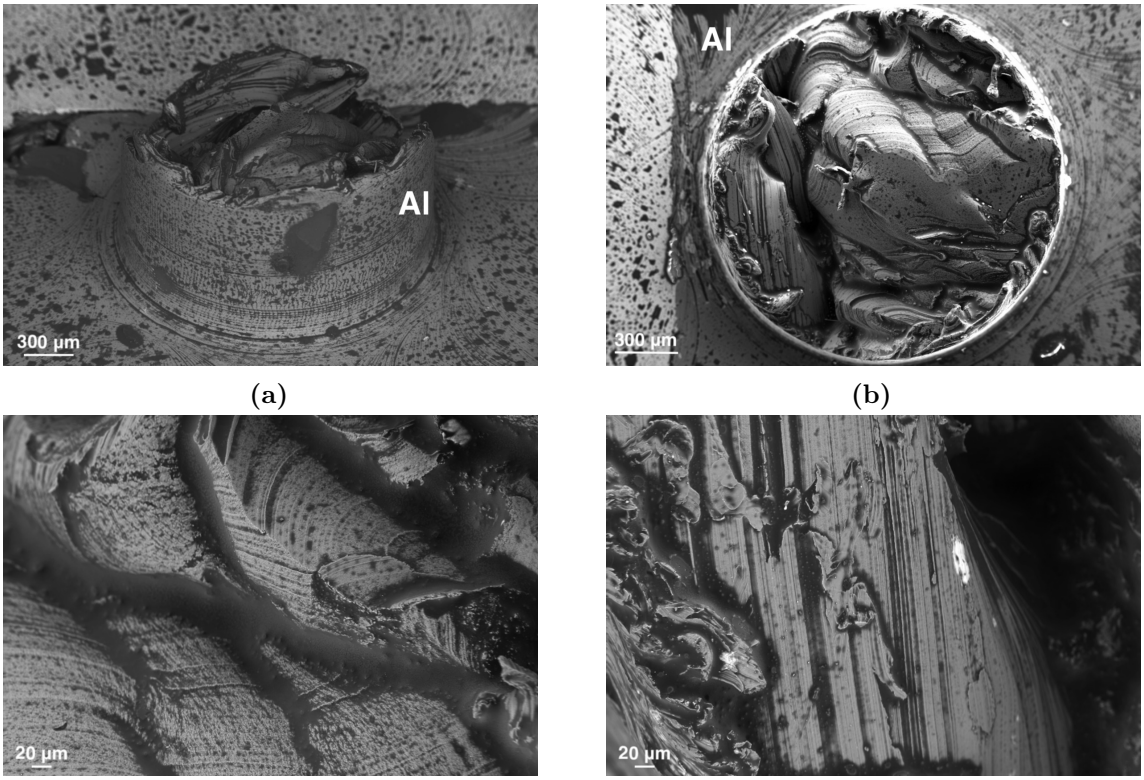

Figure H.3: *(b) SE and (a), (c) and (d) BSE images of the bottom piece of specimen 2 from the Al-Cu interface.*

Hursanay Turgun

Electron Microscopy Characterization of Aluminium-Copper-Titanium-Steel Joint made using HYB

NTNU
Kunnskap for en bedre verden